

AD-A254 932



(2)

RL-TR-92-123
Final Technical Report
June 1992



BISTATIC CLUTTER RCS SIMULATION USING SCALE MODEL ROUGH SURFACES

University of Massachusetts Research Foundation

Z. Fried, G. Phillips and J. Waldman

DTIC
ELECTE
AUG 27 1992
S A D

APPROVED FOR PUBLIC RELEASE; DISTRIBUTION UNLIMITED.

1125445
92-23739



82 8 26 039

Rome Laboratory
Air Force Systems Command
Griffiss Air Force Base, NY 13441-5700

This report has been reviewed by the Rome Laboratory Public Affairs Office (PA) and is releasable to the National Technical Information Service (NTIS). At NTIS it will be releasable to the general public, including foreign nations.

RL-TR-92-123 has been reviewed and is approved for publication.

APPROVED: KVN/Rao

K. V. N. RAO
Project Engineer

FOR THE COMMANDER:



JOHN K. SCHINDLER
Director
Electromagnetics & Reliability Directorate

If your address has changed or if you wish to be removed from the Rome Laboratory mailing list, or if the addressee is no longer employed by your organization, please notify RL(ERCE) Hanscom AFB MA 01731-5000. This will assist us in maintaining a current mailing list.

Do not return copies of this report unless contractual obligations or notices on a specific document require that it be returned.

REPORT DOCUMENTATION PAGE

Form Approved
OMB No. 0704-0188

Public reporting burden for this collection of information is estimated to average 1 hour per response, including the time for reviewing instructions, searching existing data sources, gathering and maintaining the data needed, and completing and reviewing the collection of information. Send comments regarding this burden estimate or any other aspect of this collection of information, including suggestions for reducing this burden, to Washington Headquarters Services, Directorate for Information Operations and Reports, 1215 Jefferson Davis Highway, Suite 1204, Arlington, VA 22202-4302, and to the Office of Management and Budget, Paperwork Reduction Project (0704-0188), Washington, DC 20503.

1. AGENCY USE ONLY (Leave Blank)		2. REPORT DATE June 1992	3. REPORT TYPE AND DATES COVERED Final
4. TITLE AND SUBTITLE BISTATIC CLUTTER RCS SIMULATION USING SCALE MODEL ROUGH SURFACES		5. FUNDING NUMBERS C - F19628-88-K-0020 PE - 61102F PR - 2305 TA - J4 WU - 38	
6. AUTHOR(S) Z. Fried, G. Phillips and J. Waldman		8. PERFORMING ORGANIZATION REPORT NUMBER	
7. PERFORMING ORGANIZATION NAME(S) AND ADDRESS(ES) University of Massachusetts Research Foundation 450 Aiken Street Lowell MA 01854		9. SPONSORING/MONITORING AGENCY NAME(S) AND ADDRESS(ES) Rome Laboratory (ERCE) Hanscom AFB MA 01731-5000	
10. SPONSORING/MONITORING AGENCY REPORT NUMBER RL-TR-92-123		11. SUPPLEMENTARY NOTES Rome Laboratory Project Engineer: K. V. N. Rao/ERCE(617)377-3106	
12a. DISTRIBUTION/AVAILABILITY STATEMENT Approved for public release; distribution unlimited.		12b. DISTRIBUTION CODE	
13. ABSTRACT (Maximum 200 words) Bistatic scattering cross section measurements of CO ₂ laser radiation from roughened metal and dielectric surfaces were made and compared to predictions given by the facet model. The scattered polarization state was analyzed along two directions, perpendicular (HH) and parallel (HV) to the scattering plane. The (σ ₀) _{HH} nulls predicted by the facet model have been verified at steep incident angles for both metallic and dielectric surfaces. Agreement is generally better for metals than dielectrics. At shallower angles measurements diverge from theoretical predictions. A number of calculations of polarization dependent scattering cross sections from metal and dielectric cylinders of radius r as a function of r/λ have been performed. These calculations suggest that even for large radii surfaces, rapid amplitude and phase variations are responsible for the onset of depolarization at shallower incident and scattering angles, leading to the disagreement with the tangent plane model predictions. They also clearly demonstrate why the facet model is a better approximation, in the region of validity, for metals than dielectrics. The experimental measurements are described in detail and data for both roughened metals and dielectrics are presented for several scattering aspect and depression angles.			
14. SUBJECT TERMS Bistatic scattering, Scattering measurements, Rough surface scattering			15. NUMBER OF PAGES 150
			16. PRICE CODE
17. SECURITY CLASSIFICATION OF REPORT UNCLASSIFIED	18. SECURITY CLASSIFICATION OF THIS PAGE UNCLASSIFIED	19. SECURITY CLASSIFICATION OF ABSTRACT UNCLASSIFIED	20. LIMITATION OF ABSTRACT U/L

TABLE OF CONTENTS

ABSTRACT.....	1.
INTRODUCTION.....	2.
EXPERIMENTAL SET-UP.....	8.
SCATTERING DATA.....	15.
DISCUSSION OF RESULTS.....	31.
APPENDIX A - ANALYTICAL ANGLE TRANSFORMATION.....	46.
APPENDIX B - ADDITIONAL SCATTERING DATA.....	49.

Accesion For	
NTIS	CRA&I <input checked="" type="checkbox"/>
DTIC	TAB <input type="checkbox"/>
Unannounced <input type="checkbox"/>	
Justification	
By	
Distribution /	
Availability Codes	
Dist	Avail and / or Special
A-1	

DTIC QUALITY INSPECTED 3

LABORATORY MEASUREMENTS OF SCATTERED ELECTROMAGNETIC
RADIATION FROM TWO DIMENSIONAL METALLIC AND
DIELECTRIC ROUGH SURFACES.

ABSTRACT

Bistatic and non specular scattering cross section measurements of CO₂ laser radiation from roughened metal and dielectric surfaces were made and compared to predictions given by the facet (tangent plane approximation) model. The incident radiation was linearly polarized perpendicular to the incident plane. The scattered polarization state was analyzed along two directions, perpendicular (HH) and parallel (HV) to the scattering plane. For the first time, such polarization dependent bistatic measurements are reported over the entire hemisphere, using a scattering apparatus designed especially for this work. The average slopes and radii of curvature of the roughened surfaces utilized in this study were determined from surface tracings using a mechanical profilometer. The $(\sigma_0)_{HH}$ nulls predicted by the facet model have been verified at steep incident angles for both metallic and dielectric surfaces. Agreement is generally better for metals than dielectrics. At shallower angles measurements diverge from theoretical predictions. Our data indicate that the departure from the predictions of the facet model is most likely associated with surface curvature. A number of calculations of polarization dependent scattering cross sections from metal and dielectric cylinders of radius r as a function of r/λ have been performed. These calculations suggest that even for large radii surfaces, rapid amplitude and phase variations are responsible for the onset of depolarization at shallower incident and scattering angles, leading to the disagreement with the tangent plane model predictions. They also clearly demonstrate why the facet model is a better approximation, in the region of validity, for metals than dielectrics. The role of curvature in determining the operable regions of the tangent plane model is further illuminated through a series of scattering measurements from metal wires with radius of curvature on the order of λ . The experimental measurements are described in detail and data for both roughened metals and dielectrics are presented for several scattering aspect and depression angles.

INTRODUCTION

Scattering of electromagnetic radiation by rough surfaces has been the subject of great interest for several decades^[1]. Interest in this derives from a need to study terrain characteristics of inaccessible sites and to detect and characterize small deviations from optically smooth surfaces. In either case, the goals are to relate electromagnetic scattering data to the properties of the scattering surface. In principle, knowledge of the exact shape of the scattering surface and the total electric field \mathbf{E} at the surface allows one to compute the electric field \mathbf{E}_2 at the point of observation. The exact solution is given by equation (1) where k is the magnitude of the wave vector of the incident radiation and \mathbf{R} is the distance between some point on the illuminated surface and the observation point^[2]:

$$\mathbf{E}_2(\mathbf{P}) = \frac{1}{4\pi} \int_s \left(\mathbf{E} \frac{\partial \psi}{\partial \mathbf{n}} - \psi \frac{\partial \mathbf{E}}{\partial \mathbf{n}} \right) d\mathbf{S} \quad (1)$$

where

$$\psi = \frac{e^{ik||\mathbf{R}|}}{|\mathbf{R}|} \quad (2)$$

A cursory look at equation (1) immediately confronts one with the two fundamental obstacles to finding $\mathbf{E}_2(\mathbf{P})$. One problem is that the exact shape of the surface is unknown. Secondly, given the detailed geometry of the surface, there still remains the problem of knowing the value of the total \mathbf{E} on the surface, as given by (3).

$$\mathbf{E} = \mathbf{E}_i + \mathbf{E}_s \quad (3)$$

\mathbf{E}_i and \mathbf{E}_s represent the incident and scattered electric fields on the surface, respectively. To obtain the value of \mathbf{E} , one must solve the boundary conditions for both \mathbf{E} and \mathbf{H} at the surface. Unfortunately, closed form solutions for the latter problem exist only for plane surfaces. In the high

frequency or geometrical optics (GO) limit, the ratio of scattered to incident electric field is the same as the corresponding quantities obtained from the Fresnel coefficients. Consequently, in the GO limit, this part of the problem is eliminated. The need to characterize the surface, however, remains. An exact mapping of the surface is an insurmountable task and may not be necessary. It is usually assumed that different microscopic surface shapes will yield similar scattering patterns, when illuminated over a sufficiently large area of the rough surface. The statistical characterization of rough surfaces is motivated by the need to obtain closed form expressions for $E_2(P)$ without detailed knowledge of the surface shape. A model in which one assumes a random distribution of hemispherical bosses^[3], the tangent plane model (TP)^[4] and the two scale roughness model^[5], are commonly used. The TP approximation is the most straightforward approach. In the GO limit, all shapes can be handled by the TP approximation in which only the average surface slopes are of interest. To obtain a statistical representation of the surface, it is important that the illuminated area provides an adequate representation of the surface characteristics. Papa, Lennon, and Taylor^[6], henceforth denoted as PLT, have shown that for uncorrelated heights and slope distributions, in a Gaussian surface, the physical optics approach yields identical results to those obtained in the GO limit, provided that the correlation length T is much larger than the wavelength and the average slopes are significantly less than one. Another important observation of PLT is that in the TP regime, the polarization of the scattered wave is independent of the detailed statistical properties of the surface.

Previous measurements of rough surface scattering^[7,8] were performed in the monostatic configuration or under conditions where the scattered radiation was in the plane of incidence. Such an arrangement precludes the experimental study of some interesting features of polarization dependence. These manifest themselves only in configurations where the scattering plane is different from the incident plane. The apparatus utilized in this study allows the measurement of scattered radiation in both the polar and azimuthal directions.

Unlike smooth surfaces, roughened surfaces scatter in all directions. This requires the detector to be moveable over a hemisphere. Practical considerations, especially for a liquid nitrogen cooled IR (infrared) detector, limit the motion of the detector to the horizontal plane in the laboratory. To insure accessibility of arbitrary scattering angles, the polar angle θ_s and particularly ϕ , the azimuthal angle, require that the target surface be free to rotate around two perpendicular axes. At the same time, the polarization state of the transmitted radiation must be adjusted to maintain a well defined polarization with respect to the surface normal. A description of the scattering system and the correspondence between laboratory angles in which the mean surface normal changes direction, and the conventionally defined field angles, is presented in section II.

An algorithm to compute laboratory angles for a specific set of field angles is presented in the Appendix. Data were collected in a bistatic configuration where the incident and scattered planes were different. The co-pol and cross-pol scattering cross section measurements were compared with the theoretical predictions of PLT^[6]. Using a form of the scattering cross section given by Barrick^[4] (equation 4), PLT describe the angular dependences of σ_o as a function of polarization, surface roughness, and dielectric constant. The scattering cross section is given by^[4,6]:

$$\sigma_o = |\beta_{pq}|^2 JS \quad (4)$$

In equation (4), S is the shadowing function^[4,6] and J is the probability density function^[4,6] for surface slopes. J is proportional to $(\frac{T}{\sigma})^2$ times an exponential function of $\frac{T}{\sigma}$, where T is the average facet spacing and σ is the average facet depth.

As described by Barrick⁴, a specular point in the surface reflects like a tilted plane tangent to the surface at that point. The β_{pq} in equation (4) are given below in terms of the Fresnel coefficients for HH and VV waves and spherical scattering coordinates (see Figure 2).

$$\beta_{VV} = \frac{a_2 a_3 R_{||}(i) + \sin(\theta_i) \sin(\theta_s) \sin^2(\phi_s) R_{\perp}}{a_1 a_4} \quad (5)$$

$$\beta_{HV} = \frac{\sin \phi_s [-\sin \theta_i a_3 R_{||}(i) + \sin \theta_s a_2 R_{\perp}(i)]}{a_1 a_4} \quad (6)$$

$$\beta_{VH} = \frac{\sin \phi_s [\sin \theta_s a_2 R_{||}(i) + \sin \theta_i a_3 R_{\perp}(i)]}{a_1 a_4} \quad (7)$$

$$\beta_{HH} = \frac{-\sin \theta_i \sin \theta_s \sin^2 \phi_s R_{||}(i) - a_2 a_3 R_{\perp}(i)}{a_1 a_4} \quad (8)$$

with

$$a_1 = 1 + \sin \theta_i \sin \theta_s \cos \phi_s - \cos \theta_i \cos \theta_s \quad (9)$$

$$a_2 = \cos \theta_i \sin \theta_s + \sin \theta_i \cos \theta_s \cos \phi_s \quad (10)$$

$$a_3 = \sin \theta_i \cos \theta_s + \cos \theta_i \sin \theta_s \cos \phi_s \quad (11)$$

$$a_4 = \cos \theta_i + \cos \theta_s \quad (12)$$

The angle (i) is the angle of incidence with respect to the local normal of the facet. It is defined below in terms of the scattering angles of Figure 2.

$$\cos i = \frac{1}{\sqrt{2}} [1 - \sin \theta_i \sin \theta_s \cos \phi_s + \cos \theta_i \cos \theta_s]^{1/2} \quad (13)$$

In equation (4), the J term is proportional to the average number of facets having slopes which scatter into the observation direction. The shadowing function S gives the fraction of the total number of specular points not shadowed^[9]. In the analysis of PLT, it is pointed out that neither the shadowing function nor the slope statistical J term has an influence on the position of nulls in the scattering cross section. Thus, the predicted angular position of nulls in σ_o as given by these authors is based solely on the behavior of $|\beta_{pq}|^2$ in equation (4). Furthermore, their analysis shows that for a given incident

signal polarization, there exists nulls in the co-pol scattering cross section for various angles.

In this work, the predicted polarization dependent behavior of the scattering cross section as given above was observed, for a subset of incident scattering angles. For steep incident and receive polar angles, the data given in this report conforms to predictions of the TP approximation. Deficiencies in the TP model appear for larger angles. The inability of the TP approximation to accurately describe the scattering of radiation for all angles has been noted previously in other, monostatic measurements^[7,8]. The departure from the TP model has been attributed to the neglect of small scale roughness of the surface and to neglect of multiple scattering from facets with large slopes. A convincing argument can be made that curvature inherent in rough surfaces is a major cause of the observed deviation from the facet model.

A good way to test the adequacy of the TP approximation is to juxtapose the TP predictions with exact calculations. For example, we can compare the reflection coefficients computed for the case of radiation incident on a cylinder with the results obtained if we approximate the cylinder by a set of tangent planes. It is possible to describe analytically the polarization dependent scattering amplitude and phase for perfect curved geometries, such as cylinders, in terms of the parameter, r/λ . The onset of depolarization for certain scattering geometries and the departure of data from the TP model is shown to be critically dependent on this parameter. A series of calculations of scattering from metal and dielectric cylinders is given in section IV. These calculations disclose the very rapid phase and amplitude variation of the VV and HH components of the scattered field as a function of incident angle and surface curvature. A description of these calculations and their significance in understanding scattering from rough surfaces is also contained in section IV.

A degree of insight into polarization dependent scattering can be attained from these calculations by characterizing the roughened surfaces according to slope and radius of curvature.

Metal and dielectric rough surfaces utilized in this study were prepared in the following manner. The surfaces were blasted with glass beads under a pressure of approximately 80 psi. The bead diameters ranged from 50 to 500 μm . Profilometer measurements were performed on both metal and dielectric rough surfaces. A digitization technique in which the plotted profilometer data was converted into computer readable data files was employed and programming was developed to calculate the average surface slope and radius of curvature. Utilizing these techniques, the average values of these surface parameters for the entire surface were determined as well as that percentage of the surface falling within a certain range of the parameters. Table I displays results of such measurements for the surface utilized in this study in which the radii of curvature are given in units of the wavelength. Finally, results from randomly arranged metal wires with $r \sim \lambda$ are reported, yielding further evidence that the departure from the facet model predictions is due to surface curvature.

The organization of this report is as follows.

Section II contains a discussion of the laboratory setup. Section III is devoted to a set of laboratory scattering data. In Section IV we discuss the data.

Appendix A contains formulae for transforming field angles into laboratory angles. Appendix B contains additional scattering data.

II. EXPERIMENTAL SETUP AND DISCUSSION OF LABORATORY ANGLES

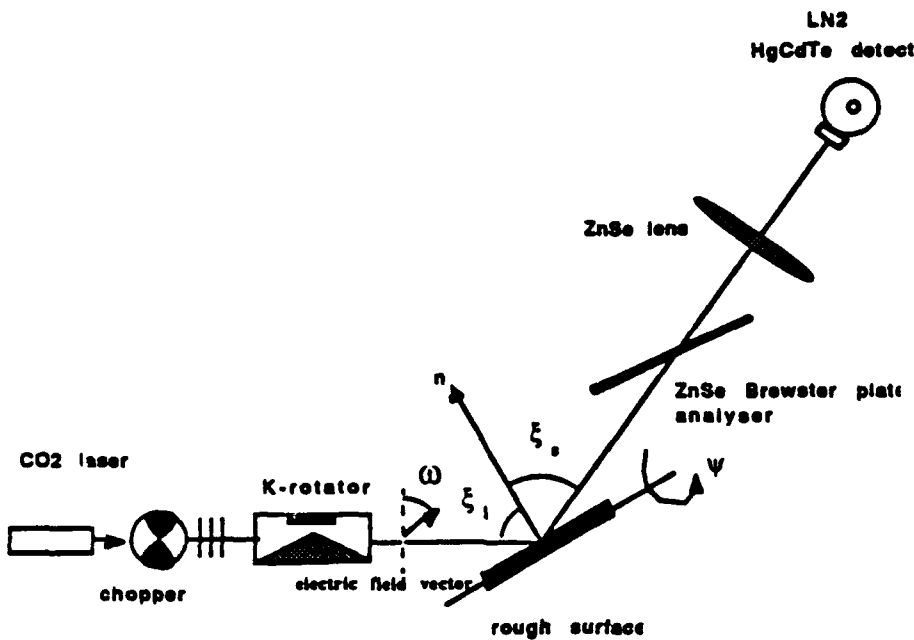


Figure 1 Component Diagram of Scatterometer System

The source of radiation is a CO₂ laser (Ultra Lasertech Model 5122) providing 10 watts of linearly polarized radiation with a choice of 48 lines between 9.2 to 10.8 microns. The ability to rotate the linearly polarized radiation to any desired angle is provided by a K-rotator. The rough surface is allowed to rotate through two degrees of freedom which, in conjunction with the position of the detector, simulates the environment of a bistatic radar in the field. At the receive end, discrimination between polarization states is accomplished by rotating a Brewster plate analyzer and wire grid polarizer analyzer. The combination of the two yields an extinction ratio of better than 1000 : 1. The radiation is collected by a two inch diameter ZnSe lens with a focal length of 20 inches. A liquid nitrogen cooled HgCdTe detector (detectivity = 10^{10} cm Hz^{1/2}/Watt), mounted on a rotatable detector arm in the focal plane of the lens, scans the resultant intensity pattern. Scanning over a finite angular spread and averaging the data is necessitated by the scintillation pattern that results from the narrow-band laser radiation scattering from the rough surface. The detector output is fed to a lock-in amplifier and the angle averaged signal displayed on a Mac II computer.

The rough surface is mounted on a goniometer which can rotate through a range of 90° . This rotation is about an axis that is parallel to a horizontal surface. The goniometer is mounted on a turn-table which rotates through a vertical axis. By means of these two components, the target surface can be rotated around two axes.

The detector has a range of 270° and is rotated independently of the target surface.

The setup can simulate the three independent field angles, ie, the incident and scattering polar angles from 0 to 90° , and the scattering azimuthal angle from 0 to 180° . The rest of the azimuthal range, 180 - 360° , can be obtained by rotating the target surface around its mean normal.

The transformation of the field angles into the corresponding laboratory angles will now be presented.

In the field frame, the target surface orientation is fixed and the transmit and receive directions (vectors) can vary independently over a hemisphere (see Figure 2). In this frame, we designate the following angles θ_i , θ_s , and ϕ_s . θ_i stands for the incident angle, the angle between the incident propagation direction and target normal.

$$\mathbf{r}_i \cdot \mathbf{n} = -\cos(\theta_i) \quad (14)$$

where \mathbf{r}_i is a unit vector along the direction of propagation, and \mathbf{n} is a unit vector along the surface normal. Similarly,

$$\mathbf{r}_s \cdot \mathbf{n} = \cos(\theta_s) \quad (15)$$

where r_s is a unit vector along the detector direction and

$$\frac{[r_i \cdot n(r_i \cdot n)]}{\sin(\theta_i)} \cdot \frac{[r_s \cdot n(r_s \cdot n)]}{\sin(\theta_s)} = \cos(\phi_s) \quad (16)$$

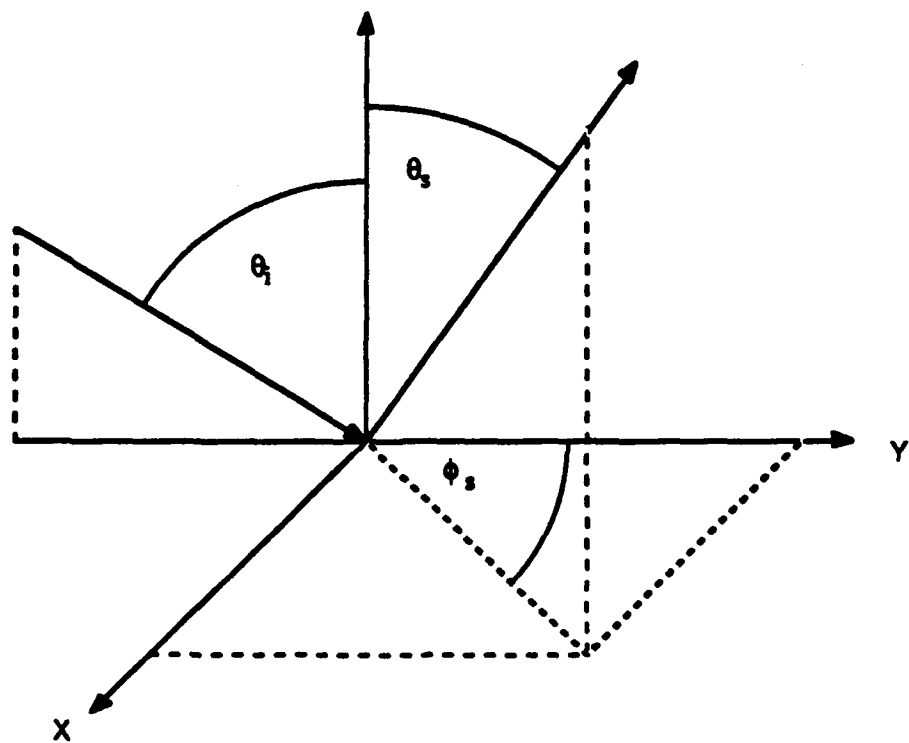


Figure 2. Definition of field angles

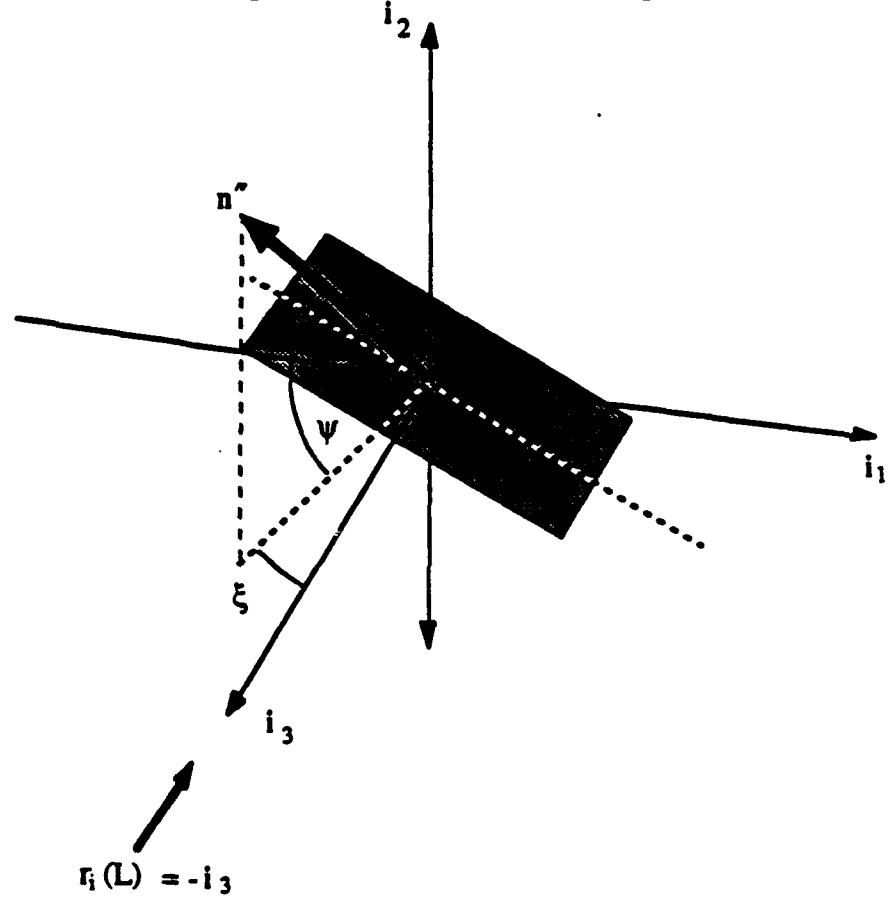


Figure 3. Definition of laboratory angles for $\xi \neq 0$ and $\psi \neq 0$

In the laboratory frame (Figure 3), the propagation direction is fixed, which is taken along the negative z-axis. Thus,

$$\mathbf{r}_i(L) = -i_3 \quad (17)$$

where L designates the laboratory frame and i_3 is a unit vector along the z-axis (Figure 3). The detector arm is in the x-z plane and can be rotated through 270° (Figure 4).

Hence

$$\mathbf{r}_D(L) = \cos(\eta) i_1 + \sin(\eta) i_3 \quad (18)$$

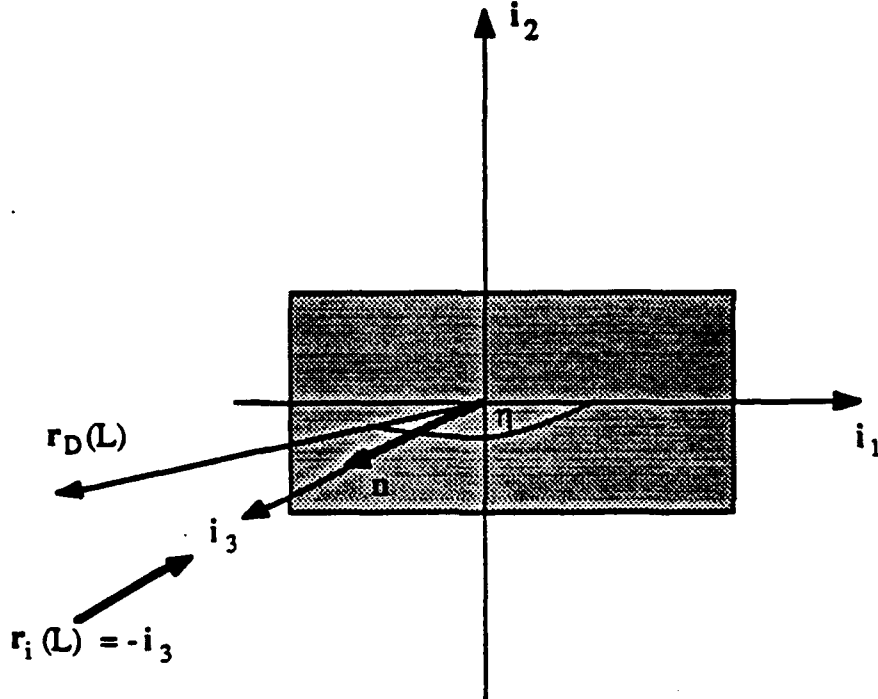


Figure 4. Laboratory system for $\psi = 0$ and $\xi = 0$ showing the detector position $\mathbf{r}_D(L)$

The target surface normal can be rotated around two perpendicular axes. One rotation is around the y-axis (Figure 4), the axis perpendicular to the x-z plane containing the transmitter and receiver. The angle describing this rotation is designated by ξ . The range of ξ is 0° to 90° . The detector arm requires a 180° range for any fixed ξ . Hence, the full range of the detector has to be 270° . Figure 5 shows the case for $\xi_i \neq 0$. The relation between ξ_s and η is $\xi_s = \eta - 90^\circ$. ξ equals the incident field depression angle, θ_i , when the target is rotated around the y-axis only.

A second rotation can be performed around the line which is the intersection of the target plane and the x-z plane (Figure 3).

The first rotation fixes ξ and the second rotation fixes ψ . When the target surface is rotated through ξ and ψ in succession, the normal to the target surface, expressed in the unit vectors of the laboratory coordinate system is:

$$\mathbf{n}'' = -\mathbf{i}_1 \sin(\xi) \cos(\psi) + \mathbf{i}_2 \sin(\psi) + \mathbf{i}_3 \cos(\xi) \cos(\psi) \quad (19)$$

While ξ_i is now not equal to the incident depression angle, we will, for convenience, refer to it as the "laboratory depression angle", and similarly refer to ψ as the laboratory aspect angle.

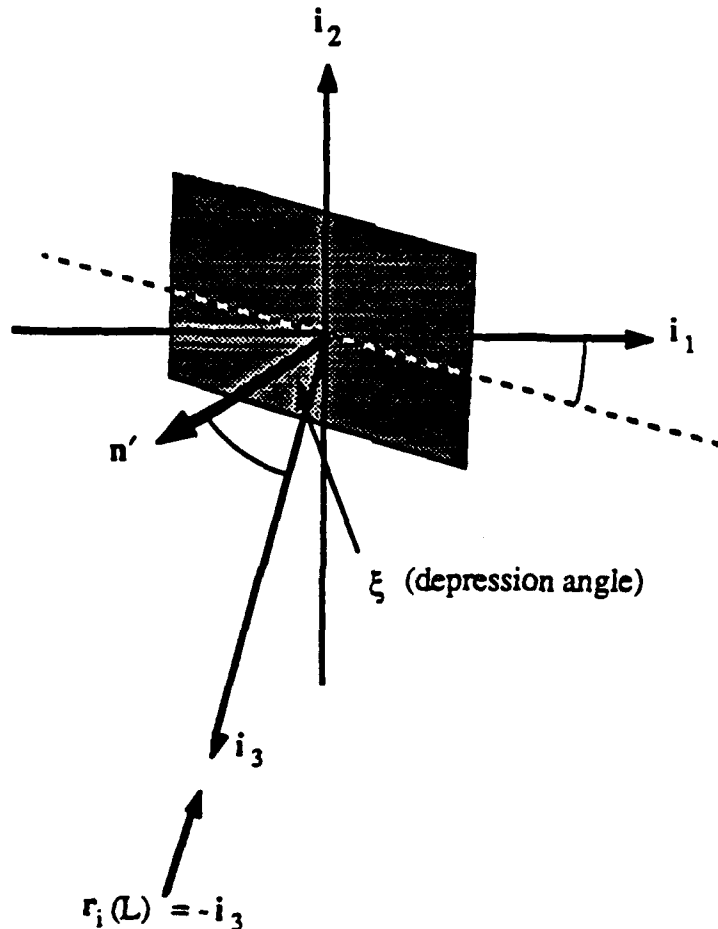


Figure 5. Laboratory system for $\xi = 0$ and $\psi = 0$

We note that the scalar products (14)-(16) defining the various field angles retain the same form when \mathbf{n}'' is substituted for \mathbf{n} . The following expressions relate laboratory angles (ξ, ψ, η) to field angles $(\theta_i, \theta_s, \phi_s)$

$$\cos(\theta_i) = \mathbf{r}_i \cdot \mathbf{n}'' = \cos(\xi) \cos(\psi) \quad (20)$$

$$\cos(\theta_s) = \mathbf{r}_D \cdot \mathbf{n}'' = \sin(\eta - \xi) \cos(\psi) \quad (21)$$

and

$$\cos(\phi_s) = \frac{\mathbf{r}_i \cdot \mathbf{r}_D - (\mathbf{r}_i \cdot \mathbf{n}'') (\mathbf{r}_D \cdot \mathbf{n}'')}{\sqrt{1 - (\mathbf{r}_i \cdot \mathbf{n}'')^2} \sqrt{1 - (\mathbf{r}_D \cdot \mathbf{n}'')^2}}. \quad (22)$$

Substituting Eqns. (17),(18),(20) and (21) into Eqn. (22) yields:

$$\cos(\phi_s) = \frac{-\sin(\eta) + \cos^2(\psi) \sin(\xi - \eta) \cos(\xi)}{\sqrt{1 - \cos^2(\xi)} \sqrt{1 - \cos^2(\psi)}} \quad (23)$$

An algorithm for computing laboratory angles, ξ, η, ψ for a given set of field angles, $\theta_i, \theta_s, \phi_s$, can be found in the Appendix.

III Scattering Data

Scattering data were obtained from roughened aluminum surfaces, roughened dielectric surfaces, randomly arranged wires, and a randomly distributed set of glass beads.

A sand blaster was used to roughen aluminum surfaces. The abrasive material used in preparing the surfaces was a collection of glass beads ranging from 50 to 500 microns in diameter. The results of profilometer tracings indicate that the roughening produces randomly distributed valleys ranging from 3 to 9 microns with an average spacing of 70 to 100 microns. Examination of the surfaces under a microscope indicated the existence of sharp edged patches. To remove these sharp edges, the surfaces were electropolished, removing approximately 1 micron of material from the upper surface. Statistical data is given in Table I indicating radius of curvature, slope, and average facet depth for the surface (EBT 4+13) studied. The histogram characterizing this surface according to distribution of facet slopes is plotted in Figure 6.

Data are presented for both copol, $\sigma_o(HH)$, and cross pol, $\sigma_o(HV)$, measurements, as well as ratios of $\sigma_o(HH)/\sigma_o(HV)$. The results are displayed in both laboratory and field coordinates. In the lab coordinates, the transmit and receive laboratory depression angles, ξ_i and ξ_s are set equal and remain fixed. The target surface is rotated around a horizontal axis. This rotation defines the laboratory aspect angle. Changing the laboratory aspect angle induces changes in both θ_i and θ_s , the incident and scattered polar angles. However, there is an intrinsic advantage to performing measurements in the laboratory coordinate system since the laboratory aspect angle is identical to the angle subtended by the global normal and the facet normal (recall that according to the TP model, the scattering at a given angle is due to facets for which the specular condition is fulfilled). Figures 7-8 display both ratios of $\sigma_o(HH)/\sigma_o(HV)$ and $\sigma_o(HH)$ and $\sigma_o(HV)$ in laboratory coordinates. The data

points plotted for $\sigma_o(HH)$ and $\sigma_o(HV)$ have been ratioed in such a way that the data at some small aspect angle coincides with the model prediction. The average slope parameter, $T/\sigma^{[6]}$, which enters into the TP model is obtained from the results of profilometer measurements (Table I). Figures 9-10 show data for $\sigma_o(HH)/\sigma_o(HV)$ and $\sigma_o(HH)$ and $\sigma_o(HV)$ for configurations in which the field angles θ_i and θ_s and the azimuthal scattering angle ϕ_s is varied.

Figures 11-12 display scattering data for roughened plastic surfaces with $n = 1.6$ and $k = 0.002$.

Roughening of the plastic surfaces was accomplished in the following manner. The plastic surfaces were softened in acetone and compressed between roughened aluminum surfaces using c-clamps. After hardening, the roughened plastic surfaces were measured using a mechanical profilometer and found to have surface depths and slopes very similar to the metal surfaces used in their preparation.

Figure 13 displays scattering data from randomly distributed glass beads. Figure 14 displays scattering data from a glass surface roughened with glass beads. Figures 15-16 show scattering data from aluminum wires randomly distributed on an absorbing flat surface.

To obtain a better understanding of both the success and failure of the tangent plane approximation, we prepared a sample target surface consisting of randomly distributed aluminum wires. Wire from a spool was continuously wound two or three layers deep in a random fashion on a flat absorbing plate. The radius $-a$ of the wire was $12.5 \mu\text{m}$ and the corresponding λ/a was 0.85. For such a large value of λ/a , the tangent plane approximation should not work at all. Interestingly, however, the data for the ratio $\sigma_o(HH)/\sigma_o(HV)$ at a 60° laboratory depression angle is remarkably similar to that obtained for the randomly roughened surfaces. A plausible reason for this similarity will be presented in the last section of this report.

Table I
Surface Slopes Depths and Radii
of Curvature for EBT 4 +13

Glass Bead (Dia.)	50 - 500 microns
Average Slope	0.081
RMS Slope	0.118
Standard Deviation	0.086
Average Facet Depth	2.88 microns
% Surface with Slope	
< 0.05	52.8
< 0.10	79.5
< 0.20	95.4
< 0.30	98.7
< 0.40	99.2
< 0.50	99.9
% of Surface with Radius	
of Curvature in Wavelengths	(microns)
< 3	3.6
< 4	5.5
< 5	7.8
< 6	10.5

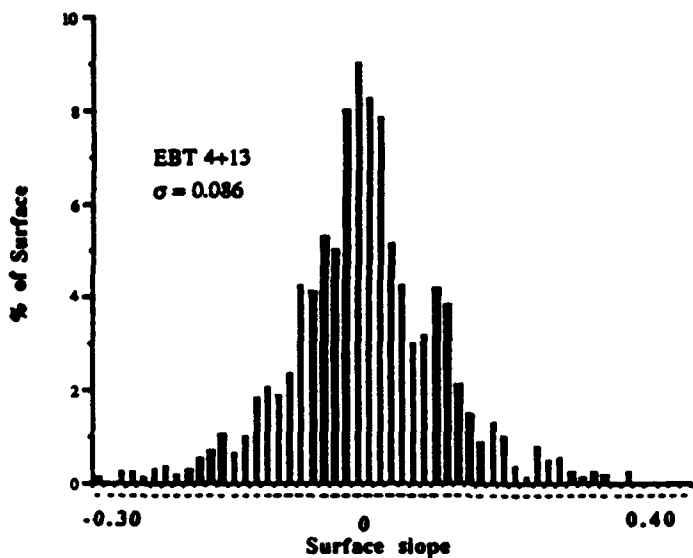


Figure 6 Distribution of Surface Slopes for EBT4+13

Aluminum data (Plots are in Laboratory Angles)

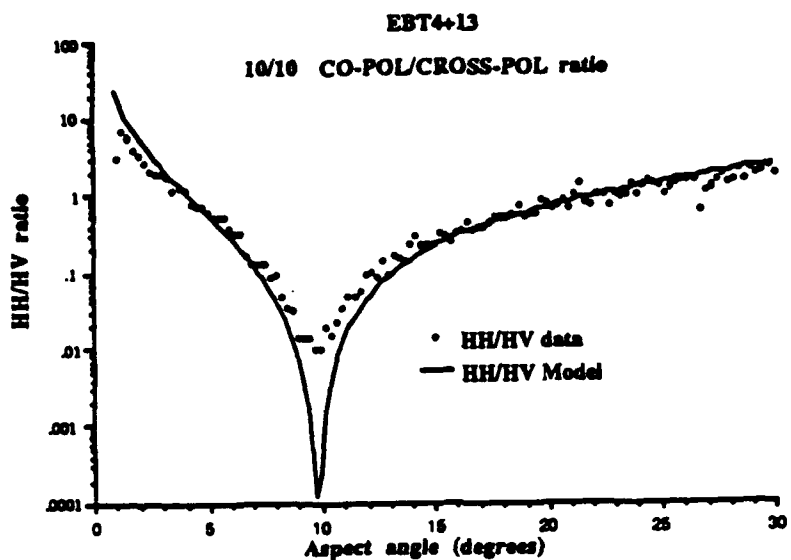


Figure 7a $\sigma_o(HH)/\sigma_o(HV)$ for laboratory depression angles $\xi_i = \xi_s = 10$

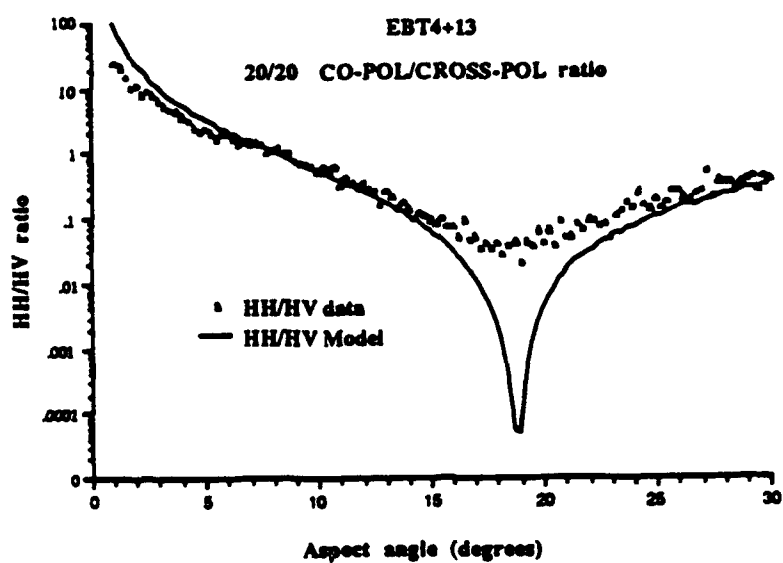


Figure 7b $\sigma_o(HH)/\sigma_o(HV)$ for laboratory depression angles $\xi_i = \xi_s = 20$

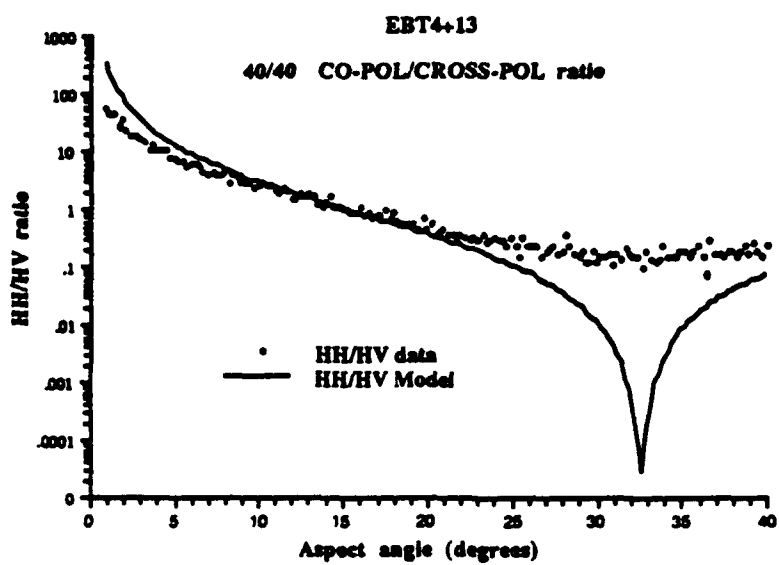


Figure 7c $\sigma_o(\text{HH})/\sigma_o(\text{HV})$ for laboratory depression angles $\xi_i = \xi_s = 40$

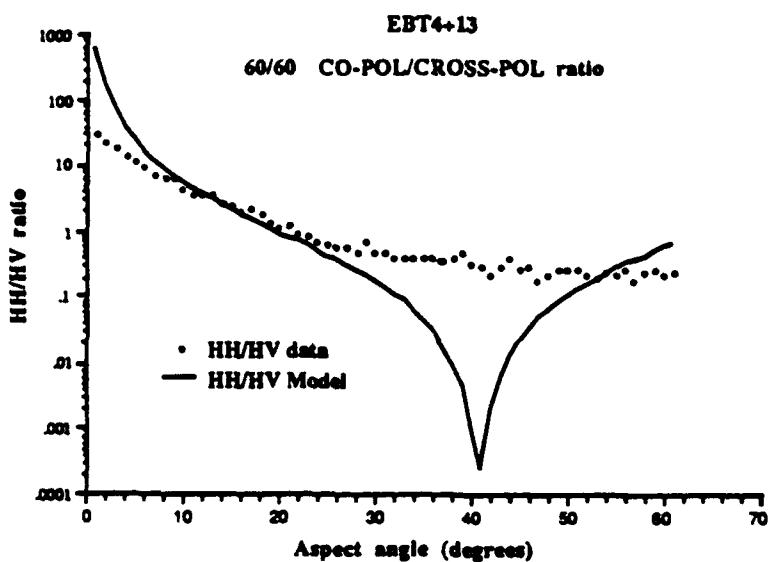


Figure 7d $\sigma_o(\text{HH})/\sigma_o(\text{HV})$ for laboratory depression angles $\xi_i = \xi_s = 60$

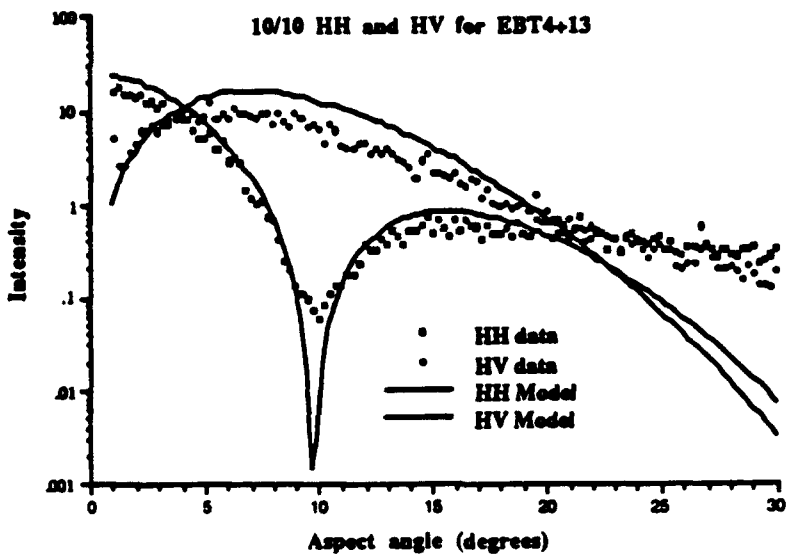


Figure 8a $\sigma_o(\text{HH})$ and $\sigma_o(\text{HV})$ for laboratory depression angles $\xi_i = \xi_s = 10$

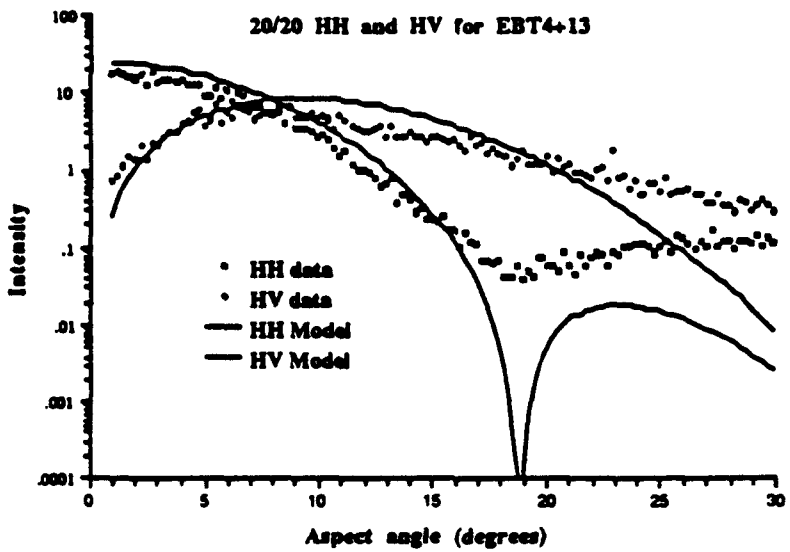


Figure 8b $\sigma_o(\text{HH})$ and $\sigma_o(\text{HV})$ for laboratory depression angles $\xi_i = \xi_s = 20$

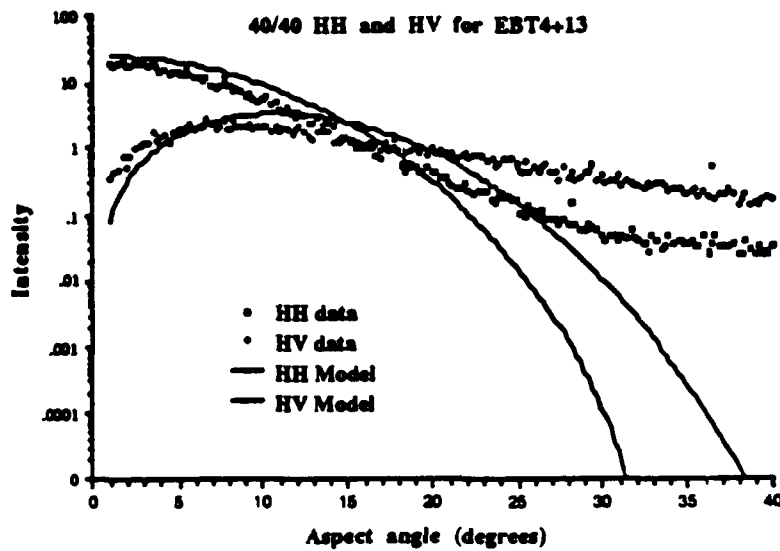


Figure 8c $\sigma_o(\text{HH})$ and $\sigma_o(\text{HV})$ for laboratory depression angles $\xi_i = \xi_s = 40$

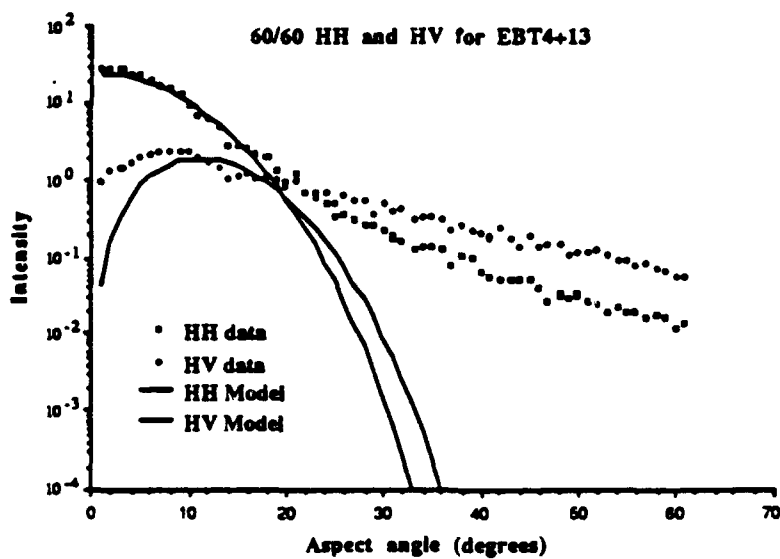


Figure 8d $\sigma_o(\text{HH})$ and $\sigma_o(\text{HV})$ for laboratory depression angles $\xi_i = \xi_s = 60$

Aluminum data (Plots are in Field Angles)

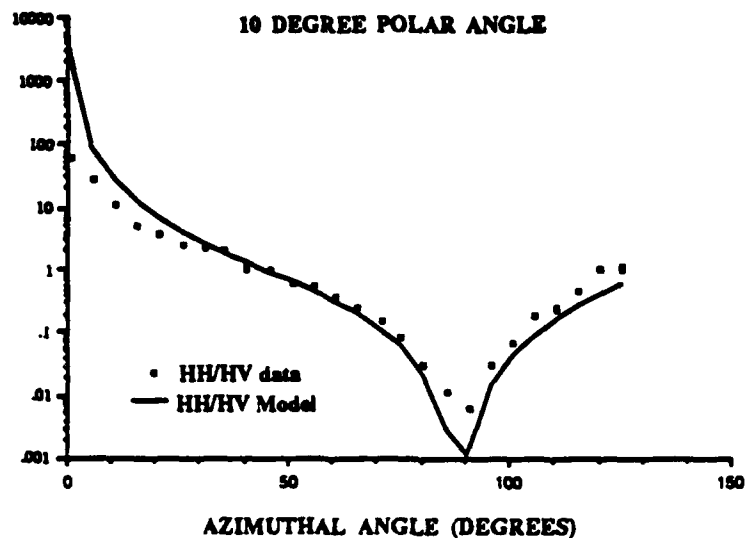


Figure 9a $\sigma_0(\text{HH})/\sigma_0(\text{HV})$ for field polar angles $\theta_i = \theta_s = 10$

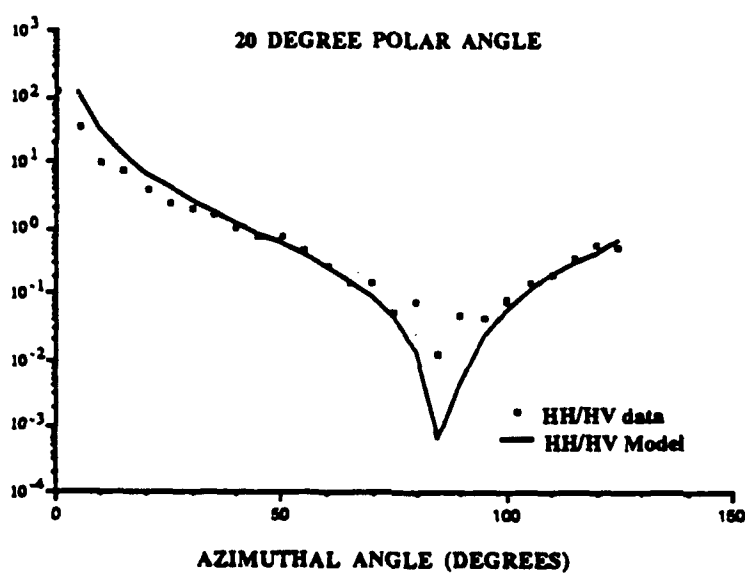


Figure 9b $\sigma_0(\text{HH})/\sigma_0(\text{HV})$ for field polar angles $\theta_i = \theta_s = 20$

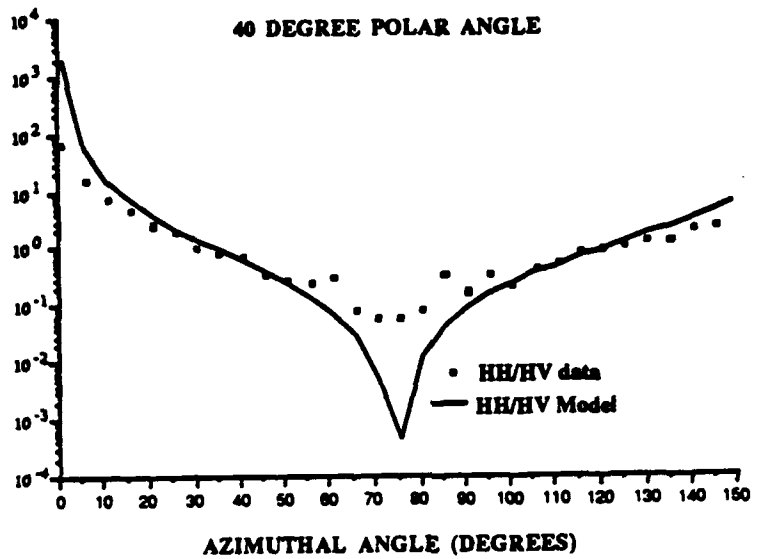


Figure 9c $\sigma_0(\text{HH})/\sigma_0(\text{HV})$ for field polar angles $\theta_i = \theta_s = 40$

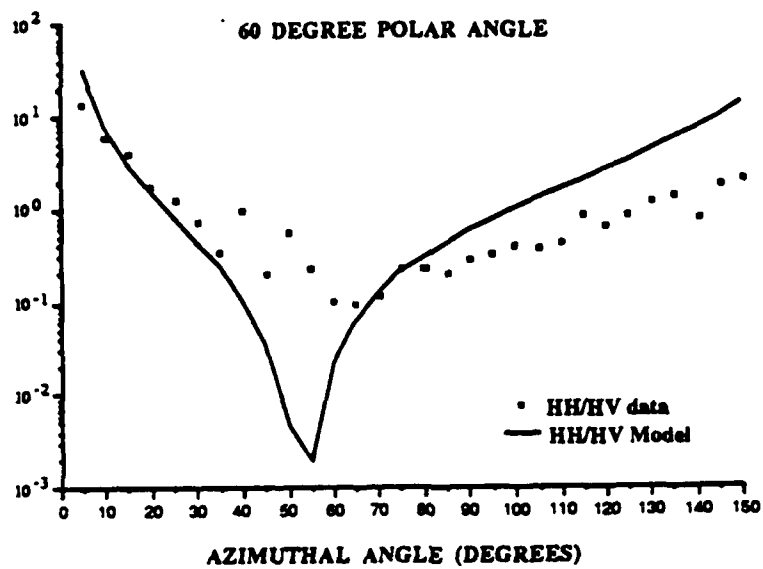


Figure 9d $\sigma_0(\text{HH})/\sigma_0(\text{HV})$ for field polar angles $\theta_i = \theta_s = 60$

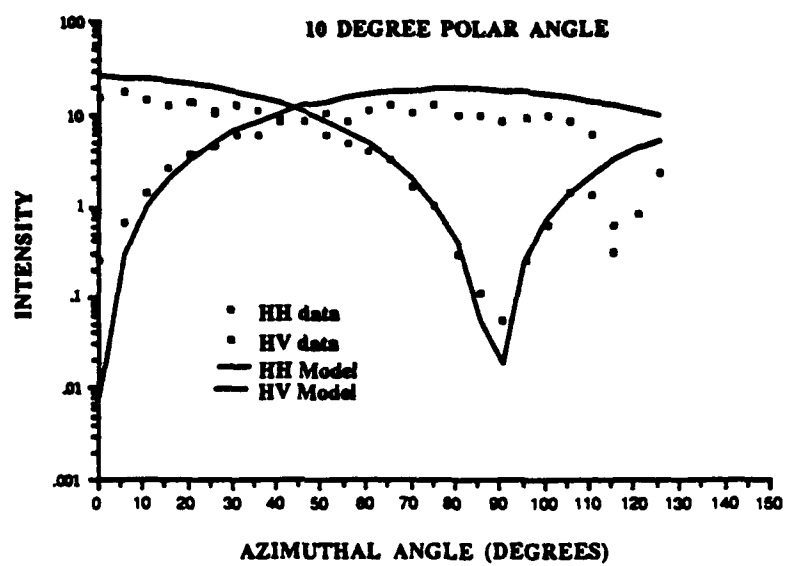


Figure 10a $\sigma_o(\text{HH})$ and $\sigma_o(\text{HV})$ for field polar angles $\theta_i = \theta_s = 10$

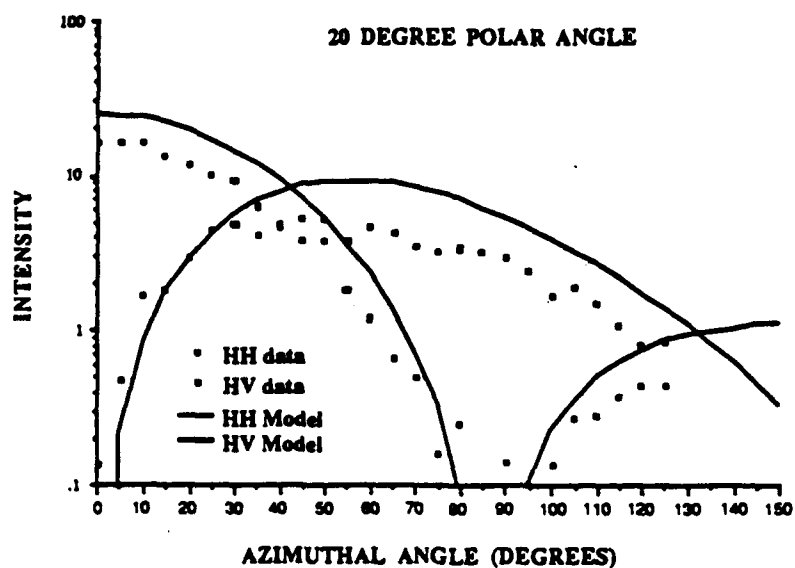


Figure 10b $\sigma_o(\text{HH})$ and $\sigma_o(\text{HV})$ for field polar angles $\theta_i = \theta_s = 20$

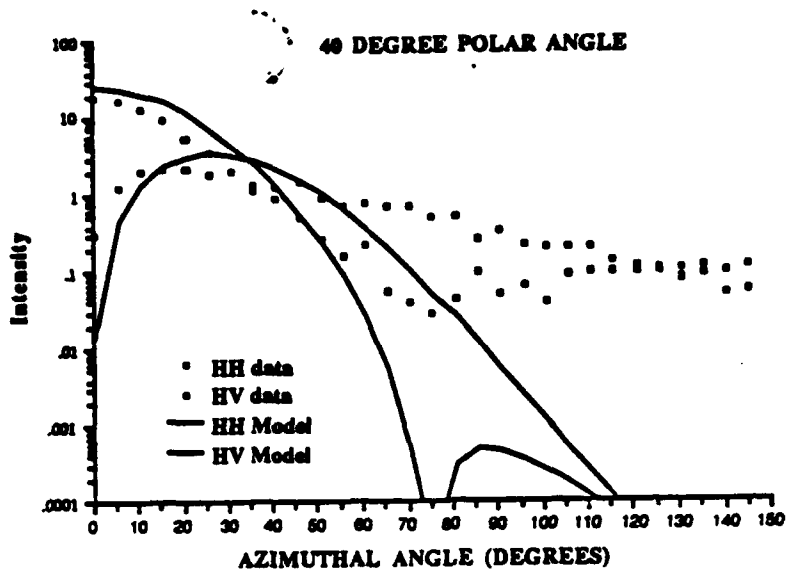


Figure 10c $\sigma_o(\text{HH})$ and $\sigma_o(\text{HV})$ for field polar angles $\theta_i = \theta_s = 40$

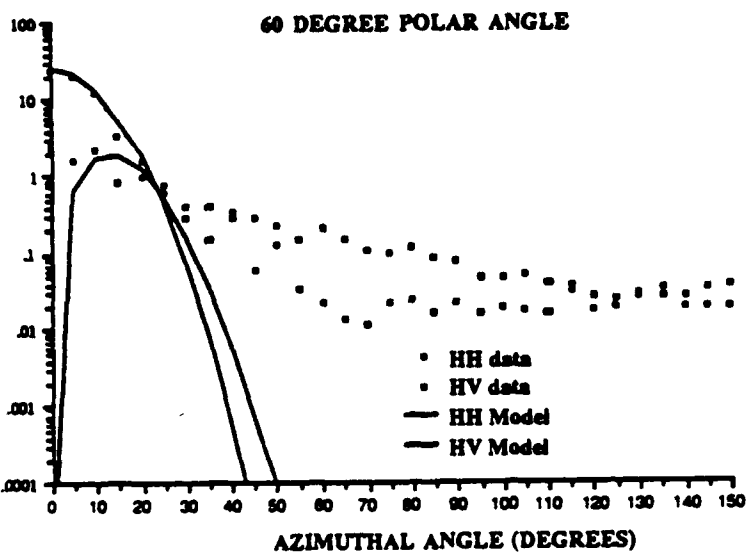


Figure 10d $\sigma_o(\text{HH})$ and $\sigma_o(\text{HV})$ for field polar angles $\theta_i = \theta_s = 60$

Plastic data (Plots are in Field Angles)

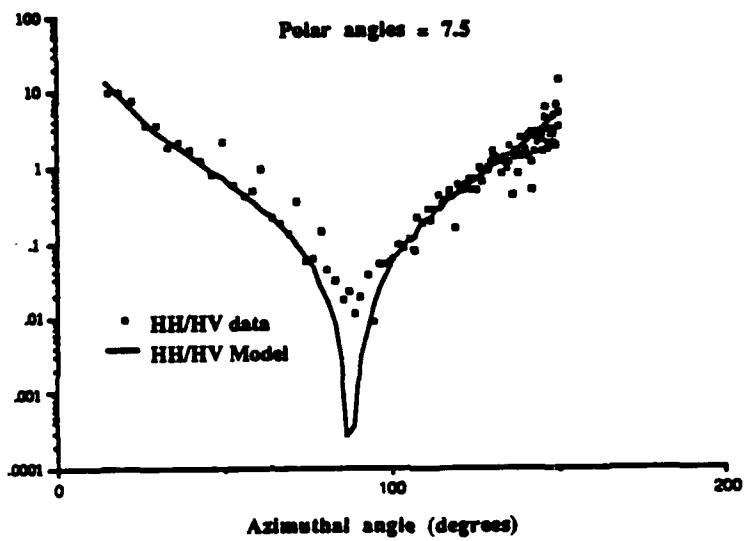


Figure 11 $\sigma_0(\text{HH})/\sigma_0(\text{HV})$ for field polar angles $\theta_i = \theta_s = 7.5$

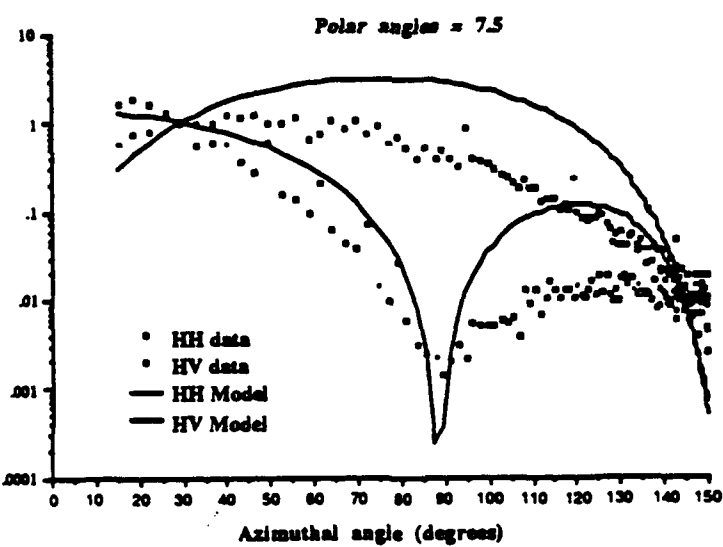


Figure 12 $\sigma_0(\text{HH})$ and $\sigma_0(\text{HV})$ for field polar angles $\theta_i = \theta_s = 7.5$

Glass data (Plots are in Laboratory Angles)

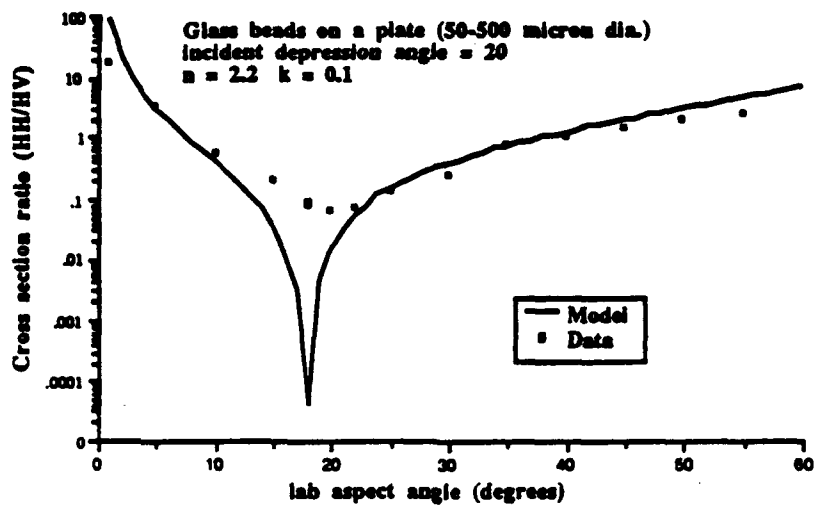


Figure 13a $\sigma_o(HH)/\sigma_o(HV)$ for laboratory depression angles $\xi_i = \xi_s = 20$

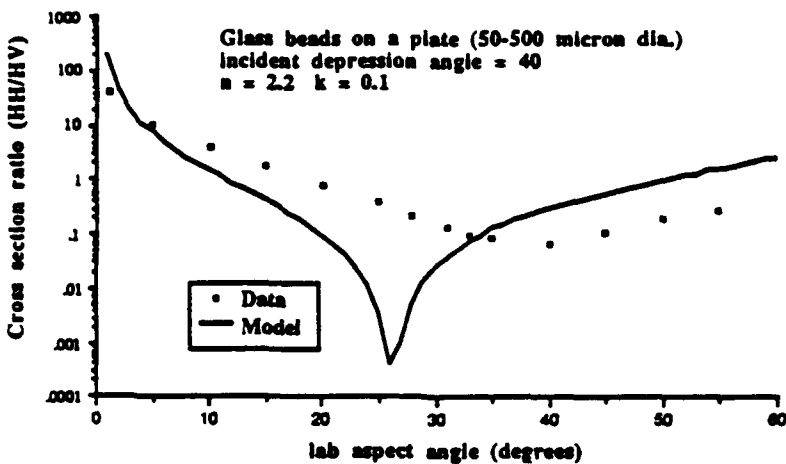


Figure 13b $\sigma_o(HH)/\sigma_o(HV)$ for laboratory depression angles $\xi_i = \xi_s = 40$

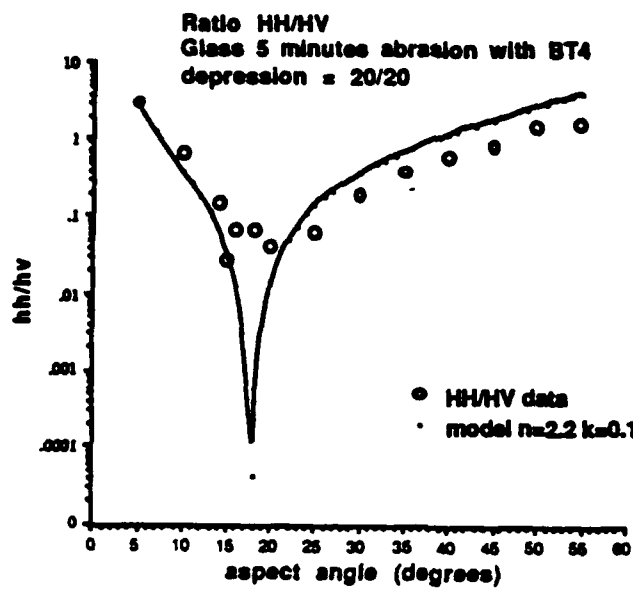


Figure 14a $\sigma_o(HH)/\sigma_o(HV)$ for laboratory depression angles $\xi_i = \xi_s = 20$

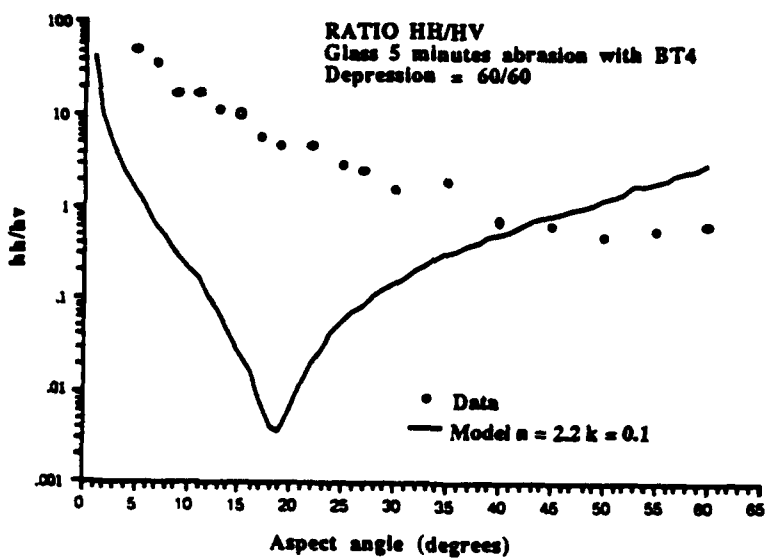


Figure 14b $\sigma_o(HH)/\sigma_o(HV)$ for laboratory depression angles $\xi_i = \xi_s = 60$

Aluminum Wire data (Plots are in Laboratory Angles)

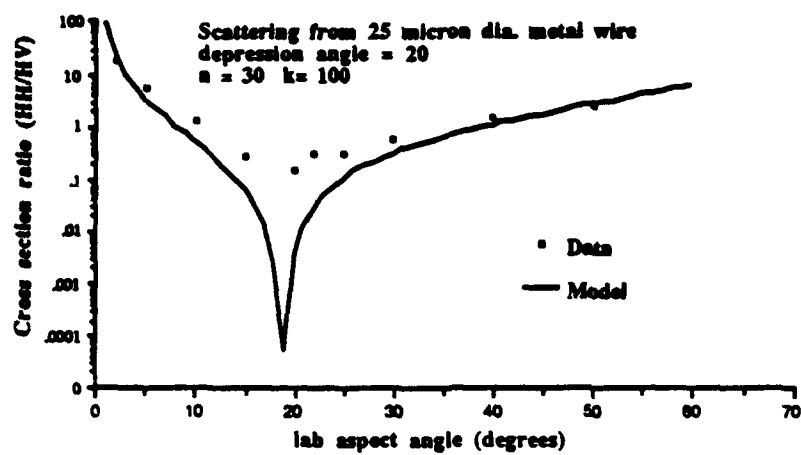


Figure 15 $\sigma_0(\text{HH})/\sigma_0(\text{HV})$ for laboratory depression angles $\theta_i = \theta_s = 20$

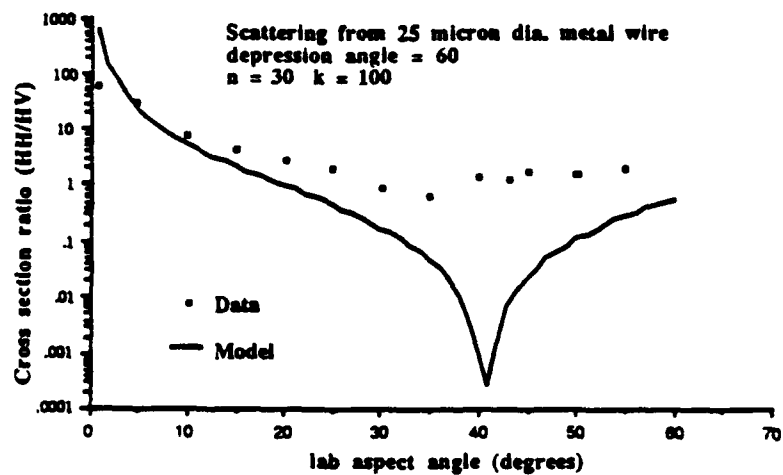


Figure 16 $\sigma_0(\text{HH})/\sigma_0(\text{HV})$ for laboratory depression angles $\theta_i = \theta_s = 60$

IV Discussion of Results

For the sake of clarity we divide our discussion into four parts. We start with scattering data from metals and divide these into two groups; data in laboratory angles, Figures 7-8, and data in field angles, Figures 9-10.

As previously noted, the facet model implies that the laboratory aspect angle is identical with the angle subtended by the facet normal with the surface (global) normal. The facets that radiate into the detector all have normals in the horizontal plane, the plane defined by the transmit and receive directions. Figures 7-8 show that agreement with the TP model is excellent up to 15° aspect angle and the onset of significant deviation from the TP model occurs at an aspect angle somewhere between 15° and 20° . The exception to this statement is the deviation of $\sigma_o(HV)$ and the ratio $\sigma_o(HH)/\sigma_o(HV)$ at very small aspect angles. According to the TP model, $\sigma_o(HV) \rightarrow 0$ as the aspect angle $\rightarrow 0$. Tentatively, this deviation can be attributed to a small amount (a few percent) of diffuse and depolarized scattering leading to a non zero $\sigma_o(HV)$ at all angles including small aspect angles. A plausible explanation for the origin of this behavior will be presented later.

Figures 9-10 exhibit data in field coordinates for fixed and identical transmit and receive polar angles as a function of the azimuthal angle. Zero azimuthal angle thus corresponds to the specular configuration. In the field representation, the deviation from the TP model predictions occurs at different azimuthal angles. Of course, the underlying source of the discrepancy between the TP model and data must be the same in both laboratory and field coordinate systems. By plotting the angle between the global and local facet normal as a function of azimuthal angle, a set of curves is generated in which each curve corresponds to a given polar angle. Looking at the data, one can find the

azimuthal angle at which there is a significant departure between the TP model and experimental data. These points are plotted as x's in Figure 17. The x's lie approximately on a straight line and show that in field coordinates, the departure of the data from the predictions of the TP model occurs when the facet normal subtends an angle of approximately 20° with the global normal.

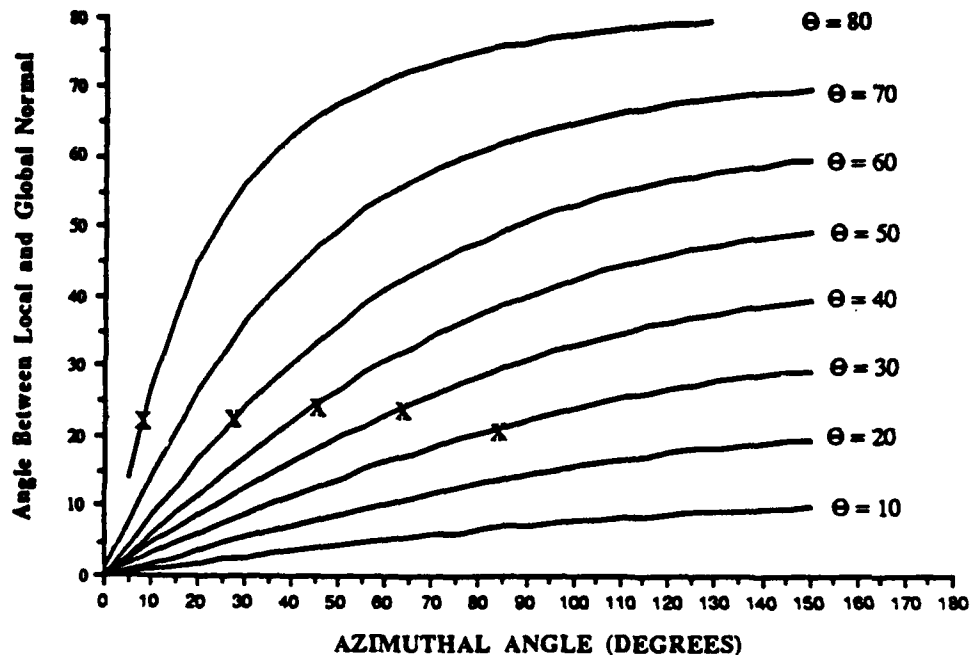


Figure 17 Facet Slope (angle of local facet normal) where Field Data
Departs from Tangent Plane Model

It has been noted before that there are limits to the validity of the TP approximation due to curvature. Brekhovskikh^[10] derived the following criterion for the validity of the TP approximation:

$$4\pi r_c \cos \vartheta \gg \lambda \quad (24)$$

where r_c is the radius of curvature and ϑ is the local angle of incidence. Unfortunately, the inequality is not specific enough to be of use in data analysis.

We present here a somewhat different argument. In a rough surface where the average slope is small (on the order of 0.1 as is the case here), larger than average slopes can occur in several ways: the

depth is larger than average and the spacing between neighboring high and low points has an average value, the depth is average and the spacing between high and low points is smaller than average, or finally, both depths and spacings are significantly different from the average value. We consider the case indicated in Figure 18 below where the depth is average and the spacing between high and low points is smaller than average.

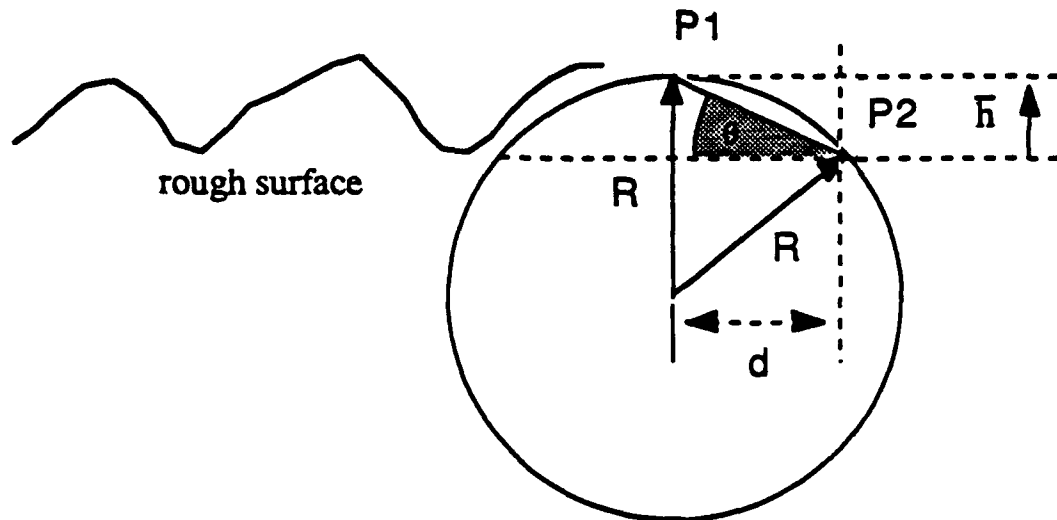


Figure 18 Circle Centered on a Rough Surface Facet of Larger than Average Slope

Let the circle be centered at a point inside the surface that is at 3λ beneath a high point on the surface such that:

$$d = \sqrt{R^2 - (R - \bar{h})^2} = \sqrt{2Rh - \bar{h}^2} \quad (25)$$

If we set $R = 3\lambda = 31.8 \mu\text{m}$ and $\bar{h} = 5.76 \mu\text{m}$ we obtain:

$$d = 18.24 \mu\text{m}$$

and

$$\theta = 17^\circ.$$

Thus, approximately half of the facets corresponding to slope angles larger than 17° will have a radius

of curvature smaller than 3λ , the onset of the resonance regime^[11] for curved surface (cylinder, sphere) scattering according to the Mie theory^[11].

Surface characteristics such as depth, facet spacing and radius of curvature, were obtained by means of a mechanical profilometer "Mitutoyo Surftest 201", with a 5 μm diameter diamond stylus. Some of the parameters, such as the diameter of the glass bead and the duration and pressure of the blast, were varied during the sand blasting operation. Four differently prepared surfaces were used in this study^[13]. After sand blasting, the surfaces were examined under a microscope and observed to display many sharp points and edges. Consequently, the samples were electropolished to remove these sharp features as has been the practice of other researchers in the field^[12]. The surface data given in Table I is tabulated according to bead size (BT #). The data displayed in Figures 7-8 were obtained for sample "EBT 4+13", an electropolished sample blasted with a mix of BT4 and BT13 beads. According to Table I, the average facet depth for this surface was 2.88 μm . This average was measured from the mean surface level. The quantity \bar{h} that enters into Eqn.(25) is double the value of the mean depth found in Table I. Table I also gives information about the radius of curvature of facets for all surfaces studied. Radius of curvature calculations were performed by fitting a parabola to groupings of data points from the digitized profilometer tracings (five data points each, spanning about 40 μm on the surface).

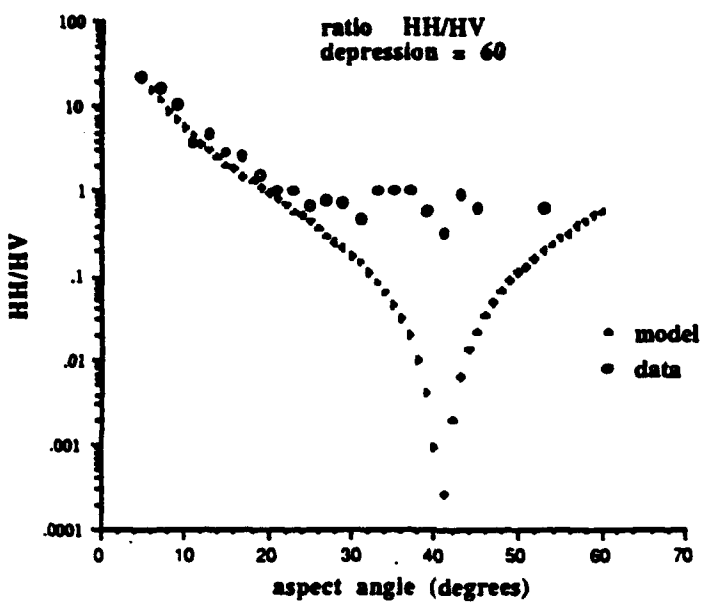


Figure 19 $\sigma_o(\text{HH})/\sigma_o(\text{HV})$ for Laboratory Depression Angles $\xi_i = \xi_s$ of 60°

Some of the earlier measurements obtained in the course of this work were made using a rough surface referred to as "original EBT4" having an average facet depth of $8.68 \mu\text{m}$. The slope angle associated with this depth is approximately 22° . At larger angles the facet model deviates from the measured values. Figure 19 is consistent with our prediction and displays data for $\sigma_o(\text{HH})/\sigma_o(\text{HV})$ at a 60° laboratory depression angle. This plot shows that there is an excellent fit up to a laboratory aspect angle of 24° .

As a further check on our hypothesis that curvature effects reduce the effectiveness of the TP approximation, we prepared a surface consisting of randomly wound aluminum wires on an absorbing substrate. These measurements are displayed in Figures 15 and 16. Among the interesting features of these data is the observation that at small aspect angles the fit to the TP model is good, and at large aspect angles (Figure 16), the data follow the same pattern as the roughened surface at a 60° laboratory

depression angle (Figure 19).

Figures 11-12 show plots of measurements for plastic in comparison with the facet model predictions. The roughened plastic surface was prepared by pressing an acetone treated smooth plastic surface against a roughened aluminum surface. After hardening, the plastic surface had a roughness which was verified by profilometer to be similar to the rough metal. The complex index of refraction of this plastic at 10.6 μm was $n = 1.6$ and $k = 0.002$. The penetration depth is given by $\alpha^{-1} = \lambda/4\pi k = 422 \mu\text{m}$. This is too large given that the theoretical calculations assume that all scattering takes place on the surface without transmission through the facet. The scattering in the data points shown in Figures 11-12 may be due to the transmission associated with small k .

To remedy this situation, we performed additional measurements on rough glass surfaces. Glass has a complex index of refraction of $n = 2.2$ and $k = 0.1$ at 10.6 μm . The penetration depth of glass at 10.6 μm is 8.4 μm , sufficiently small to justify the neglect of transmission through facets. Two types of rough glass surfaces were prepared. Figure 13 displays scattering data from randomly stacked glass beads of varying radii on a glass substrate. Here the deviation from the facet model is at very small laboratory aspect angles. The other set of glass scattering data are displayed in Figure 14. This target surface was prepared by abrading a flat glass surface with glass beads under pressure. Rough glass surfaces prepared in this manner displayed many deep fissures when observed under a microscope.

This surface did not quite satisfy the surface criteria necessary to test the theory. Nevertheless, at steep angles (Figure 14), the data seemed to validate the facet model prediction up to a laboratory aspect angle of 15°. It is instructive to compare Figure 14 with Figure 7 (10/10 data). Both appear to have the same range of validity. Both display an HH null with a depth of 0.1. When comparing Figures 13 and 14 with Figures 7 and 8, one observes that the deviation from theory is more

pronounced for dielectrics than metals at larger laboratory depression angles.

To obtain a better understanding of the limitations of the TP approximation, we present some numerical results of polarization state dependent scattering amplitudes for both metal and dielectric cylinders of different radii.

The underlying rationale for doing this is to juxtapose the TP approximation with exact calculations for curved surfaces where solutions to Maxwell's equations with associated boundary conditions can be obtained numerically. If the tangent plane approximation were to be valid independently of the surface curvature, one should be able to approximate the scattering amplitude from any cylinder of arbitrary radius by the Fresnel coefficients of the tangent plane. Thus, in the case of a metal cylinder, one would conclude that the scattering intensity for a cylinder is independent of the azimuthal angle ϕ and the orientation of the incident linear polarization. This, however, is not the case. An understanding of the structure of the polarization dependent scattering amplitudes as a function of a/λ is one way to put the tangent plane approximation in its proper perspective.

The validity of the tangent plane approximation will depend on how close the ratio of HH/VV for a cylinder divided by HH/VV for a plane is to unity. An additional requirement is that the phase differences for HH and VV amplitudes for planes and cylinders remain the same. It is of interest to note that the HH-VV phase differences for cylinders and planes are the same except in the immediate vicinity of the Brewster angle.

Figure 20 displays the amplitude ratios for metal cylinders of increasing radii. The radius ranges from 3.18λ to 9.54λ . The plots confirm qualitatively the inequality of Eqn.(A1), ie, the larger the radius of curvature, the better the TP approximation. One observes that for large angles of incidence the TP approximation fails even for a radius of curvature on the order of 10λ . On the other

hand, for steep angles of incidence, the TP approximation is effective even for small radii of curvature. This is consistent with our measurements on roughened aluminum surfaces, dielectric surfaces, and metal wire surfaces at steep angles of incidence.

Similar results are displayed in Figure 21 for dielectric cylinders with $n = 1.6$ and $k = 0.1$. These differ from the cylinder plots for metals and indicate that the TP approximation for dielectrics fails at smaller angles than for metals with the same radius.

One notes that the inequality derived in reference 10 doesn't distinguish between dielectrics and metals.

Reviewing our data in light of these model calculations, we reach the following conclusion. The bulk of the scattered radiation (~ 95%) is accounted for by the facet model. There is, however, a small but finite component of diffuse radiation with a polarization that varies rapidly as a function of angle. It is the latter which gives rise to deviations from the predictions of the TP approximation. These deviations are especially pronounced in polarization states and at angles where the TP model predicts no scattering or small amounts of scattering. Thus, at an azimuthal angle of 0° , where the TP model predicts $\sigma_o(HV) = 0$, a small but finite $\sigma_o(HV)$ appears consistently. The other area of pronounced deviation from the TP model is at scattering angles that are significantly different from the specular direction. Here, the intensity of the scattered radiation should fall off exponentially. This, however, is not the case due to the underlying diffuse background. The most likely cause for this is the existence of areas on the rough surface with small radii of curvature. This hypothesis is consistent with the differences observed between metals and dielectrics, and with the scattering observed from randomly distributed wires.

Other investigators have attributed depolarization effects to multiple scattering^[7]. Another

plausible source of depolarization may be found in two scales of roughness^[14]. These issues will be addressed in a subsequent publication.

We also express our thanks to M. Coulombe, T. Horgan, M. Grund, M. Yoon, E. Jordan and C. Laramee for technical assistance.

Amplitude Ratios (VV/HH) for Conducting Cylinders and Planes

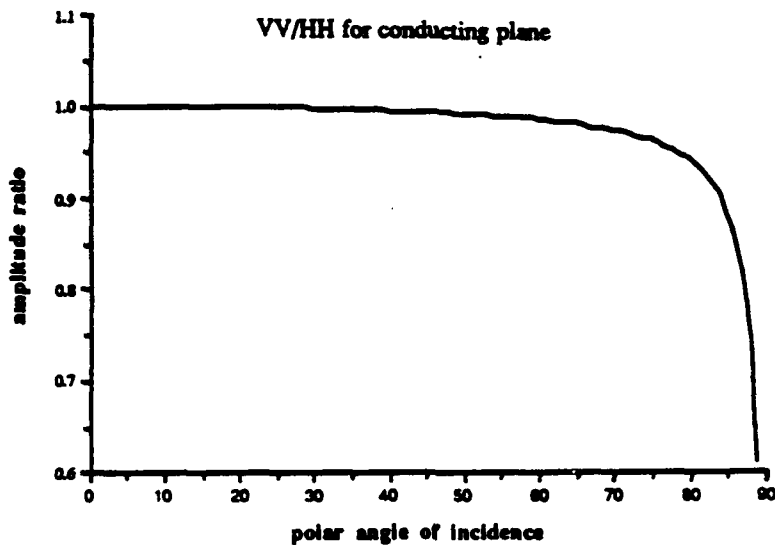


Figure 20a VV/HH for a Conducting Plane

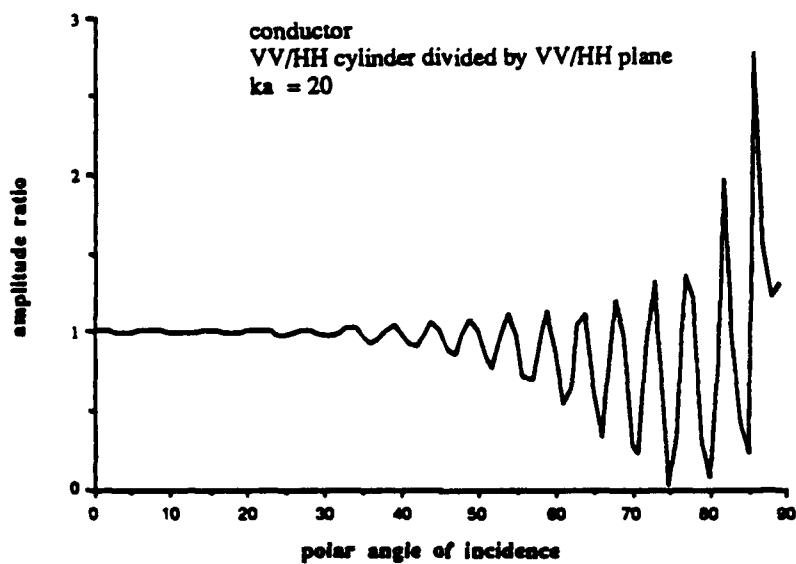


Figure 20b VV/HH for a Conducting Cylinder with $ka = 20$ divided by VV/HH for a Conducting Plane

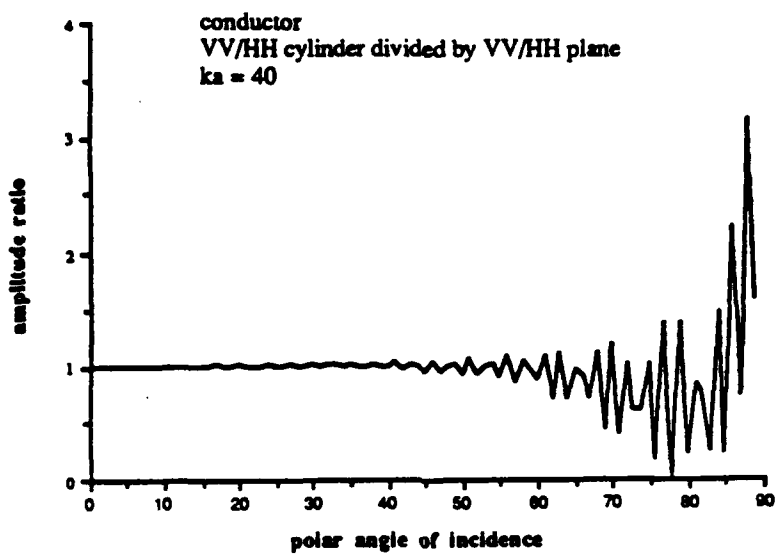


Figure 20c VV/HH for a Conducting Cylinder with $ka = 40$ divided by VV/HH for a Conducting Plane

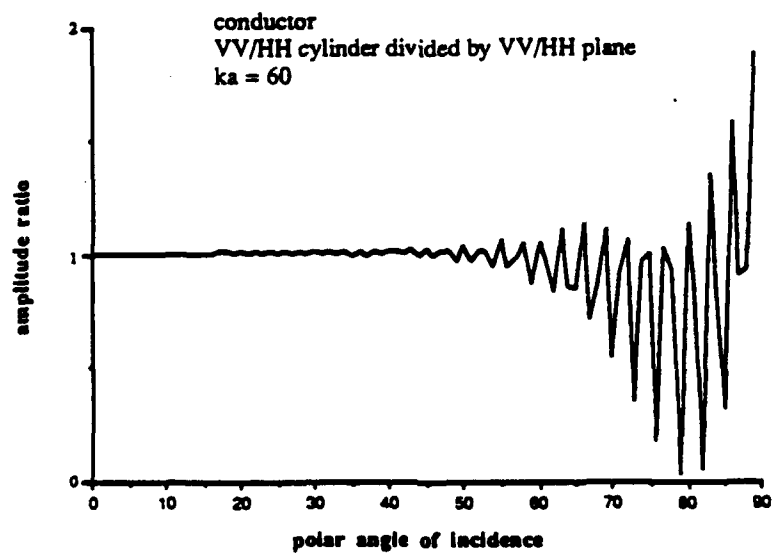


Figure 20d VV/HH for a Conducting Cylinder with $ka = 60$ divided by VV/HH for a Conducting Plane

Amplitude Ratios (VV/HH) for Dielectric Cylinders and Planes

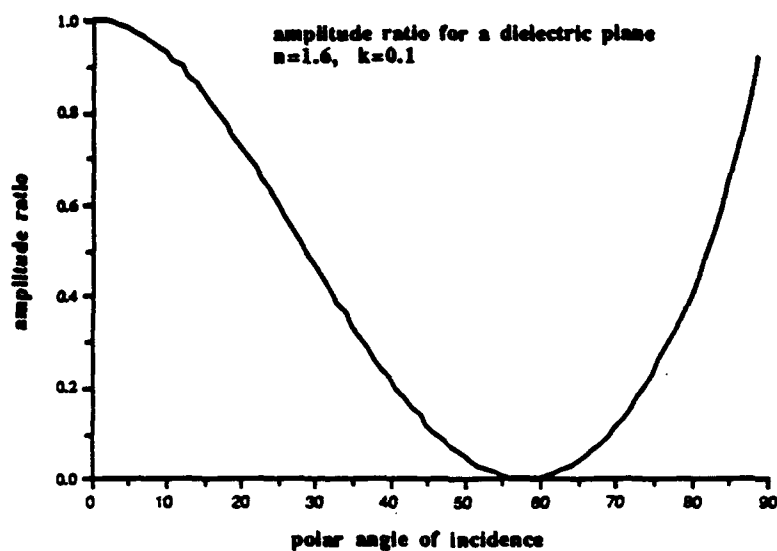


Figure 21a VV/HH for a Dielectric Plane

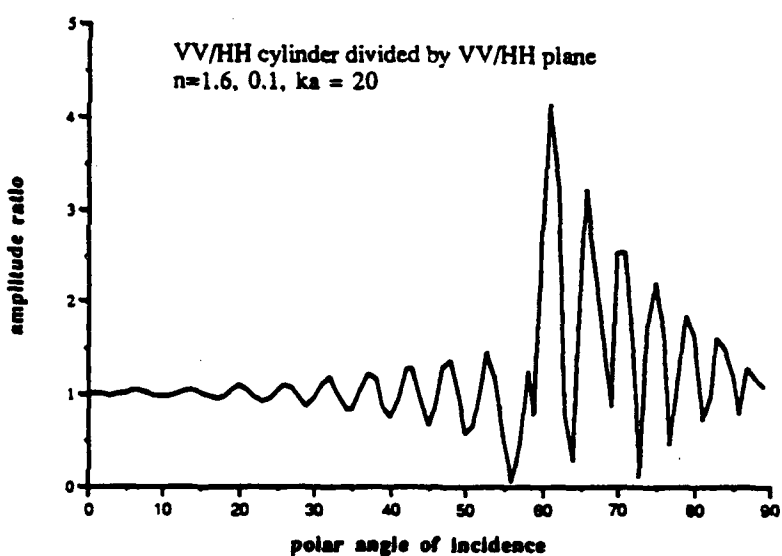


Figure 21b VV/HH for a Dielectric Cylinder with $ka = 20$ divided by VV/HH for a Dielectric Plane

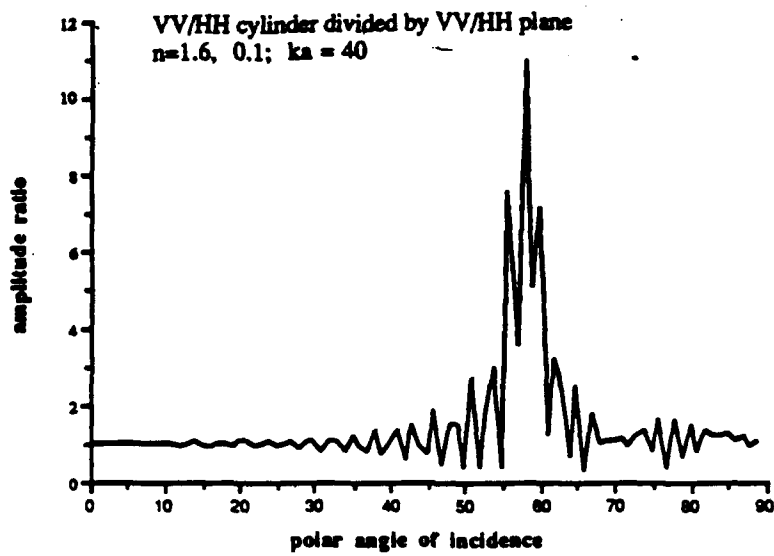


Figure 21c VV/HH for a Dielectric Cylinder with $ka = 40$ divided by VV/HH for a Dielectric Plane

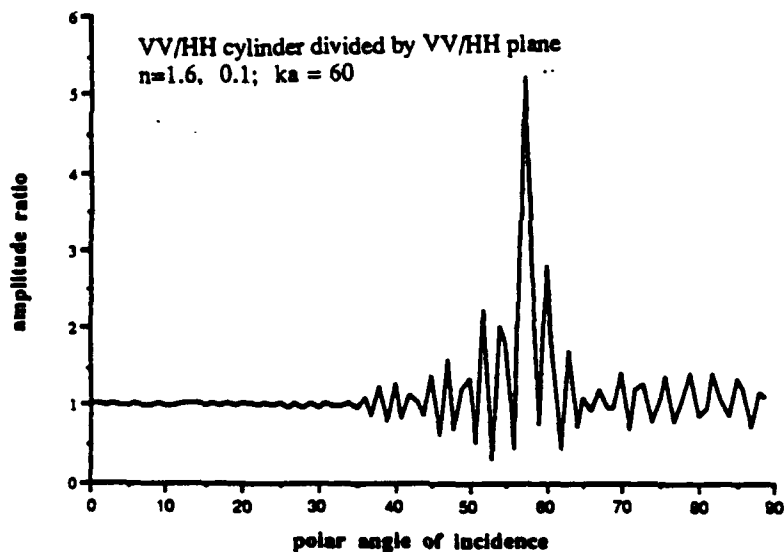


Figure 21d VV/HH for a Dielectric Cylinder with $ka = 60$ divided by VV/HH for a Dielectric Plane

References

- [1] Petr Beckmann, Andre Spizzichino, (1963) *The Scattering of Electromagnetic Waves from Rough Surfaces*, Pergamon Press, New York.
- [2] ibid, pg. 178.
- [3] Victor Twersky, (1957), *On Multiple Scattering and Reflection of Waves by Rough Surfaces*, IRE Trans. Antennas Propagat., AP-5(No.81).
- [4] Donald E. Barrick, (1986) *Rough Surface Scattering Based on the Specular Point Theory*, IEEE Trans. Antennas Propagat., AP-16(No.4).
- [5] A. K. Fung and Hsiao-Lien Chan, (1969) *Backscattering of waves by Composite Rough Surfaces*, IEEE Trans. Antennas Propagat., AP-17,(No.5):590-597 also D.E. Barrick (1970) *Radar Cross Section Handbook*, Vol. 2, Plenum Press, New York.
- [6] Robert J. Papa, John L. Lennon, Richard L. Taylor, (1986) *The Variation of Bistatic Rough Surface Scattering Cross Section for a Physical Optics Model*, IEEE Trans. Antennas Propagat., AP-34(No.10):1229-1237.
- [7] J. Renau, P. K. Cheo, and H. G. Cooper, (1967) *Depolarization of Linearly Polarized EM Waves Backscattered from Rough Metals and Inhomogeneous Dielectrics*, J. Opt. Soc. Am, AP-57(No.4).
- [8] M. J. Kim, J. C. Dainty, A. J. Friberg, and A. J. Sant, (1990) *Experimental Study of Enhanced Backscatter from One and Two Dimensional Random Rough Surfaces*, J. Opt. Soc. Am, AP-7(No.4).
- [9] Maurice I. Sancer, (1969) *Shadow Corrected Electromagnetic Scattering from Randomly Rough Surfaces*, IEEE Trans. Antennas Propagat., AP-17(No.5).
- [10] L. M. Brekhovskikh, (1952) *The Diffraction of Waves by a Rough Surface*, Zh. Eksper. i Teor. Fiz. 23:289-304, (manuscript untranslated in Russian).

- [11] Ruck, Barrick, Stuart, Krichbaum, (1970) *Radar Cross Section Handbook*, Plenum Press, New York.
- [12] Jacques Renau, James A. Collinson, (1965) *Measurements of Electromagnetic Backscattering from Known Rough Surfaces*, The Bell System Tech. Journal, 44:(No.10).
- [13] Four surfaces were prepared and analyzed in this study. Scattering data are found in Appendix C.
- [14] R. J. Papa, (1990) private communication.

Appendix A

An Algorithm for Transforming Field Angles into Laboratory Angles

Having defined laboratory angles ξ , η , and ψ in section II, we proceed with further analysis to obtain an algorithm that will yield a unique set of ξ , η , ψ for a given set of θ_i , θ_s , and ϕ_s .

We first show that for a fixed θ_i and θ_s both larger than 0° (0° is a point of degeneracy) $\cos(\phi_s)$ can assume all values between -1 and +1. Denoting $\cos(\theta_i) = x$ and $\cos(\theta_s) = y$, equation (23) can be written as:

$$\cos(\phi_s) = \frac{-\sin(\eta) + yx}{\sqrt{1 - x^2} \sqrt{1 - y^2}} \quad (A1)$$

For a fixed ψ and ξ and a fixed y , η is not an independent variable. We therefore express $\sin(\eta)$ in terms of x , y , and ψ .

$$\sin(\eta) = \sin(\eta - \xi + \xi) = \sin(\eta - \xi) \cos(\xi) + \cos(\eta - \xi) \sin(\xi) \quad (A2)$$

or

$$\sin(\eta) = \frac{xy \pm [\cos^2(\psi) - y^2] [\cos^2(\psi) - x^2]}{\cos^2(\psi)} \quad (A3)$$

The minus sign in front of the square root has to be inserted when $(\eta - \xi) > 90^\circ$. Combining (23), and (A1)-(A3) one writes:

$$\cos(\phi_s) = \frac{-xy \tan^2 \psi \pm \sqrt{1 - \frac{y^2}{\cos^2 \psi}} \sqrt{1 - \frac{x^2}{\cos^2 \psi}}}{\sqrt{1 - y^2} \sqrt{1 - x^2}} \quad (A4)$$

We first show that $\cos(\phi_s)$ can assume the extreme values of ± 1 . This can be seen by setting $\psi = 0$. The + sign in front of the square root yields +1, and the - sign yields -1. It is useful to rewrite the expression (14) as two equations each valid in a given range of $\cos(\phi_s)$. Assuming that $y > x$:

$$\cos(\phi_s) = \frac{-xy \tan^2 \psi + \sqrt{1 - \frac{y^2}{\cos^2 \psi}} \sqrt{1 - \frac{x^2}{\cos^2 \psi}}}{\sqrt{1 - y^2} \sqrt{1 - x^2}} \quad (A5)$$

Eqn. (A5) is valid for :

$$-\frac{x}{y} \sqrt{\frac{1 - y^2}{1 - x^2}} \leq \cos(\phi_s) \leq 1$$

and

$$\cos(\phi_s) = \frac{-xy \tan^2 \psi - \sqrt{1 - \frac{y^2}{\cos^2 \psi}} \sqrt{1 - \frac{x^2}{\cos^2 \psi}}}{\sqrt{1 - y^2} \sqrt{1 - x^2}} \quad (A6)$$

Eqn. (A6) is valid for :

$$-1 \leq \cos(\phi_s) \leq -\frac{x}{y} \sqrt{\frac{1 - y^2}{1 - x^2}}$$

For $x > y$, $-\frac{x}{y} \sqrt{\frac{1 - y^2}{1 - x^2}}$ must be replaced with $-\frac{y}{x} \sqrt{\frac{1 - x^2}{1 - y^2}}$. Since both functions are continuous functions of ψ , for $0 \leq \psi \leq \cos^{-1}(y)$, $\cos(\phi_s)$ assumes all values in between.

The algorithm for determining ξ, η, ψ for a given $\theta_i, \theta_s, \phi_s$ is as follows. Compute $\cos(\phi_s)$

and select the larger of $\cos(\theta_s)$ or $\cos(\theta_i)$, thereby setting the appropriate range for equations (A5) and (A6). The value of $\cos(\phi_s)$ determines whether Eqn. (A5) or (A6) is to be used. Having selected the correct equation, one solves for $\cos(\psi)$ and determines ψ . Given $\cos(\psi)$, one then can determine $\cos(\xi)$ or ξ . η remains to be determined and is obtained from: $y = \cos(\theta_s) = \sin(\eta - \xi) \cos(\psi)$.

Since $\sin(\eta - \xi)$ is symmetric around 90° , a unique determination of η depends on whether Eqn. (A5) or (A6) was used. For Eqn. (A5), $\eta - \xi \geq 90^\circ$ and for Eqn. (A6) $\eta - \xi \leq 90^\circ$.

To complete this section, we write down the direction of linear polarization that corresponds to an H transmit state. It is given by:

$$\mathbf{r}_i \times \mathbf{n}'' = -i_1 \sin(\psi) + i_2 \sin(\xi) \cos(\psi) \quad (A7)$$

An H receive state is given by:

$$\mathbf{r}_D \times \mathbf{n}'' = -[i_1 \sin(\eta) \cos(\xi) + i_2 \cos(\eta - \xi)] \cos(\psi) + i_3 \cos(\eta) \sin(\psi) \quad (A8)$$

The V receive state is obtained from:

$$\mathbf{r}_D \times (\mathbf{r}_D \times \mathbf{n}'') = \mathbf{r}_D (\mathbf{r}_D \cdot \mathbf{n}'') - \mathbf{n}'' \quad (A9)$$

or

$$\begin{aligned} \mathbf{r}_D \times (\mathbf{r}_D \times \mathbf{n}'') = & i_1 [\cos(\eta) \sin(\eta - \xi) + \sin(\xi)] \cos(\psi) + i_2 [\sin(\eta) \sin(\eta - \xi) \dots \\ & \dots \cos(\psi) - \sin(\psi)] - i_3 \cos(\xi) \cos(\psi) \end{aligned} \quad (A10)$$

Appendix B

Additional Scattering Data

To corroborate our hypothesis that the deviation from the TPA (Tangent Plane Approximation) model is due to the small amounts of surface curvature, we prepared a set of roughened aluminum surfaces that were blasted with different size glass beads. Half of the surfaces were electropolished after blasting, the other half were left untouched after blasting.

Figures AC1 (Appendix C1) to Figure AC14 display data in laboratory angles as a function of laboratory aspect angle. The roughened surfaces from which these data were obtained is designated EBT4. E stands for electropolished and BT4 signifies that the surface was blasted with glass beads BT4.

Figures AC15 to AC26 display data from the same surface in field angles. Here the incident and scattered polar angles are fixed and the azimuthal scattering angle is varied.

Figures AC27 to AC40 contain plots as a function of laboratory aspect angles from another surface designated by EBT6. Figures AC41 to AC54 represent data from EBT6 in field angles. Figures AC55 to AC68 display data in laboratory coordinates from a third surface, designated EBT13. Figures AC69 to AC82 contain scattering data in field coordinates for surface EBT 4+13.

In figures AC109 to AC162 scattering data for laboratory angles from the four different surfaces NBT4, NBT6, NBT13, and NBT4+13 are displayed. N stands for non-electropolished. The designation BT4, BT6, BT13, and BT4+13 refer to three different glass beads used in the sand blasting process.

Figures AC163 to 170 are histograms displaying percent of surface Vs slope.

Tables I and II summarize profilometric surface data including the percentage of surface that has a curvature of less than 3λ ($31.8\mu\text{m}$). Tables III and IV display the depth of the HH nulls. The TPA predicts an absolute zero at the location of the null, and in practice would be limited by instrumental uncertainty, ie., the extinction ratio of the polarization state analyzer. If the measured null

is above the instrumental threshold, it would indicate that another source is present. In Tables II and III we demonstrate another correlation between the depth of the HH nulls and percentage of curvature. The smaller the percentage of curvature, ($r < 3\lambda$), the deeper the HH null.

EBT 4

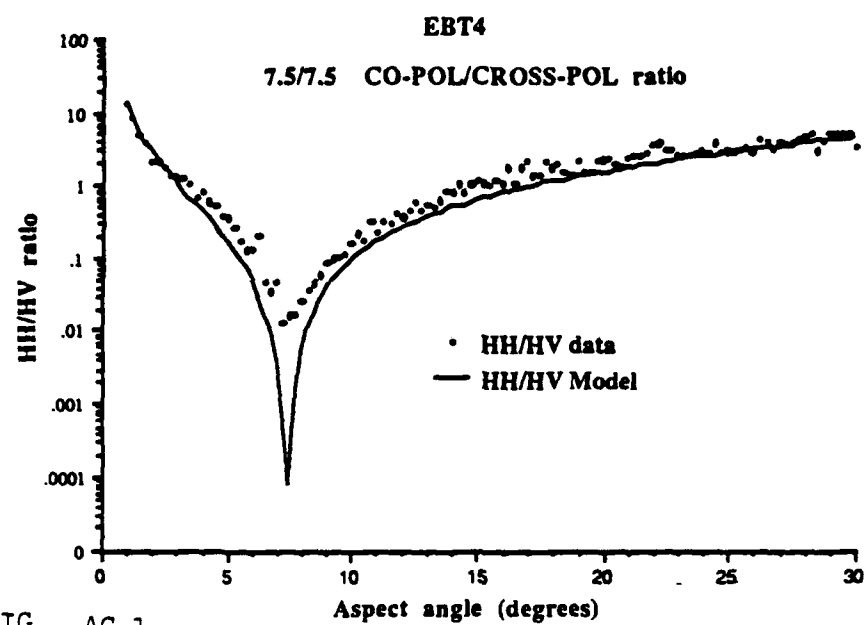


FIG. AC-1

$\sigma_o(HH)/\sigma_o(HV)$ for laboratory depression angles $\xi_i = \xi_s = 7.5$

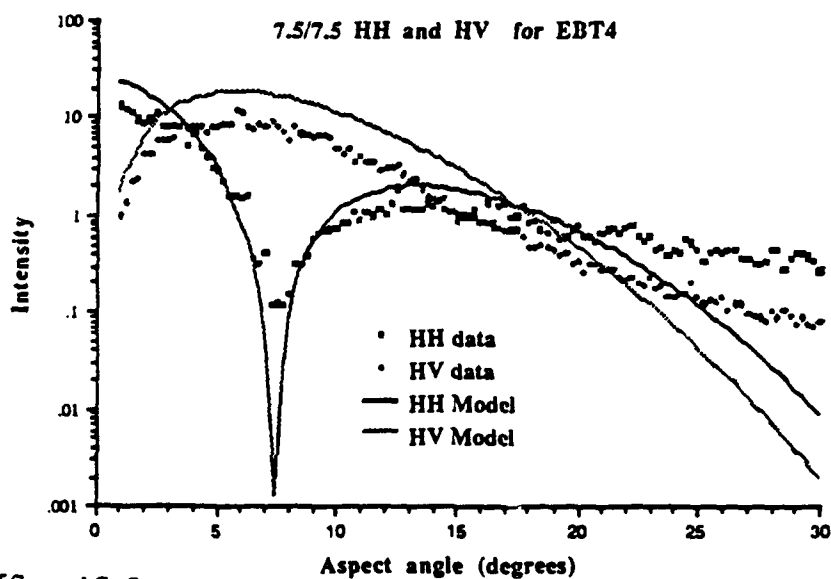


FIG. AC-2

$\sigma_o(HH)$ and $\sigma_o(HV)$ for laboratory depression angles $\xi_i = \xi_s = 7.5$

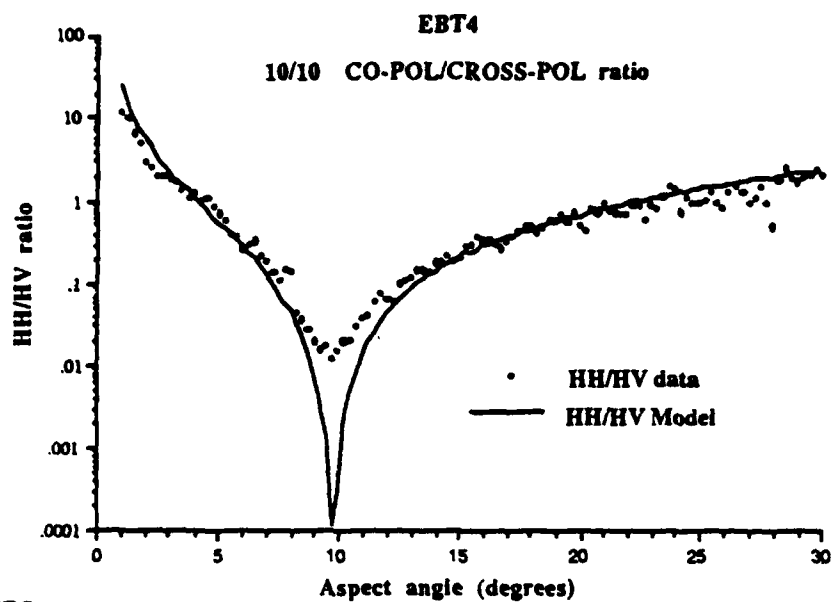


FIG. AC-3

$\sigma_o(\text{HH})/\sigma_o(\text{HV})$ for laboratory depression angles $\xi_i = \xi_s = 10$

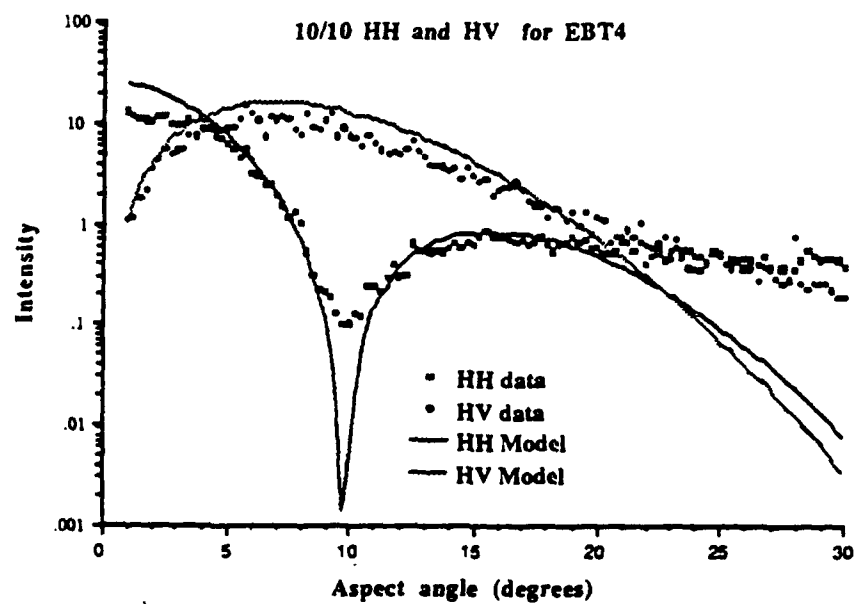


FIG. AC-4

$\sigma_o(\text{HH})$ and $\sigma_o(\text{HV})$ for laboratory depression angles $\xi_i = \xi_s = 10$

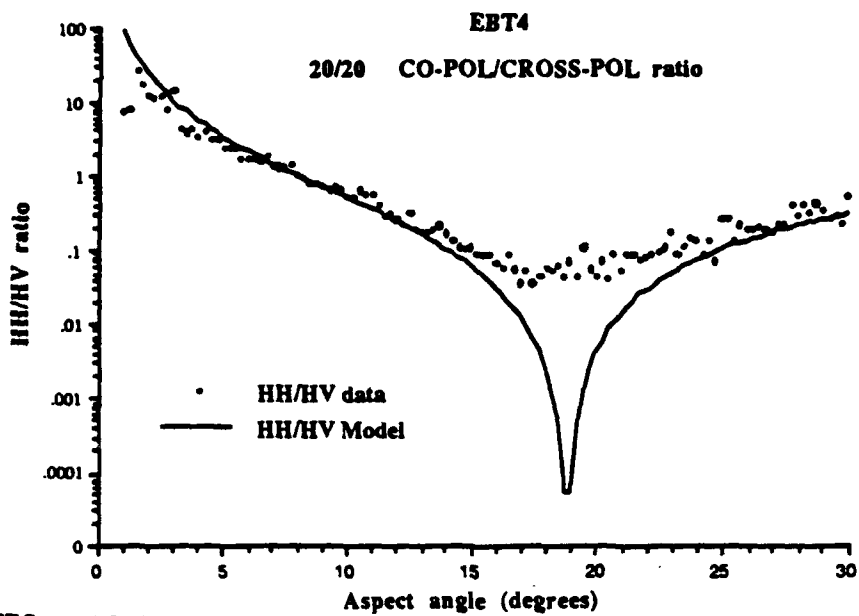


FIG. AC-5

$\sigma_o(\text{HH})/\sigma_o(\text{HV})$ for laboratory depression angles $\xi_i = \xi_s = 20$

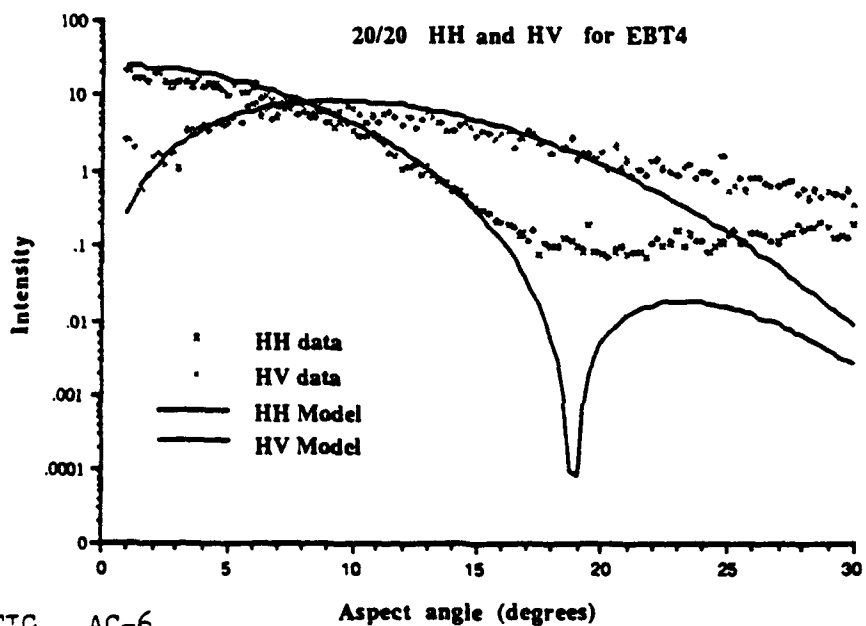


FIG. AC-6

$\sigma_o(\text{HH})$ and $\sigma_o(\text{HV})$ for laboratory depression angles $\xi_i = \xi_s = 20$

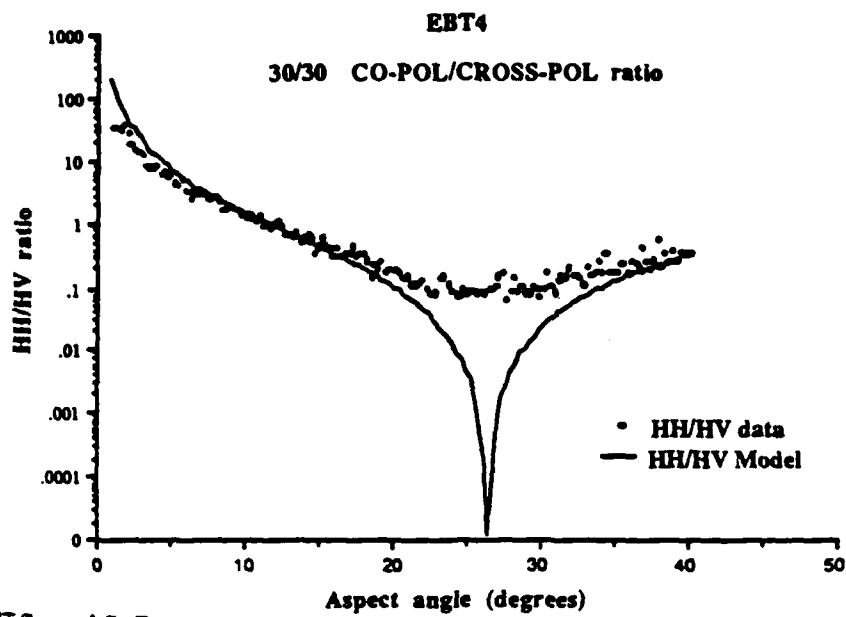


FIG. AC-7

$\sigma_o(\text{HH})/\sigma_o(\text{HV})$ for laboratory depression angles $\xi_i = \xi_s = 30$

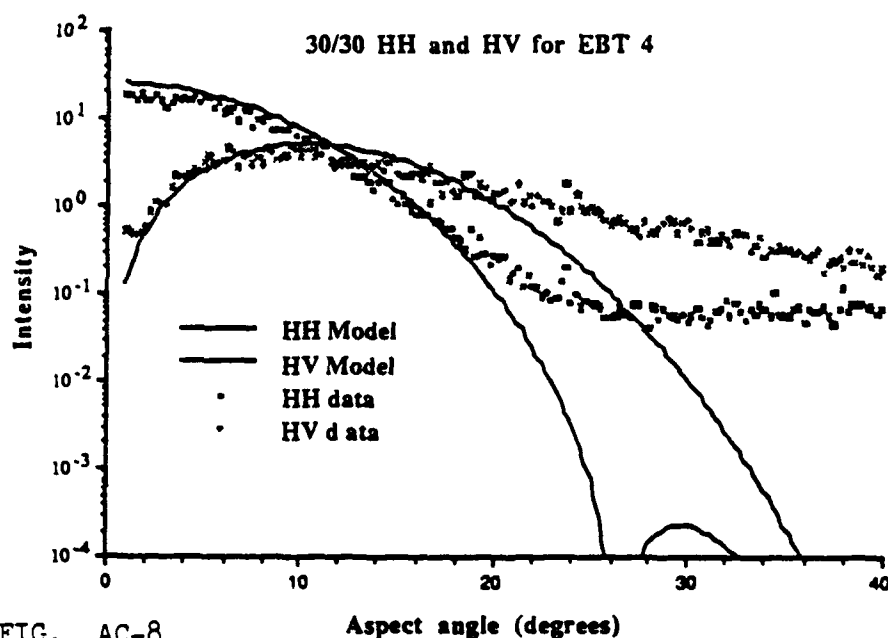


FIG. AC-8

$\sigma_o(\text{HH})$ and $\sigma_o(\text{HV})$ for laboratory depression angles $\xi_i = \xi_s = 30$

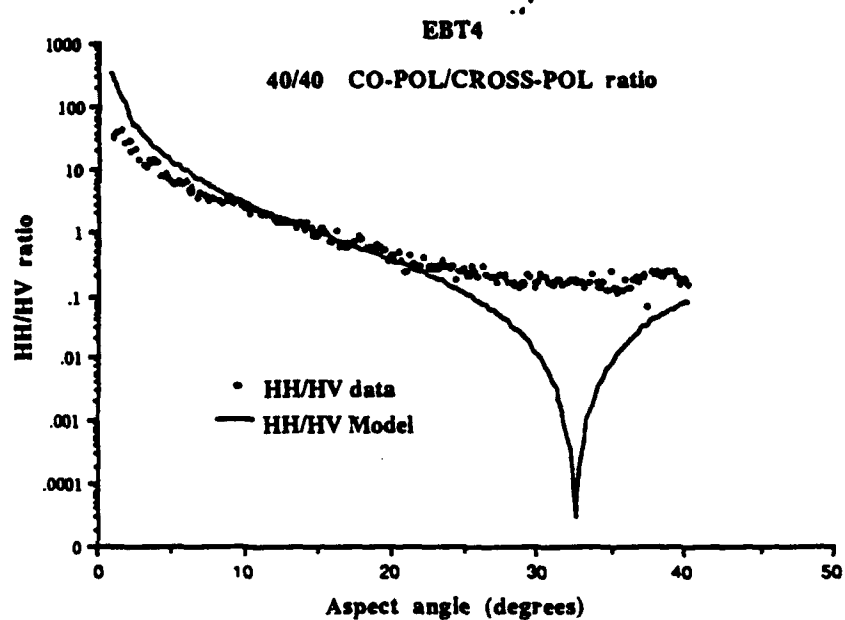


FIG. AC-9

$\sigma_o(\text{HH})/\sigma_o(\text{HV})$ for laboratory depression angles $\xi_i = \xi_s = 40$

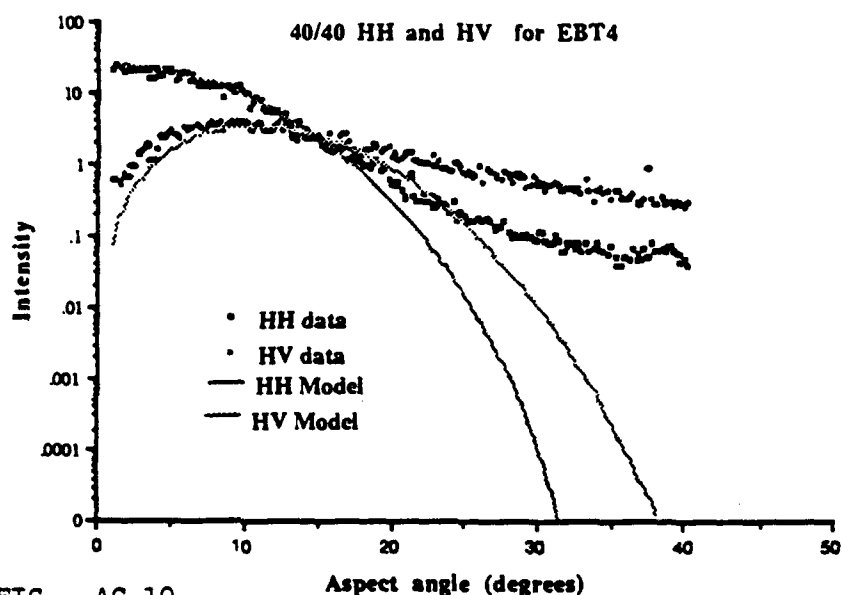


FIG. AC-10

$\sigma_o(\text{HH})$ and $\sigma_o(\text{HV})$ for laboratory depression angles $\xi_i = \xi_s = 40$

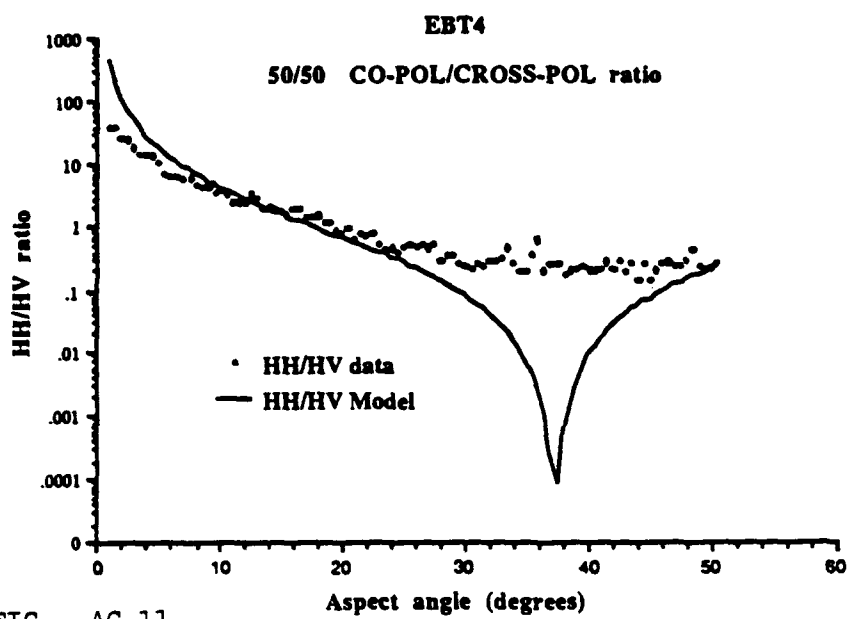


FIG. AC-11

$\sigma_o(HH)/\sigma_o(HV)$ for laboratory depression angles $\xi_i = \xi_s = 50$

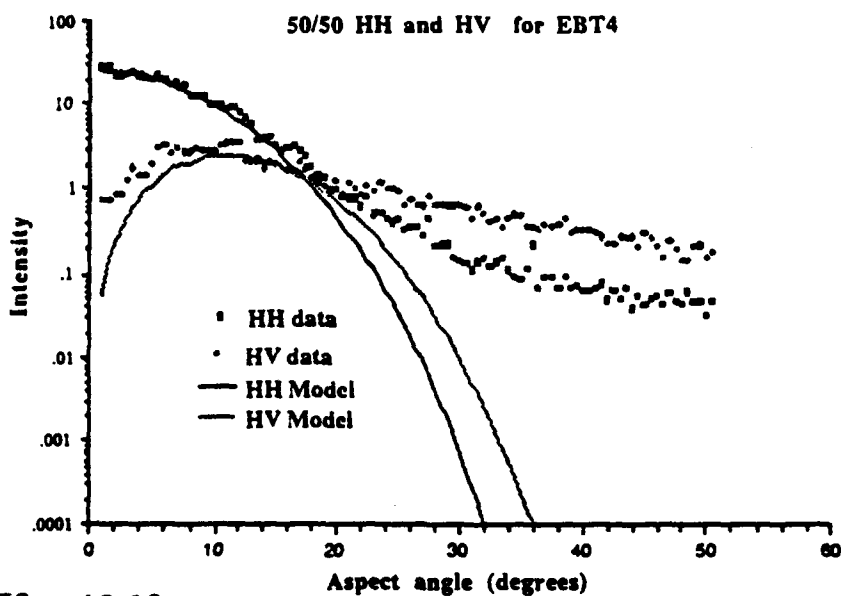


FIG. AC-12

$\sigma_o(HH)$ and $\sigma_o(HV)$ for laboratory depression angles $\xi_i = \xi_s = 50$

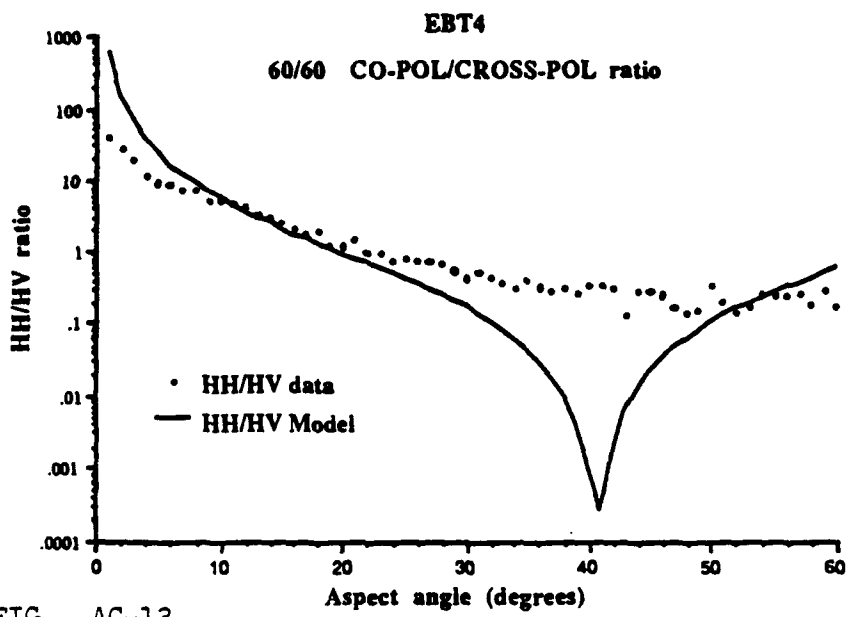


FIG. AC-13

$\sigma_o(HH)/\sigma_o(HV)$ for laboratory depression angles $\xi_i = \xi_s = 60$

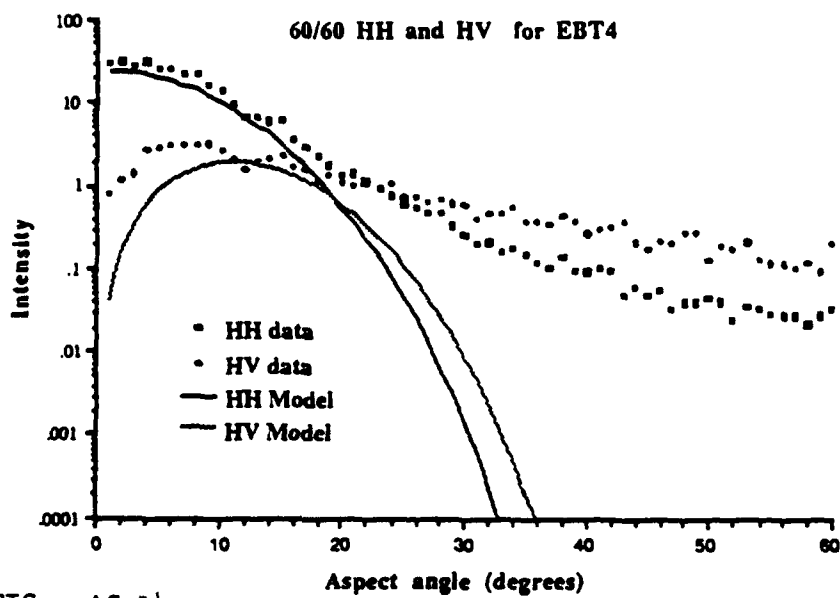


FIG. AC-14

$\sigma_o(HH)$ and $\sigma_o(HV)$ for laboratory depression angles $\xi_i = \xi_s = 60$

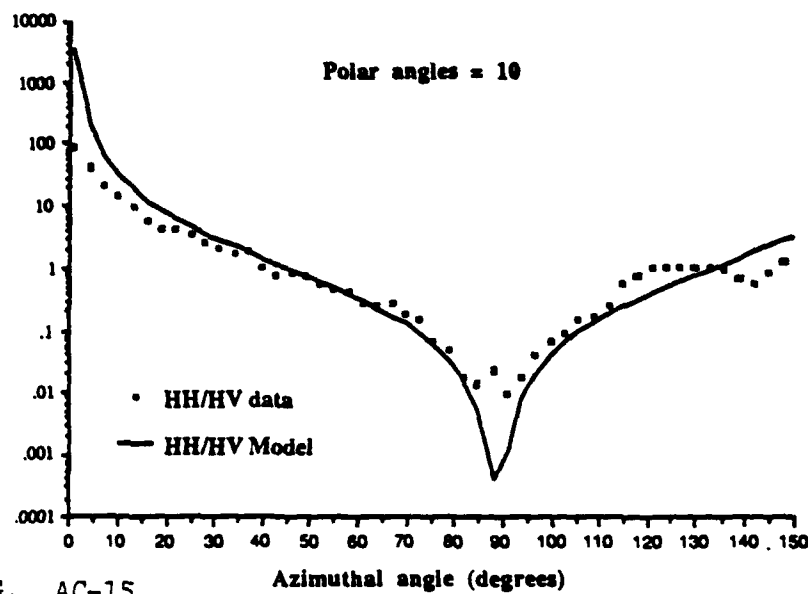


FIG. AC-15

$\sigma_0(\text{HH})/\sigma_0(\text{HV})$ for field polar angles $\theta_i = \theta_s = 10$

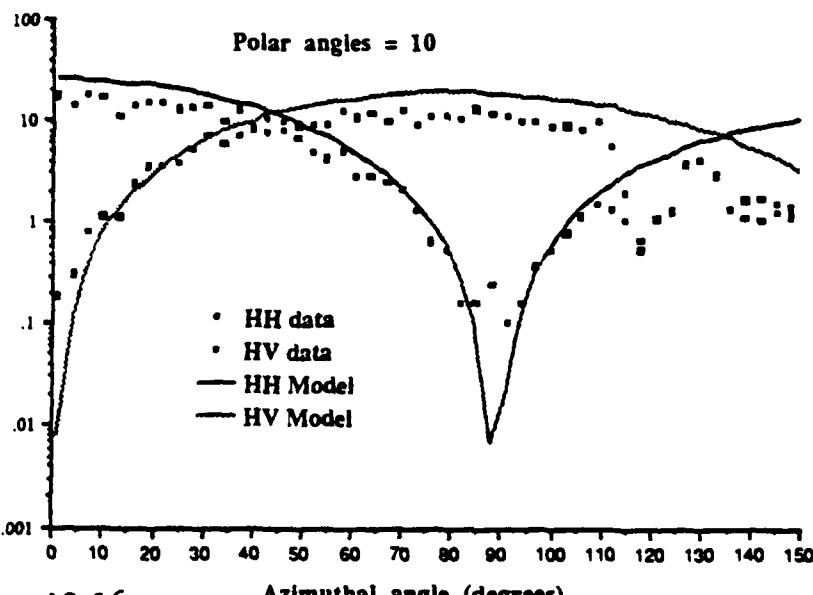


FIG. AC-16

$\sigma_0(\text{HH})$ and $\sigma_0(\text{HV})$ for field polar angles $\theta_i = \theta_s = 10$

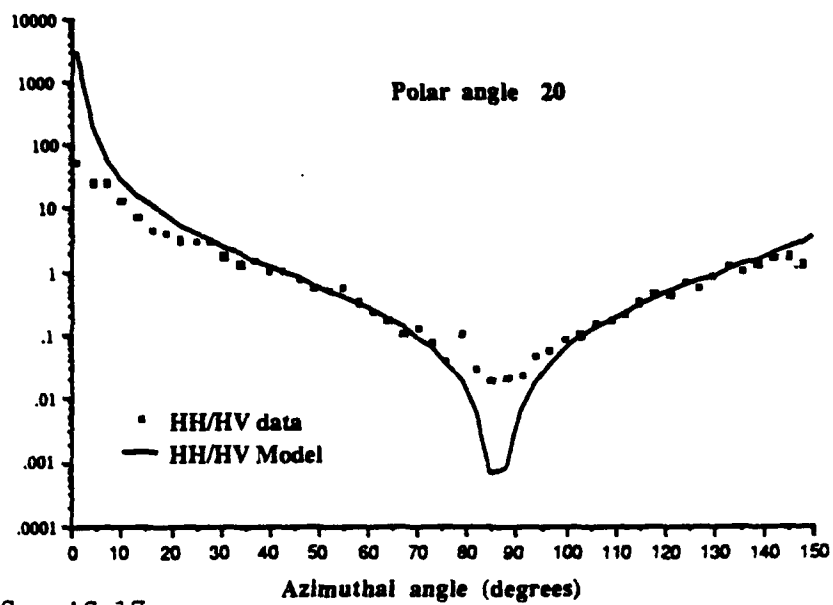


FIG. AC-17

$\sigma_0(\text{HH})/\sigma_0(\text{HV})$ for field polar angles $\theta_i = \theta_s = 20$

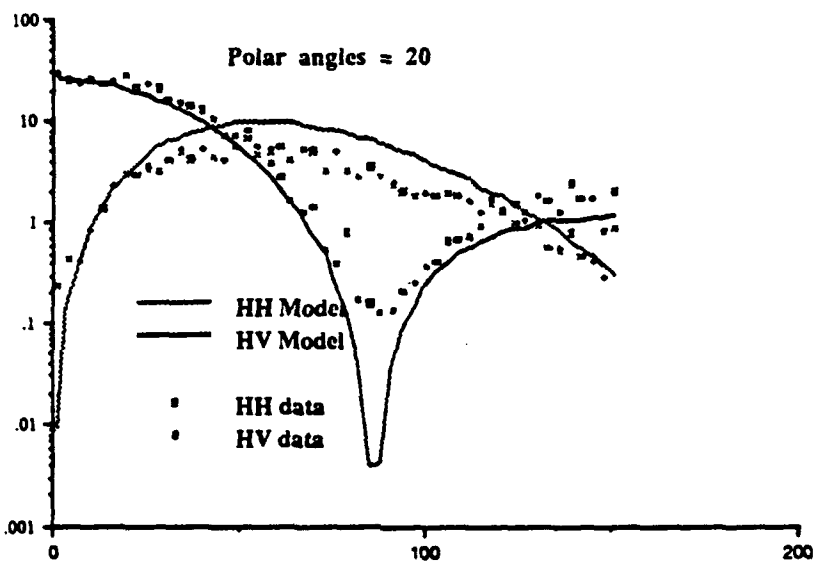


FIG. AC-18

$\sigma_0(\text{HH})$ and $\sigma_0(\text{HV})$ for field polar angles $\theta_i = \theta_s = 20$

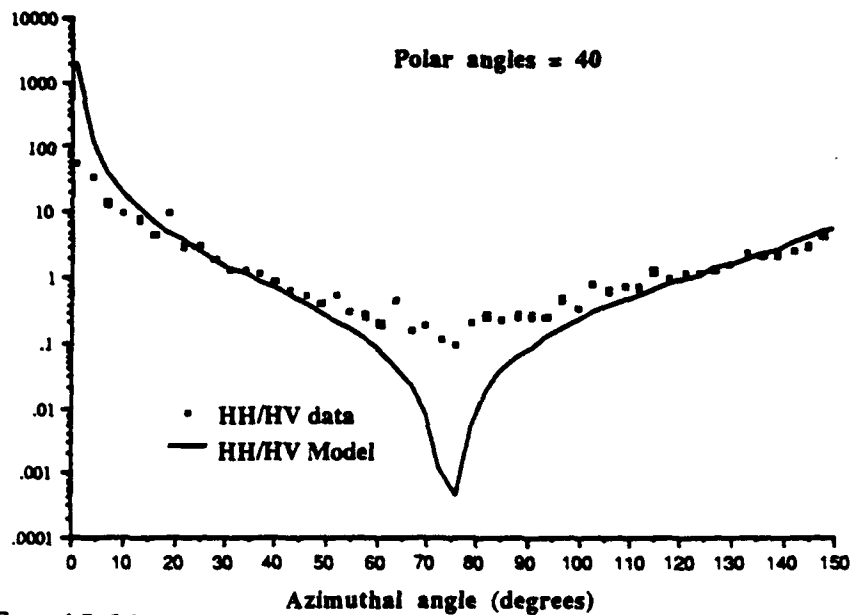


FIG. AC-19

$\sigma_o(HH)/\sigma_o(HV)$ for field polar angles $\theta_i = \theta_s = 30$

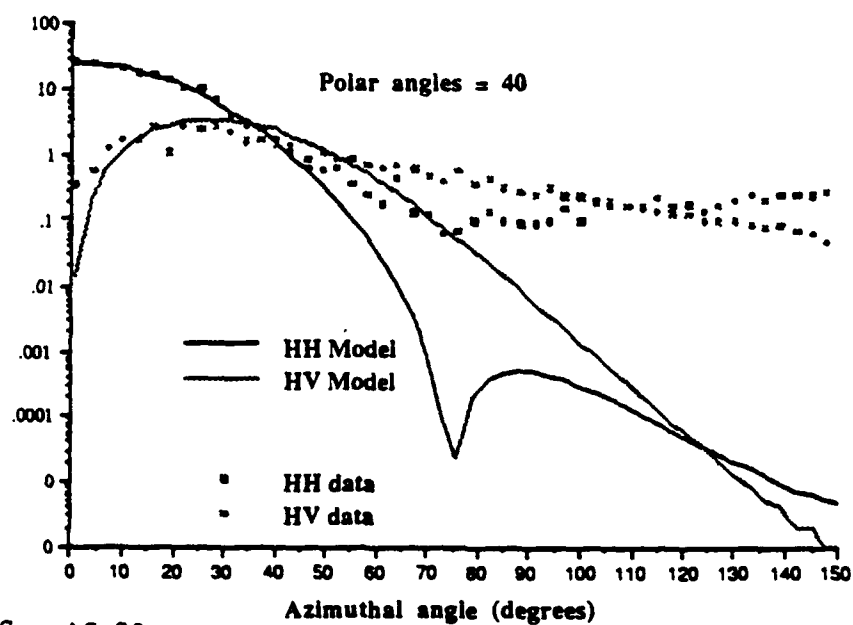


FIG. AC-20

$\sigma_o(HH)$ and $\sigma_o(HV)$ for field polar angles $\theta_i = \theta_s = 30$

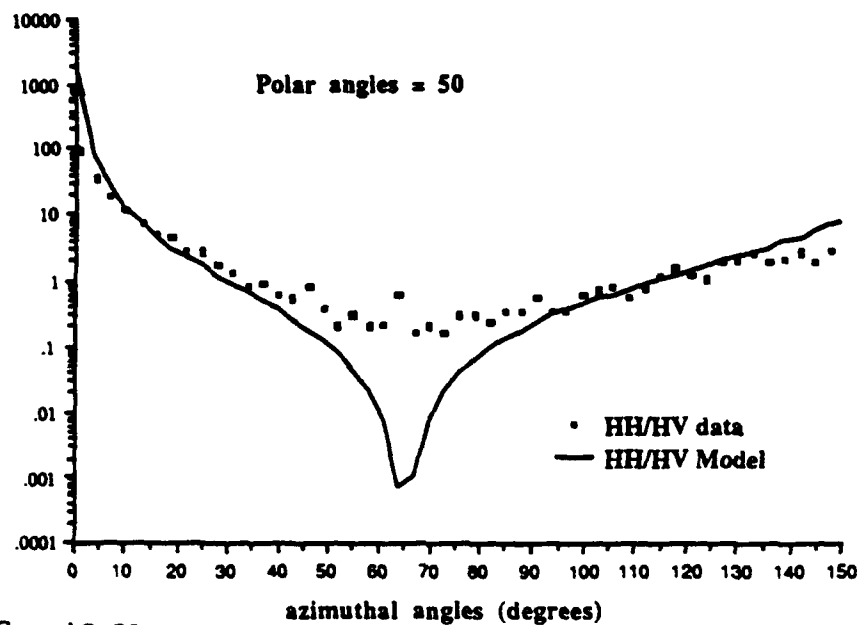


FIG. AC-21

$\sigma_0(\text{HH})/\sigma_0(\text{HV})$ for field polar angles $\theta_i = \theta_s = 40$

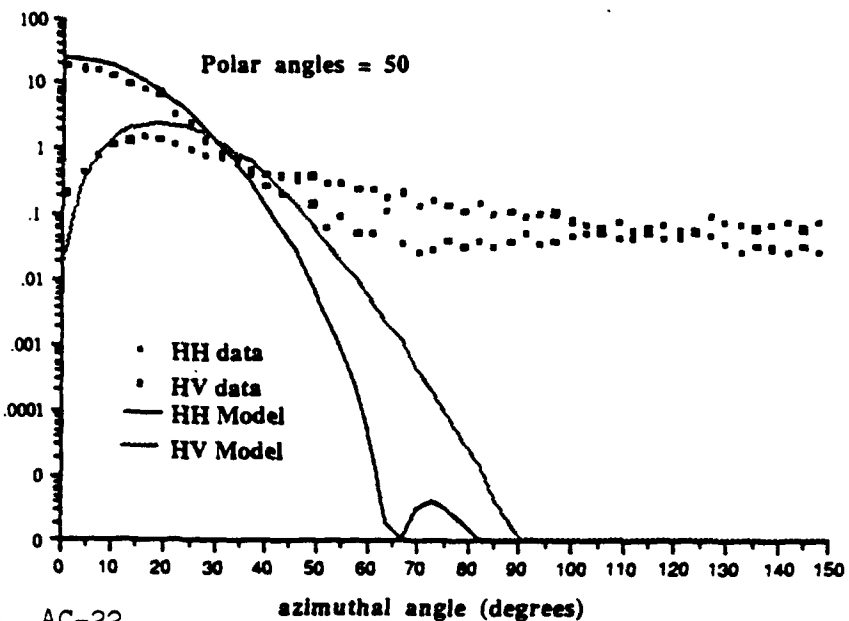


FIG. AC-22

$\sigma_0(\text{HH})$ and $\sigma_0(\text{HV})$ for field polar angles $\theta_i = \theta_s = 40$

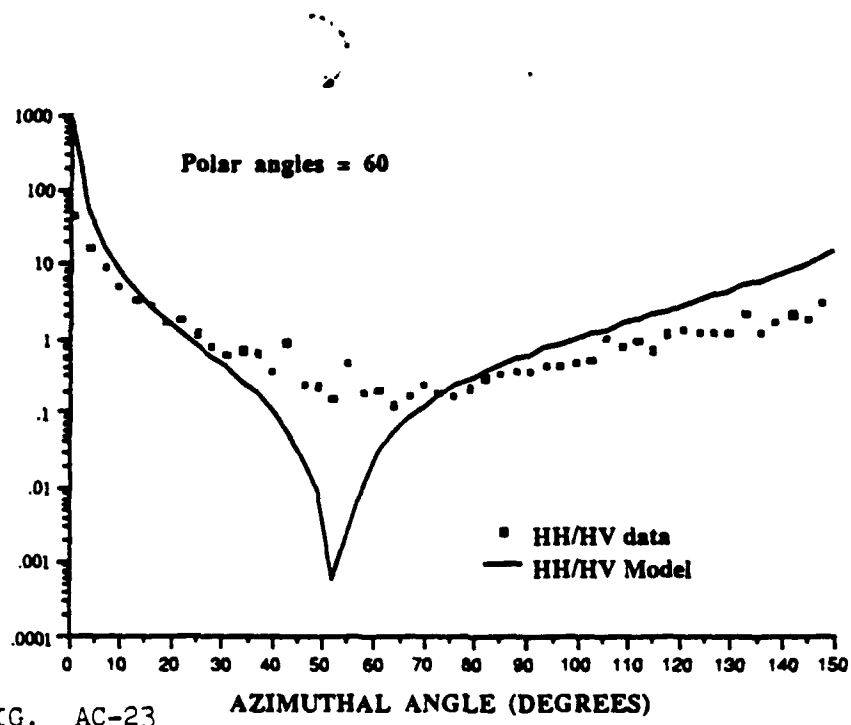


FIG. AC-23

$\sigma_o(\text{HH})/\sigma_o(\text{HV})$ for field polar angles $\theta_i = \theta_s = 50$

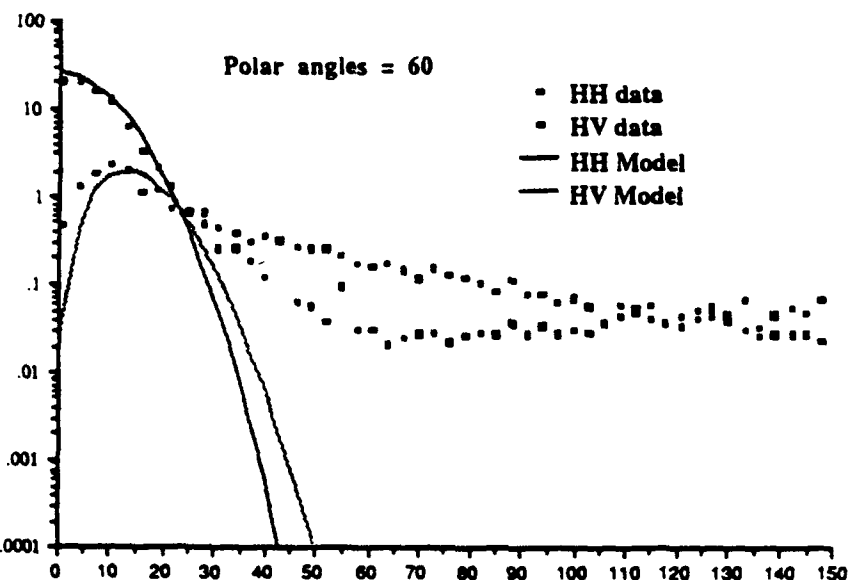


FIG. AC-24

$\sigma_o(\text{HH})$ and $\sigma_o(\text{HV})$ for field polar angles $\theta_i = \theta_s = 50$

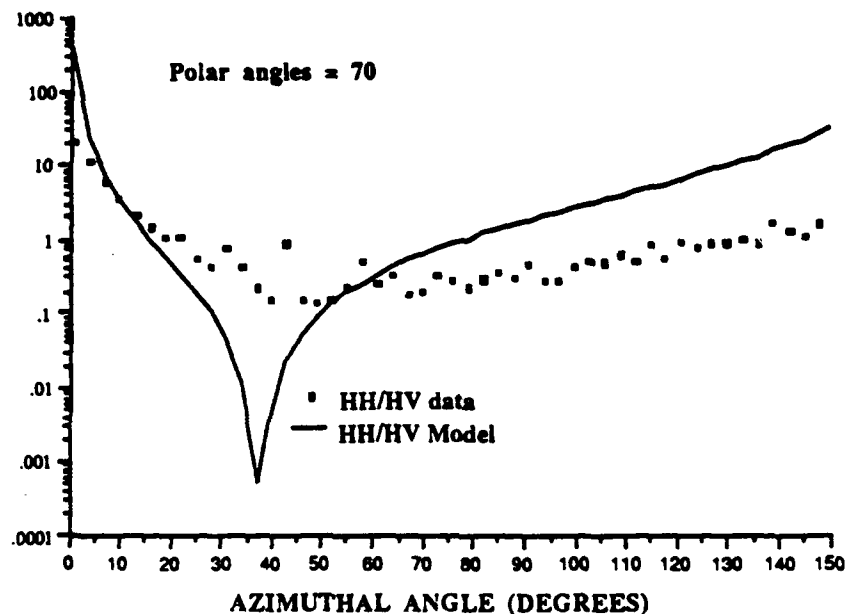


FIG. AC-25

$$\sigma_0(\text{HH})/\sigma_0(\text{HV}) \text{ for field polar angles } \theta_i = \theta_s = 60$$

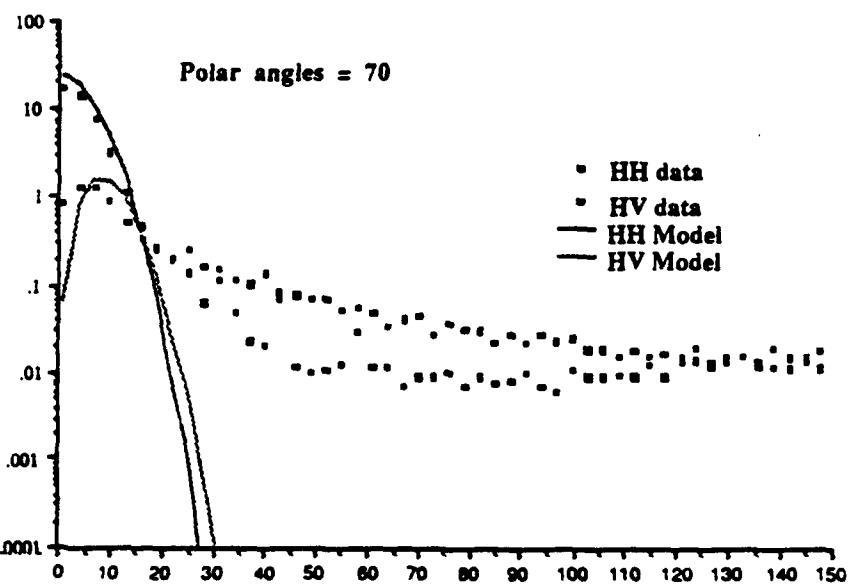


FIG. AC-26

AZIMUTHAL ANGLE (DEGREES)

$$\sigma_0(\text{HH}) \text{ and } \sigma_0(\text{HV}) \text{ for field polar angles } \theta_i = \theta_s = 60$$

EBT6

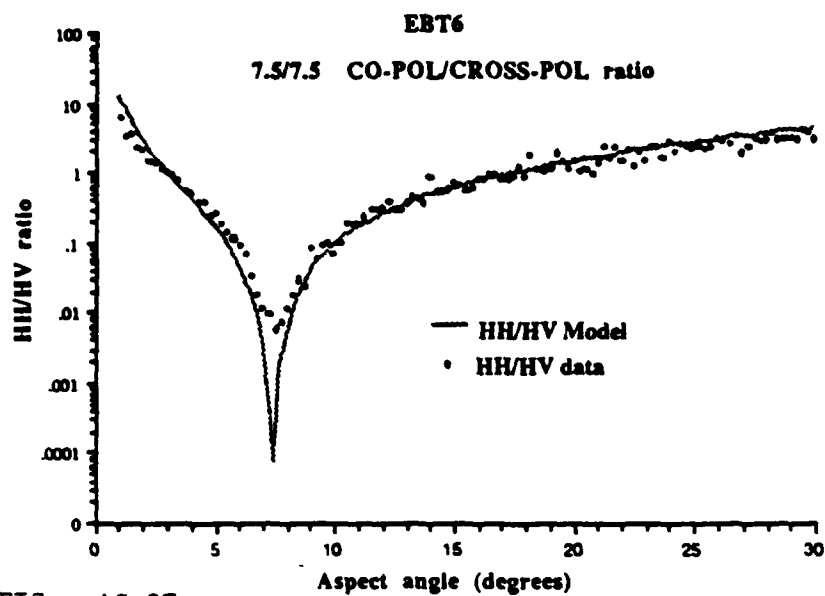


FIG. AC-27

$\sigma_o(\text{HH})/\sigma_o(\text{HV})$ for laboratory depression angles $\xi_i = \xi_s = 7.5$

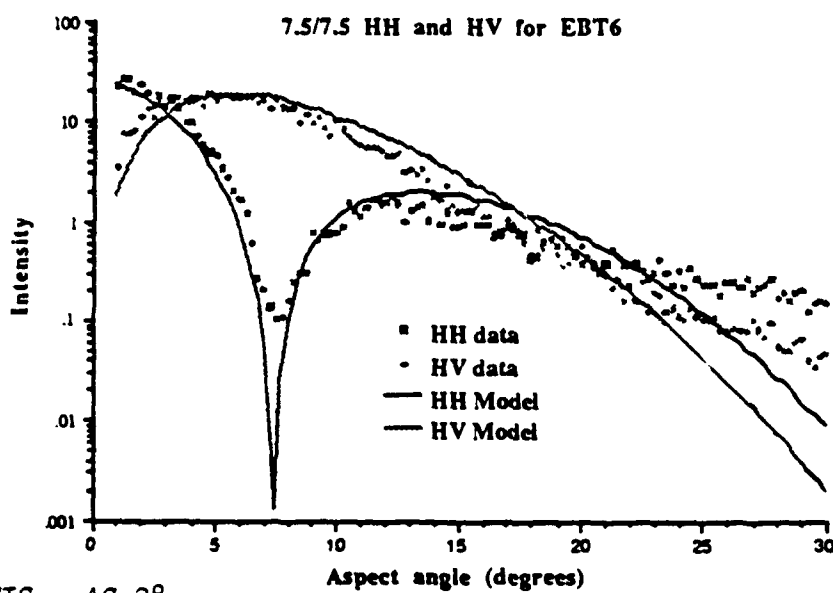


FIG. AC-28

$\sigma_o(\text{HH})$ and $\sigma_o(\text{HV})$ for laboratory depression angles $\xi_i = \xi_s = 7.5$

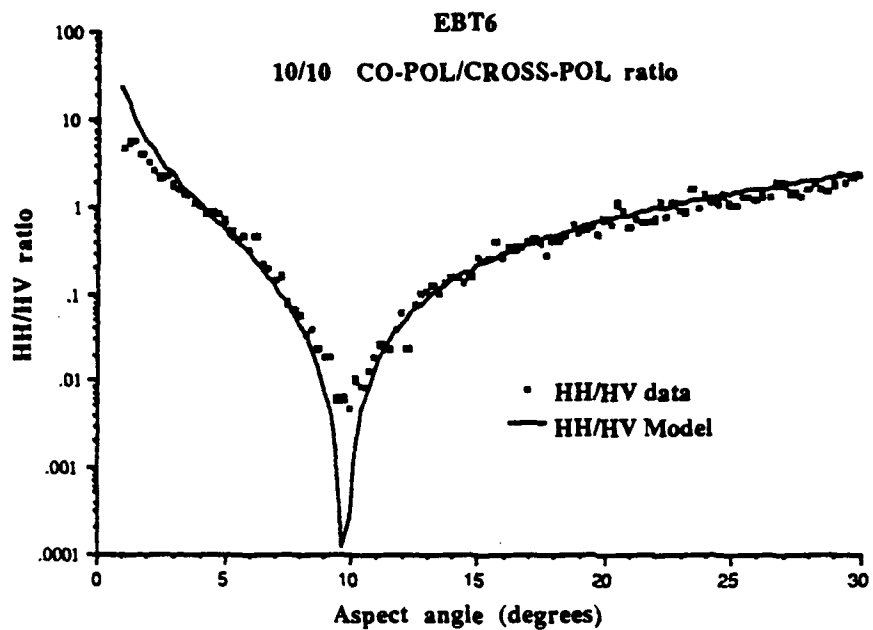


FIG. AC-29

$\sigma_o(\text{HH})/\sigma_o(\text{HV})$ for laboratory depression angles $\xi_i = \xi_s = 10$

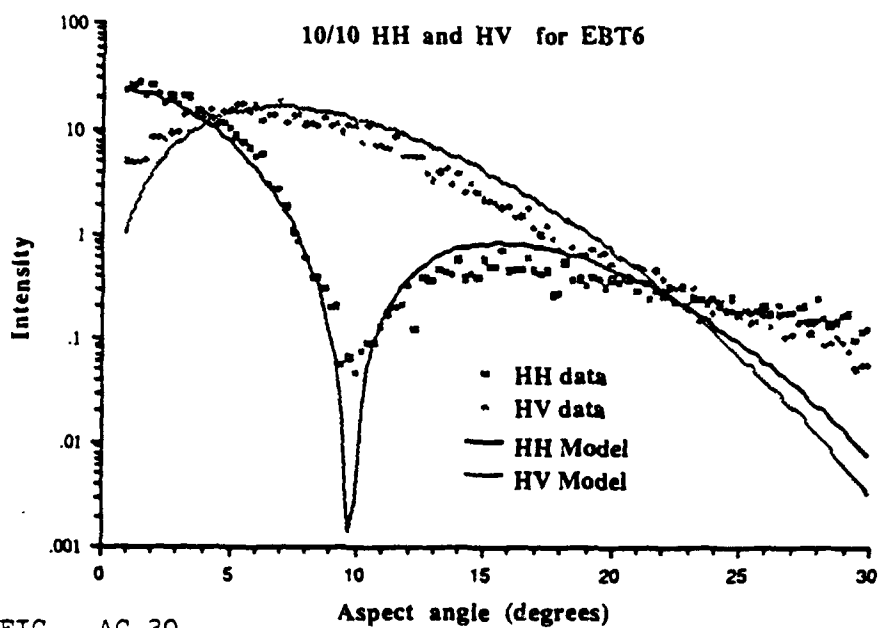


FIG. AC-30

$\sigma_o(\text{HH})$ and $\sigma_o(\text{HV})$ for laboratory depression angles $\xi_i = \xi_s = 10$

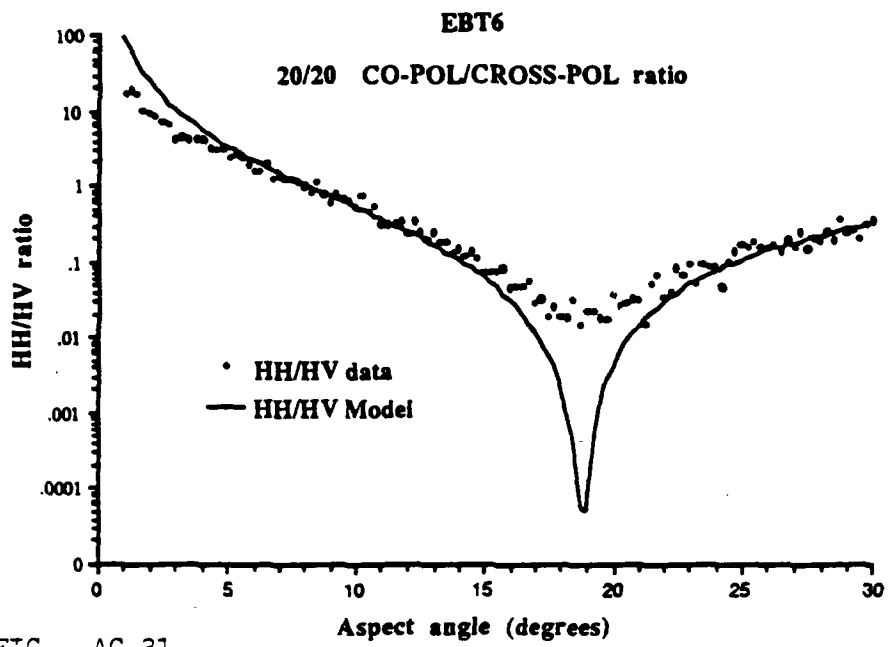


FIG. AC-31

$\sigma_o(HH)/\sigma_o(HV)$ for laboratory depression angles $\xi_i = \xi_s = 20$

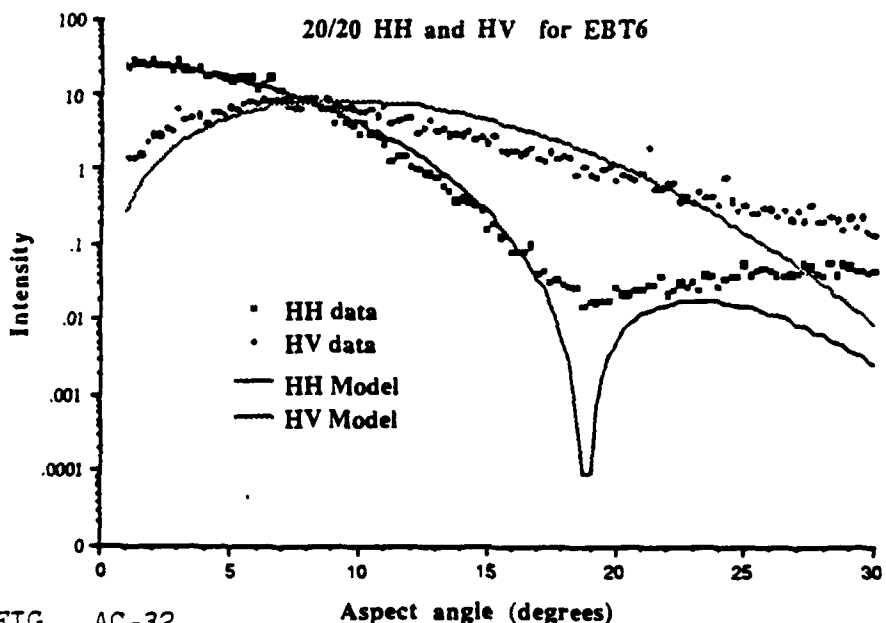


FIG. AC-32

$\sigma_o(HH)$ and $\sigma_o(HV)$ for laboratory depression angles $\xi_i = \xi_s = 20$

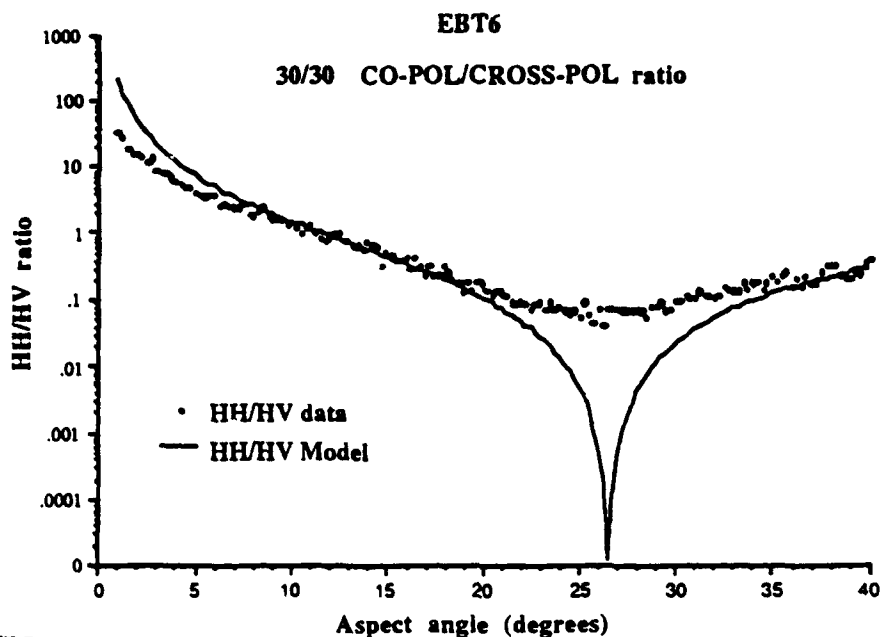


FIG. AC-33

$\sigma_o(\text{HH})/\sigma_o(\text{HV})$ for laboratory depression angles $\xi_i = \xi_s = 30$

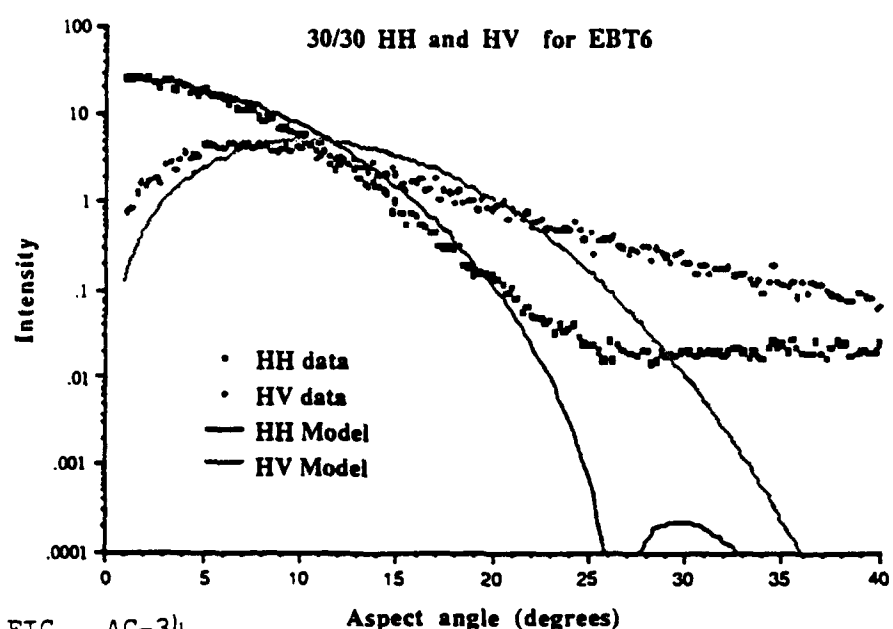


FIG. AC-34

$\sigma_o(\text{HH})$ and $\sigma_o(\text{HV})$ for laboratory depression angles $\xi_i = \xi_s = 30$

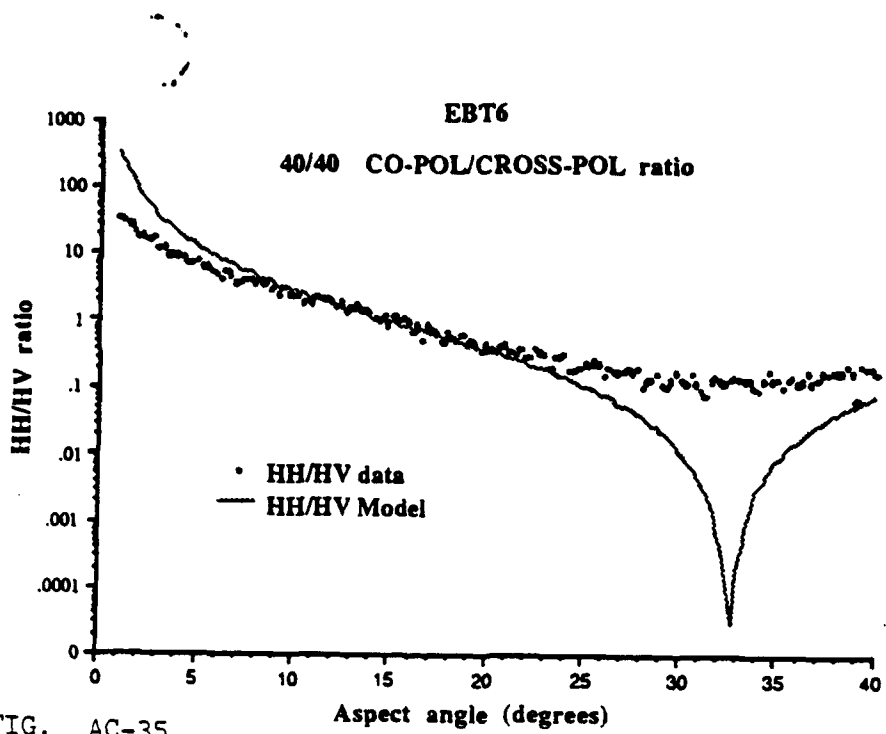


FIG. AC-35

$\sigma_o(\text{HH})/\sigma_o(\text{HV})$ for laboratory depression angles $\xi_i = \xi_s = 40$

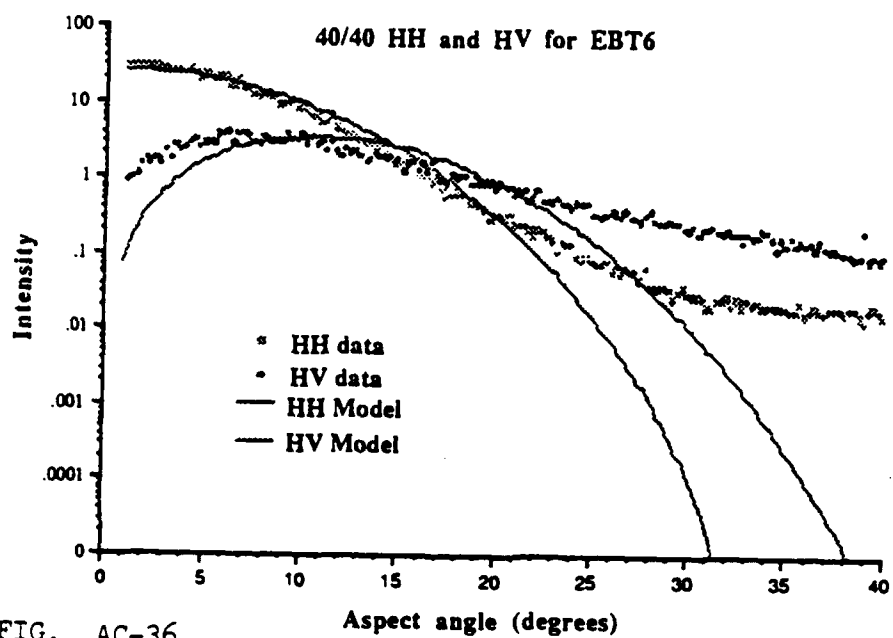


FIG. AC-36

$\sigma_o(\text{HH})$ and $\sigma_o(\text{HV})$ for laboratory depression angles $\xi_i = \xi_s = 40$

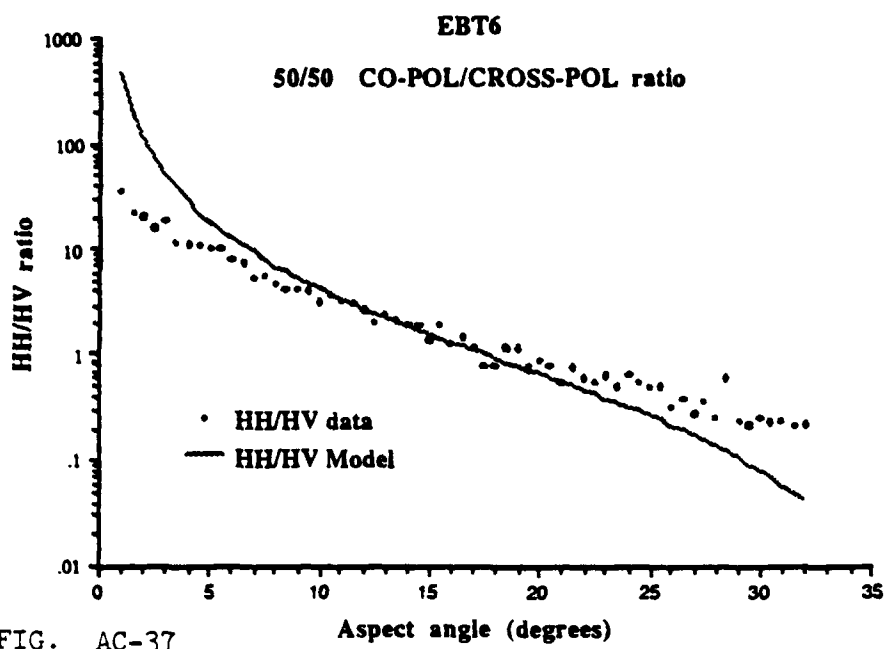


FIG. AC-37

$\sigma_o(HH)/\sigma_o(HV)$ for laboratory depression angles $\xi_i = \xi_s = 50$

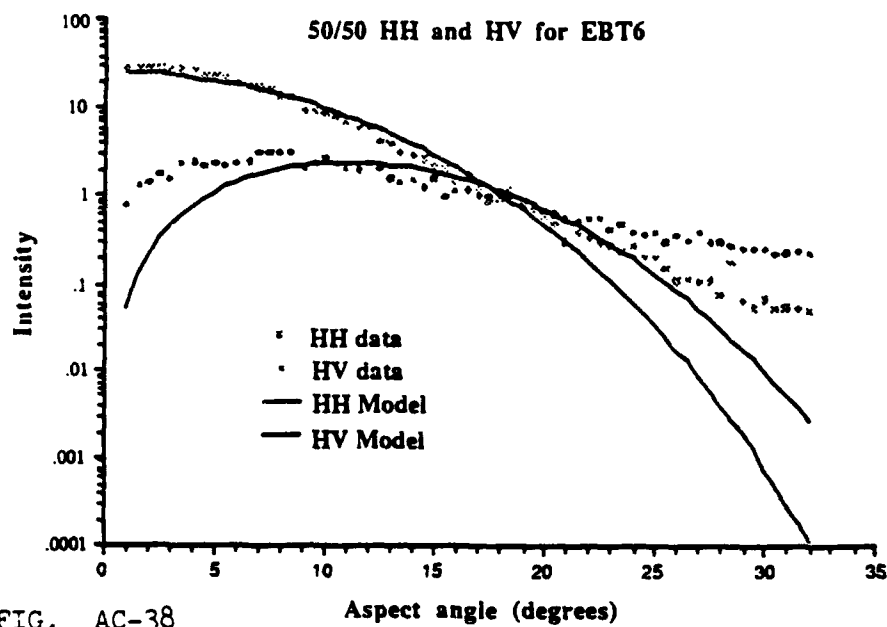


FIG. AC-38

$\sigma_o(HH)$ and $\sigma_o(HV)$ for laboratory depression angles $\xi_i = \xi_s = 50$

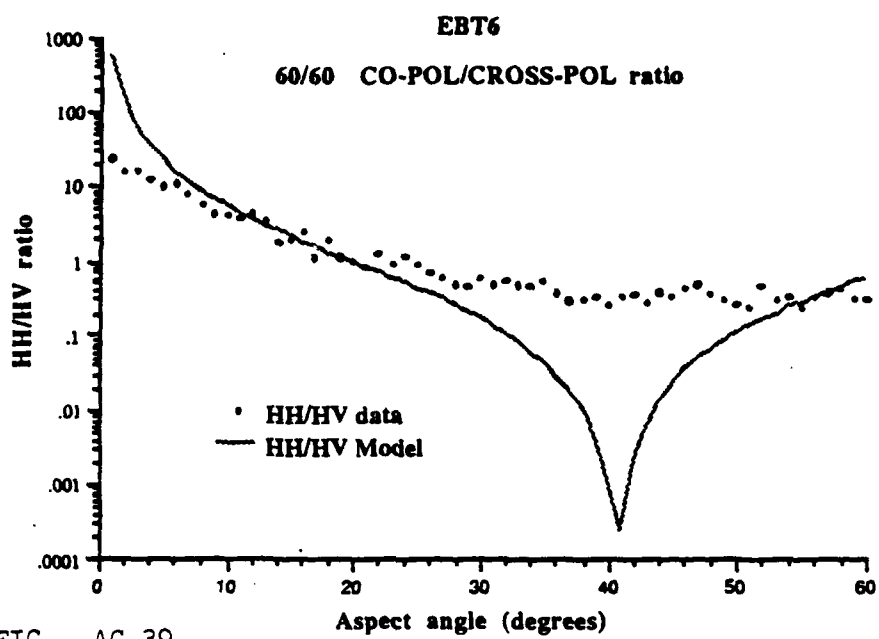


FIG. AC-39

$\sigma_o(\text{HH})/\sigma_o(\text{HV})$ for laboratory depression angles $\xi_i = \xi_s = 60$

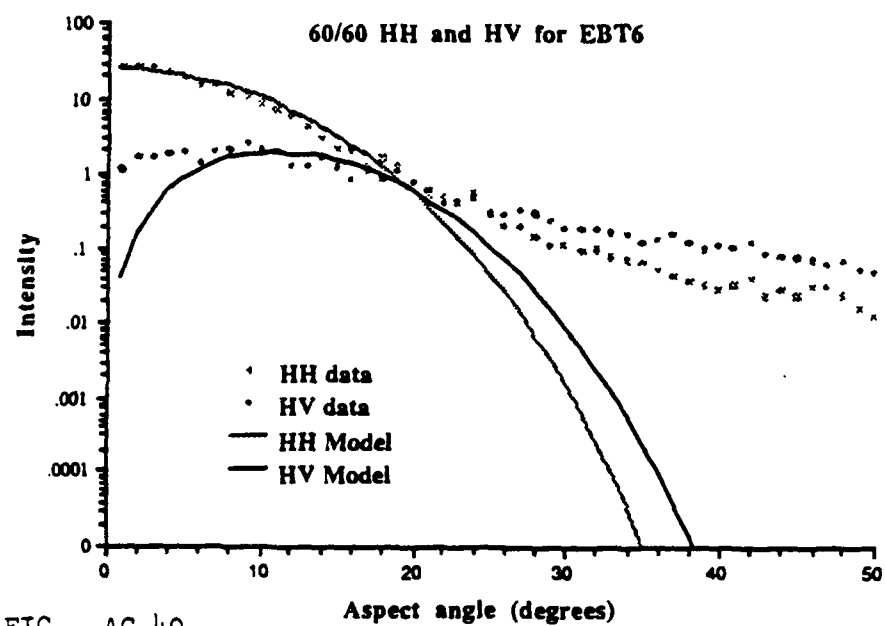


FIG. AC-40

$\sigma_o(\text{HH})$ and $\sigma_o(\text{HV})$ for laboratory depression angles $\xi_i = \xi_s = 60$

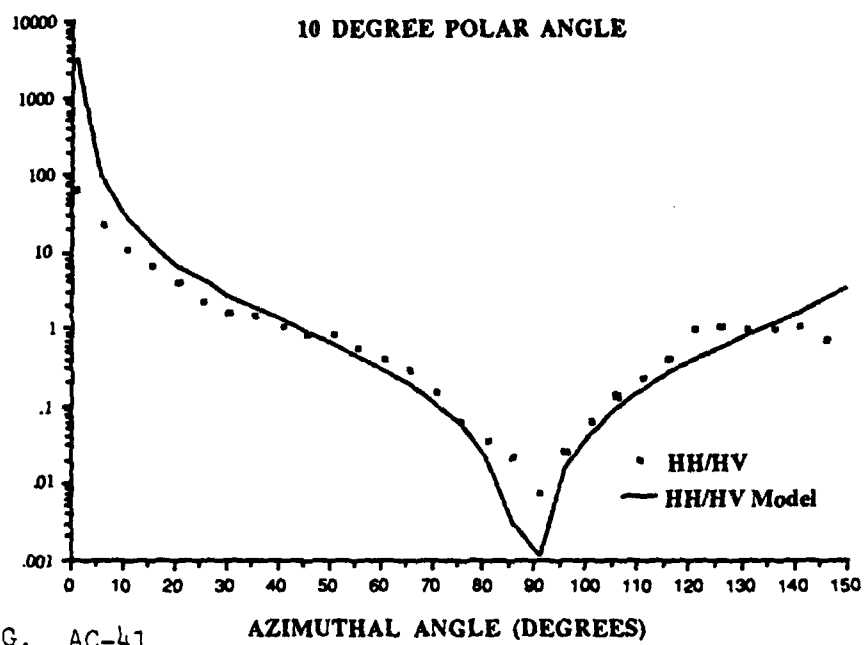


FIG. AC-41

$\sigma_0(\text{HH})/\sigma_0(\text{HV})$ for field polar angles $\theta_i = \theta_s = 10$

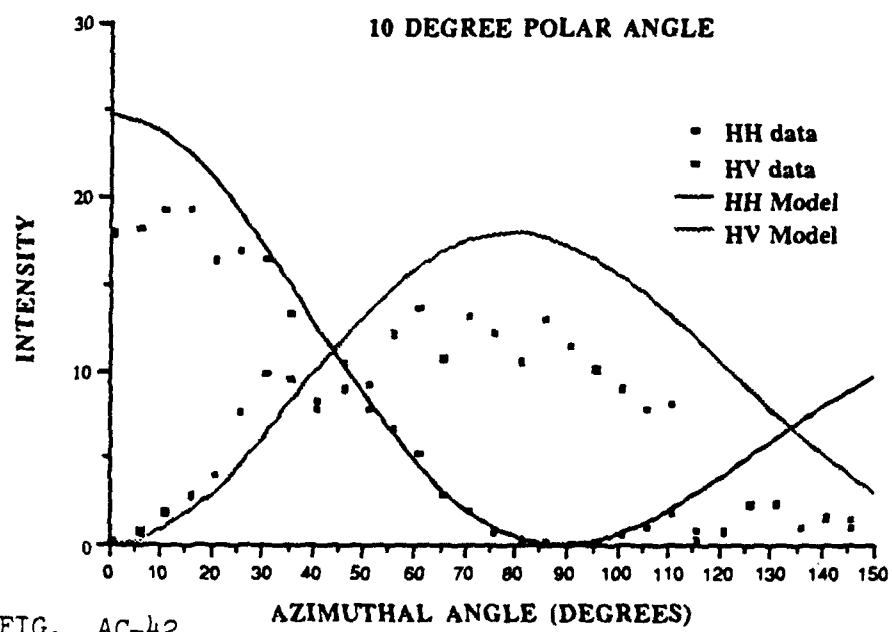


FIG. AC-42

$\sigma_o(HH)$ and $\sigma_o(HV)$ for field polar angles $\theta_i = \theta_s = 10$

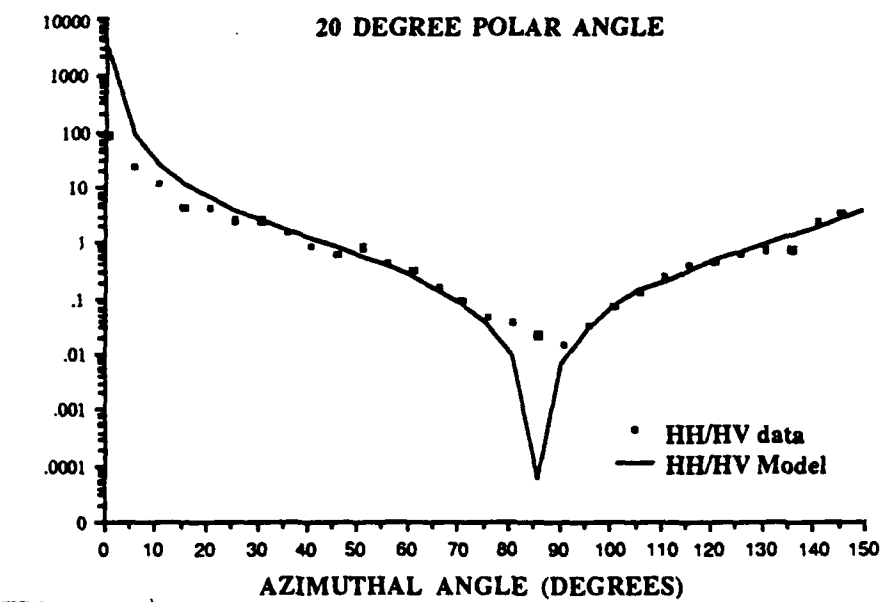


FIG. AC-43

$\sigma_o(HH)/\sigma_o(HV)$ for laboratory depression angles $\xi_i = \xi_s = 20$

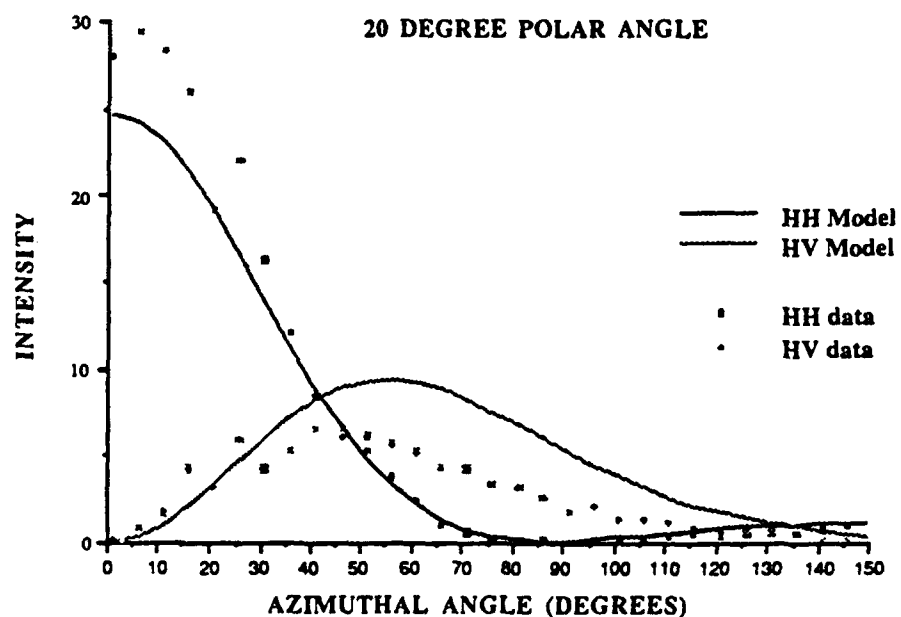


FIG. AC-44

$\sigma_o(HH)$ and $\sigma_o(HV)$ for field polar angles $\theta_i = \theta_s = 20$

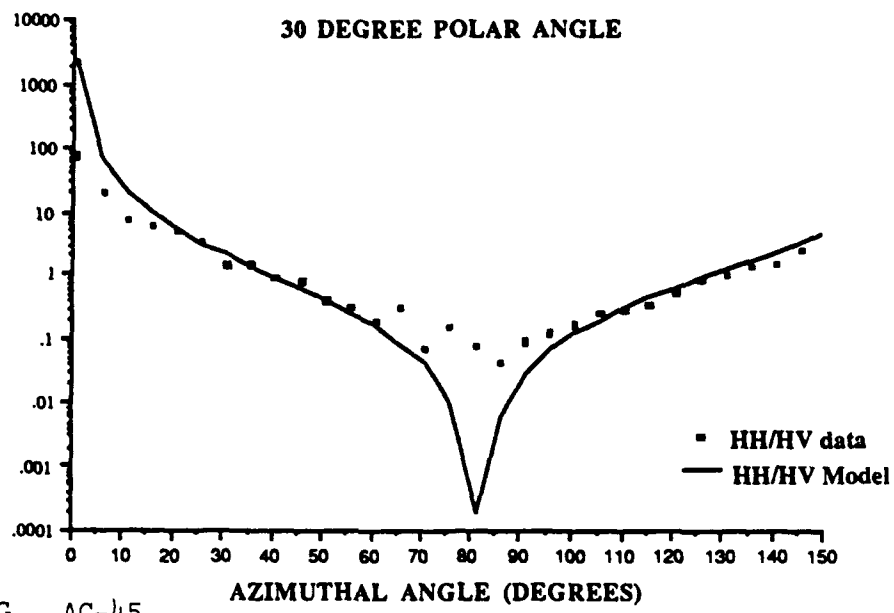


FIG. AC-45

$\sigma_o(\text{HH})/\sigma_o(\text{HV})$ for field polar angles $\theta_i = \theta_s = 30$

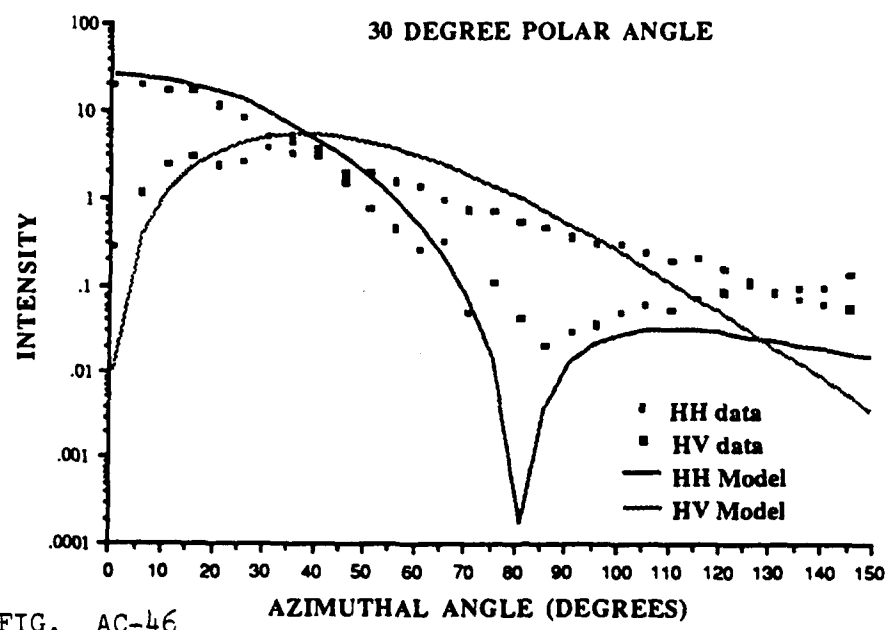


FIG. AC-46

$\sigma_o(\text{HH})$ and $\sigma_o(\text{HV})$ for field polar angles $\theta_i = \theta_s = 30$

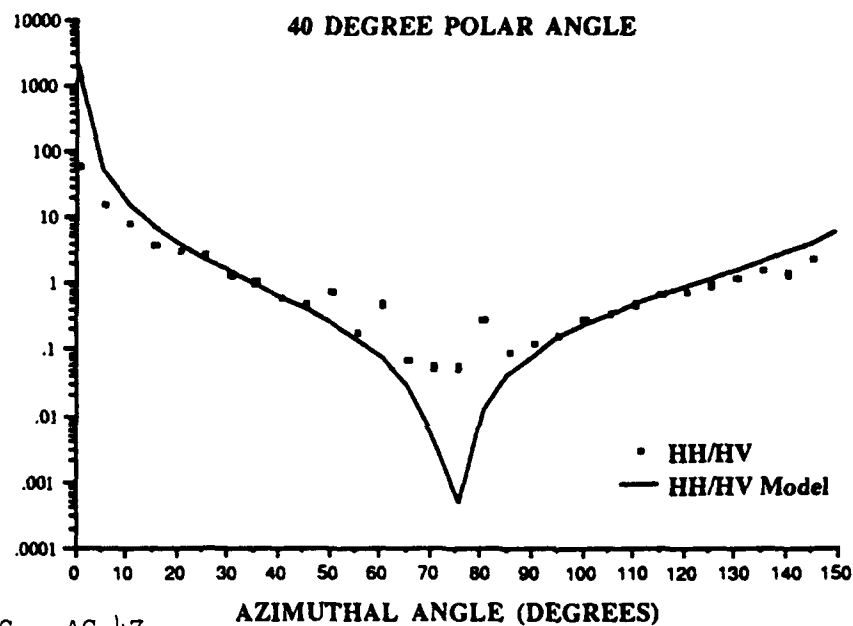


FIG. AC-47

$\sigma_o(\text{HH})/\sigma_o(\text{HV})$ for field polar angles $\theta_i = \theta_s = 40$

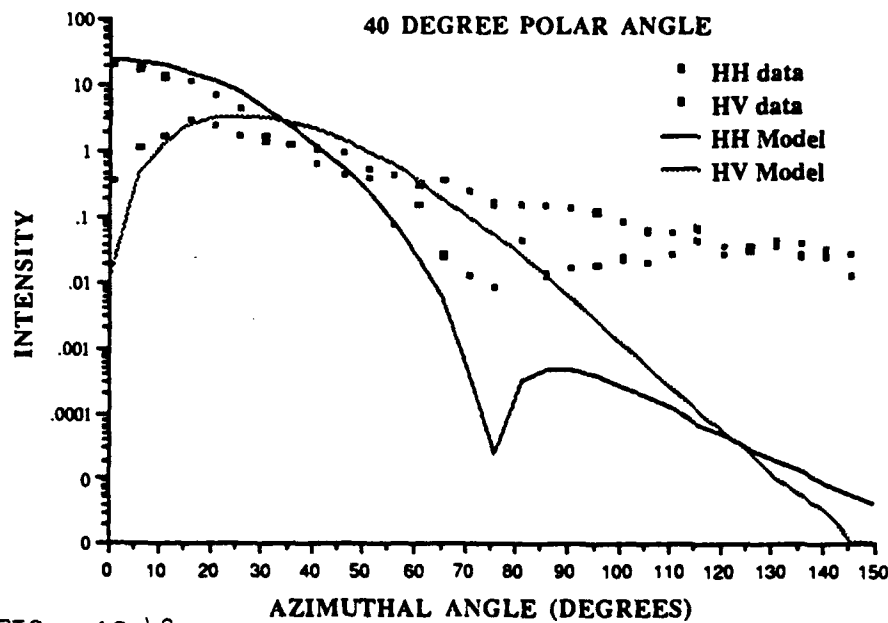


FIG. AC-48

$\sigma_o(\text{HH})$ and $\sigma_o(\text{HV})$ for field polar angles $\theta_i = \theta_s = 40$

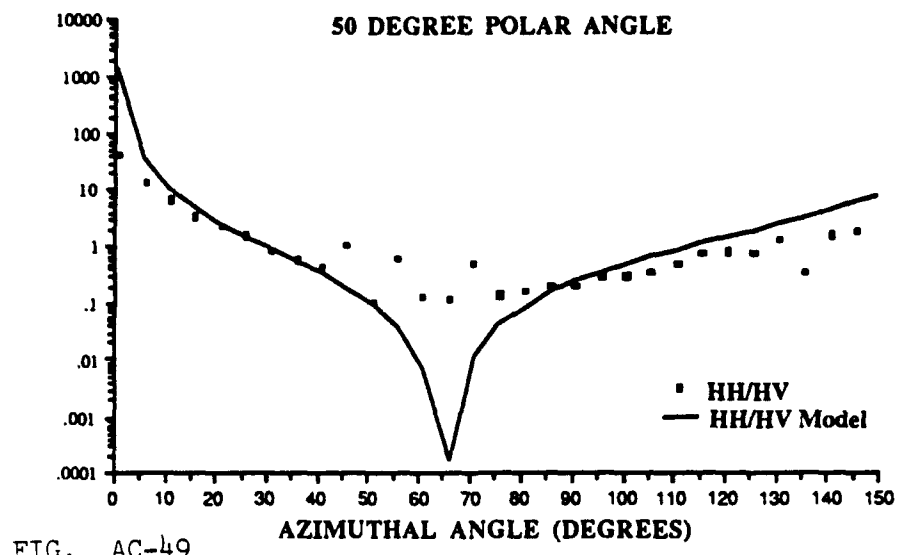


FIG. AC-49

$\sigma_o(\text{HH})/\sigma_o(\text{HV})$ for field polar angles $\theta_i = \theta_s = 50$

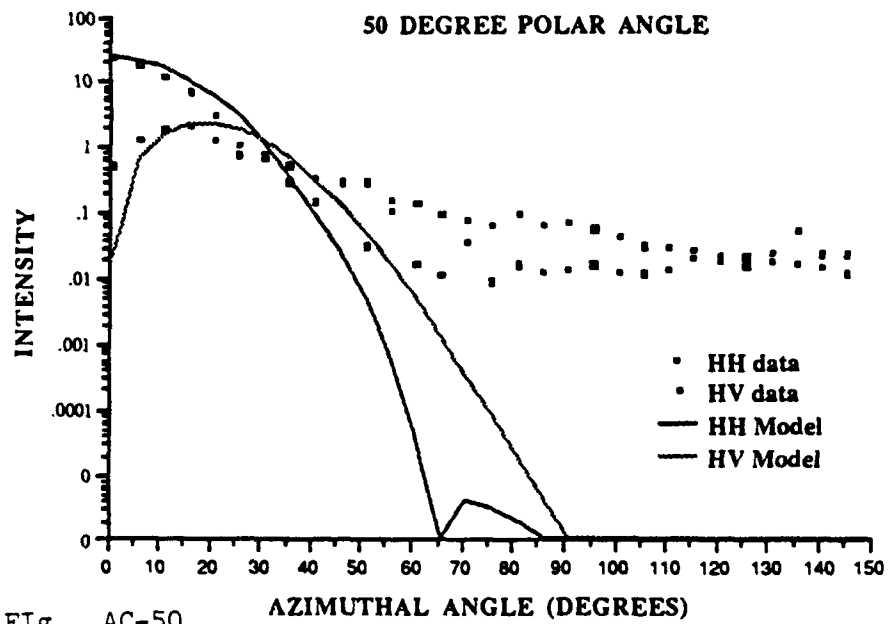


FIG. AC-50

$\sigma_o(\text{HH})$ and $\sigma_o(\text{HV})$ for field polar angles $\theta_i = \theta_s = 50$

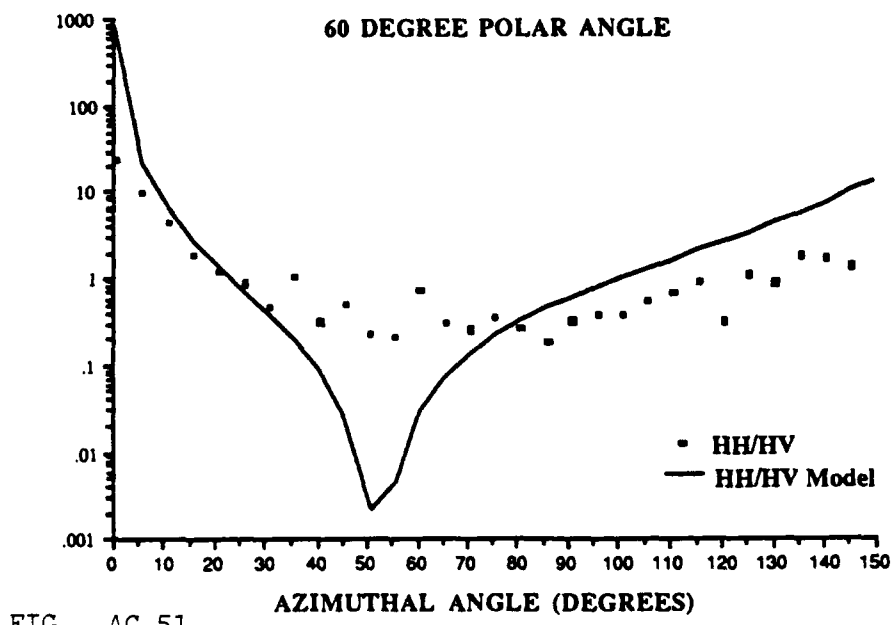


FIG. AC-51

$\sigma_o(\text{HH})/\sigma_o(\text{HV})$ for field polar angles $\theta_i = \theta_s = 60$

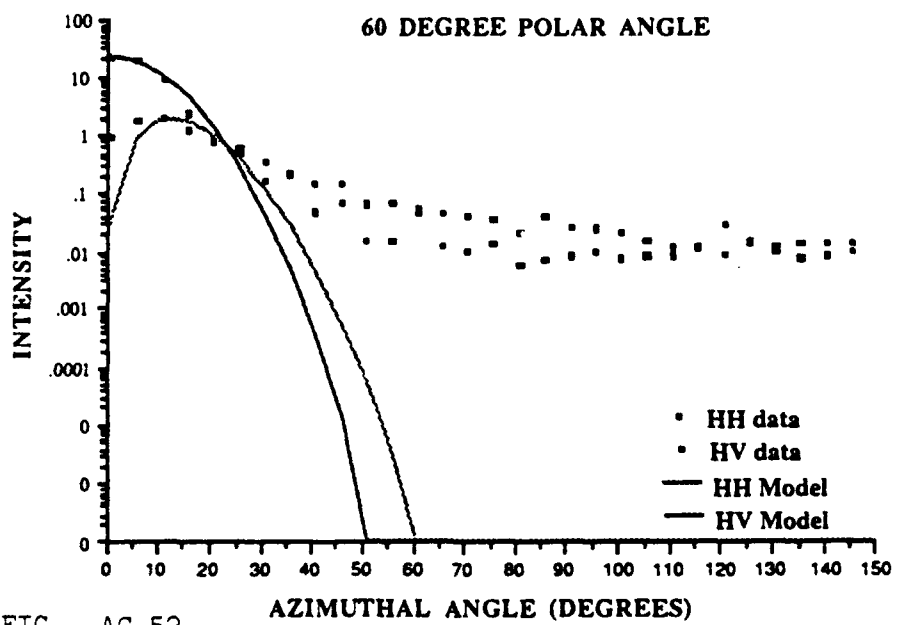


FIG. AC-52

$\sigma_o(\text{HH})$ and $\sigma_o(\text{HV})$ for field polar angles $\theta_i = \theta_s = 60$

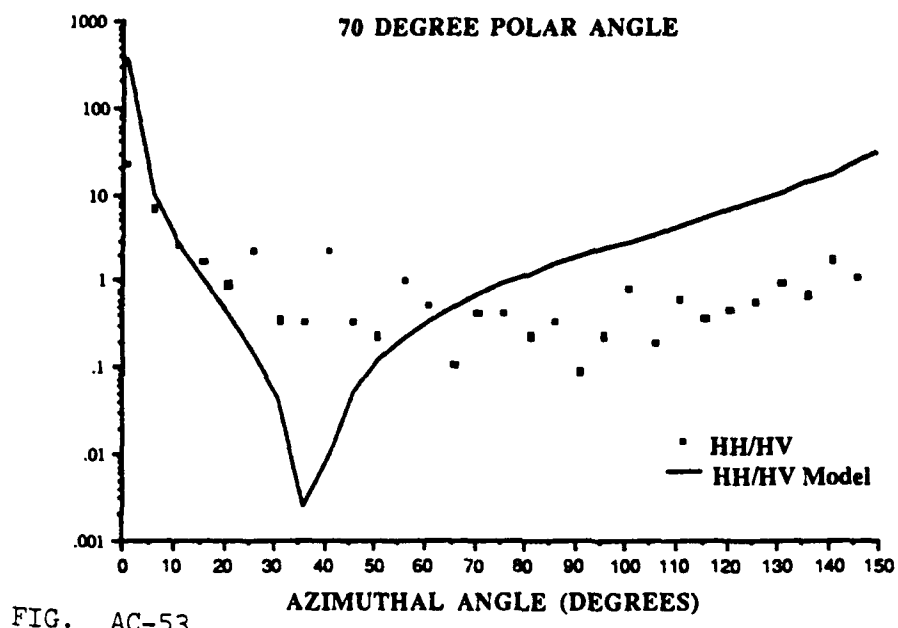


FIG. AC-53

$\sigma_o(\text{HH})/\sigma_o(\text{HV})$ for field polar angles $\theta_i = \theta_s = 70$

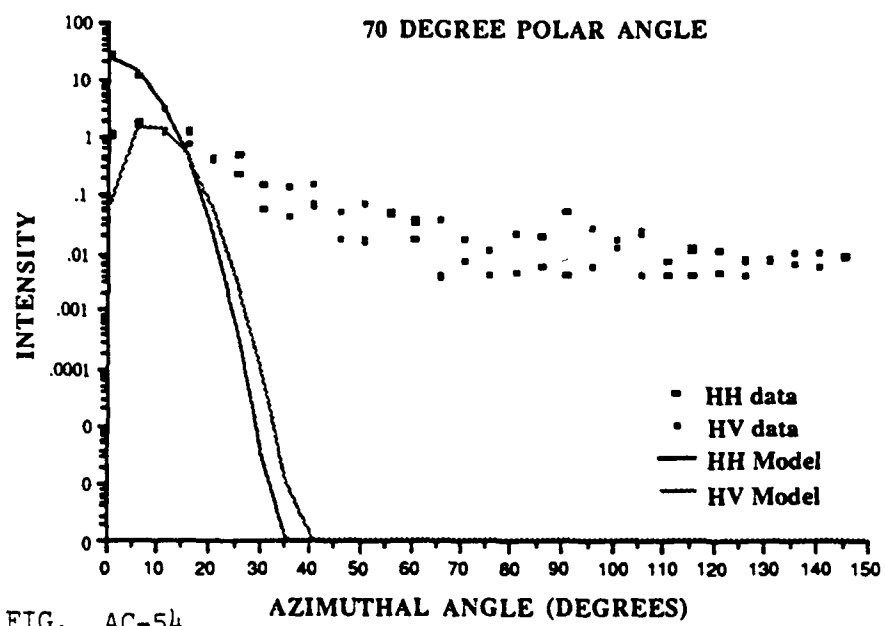


FIG. AC-54

$\sigma_o(\text{HH})$ and $\sigma_o(\text{HV})$ for field polar angles $\theta_i = \theta_s = 70$

EBT13

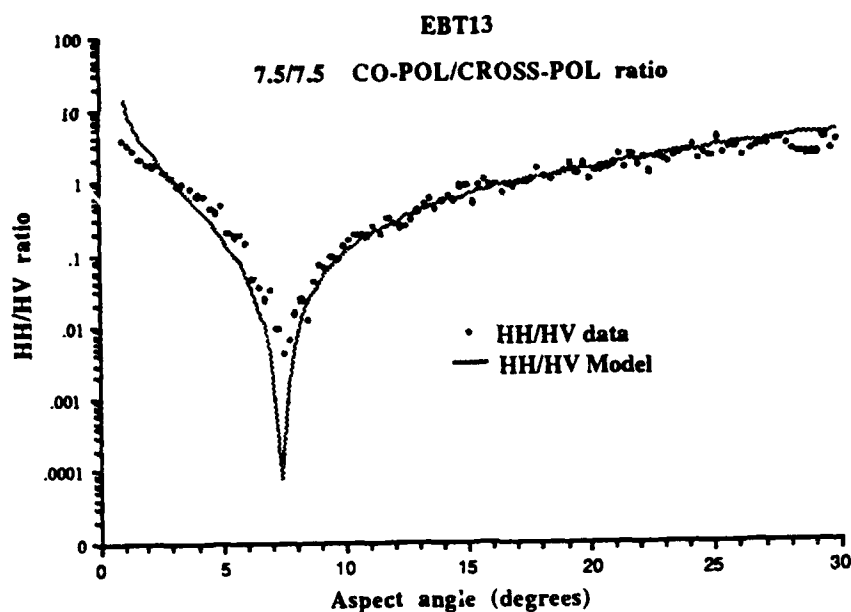


FIG. AC-55

$\sigma_o(\text{HH})/\sigma_o(\text{HV})$ for laboratory depression angles $\xi_i = \xi_s = 7.5$

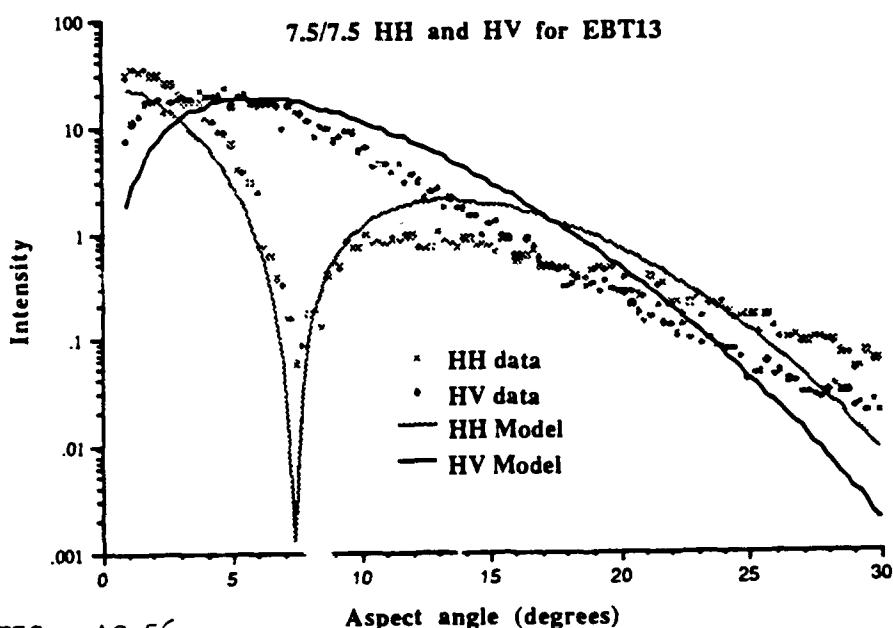


FIG. AC-56

$\sigma_o(\text{HH})$ and $\sigma_o(\text{HV})$ for laboratory depression angles $\xi_i = \xi_s = 7.5$

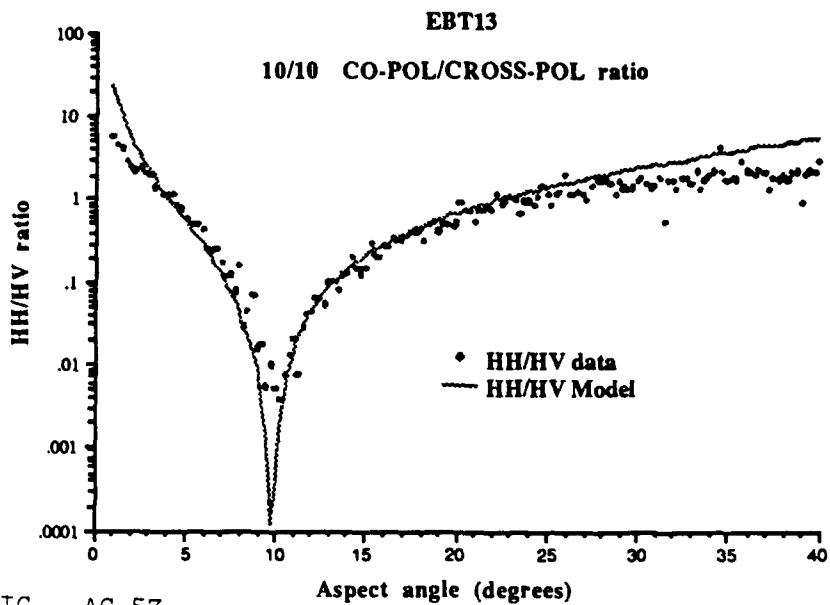


FIG. AC-57

$\sigma_o(\text{HH})/\sigma_o(\text{HV})$ for laboratory depression angles $\xi_i = \xi_s = 10$

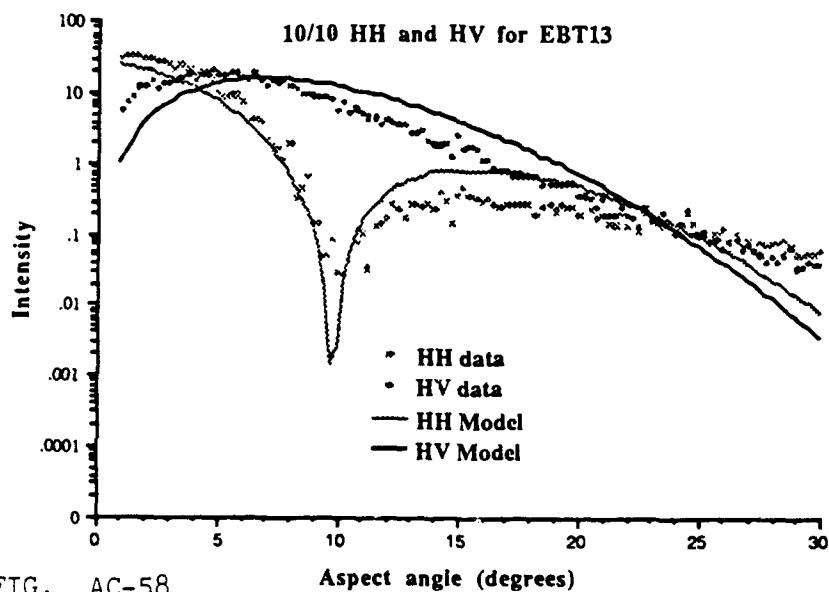


FIG. AC-58

$\sigma_o(\text{HH})$ and $\sigma_o(\text{HV})$ for laboratory depression angles $\xi_i = \xi_s = 10$

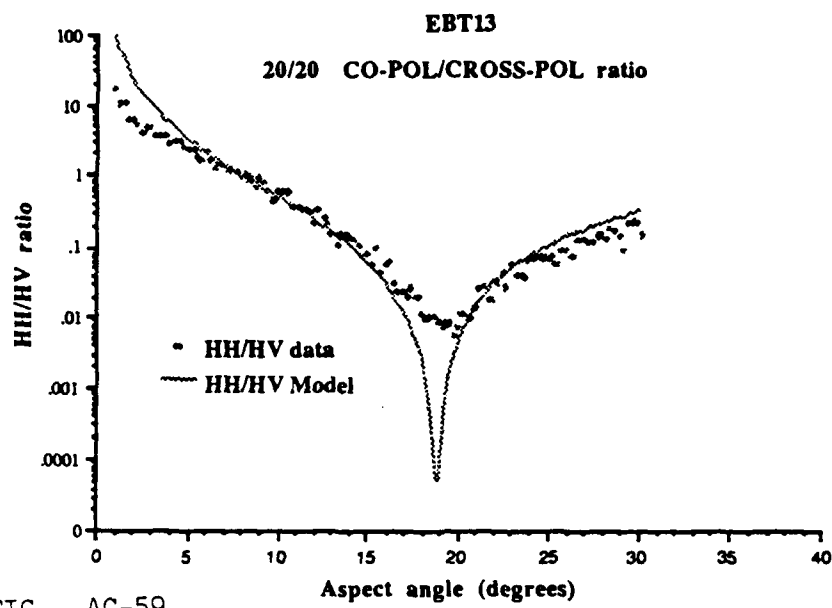


FIG. AC-59

10

$\sigma_0(\text{HH})/\sigma_0(\text{HV})$ for laboratory depression angles $\xi_i = \xi_s = 20$

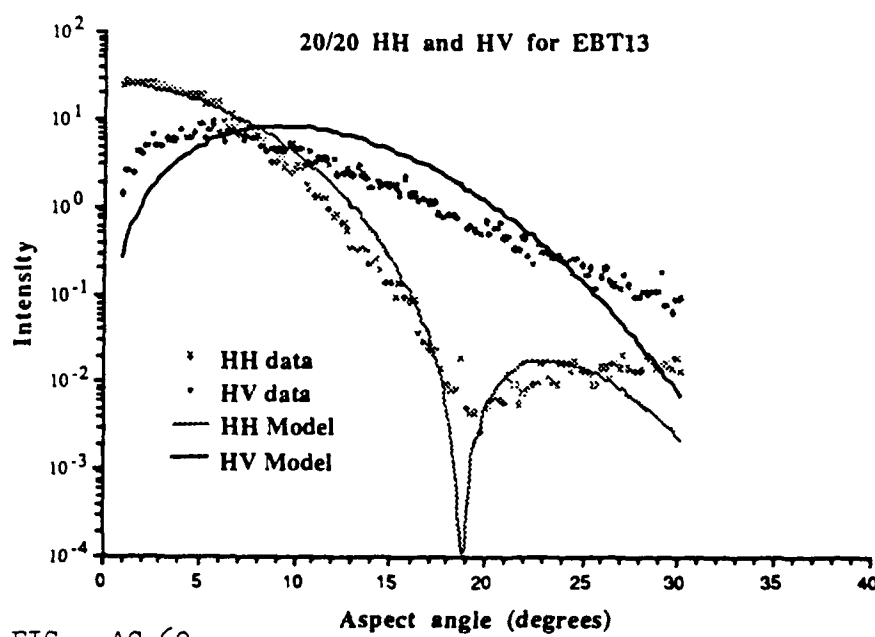


FIG. AC-60

$\sigma_0(\text{HH})$ and $\sigma_0(\text{HV})$ for laboratory depression angles $\xi_i = \xi_s = 20$

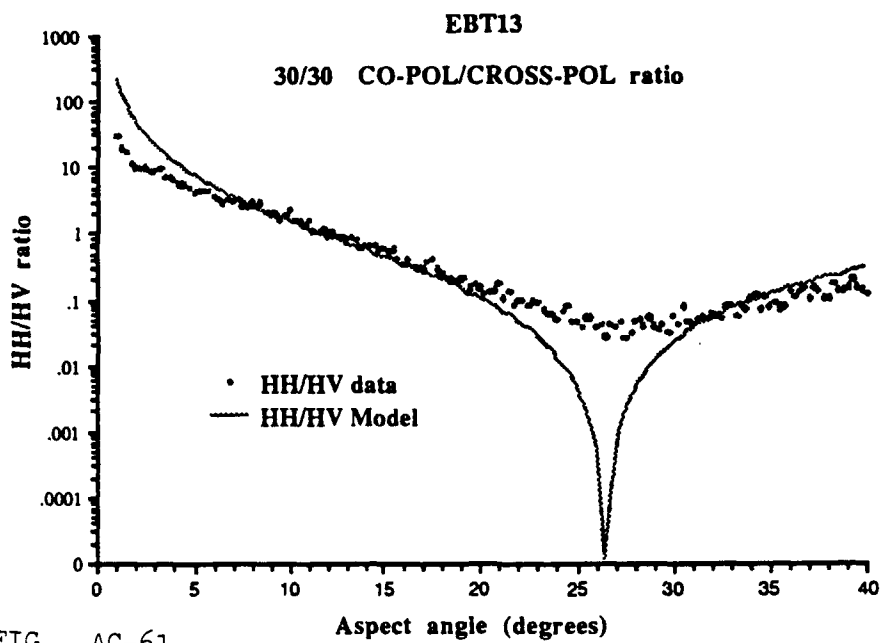


FIG. AC-61

$\sigma_o(\text{HH})/\sigma_o(\text{HV})$ for laboratory depression angles $\xi_i = \xi_s = 30$

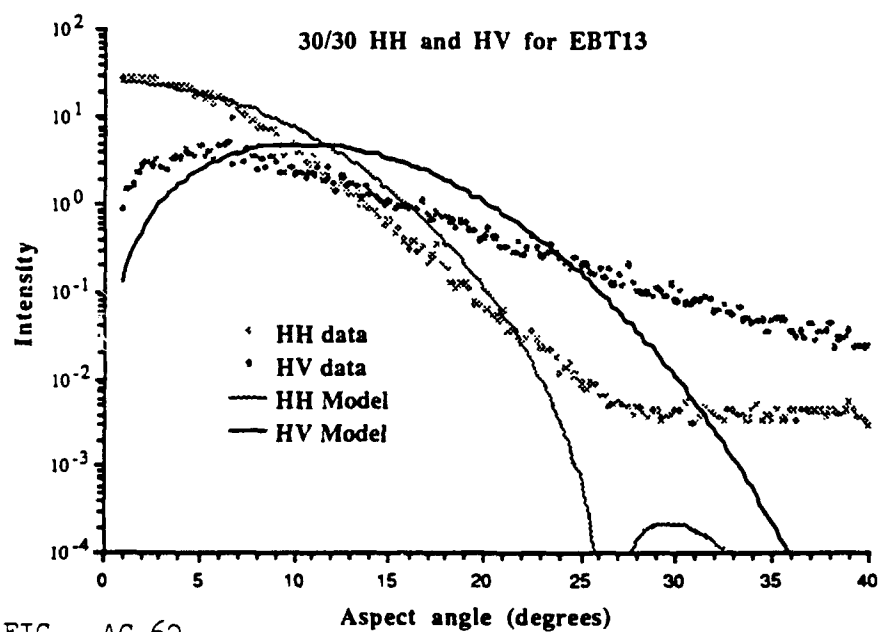


FIG. AC-62

$\sigma_o(\text{HH})$ and $\sigma_o(\text{HV})$ for laboratory depression angles $\xi_i = \xi_s = 30$

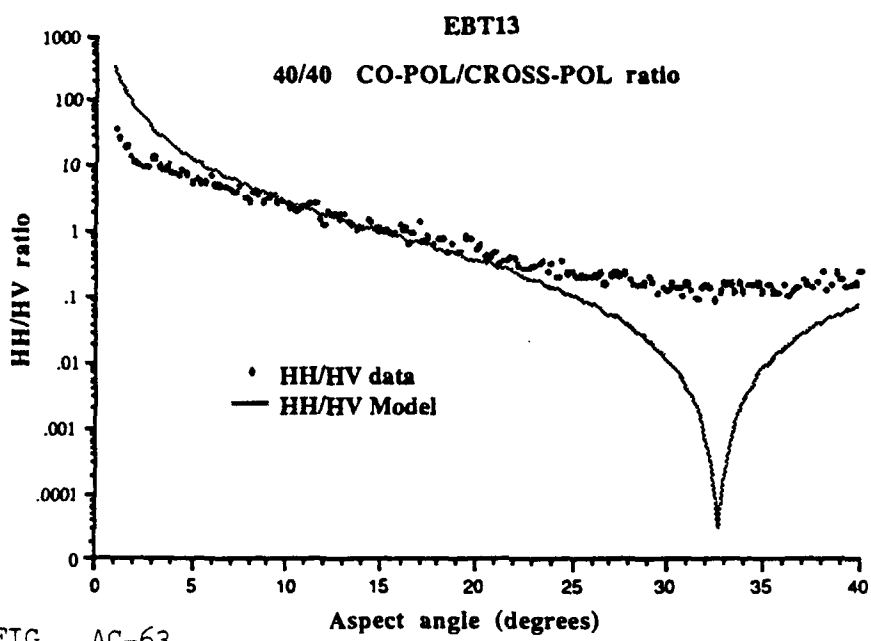


FIG. AC-63

$\sigma_o(\text{HH})/\sigma_o(\text{HV})$ for laboratory depression angles $\xi_i = \xi_s = 40$

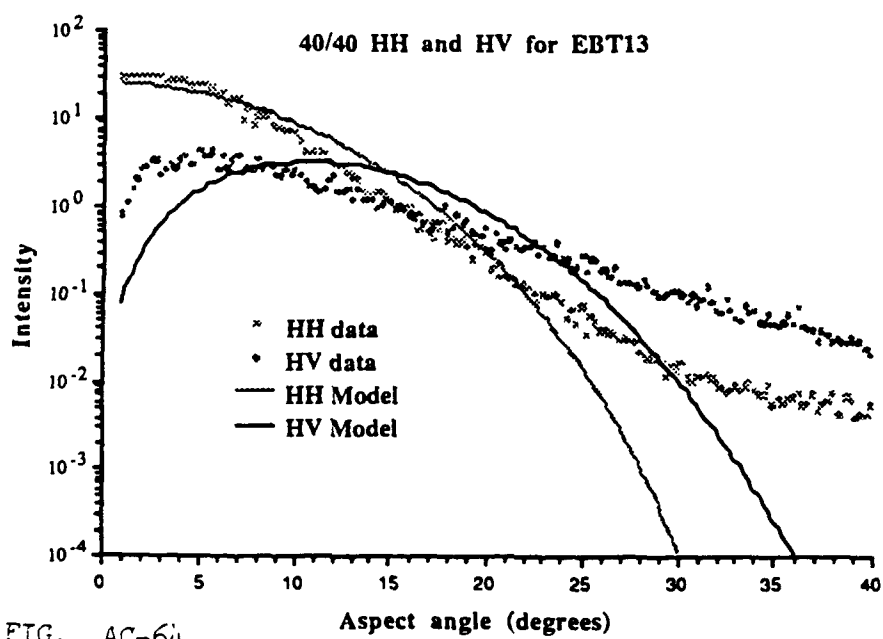


FIG. AC-64

$\sigma_o(\text{HH})$ and $\sigma_o(\text{HV})$ for laboratory depression angles $\xi_i = \xi_s = 40$

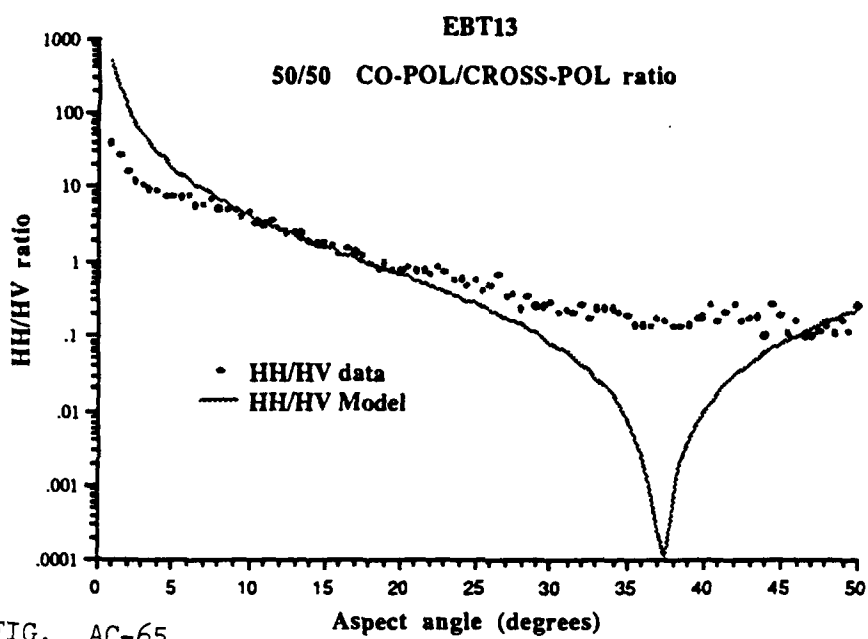


FIG. AC-65

$\sigma_o(\text{HH})/\sigma_o(\text{HV})$ for laboratory depression angles $\xi_i = \xi_s = 50$

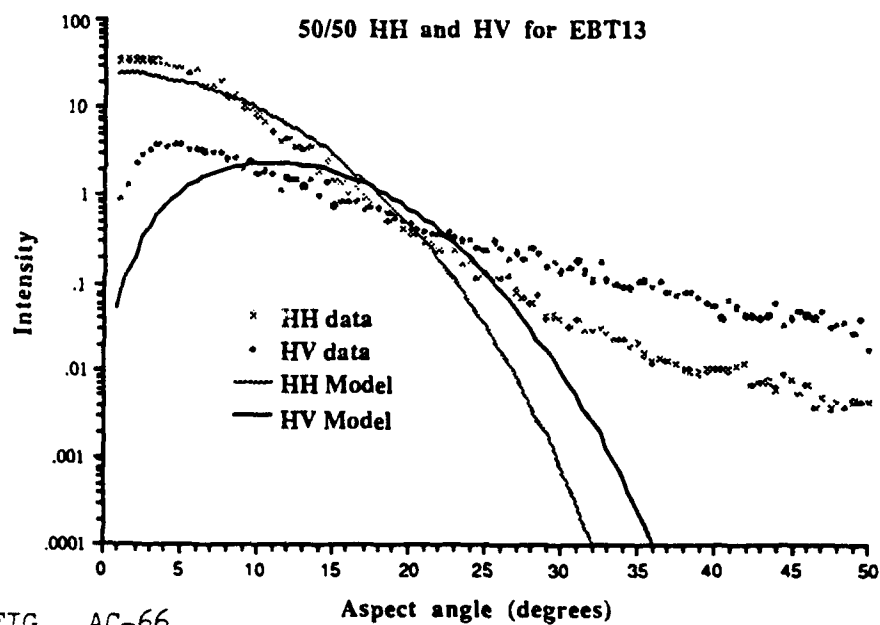


FIG. AC-66

$\sigma_o(\text{HH})$ and $\sigma_o(\text{HV})$ for laboratory depression angles $\xi_i = \xi_s = 50$

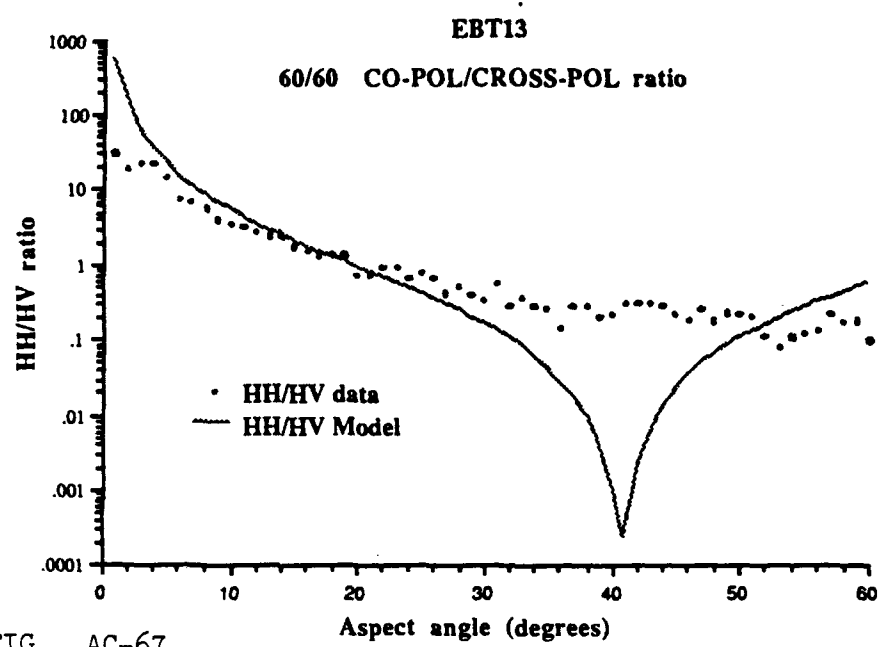


FIG. AC-67

$\sigma_o(\text{HH})/\sigma_o(\text{HV})$ for laboratory depression angles $\xi_i = \xi_s = 60$

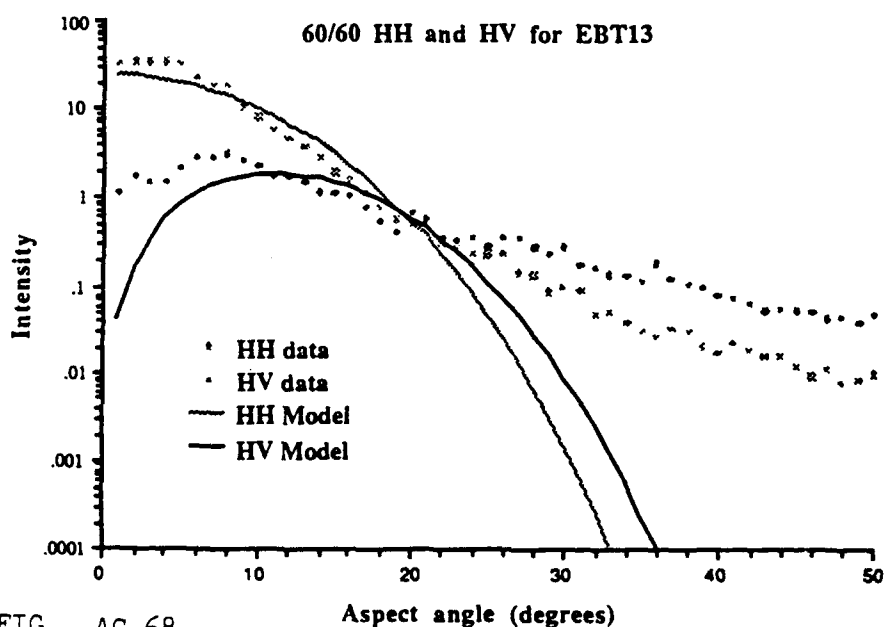


FIG. AC-68

$\sigma_o(\text{HH})$ and $\sigma_o(\text{HV})$ for laboratory depression angles $\xi_i = \xi_s = 60$

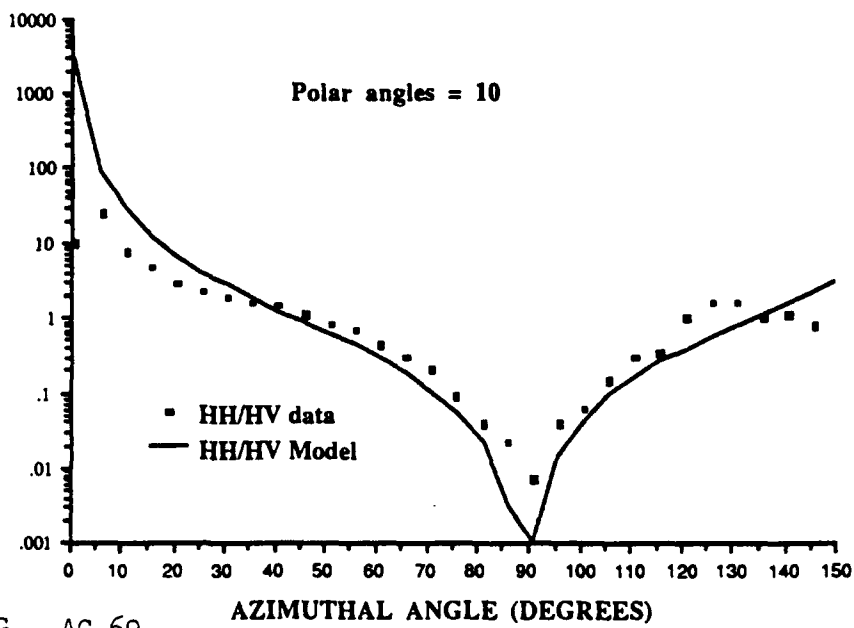


FIG. AC-69

$\sigma_o(\text{HH})/\sigma_o(\text{HV})$ for field polar angles $\theta_i = \theta_s = 10$

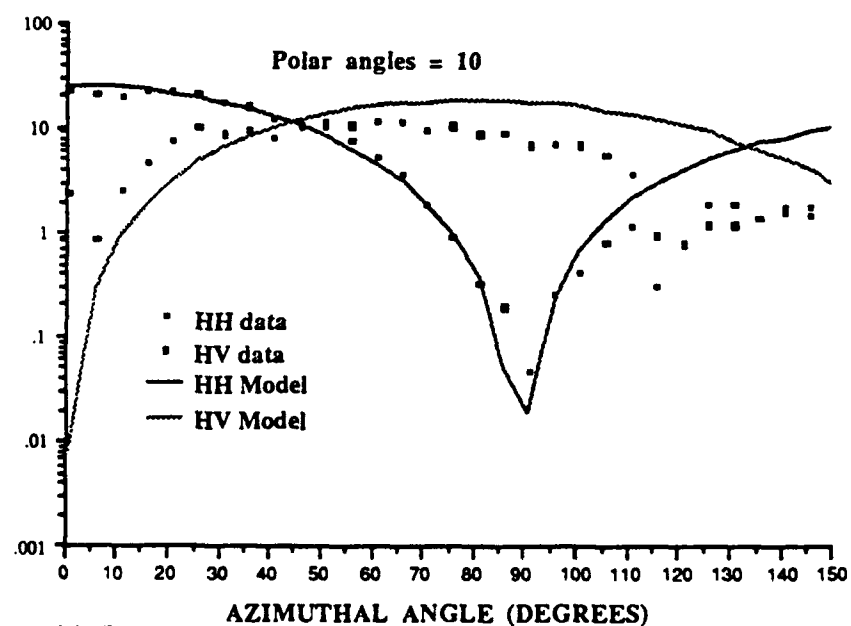


FIG. AC-70

$\sigma_o(\text{HH})$ and $\sigma_o(\text{HV})$ for field polar angles $\theta_i = \theta_s = 10$

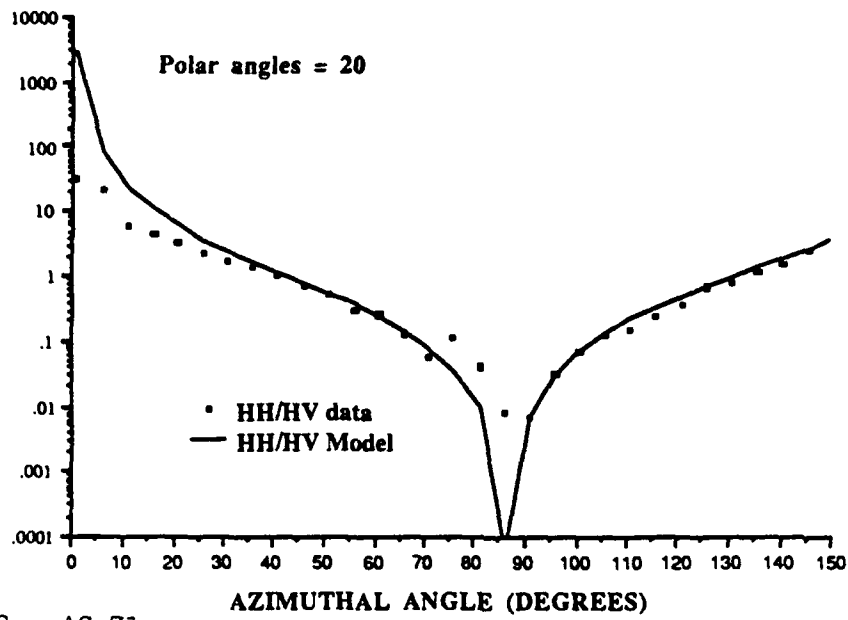


FIG. AC-71

$\sigma_0(\text{HH})/\sigma_0(\text{HV})$ for field polar angles $\theta_i = \theta_s = 20$

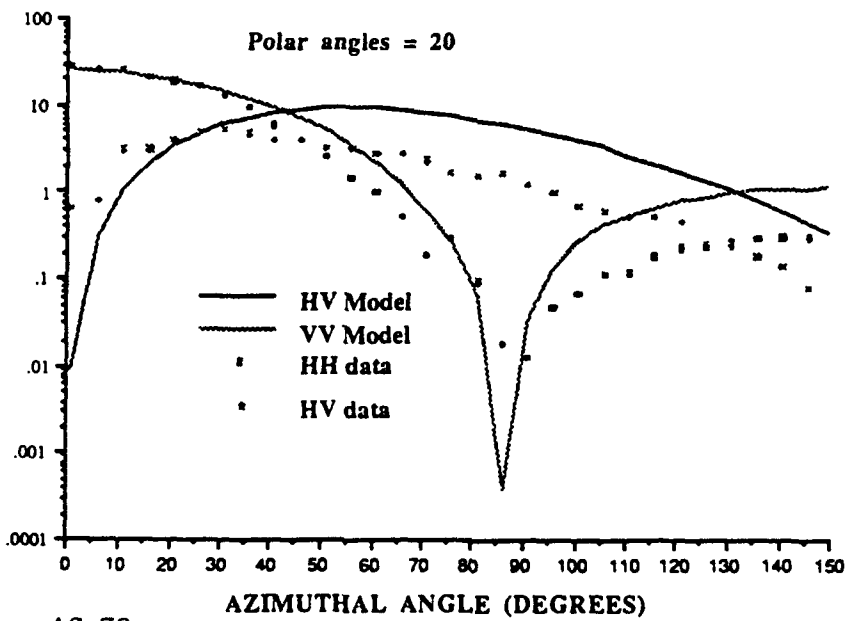


FIG. AC-72

$\sigma_0(\text{HH})$ and $\sigma_0(\text{HV})$ for field polar angles $\theta_i = \theta_s = 20$

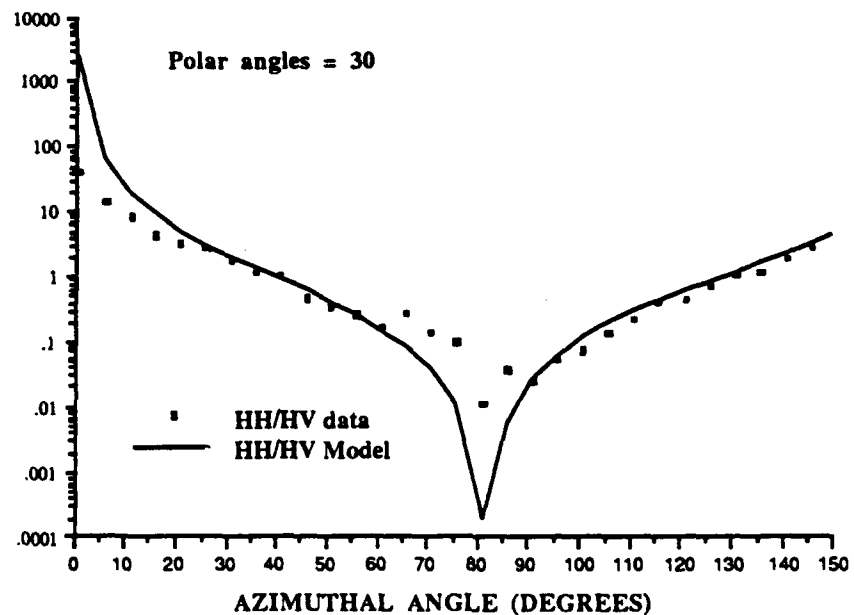


FIG. AC-73

$\sigma_0(\text{HH})/\sigma_0(\text{HV})$ for field polar angles $\theta_i = \theta_s = 30$

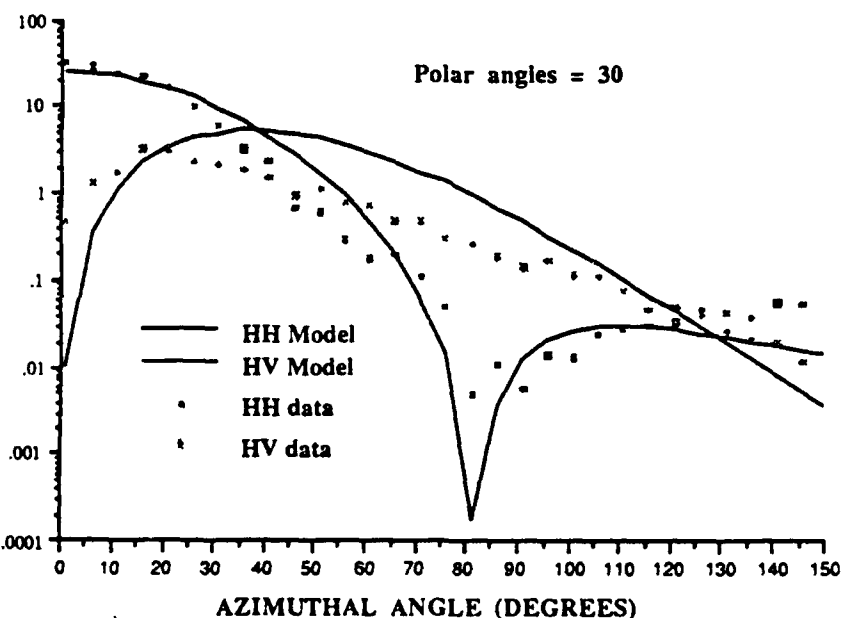


FIG. AC-74

$\sigma_0(\text{HH})$ and $\sigma_0(\text{HV})$ for field polar angles $\theta_i = \theta_s = 30$

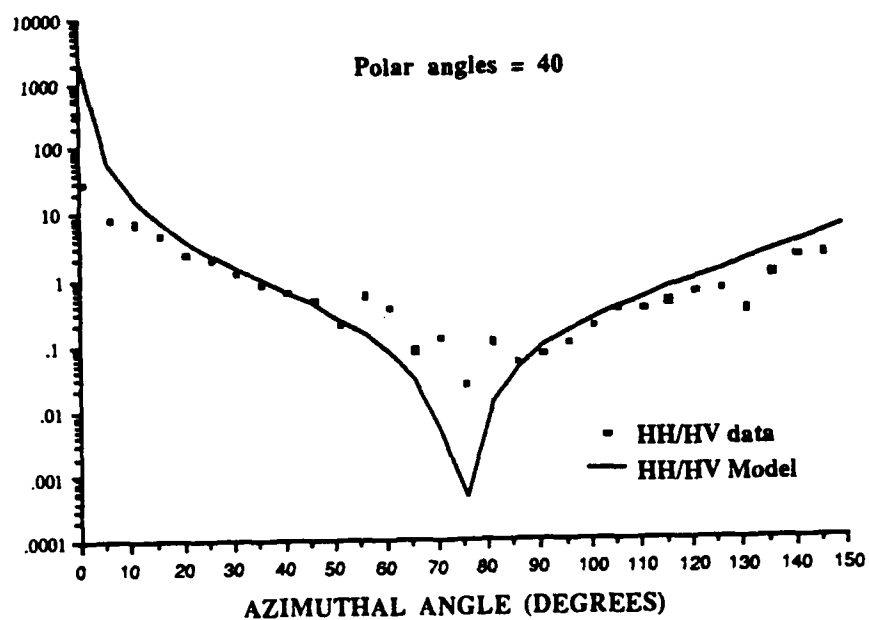


FIG. AC-75

$$\sigma_0(\text{HH})/\sigma_0(\text{HV}) \text{ for field polar angles } \theta_i = \theta_s = 40$$

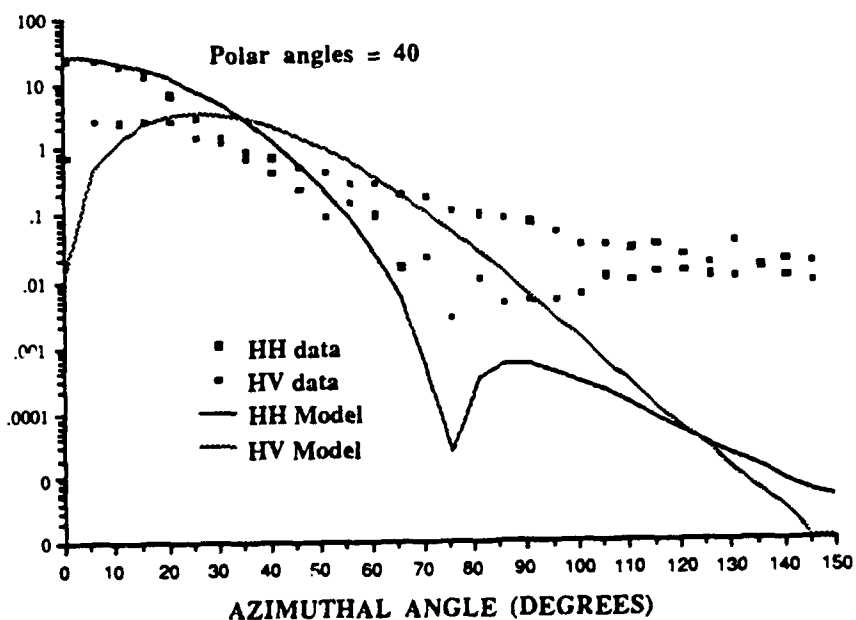


FIG. AC-76

$$\sigma_0(\text{HH}) \text{ and } \sigma_0(\text{HV}) \text{ for field polar angles } \theta_i = \theta_s = 40$$

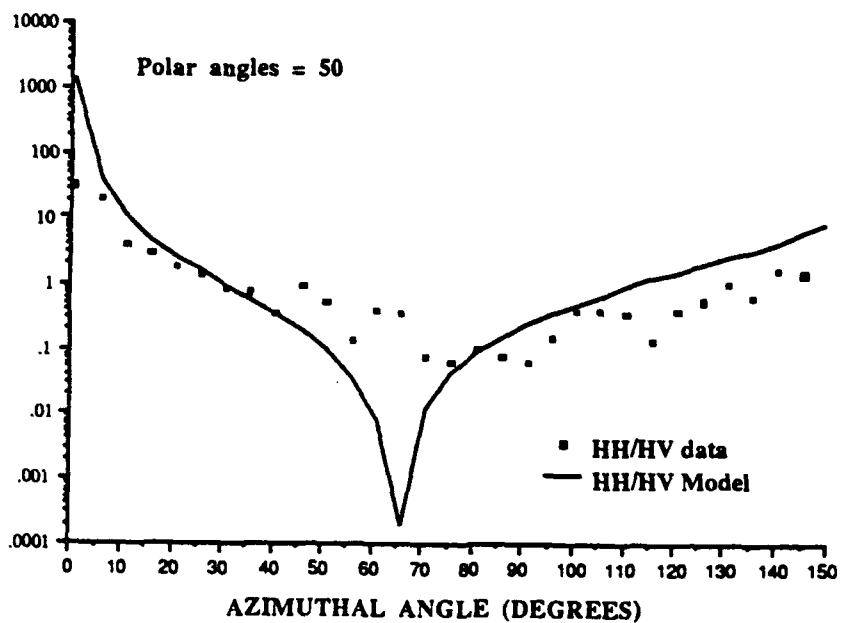


FIG. AC-77

$\sigma_0(\text{HH})/\sigma_0(\text{HV})$ for field polar angles $\theta_i = \theta_s = 50$

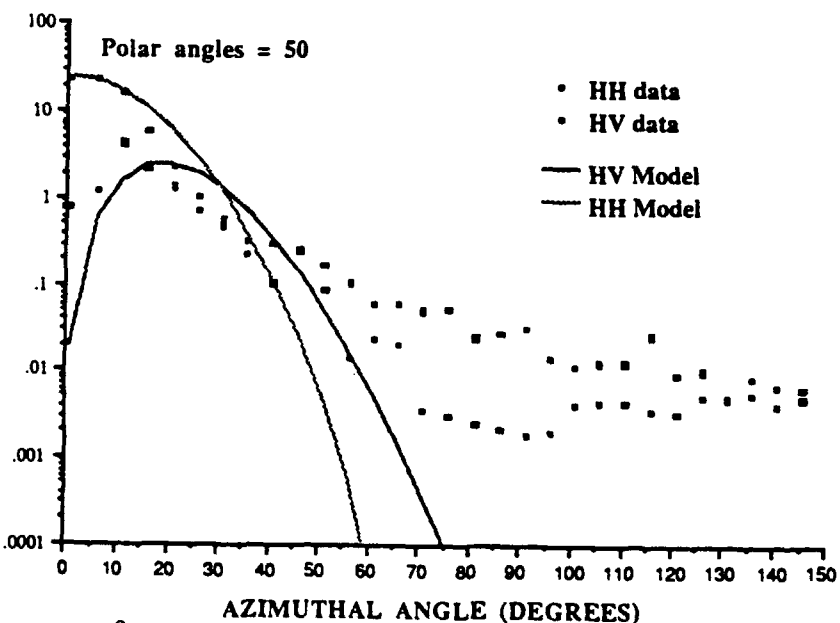


FIG. AC-78

$\sigma_0(\text{HH})$ and $\sigma_0(\text{HV})$ for field polar angles $\theta_i = \theta_s = 50$

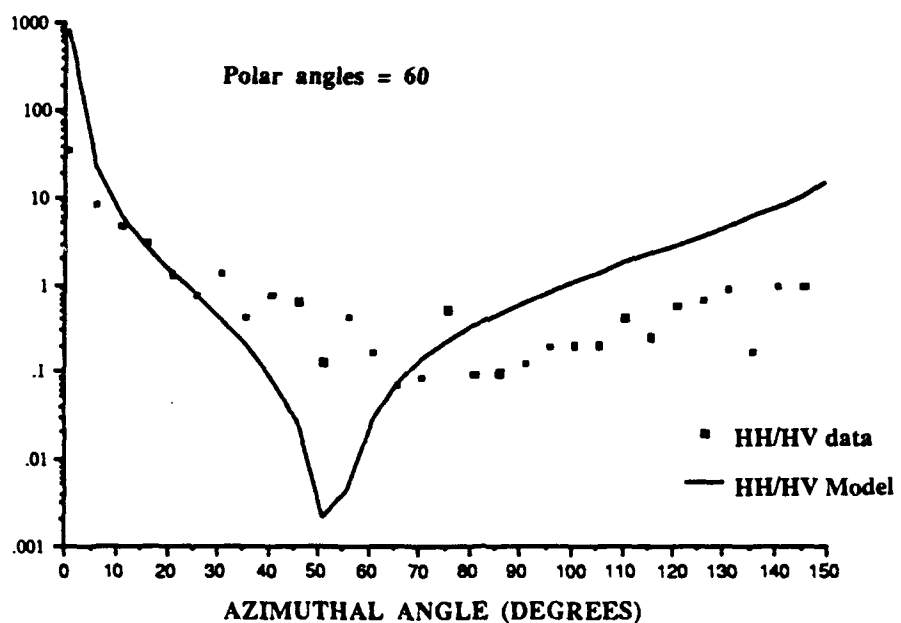


FIG. AC-79

$\sigma_o(\text{HH})/\sigma_o(\text{HV})$ for field polar angles $\theta_i = \theta_s = 60$

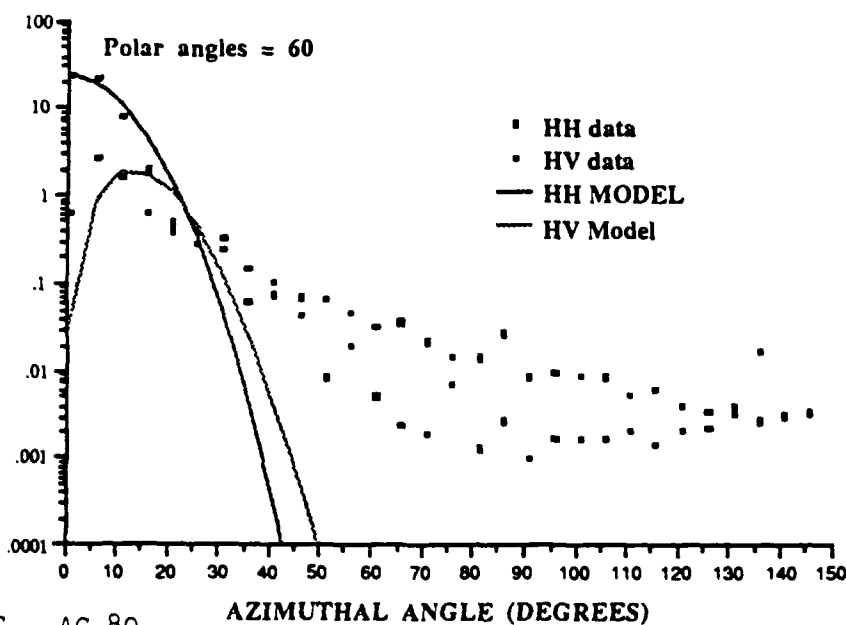


FIG. AC-80

$\sigma_o(\text{HH})$ and $\sigma_o(\text{HV})$ for field polar angles $\theta_i = \theta_s = 60$

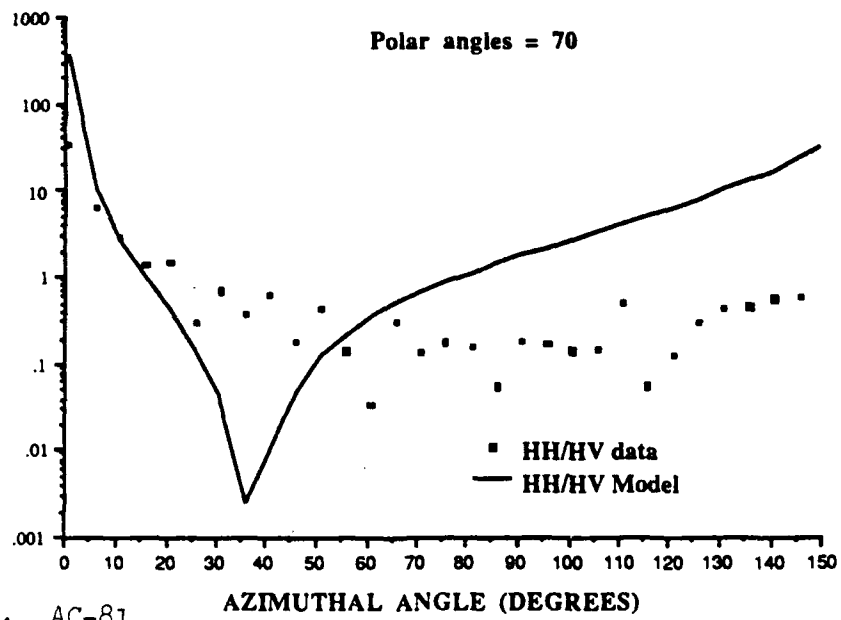


FIG. AC-81

$\sigma_0(\text{HH})/\sigma_0(\text{HV})$ for field polar angles $\theta_i = \theta_s = 70$

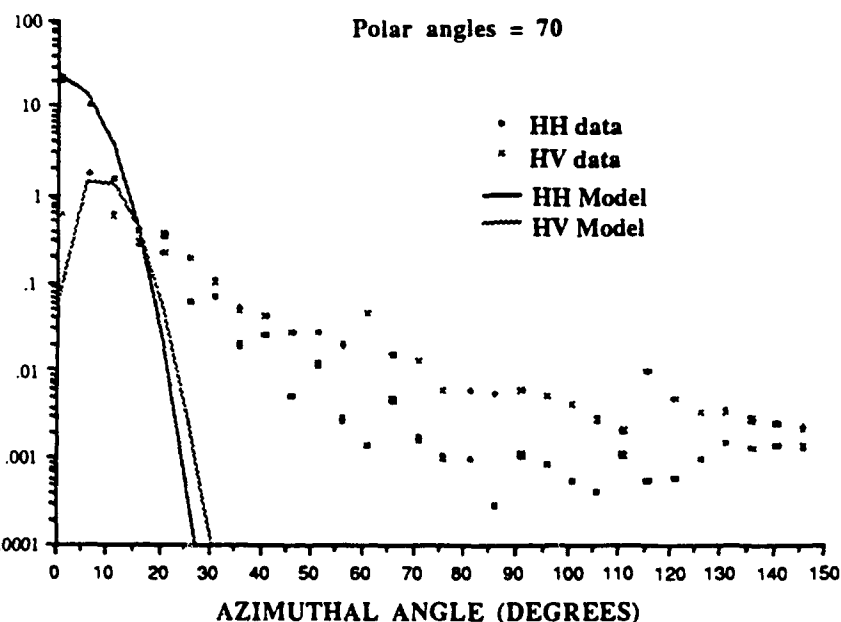


FIG. AC-82

$\sigma_0(\text{HH})$ and $\sigma_0(\text{HV})$ for field polar angles $\theta_i = \theta_s = 70$

EBT 4+13

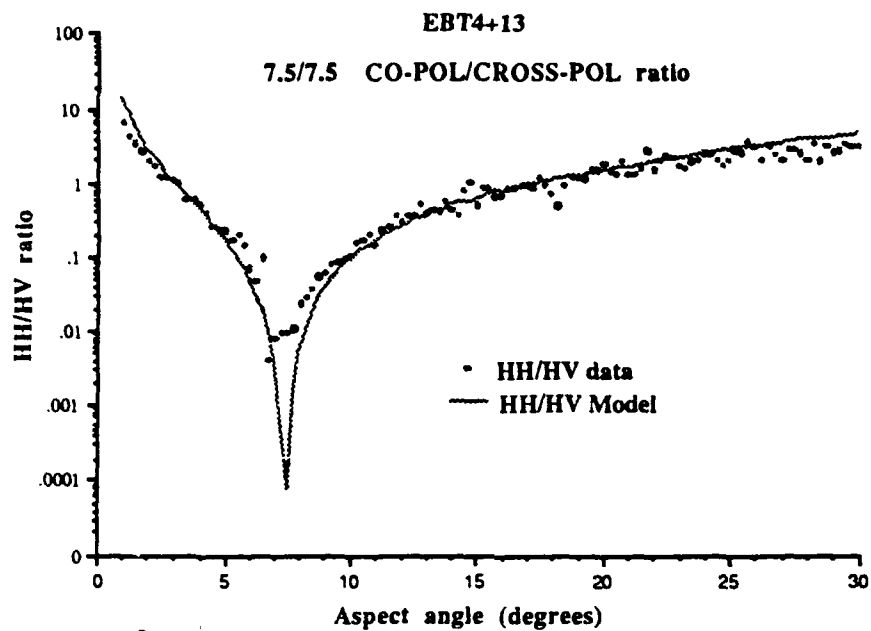


FIG. AC-83

$\sigma_o(\text{HH})/\sigma_o(\text{HV})$ for laboratory depression angles $\xi_i = \xi_s = 7.5$

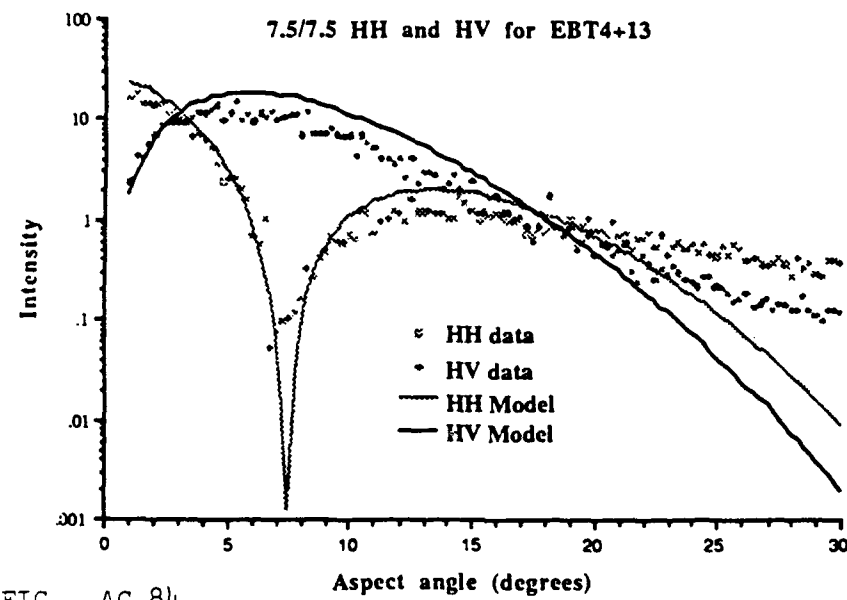


FIG. AC-84

$\sigma_o(\text{HH})$ and $\sigma_o(\text{HV})$ for laboratory depression angles $\xi_i = \xi_s = 7.5$

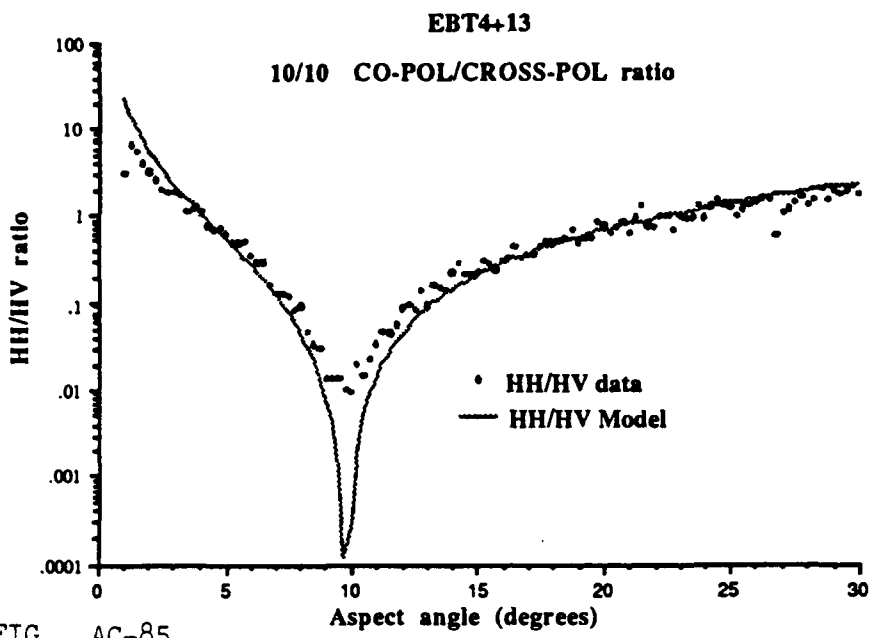


FIG. AC-85

$\sigma_o(\text{HH})/\sigma_o(\text{HV})$ for laboratory depression angles $\xi_i = \xi_s = 10$

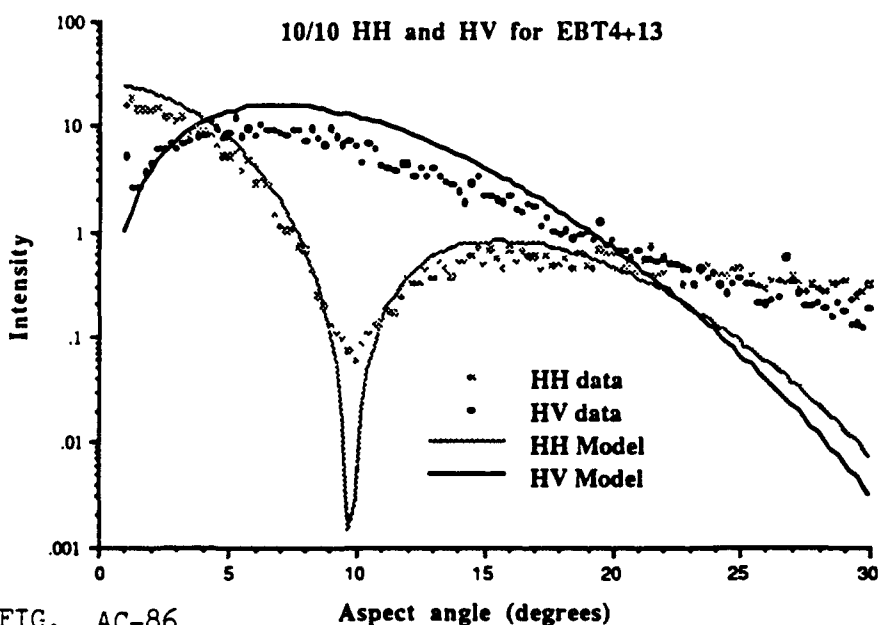


FIG. AC-86

$\sigma_o(\text{HH})$ and $\sigma_o(\text{HV})$ for laboratory depression angles $\xi_i = \xi_s = 10$

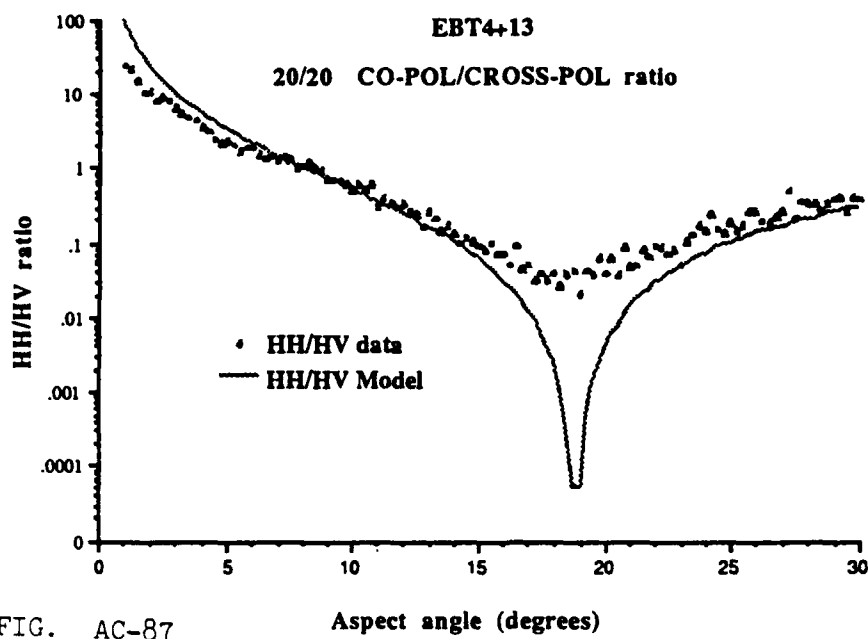


FIG. AC-87

Aspect angle (degrees)

$\sigma_o(\text{HH})/\sigma_o(\text{HV})$ for laboratory depression angles $\xi_i = \xi_s = 20$

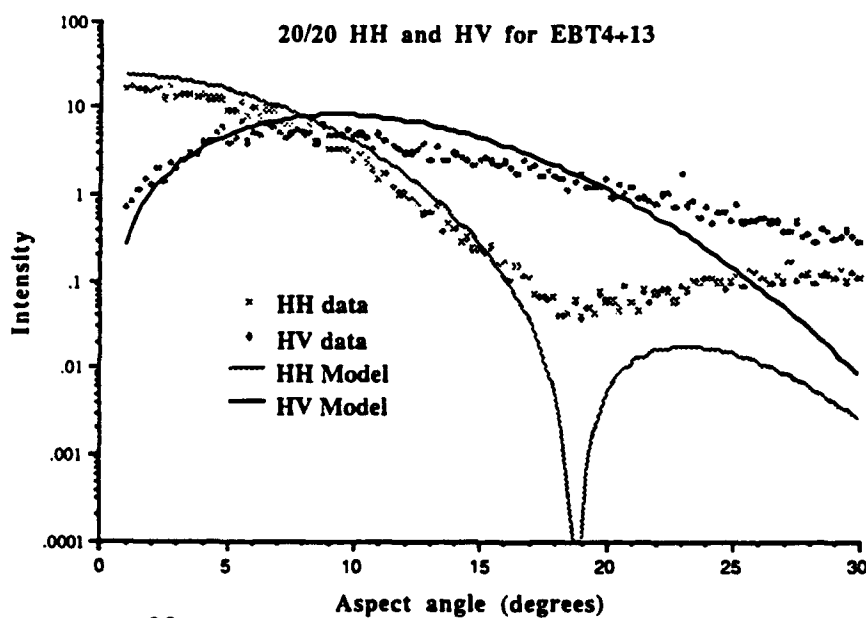


FIG. AC-88

$\sigma_o(\text{HH})$ and $\sigma_o(\text{HV})$ for laboratory depression angles $\xi_i = \xi_s = 20$

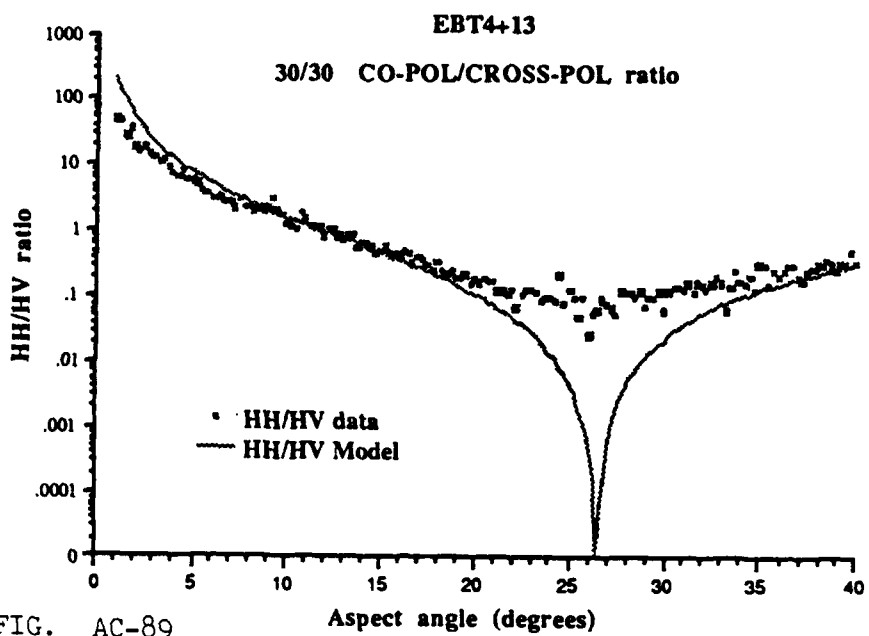


FIG. AC-89

$\sigma_o(\text{HH})/\sigma_o(\text{HV})$ for laboratory depression angles $\xi_i = \xi_s = 30$

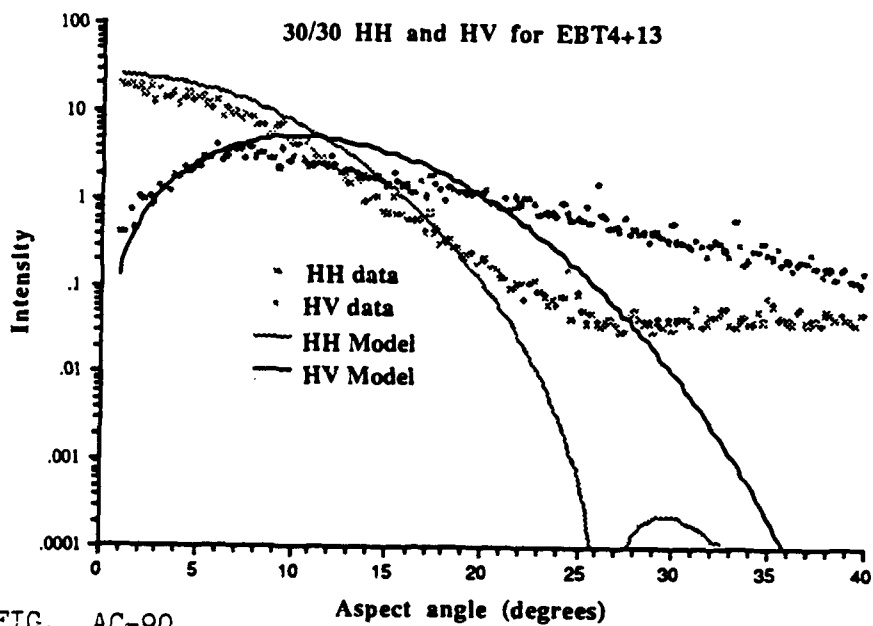


FIG. AC-90

$\sigma_o(\text{HH})$ and $\sigma_o(\text{HV})$ for laboratory depression angles $\xi_i = \xi_s = 30$

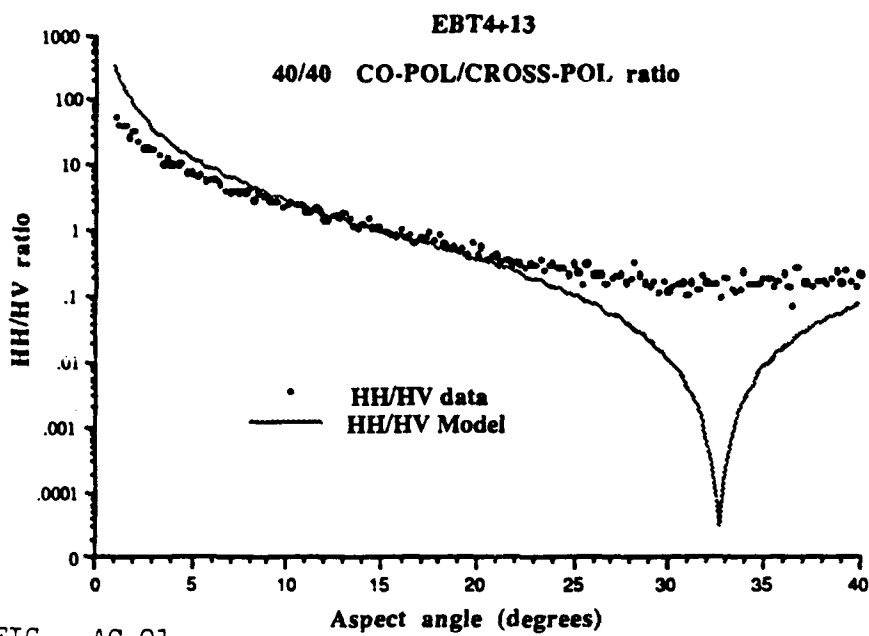


FIG. AC-91

$\sigma_o(\text{HH})/\sigma_o(\text{HV})$ for laboratory depression angles $\xi_i = \xi_s = 40$

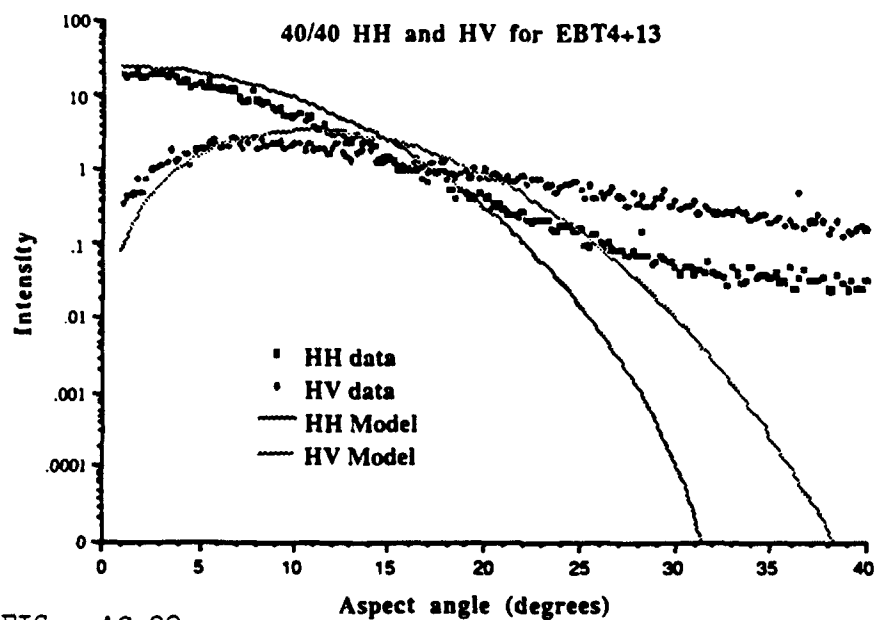


FIG. AC-92

$\sigma_o(\text{HH})$ and $\sigma_o(\text{HV})$ for laboratory depression angles $\xi_i = \xi_s = 40$

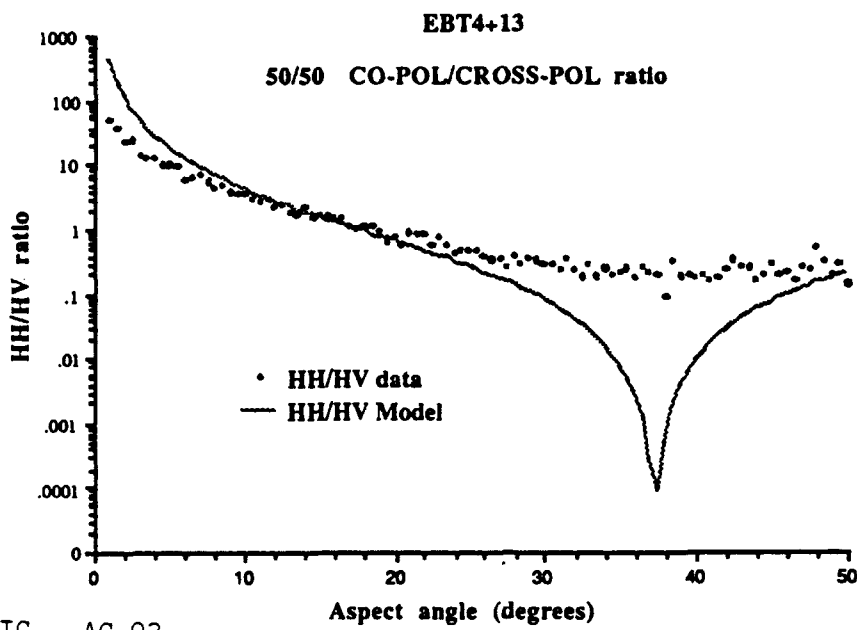


FIG. AC-93

$\sigma_o(\text{HH})/\sigma_o(\text{HV})$ for laboratory depression angles $\xi_i = \xi_s = 50$

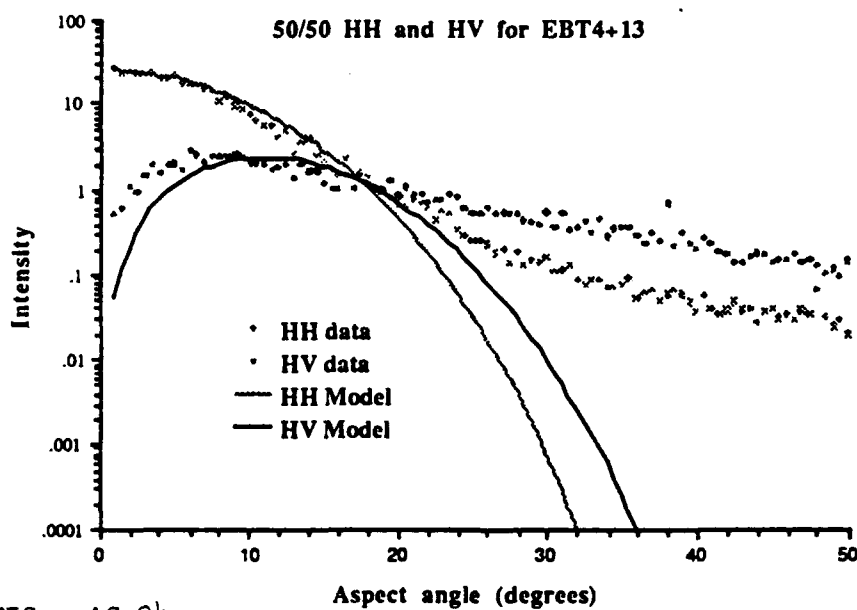


FIG. AC-94

$\sigma_o(\text{HH})$ and $\sigma_o(\text{HV})$ for laboratory depression angles $\xi_i = \xi_s = 50$

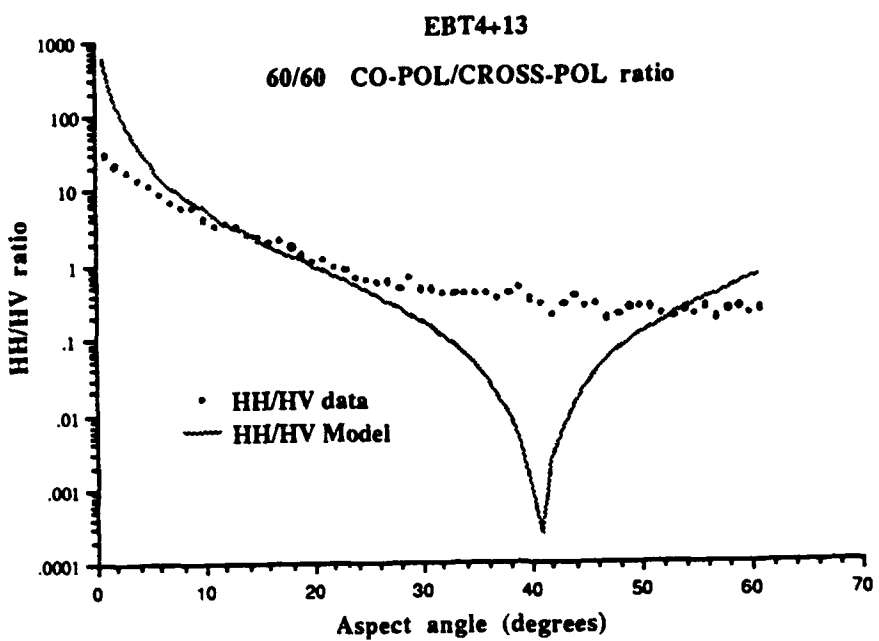


FIG. AC-95

$\sigma_o(\text{HH})/\sigma_o(\text{HV})$ for laboratory depression angles $\xi_i = \xi_s = 60$

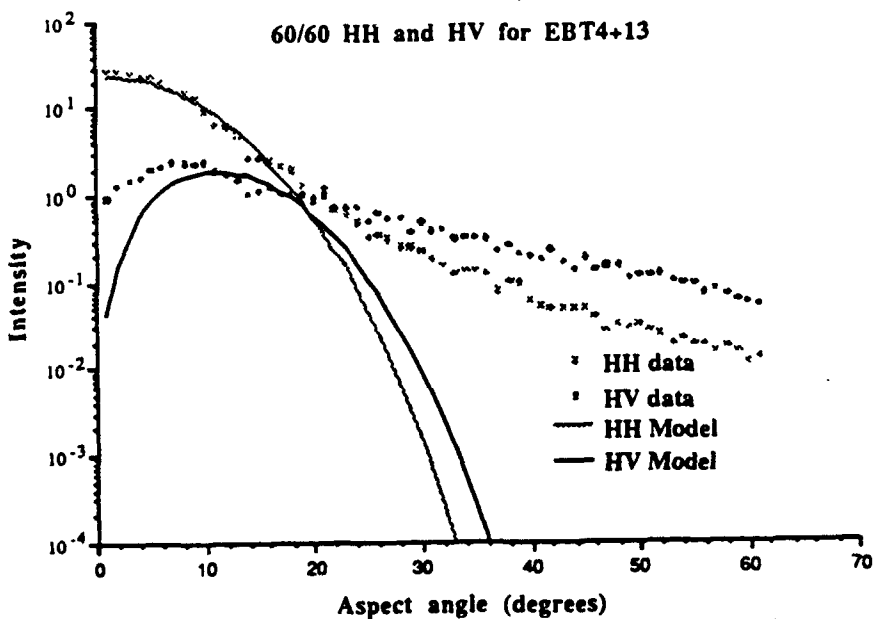


FIG. AC-96

$\sigma_o(\text{HH})$ and $\sigma_o(\text{HV})$ for laboratory depression angles $\xi_i = \xi_s = 60$

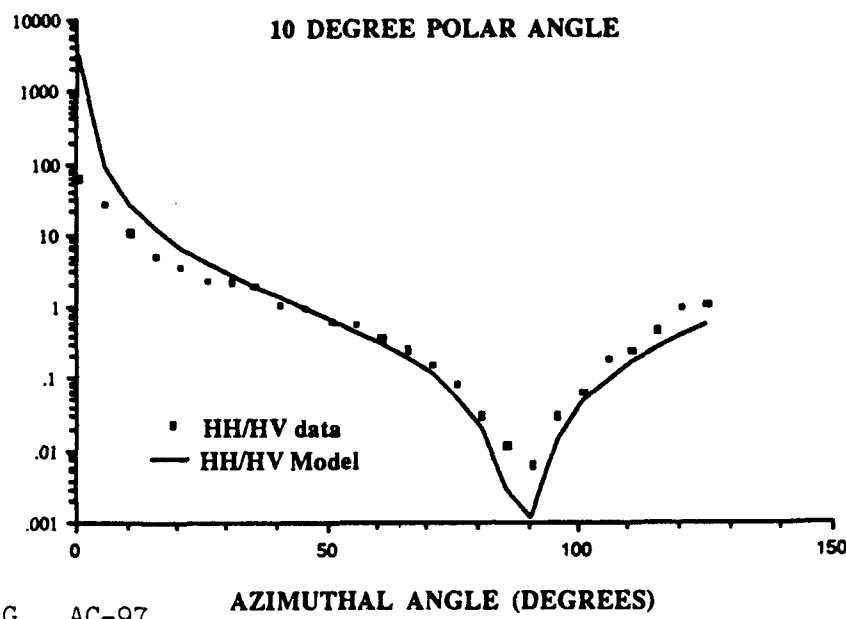


FIG. AC-97

$\sigma_o(\text{HH})/\sigma_o(\text{HV})$ for field polar angles $\theta_i = \theta_s = 10$

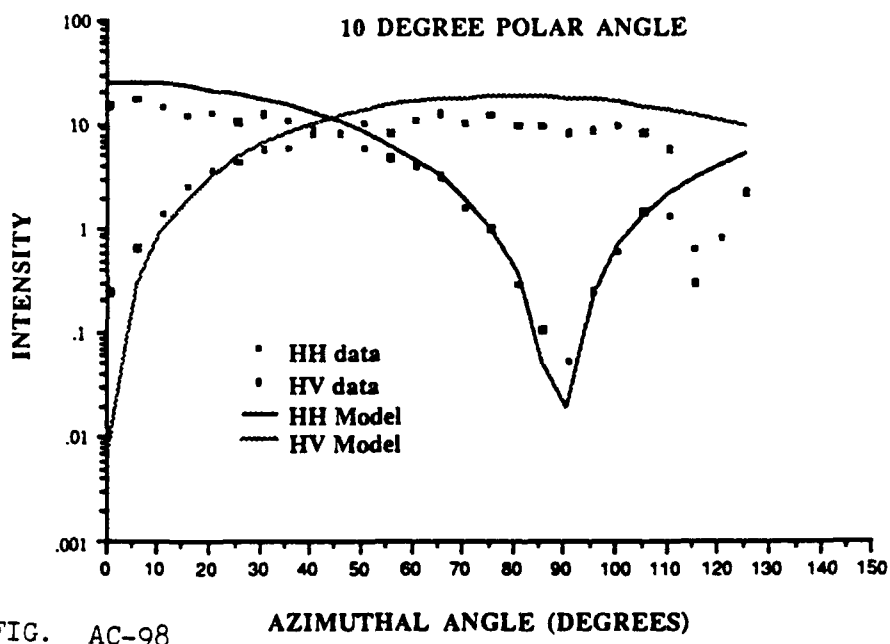


FIG. AC-98

$\sigma_o(\text{HH})$ and $\sigma_o(\text{HV})$ for field polar angles $\theta_i = \theta_s = 10$

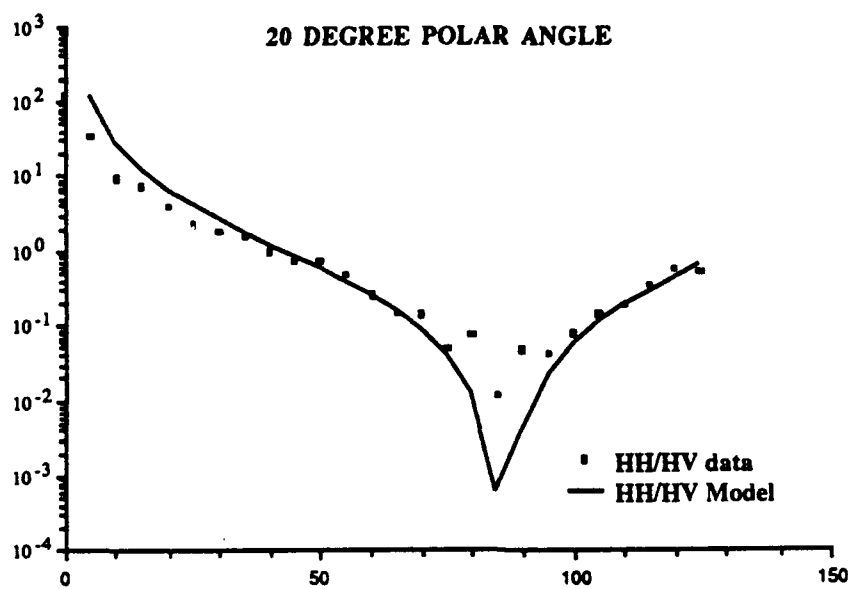


FIG. AC-99 AZIMUTHAL ANGLE (DEGREES)

$\sigma_o(\text{HH})/\sigma_o(\text{HV})$ for field polar angles $\theta_i = \theta_s = 20$

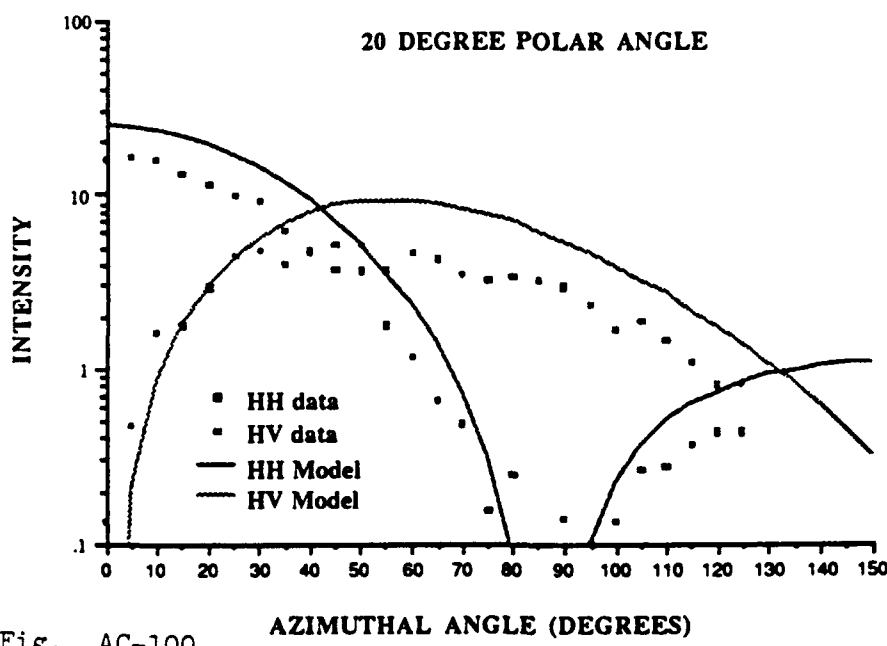


Fig. AC-100 AZIMUTHAL ANGLE (DEGREES)

$\sigma_o(\text{HH})$ and $\sigma_o(\text{HV})$ for field polar angles $\theta_i = \theta_s = 20$

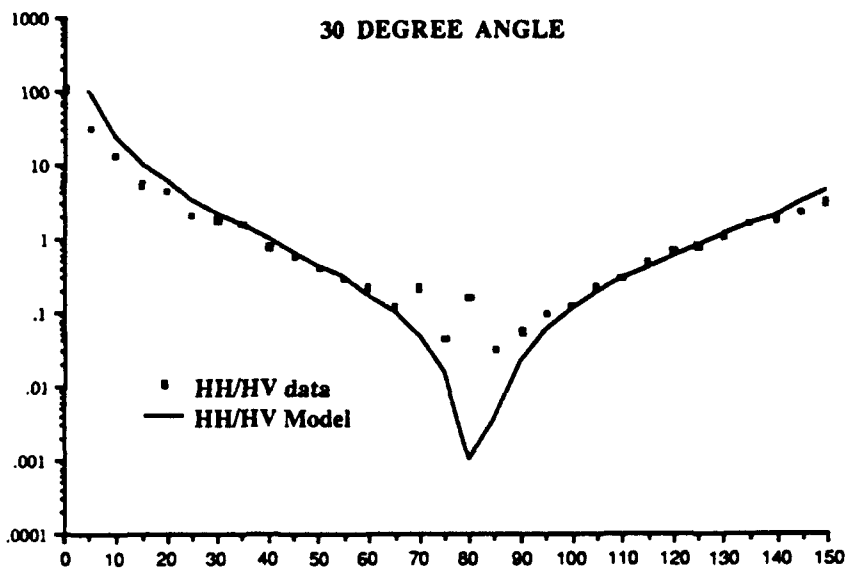


FIG. AC-101 AZIMUTHAL ANGLE (DEGREES)

$$\sigma_o(\text{HH})/\sigma_o(\text{HV}) \text{ for field polar angles } \theta_i = \theta_s = 30$$

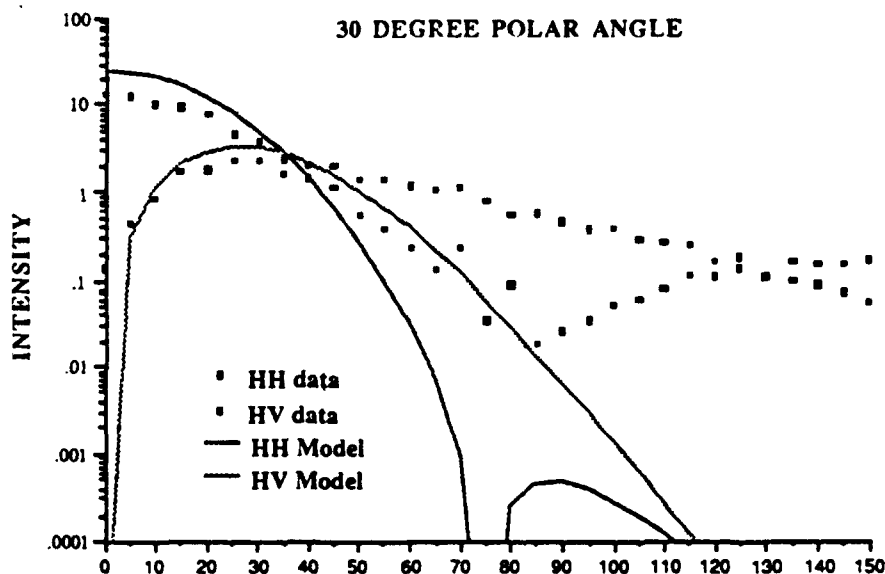


FIG. AC-102 AZIMUTHAL ANGLE (DEGREES)

$$\sigma_o(\text{HH}) \text{ and } \sigma_o(\text{HV}) \text{ for field polar angles } \theta_i = \theta_s = 30$$

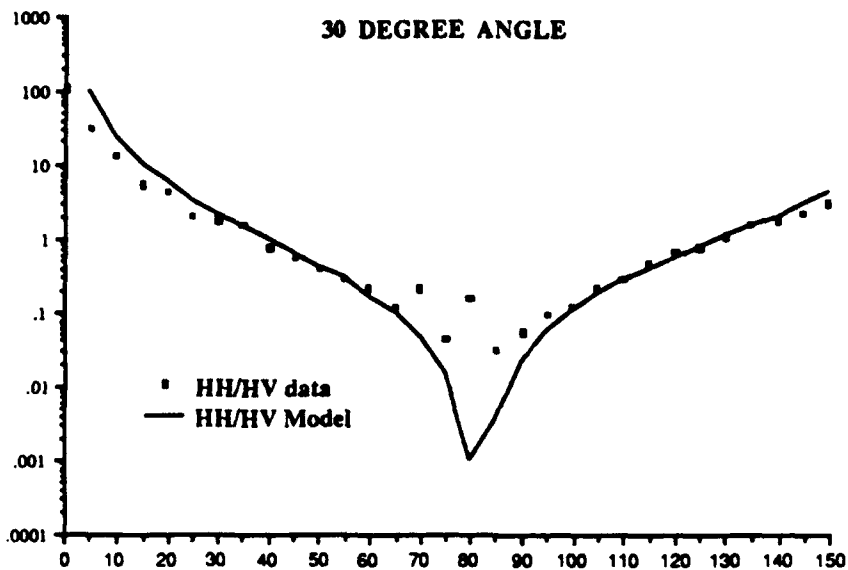


FIG. AC-103

AZIMUTHAL ANGLE (DEGREES)

$\sigma_o(\text{HH})/\sigma_o(\text{HV})$ for field polar angles $\theta_i = \theta_s = 40$

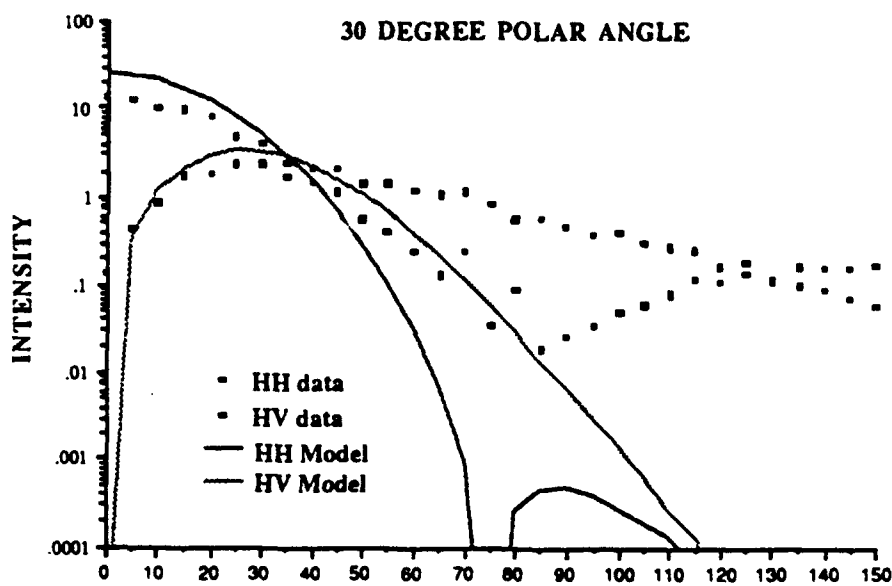


FIG. AC-104

AZIMUTHAL ANGLE (DEGREES)

$\sigma_o(\text{HH})$ and $\sigma_o(\text{HV})$ for field polar angles $\theta_i = \theta_s = 40$

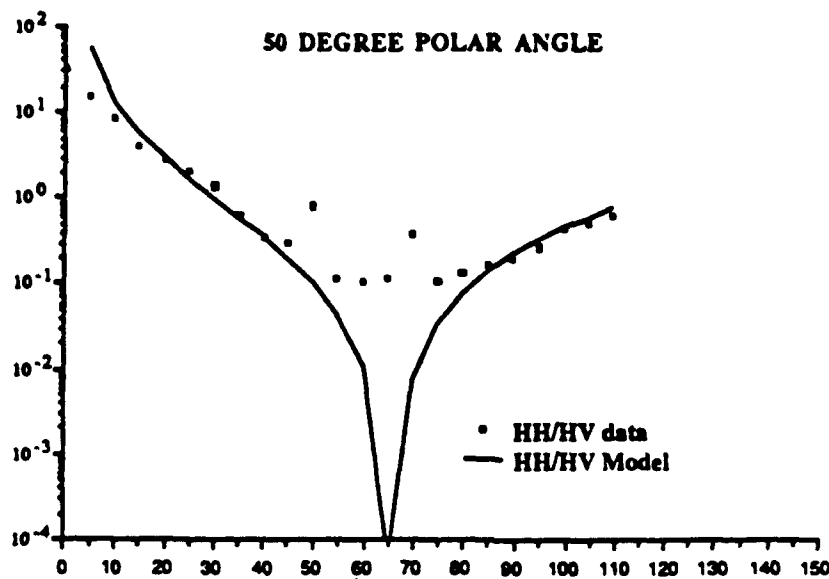


FIG. AC-105 AZIMUTHAL ANGLE (DEGREES)

$\sigma_o(\text{HH})/\sigma_o(\text{HV})$ for field polar angles $\theta_i = \theta_s = 50$

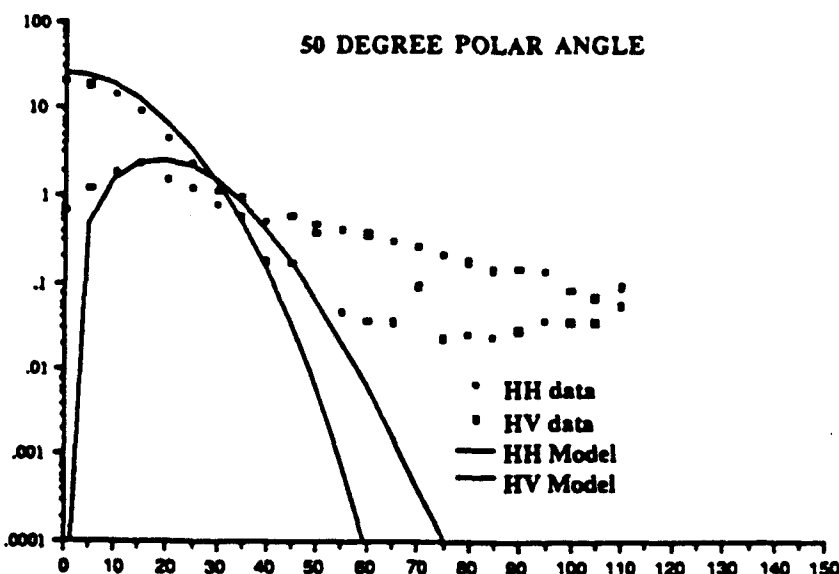


FIG. AC-106 AZIMUTHAL ANGLE (DEGREES)

$\sigma_o(\text{HH})$ and $\sigma_o(\text{HV})$ for field polar angles $\theta_i = \theta_s = 50$

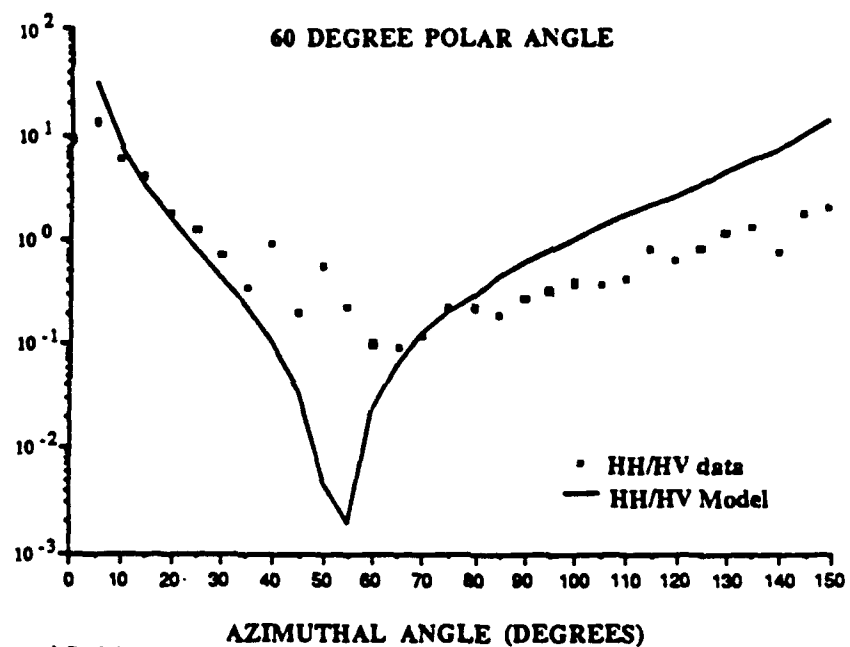


FIG. AC-107

$\sigma_o(\text{HH})/\sigma_o(\text{HV})$ for field polar angles $\theta_i = \theta_s = 60$

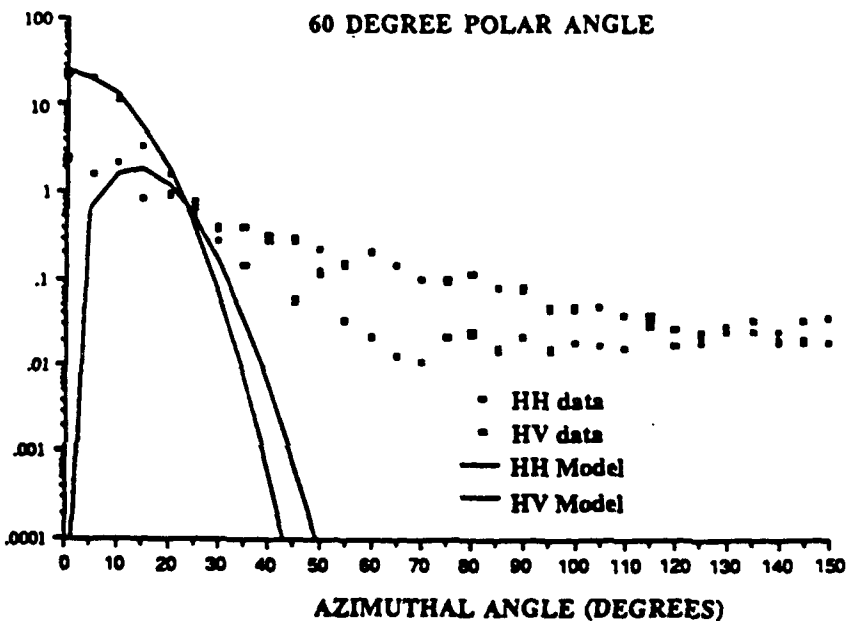


FIG. AC-108

$\sigma_o(\text{HH})$ and $\sigma_o(\text{HV})$ for field polar angles $\theta_i = \theta_s = 60$

NBT 4

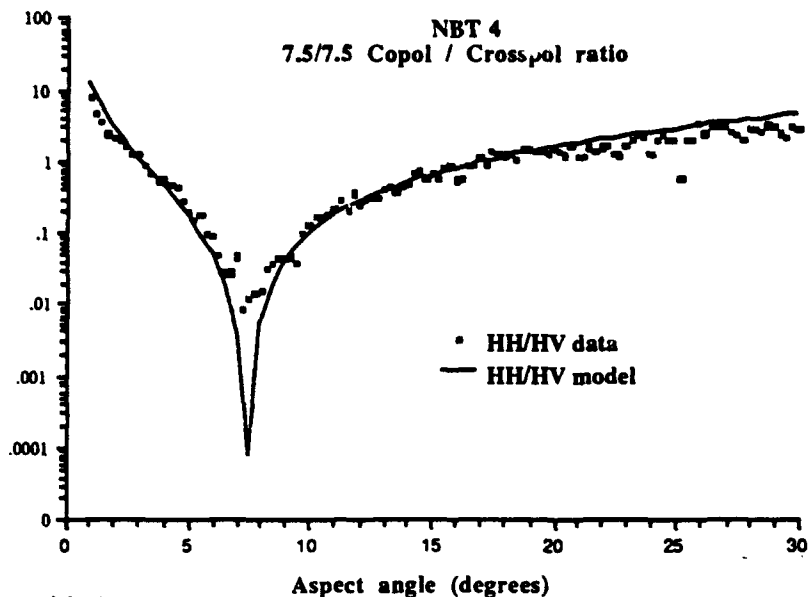


FIG. AC-109

$\sigma_0(\text{HH})/\sigma_0(\text{HV})$ for laboratory depression angles $\xi_i = \xi_s = 7.5$

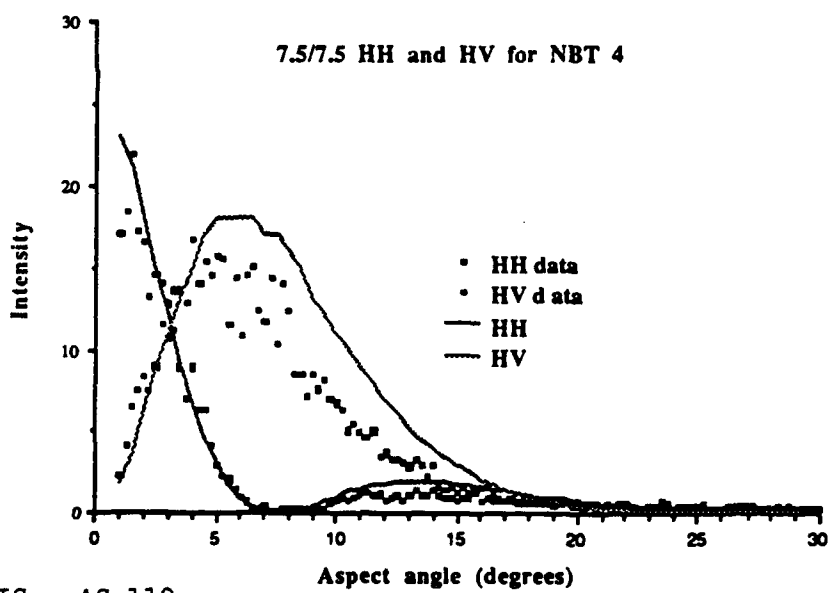


FIG. AC-110

$\sigma_0(\text{HH})$ and $\sigma_0(\text{HV})$ for laboratory depression angles $\xi_i = \xi_s = 7.5$

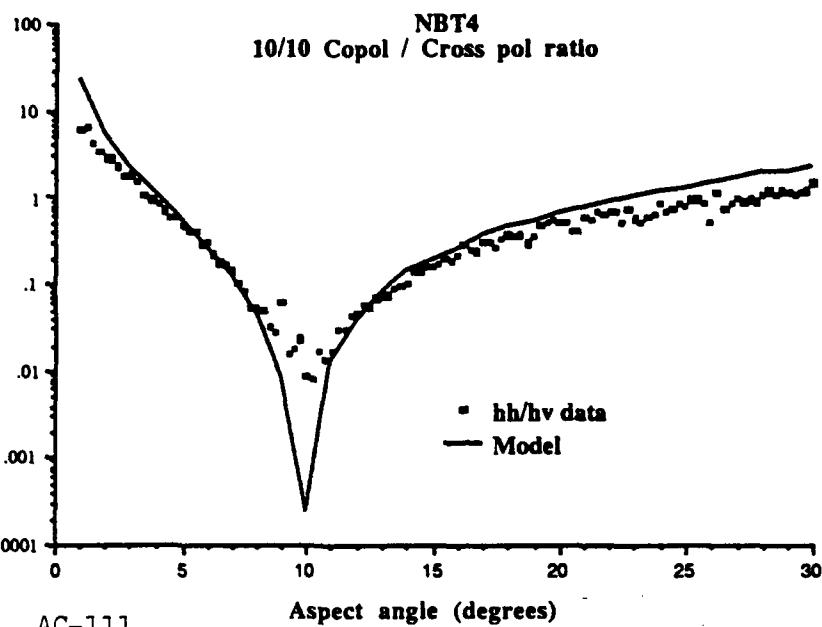


FIG. AC-111

$\sigma_o(\text{HH})/\sigma_o(\text{HV})$ for laboratory depression angles $\xi_i = \xi_s = 10$

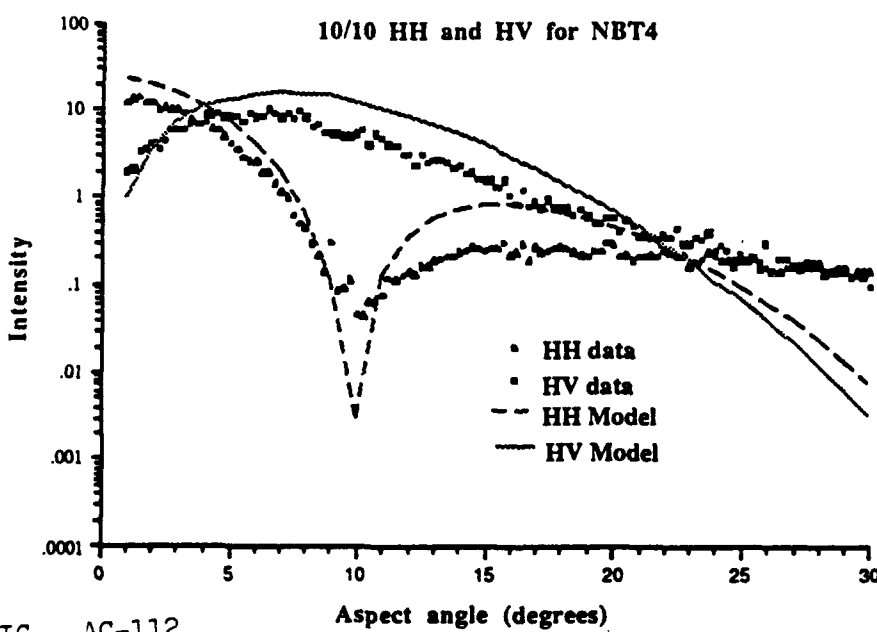


FIG. AC-112

$\sigma_o(\text{HH})$ and $\sigma_o(\text{HV})$ for laboratory depression angles $\xi_i = \xi_s = 10$

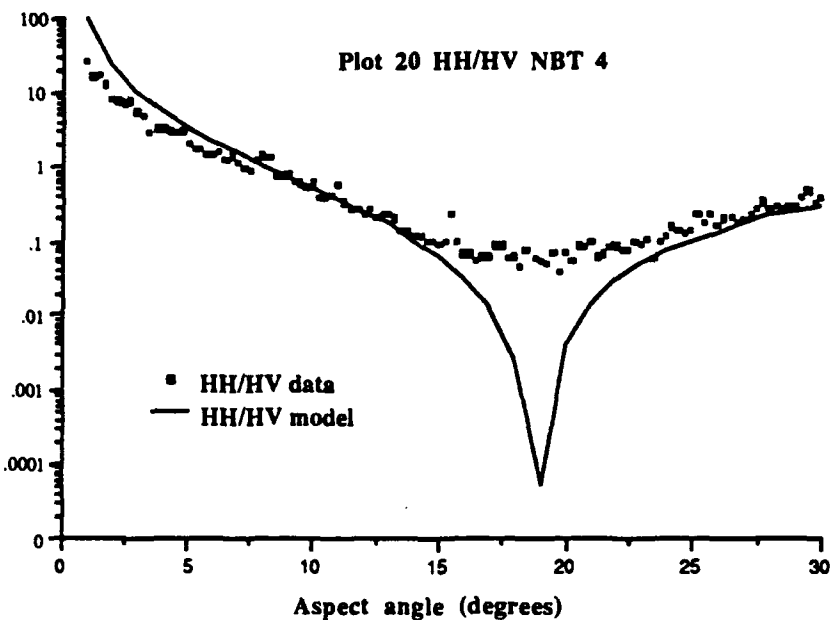


FIG. AC-113

$\sigma_o(\text{HH})/\sigma_o(\text{HV})$ for laboratory depression angles $\xi_i = \xi_s = 20$

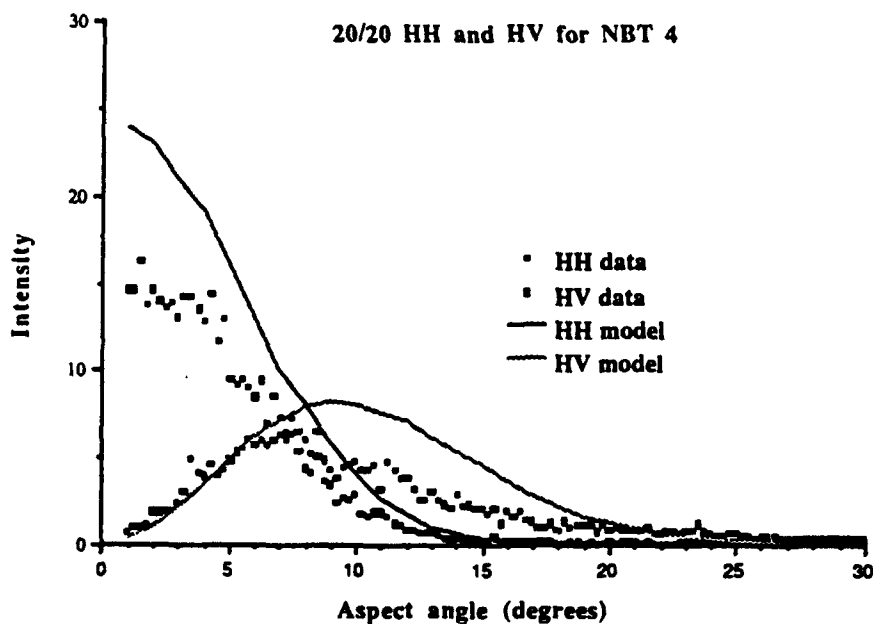


FIG. AC-114

$\sigma_o(\text{HH})$ and $\sigma_o(\text{HV})$ for laboratory depression angles $\xi_i = \xi_s = 20$

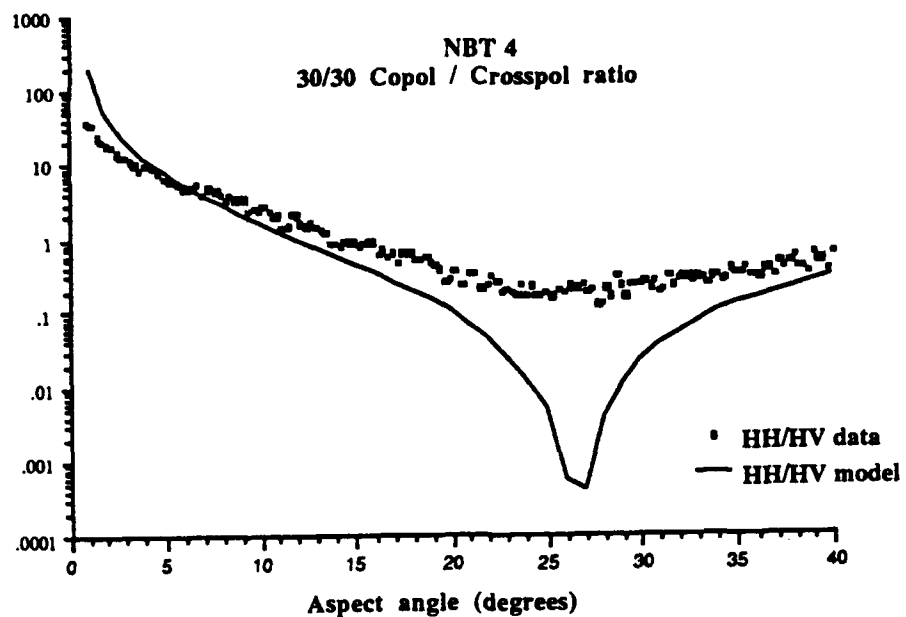


FIG. AC-115

$\sigma_o(HH)/\sigma_o(HV)$ for laboratory depression angles $\xi_i = \xi_s = 30$

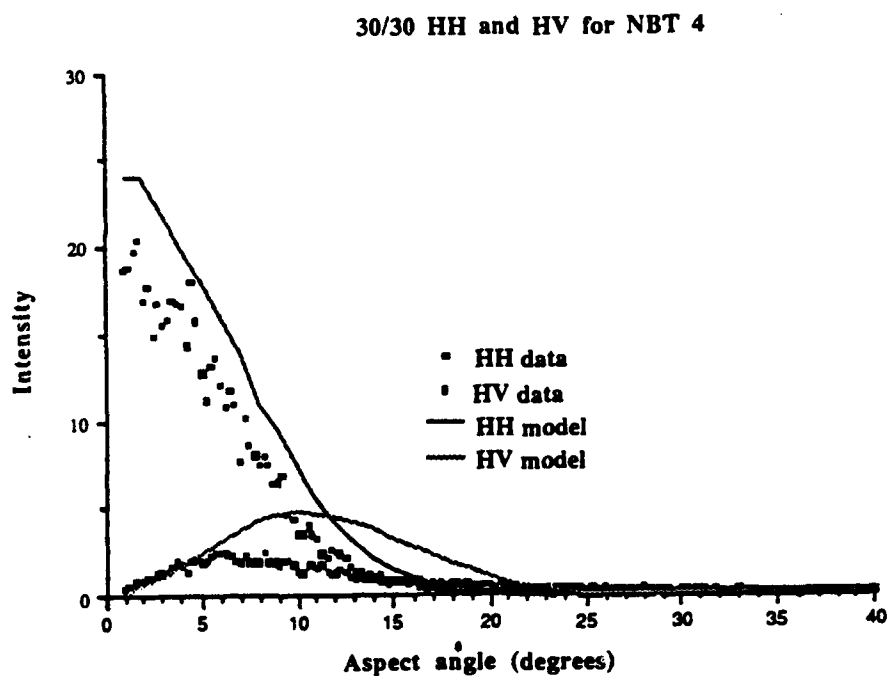


FIG. AC-116

$\sigma_o(HH)$ and $\sigma_o(HV)$ for laboratory depression angles $\xi_i = \xi_s = 30$

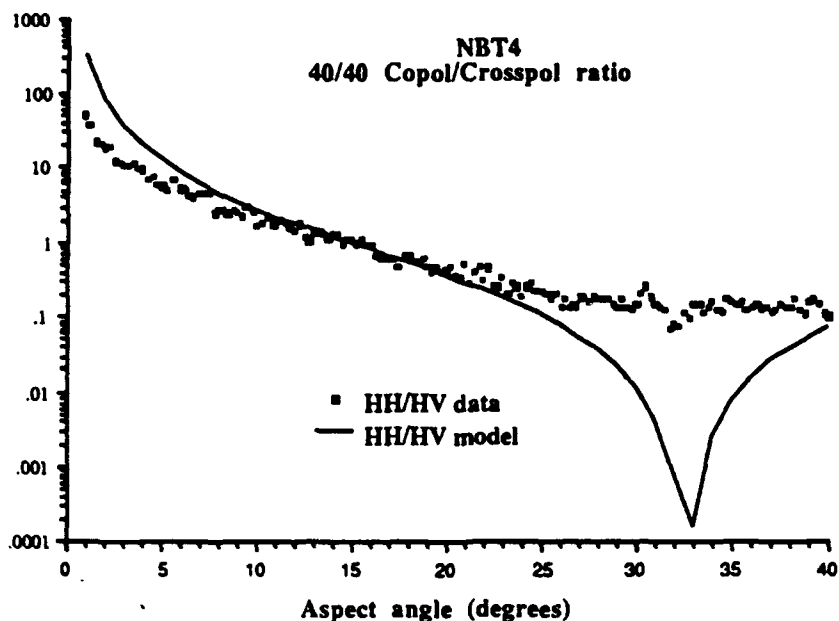


FIG. AC-117

$\sigma_o(\text{HH})/\sigma_o(\text{HV})$ for laboratory depression angles $\xi_i = \xi_s = 40$

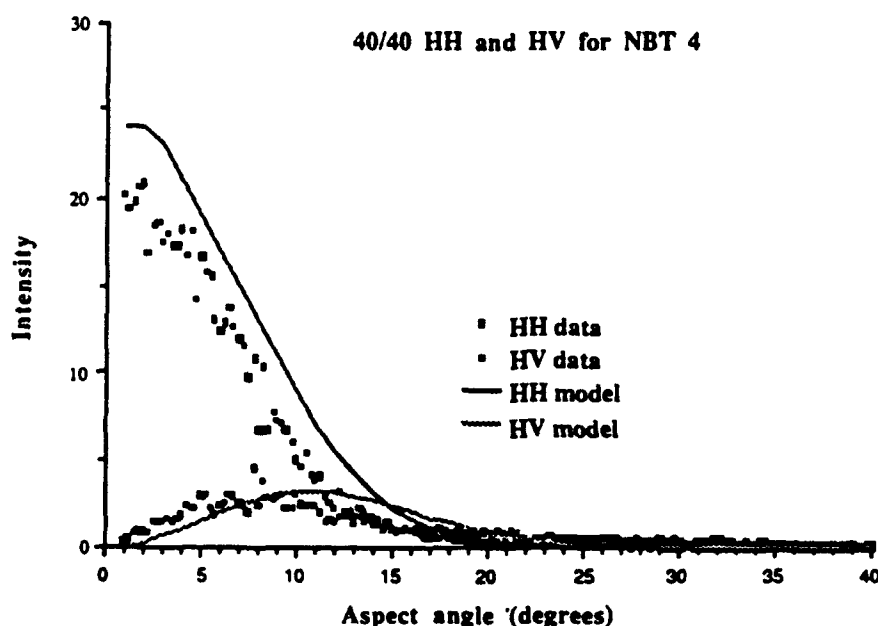


FIG. AC-118

$\sigma_o(\text{HH})$ and $\sigma_o(\text{HV})$ for laboratory depression angles $\xi_i = \xi_s = 40$

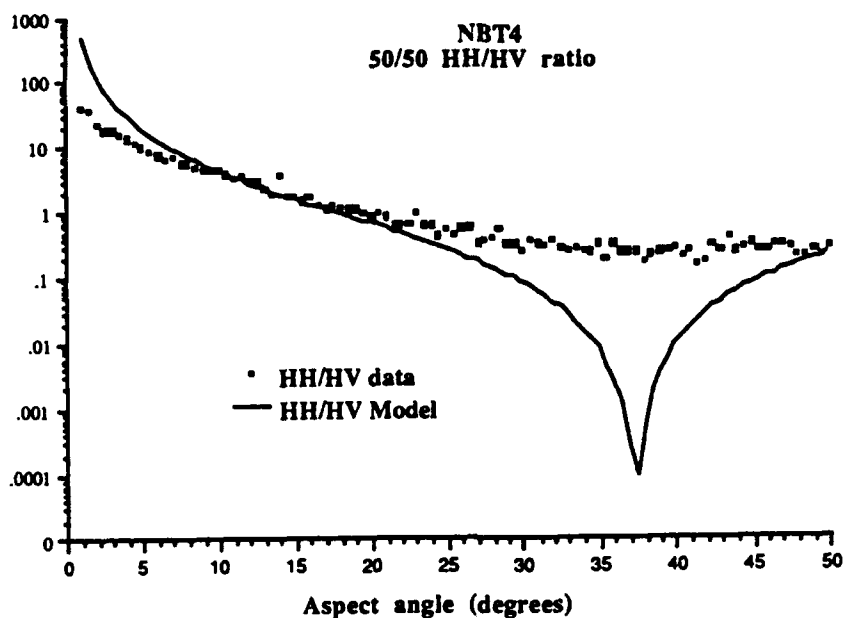


FIG. AC-119

$\sigma_o(\text{HH})/\sigma_o(\text{HV})$ for laboratory depression angles $\xi_i = \xi_s = 50$

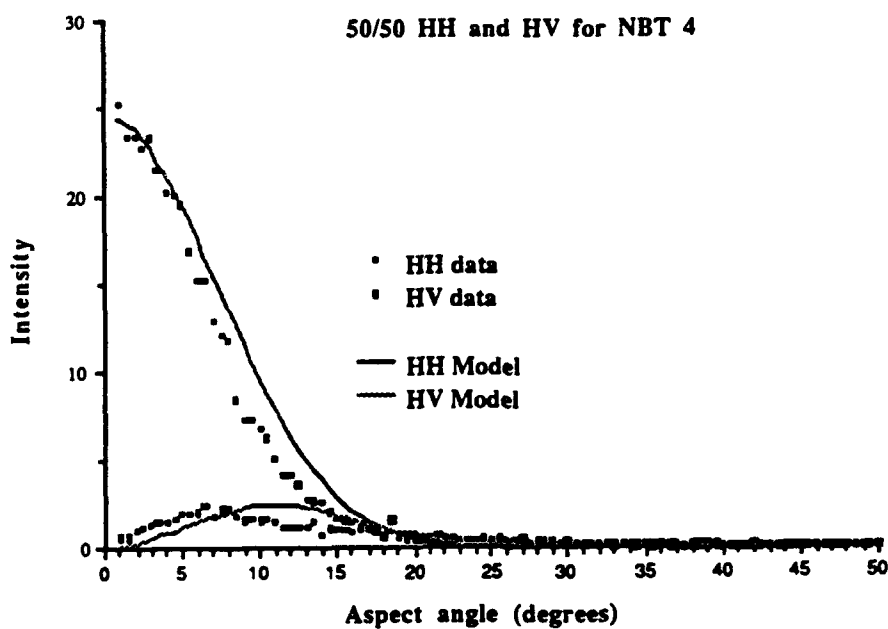


FIG. AC-120

$\sigma_o(\text{HH})$ and $\sigma_o(\text{HV})$ for laboratory depression angles $\xi_i = \xi_s = 50$

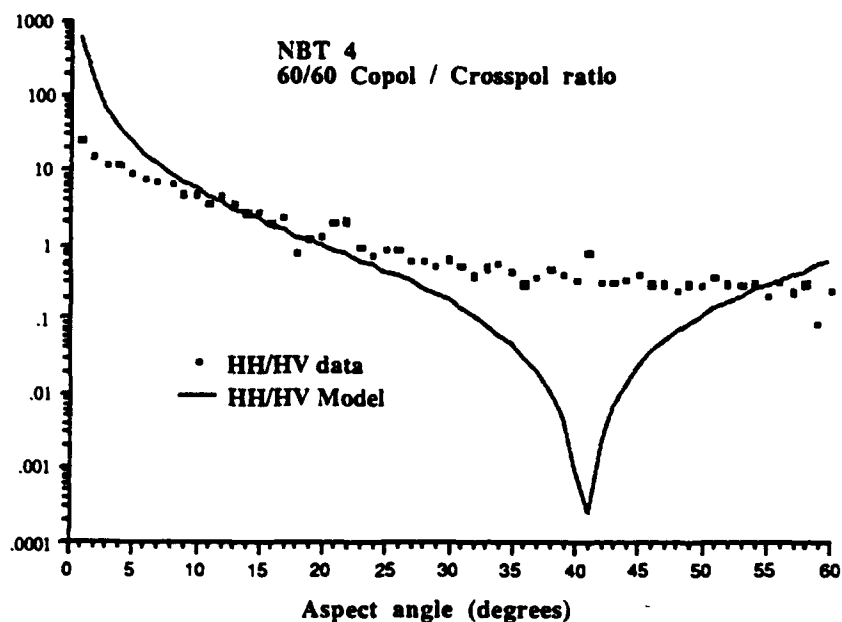


FIG. AC-121

$\sigma_o(\text{HH})/\sigma_o(\text{HV})$ for laboratory depression angles $\xi_i = \xi_s = 60$

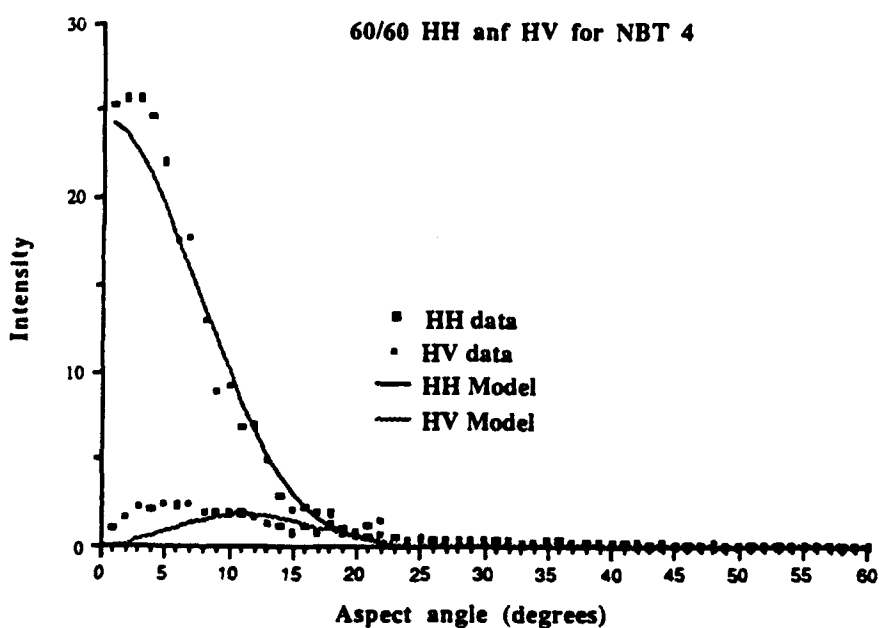


FIG. AC-122

$\sigma_o(\text{HH})$ and $\sigma_o(\text{HV})$ for laboratory depression angles $\xi_i = \xi_s = 60$

NBT 6

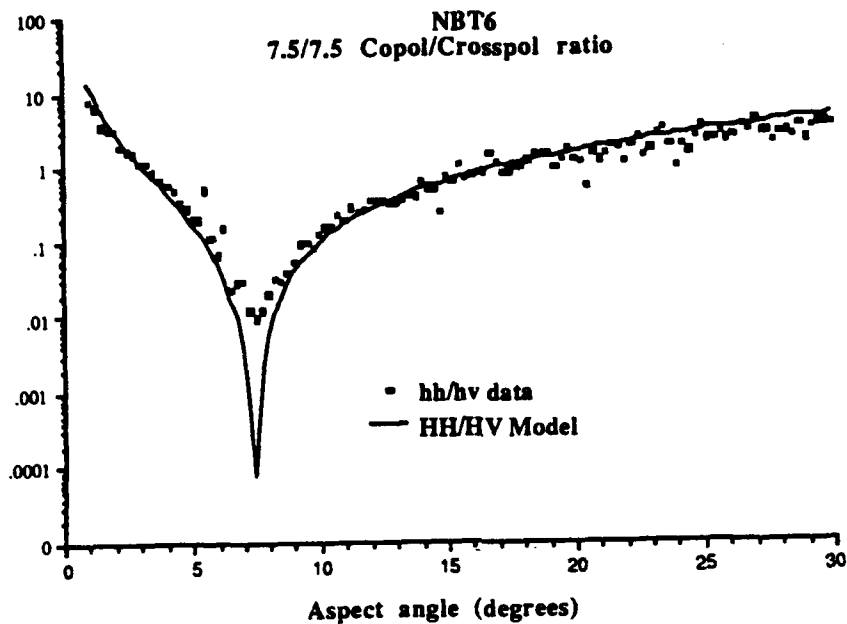


FIG. AC-123

$\sigma_o(\text{HH})/\sigma_o(\text{HV})$ for laboratory depression angles $\xi_i = \xi_s = 7.5$

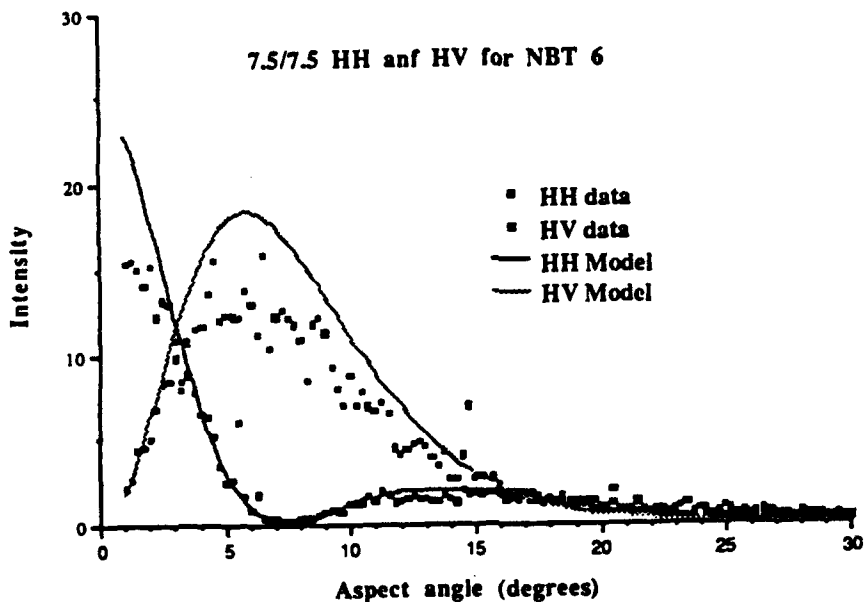


FIG. AC-124

$\sigma_o(\text{HH})$ and $\sigma_o(\text{HV})$ for laboratory depression angles $\xi_i = \xi_s = 7.5$

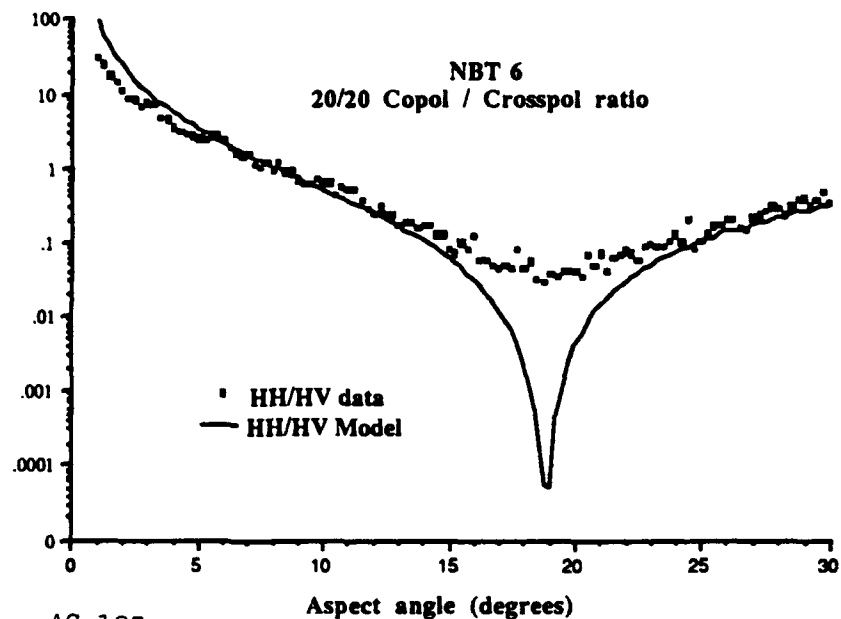


FIG. AC-125

$\sigma_o(\text{HH})/\sigma_o(\text{HV})$ for laboratory depression angles $\xi_i = \xi_s = 20$

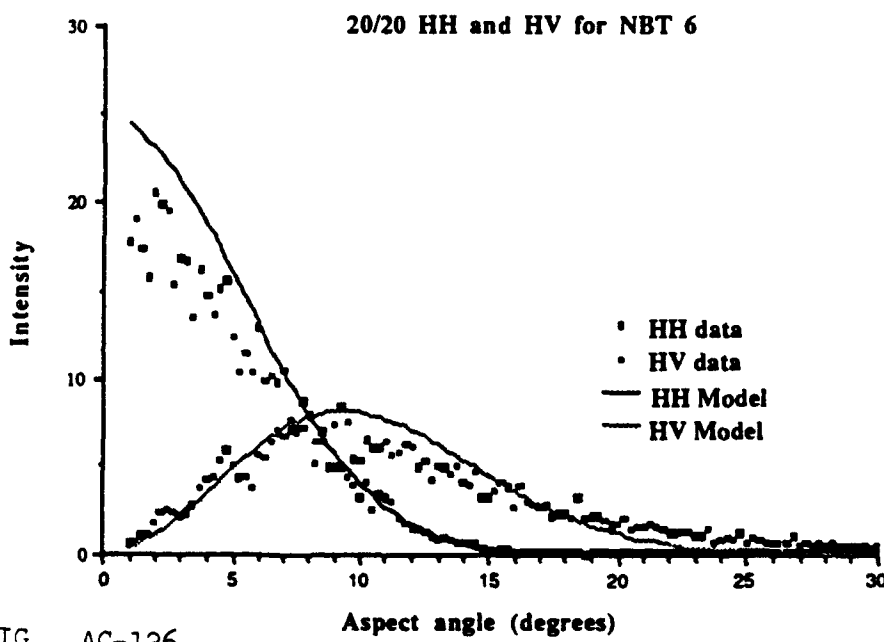


FIG. AC-126

$\sigma_o(\text{HH})$ and $\sigma_o(\text{HV})$ for laboratory depression angles $\xi_i = \xi_s = 20$

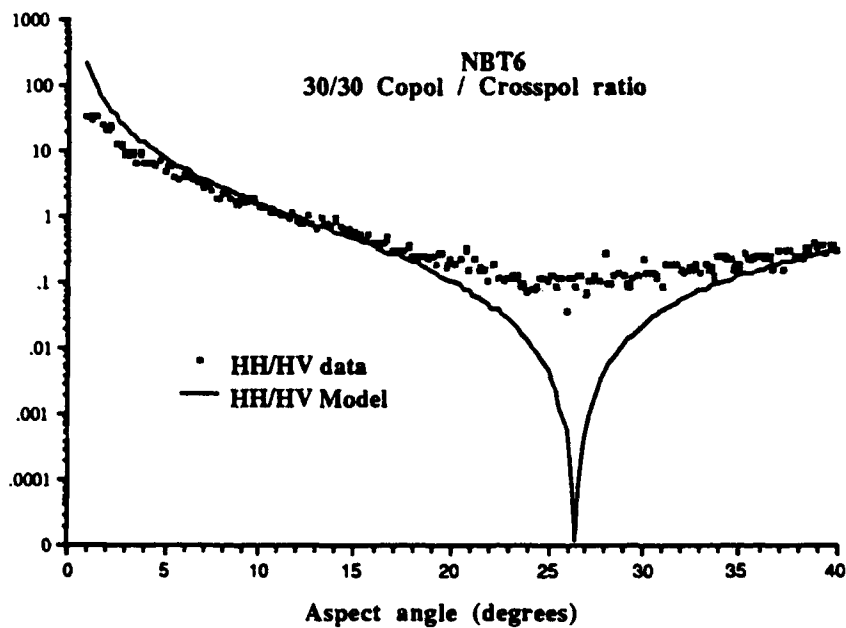


FIG. AC-127

$\sigma_o(\text{HH})/\sigma_o(\text{HV})$ for laboratory depression angles $\xi_i = \xi_s = 30$

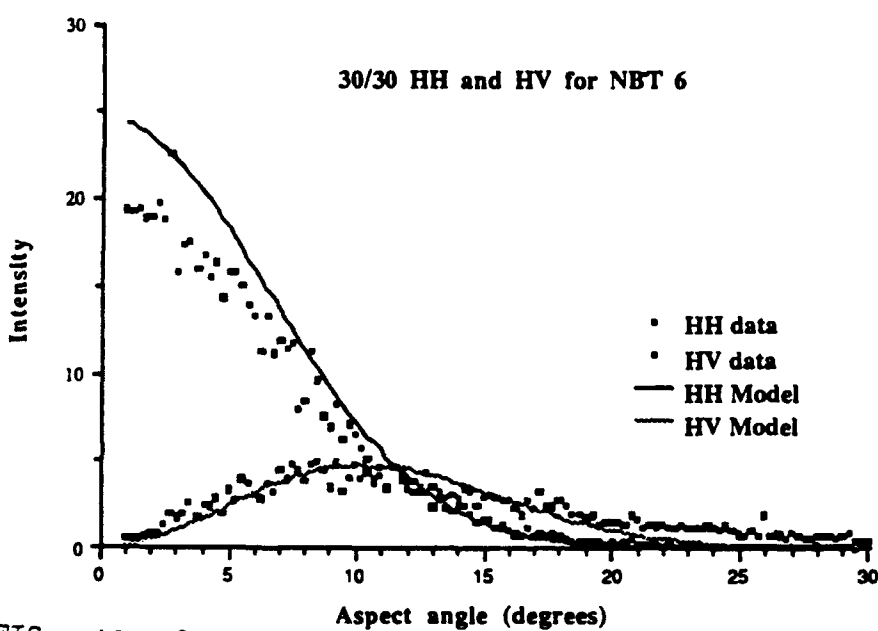


FIG. AC-128

$\sigma_o(\text{HH})$ and $\sigma_o(\text{HV})$ for laboratory depression angles $\xi_i = \xi_s = 30$

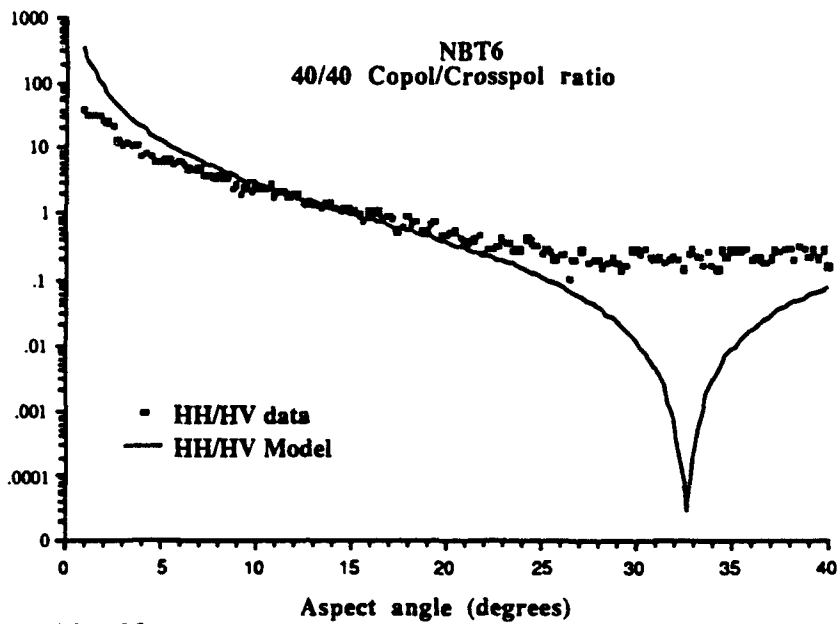


FIG. AC-129

$\sigma_o(\text{HH})/\sigma_o(\text{HV})$ for laboratory depression angles $\xi_i = \xi_s = 40$

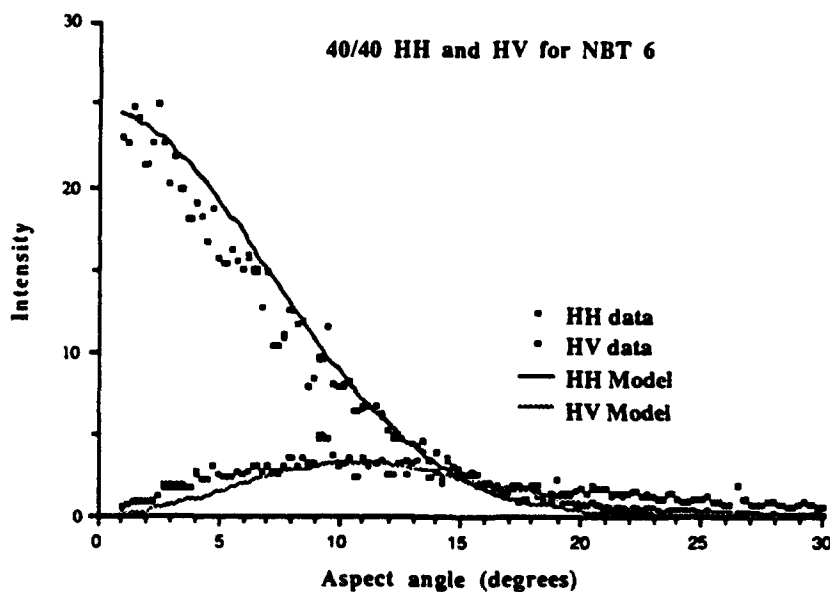


FIG. AC-130

$\sigma_o(\text{HH})$ and $\sigma_o(\text{HV})$ for laboratory depression angles $\xi_i = \xi_s = 40$

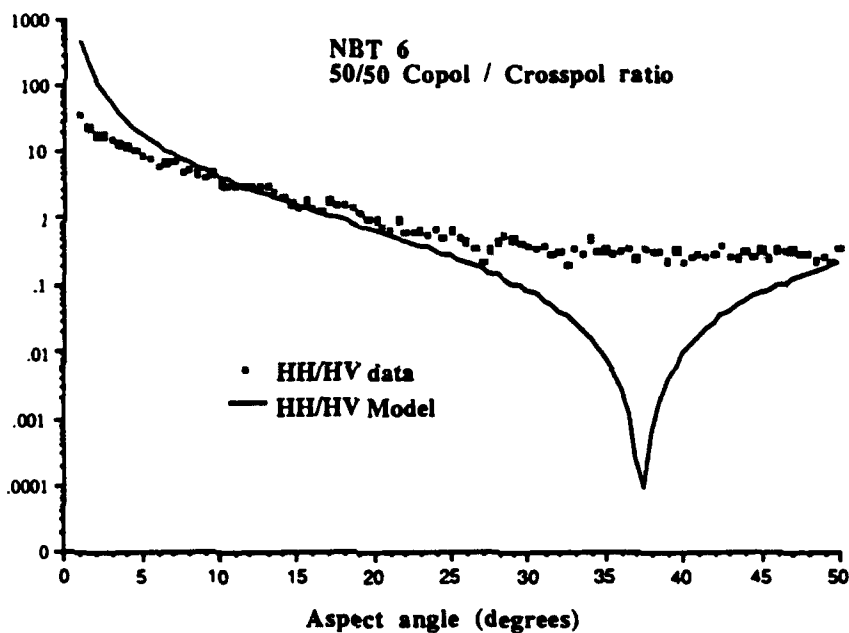


FIG. AC-131

$\sigma_o(\text{HH})/\sigma_o(\text{HV})$ for laboratory depression angles $\xi_i = \xi_s = 50$

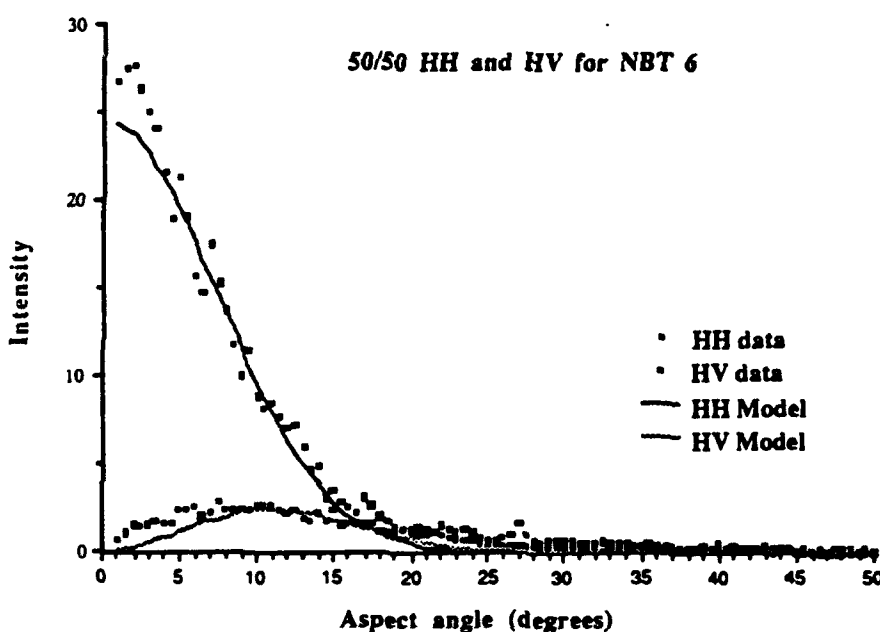


FIG. AC-132

$\sigma_o(\text{HH})$ and $\sigma_o(\text{HV})$ for laboratory depression angles $\xi_i = \xi_s = 50$

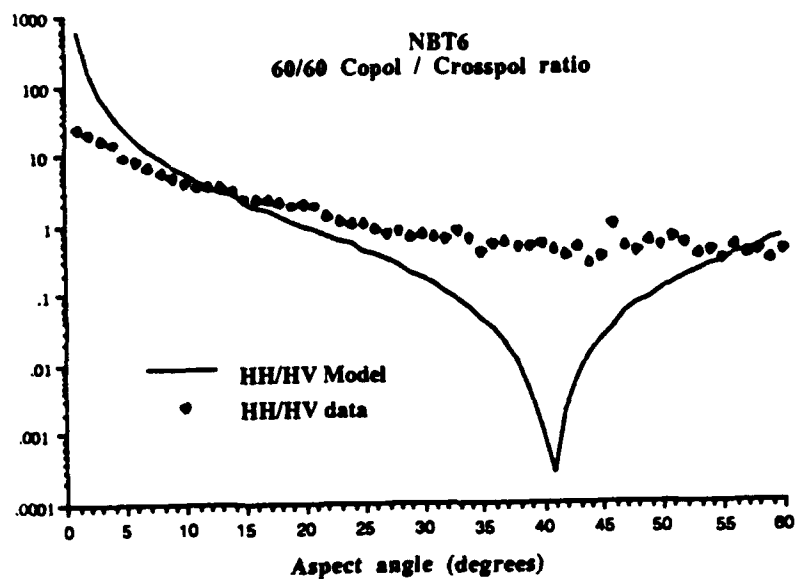


FIG. AC-133

$\sigma_o(\text{HH})/\sigma_o(\text{HV})$ for laboratory depression angles $\xi_i = \xi_s = 60$

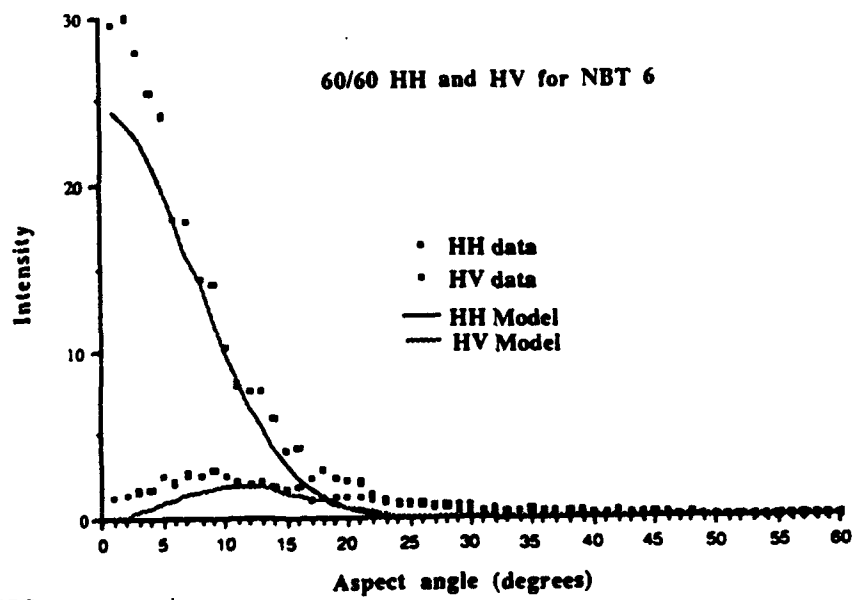


FIG. AC-134

$\sigma_o(\text{HH})$ and $\sigma_o(\text{HV})$ for laboratory depression angles $\xi_i = \xi_s = 60$

NBT 13

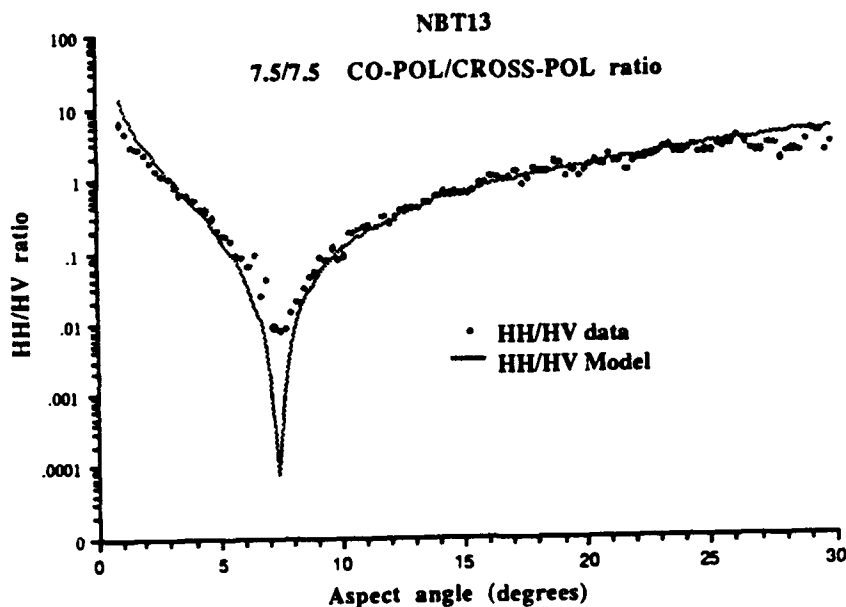


FIG. AC-135

$\sigma_o(HH)/\sigma_o(HV)$ for laboratory depression angles $\xi_i = \xi_s = 7.5$

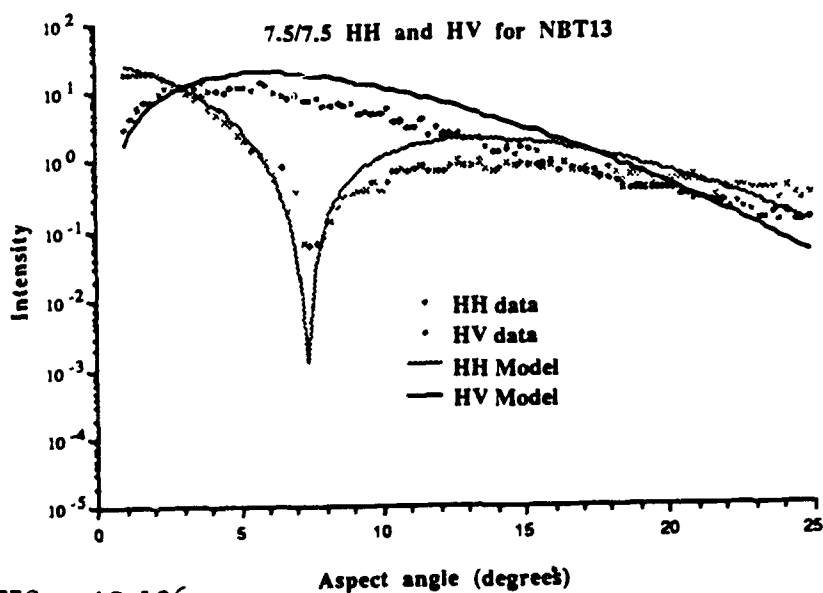


FIG. AC-136

$\sigma_o(HH)$ and $\sigma_o(HV)$ for laboratory depression angles $\xi_i = \xi_s = 7.5$

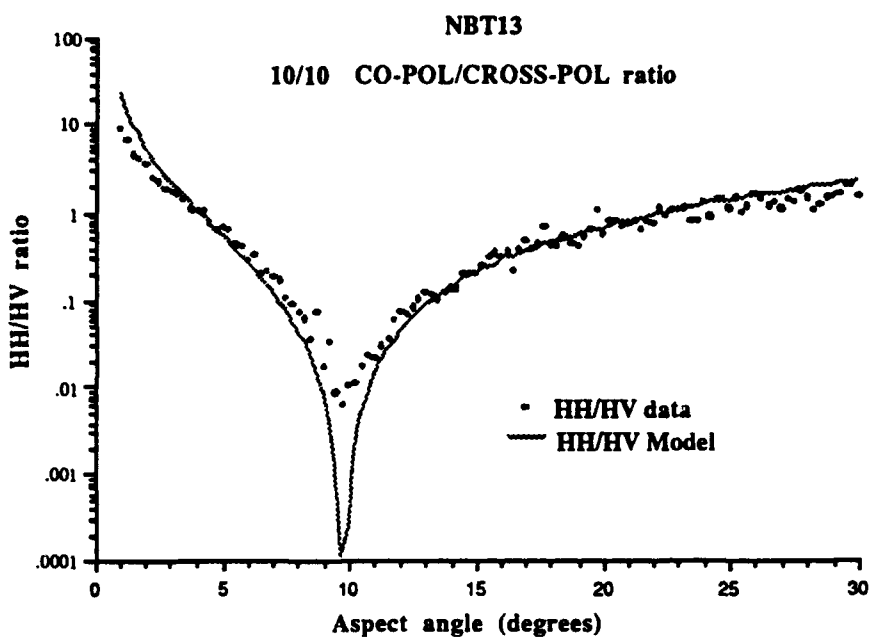


FIG. AC-137

$\sigma_o(\text{HH})/\sigma_o(\text{HV})$ for laboratory depression angles $\xi_i = \xi_s = 10$

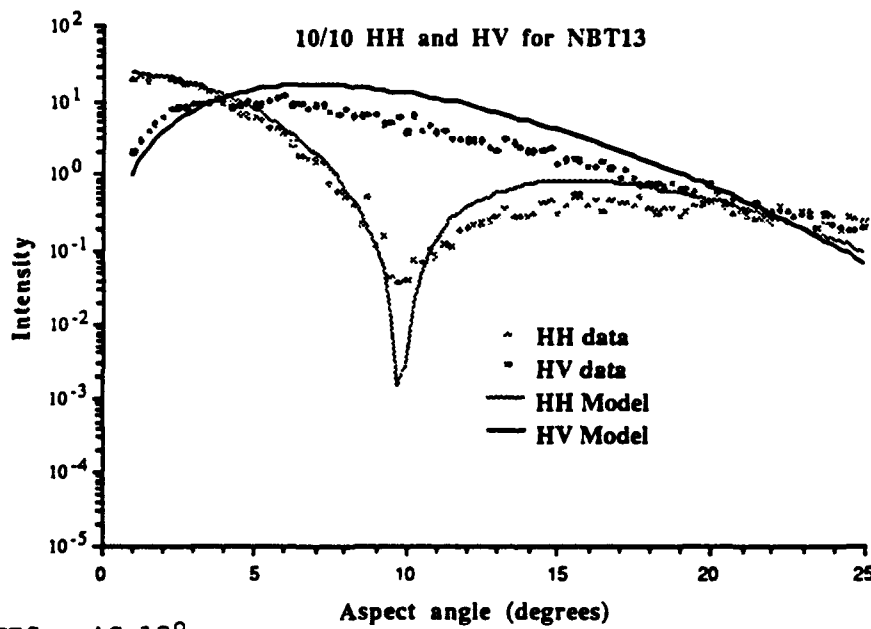


FIG. AC-138

$\sigma_o(\text{HH})$ and $\sigma_o(\text{HV})$ for laboratory depression angles $\xi_i = \xi_s = 10$

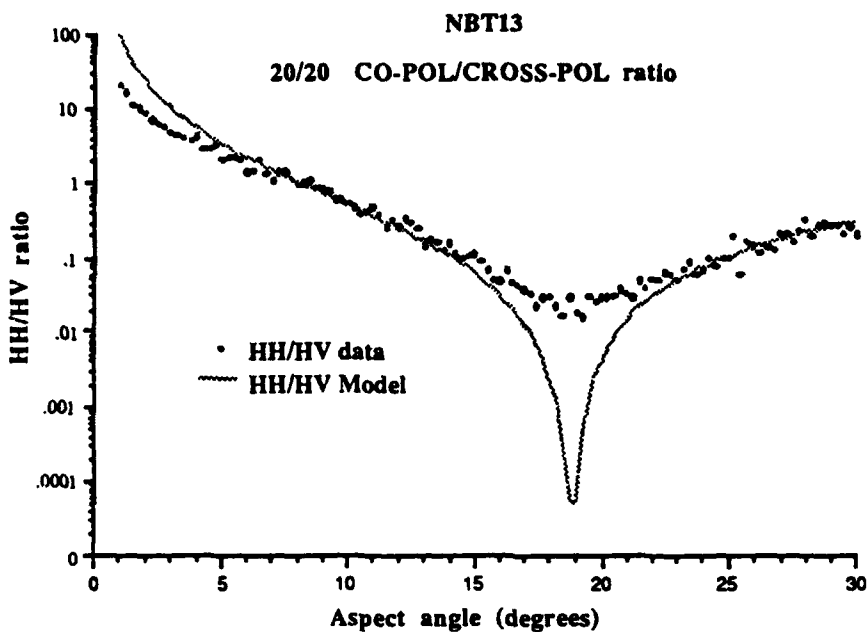


FIG. AC-139

$\sigma_o(\text{HH})/\sigma_o(\text{HV})$ for laboratory depression angles $\xi_i = \xi_s = 20$

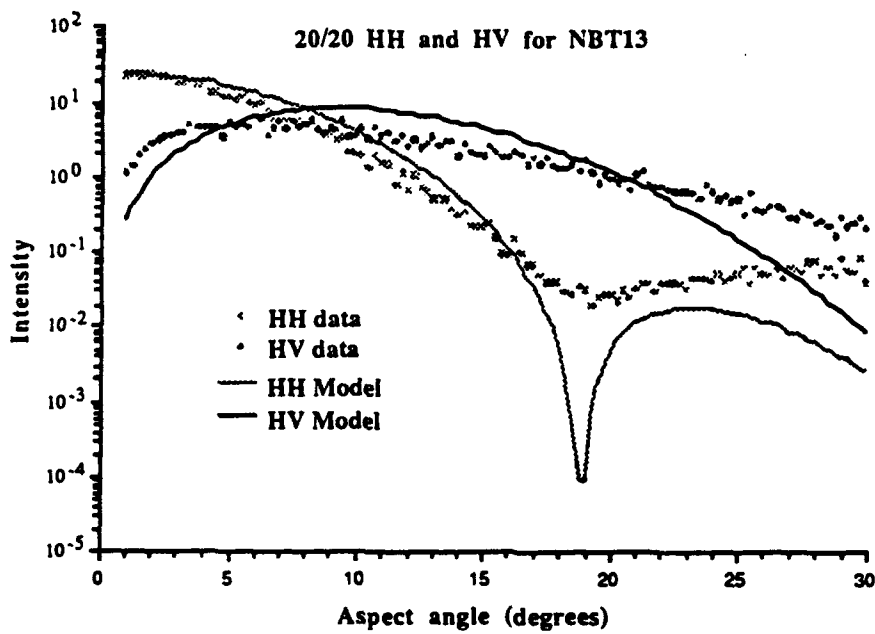


FIG. AC-140

$\sigma_o(\text{HH})$ and $\sigma_o(\text{HV})$ for laboratory depression angles $\xi_i = \xi_s = 20$

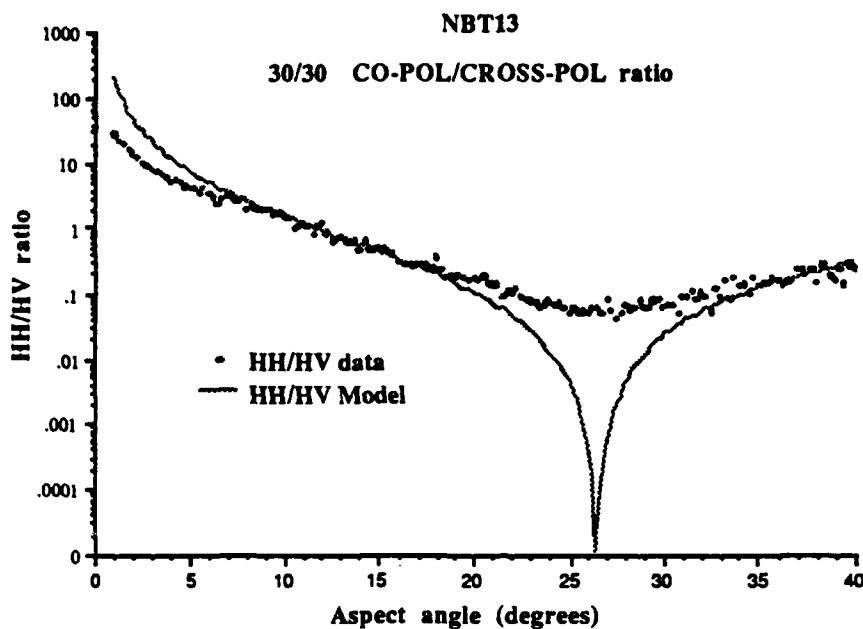


FIG. AC-141

$\sigma_o(HH)/\sigma_o(HV)$ for laboratory depression angles $\xi_i = \xi_s = 30$

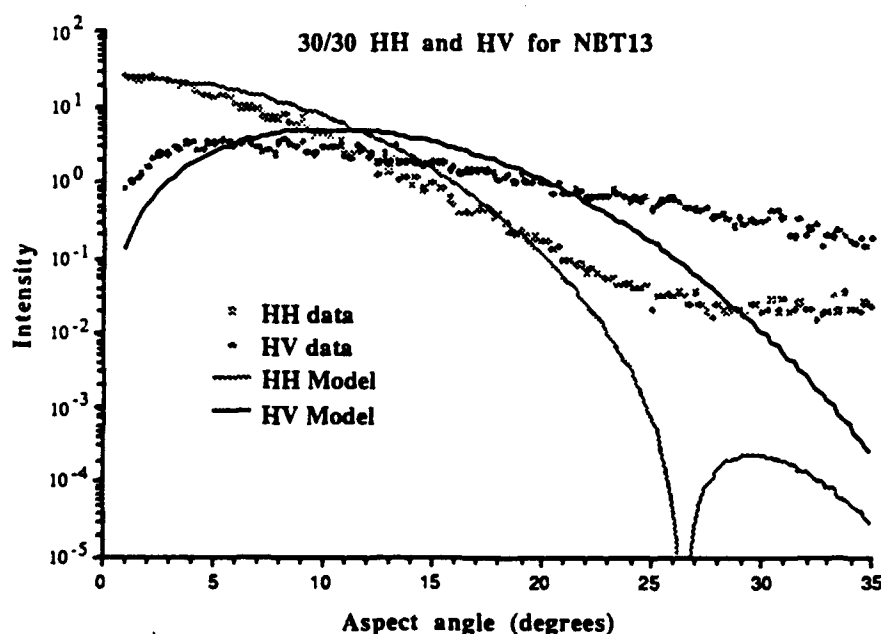


FIG. AC-142

$\sigma_o(HH)$ and $\sigma_o(HV)$ for laboratory depression angles $\xi_i = \xi_s = 30$

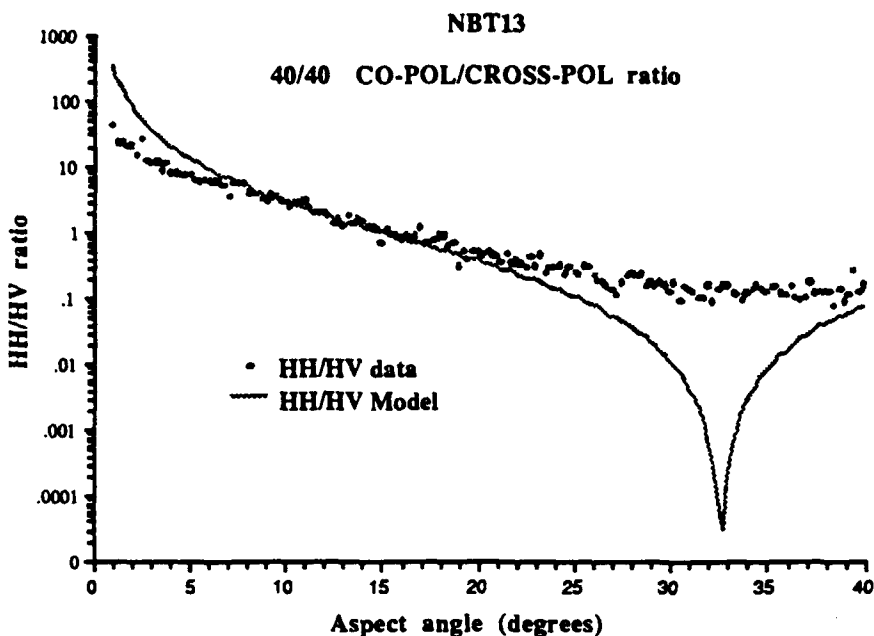


FIG. AC-143

$\sigma_o(\text{HH})/\sigma_o(\text{HV})$ for laboratory depression angles $\xi_i = \xi_s = 40$

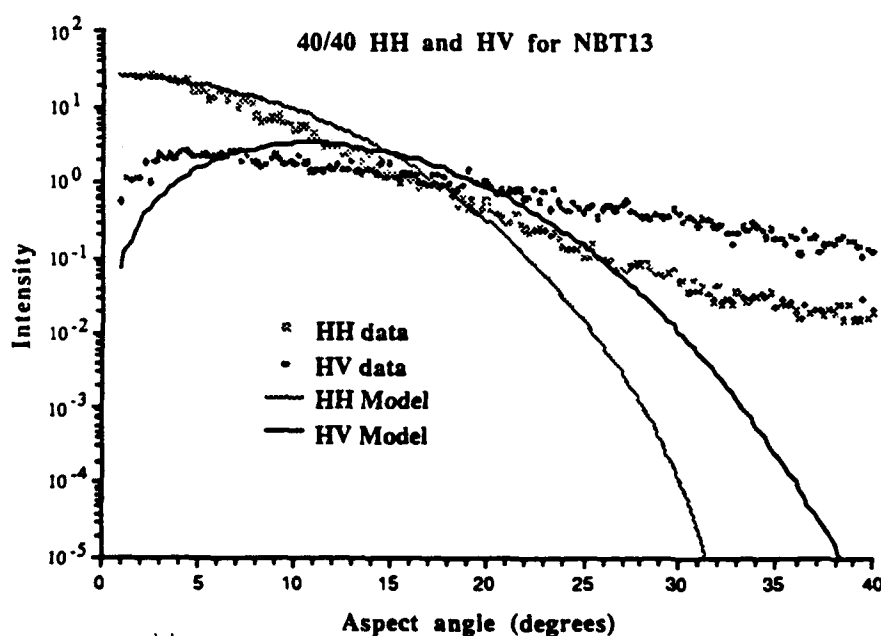


FIG. AC-144

$\sigma_o(\text{HH})$ and $\sigma_o(\text{HV})$ for laboratory depression angles $\xi_i = \xi_s = 40$

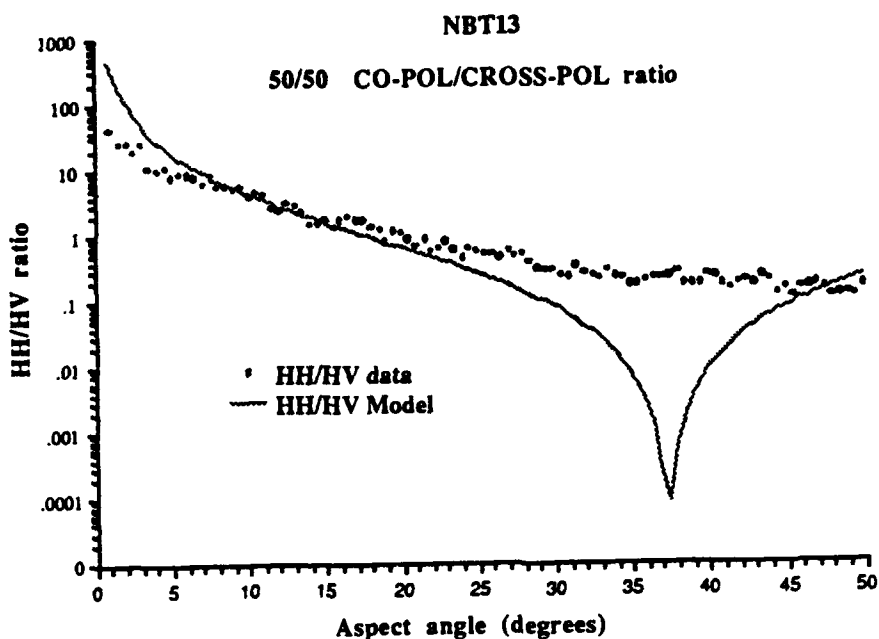


FIG. AC-145

$\sigma_o(\text{HH})/\sigma_o(\text{HV})$ for laboratory depression angles $\xi_i = \xi_s = 50$

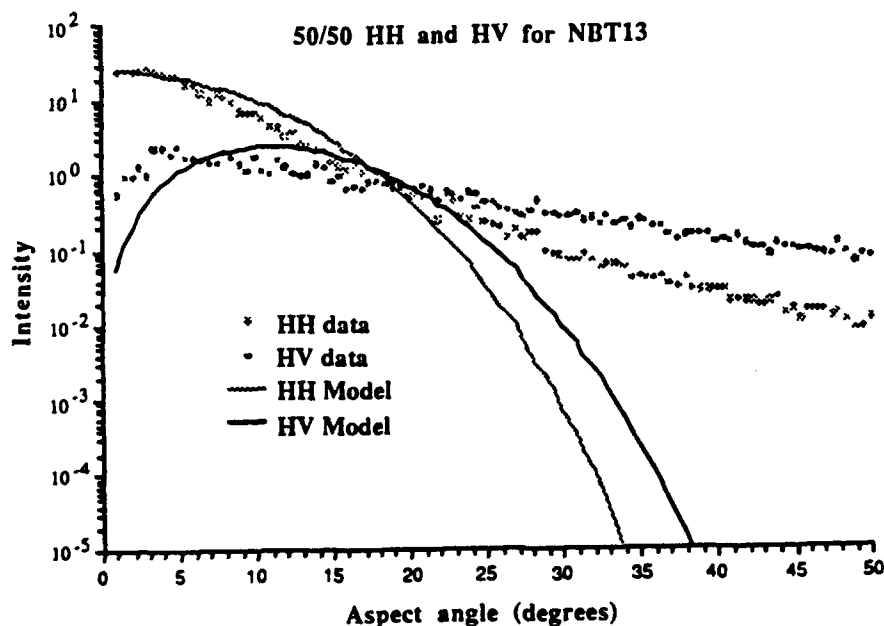


FIG. AC-146

$\sigma_o(\text{HH})$ and $\sigma_o(\text{HV})$ for laboratory depression angles $\xi_i = \xi_s = 50$

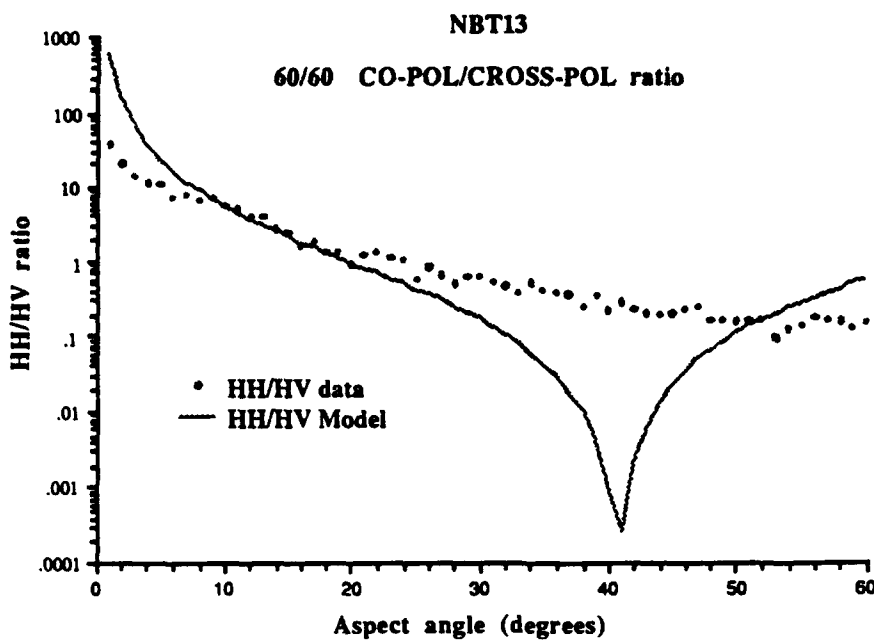


FIG. AC-147

$\sigma_0(\text{HH})/\sigma_0(\text{HV})$ for laboratory depression angles $\xi_i = \xi_s = 60$

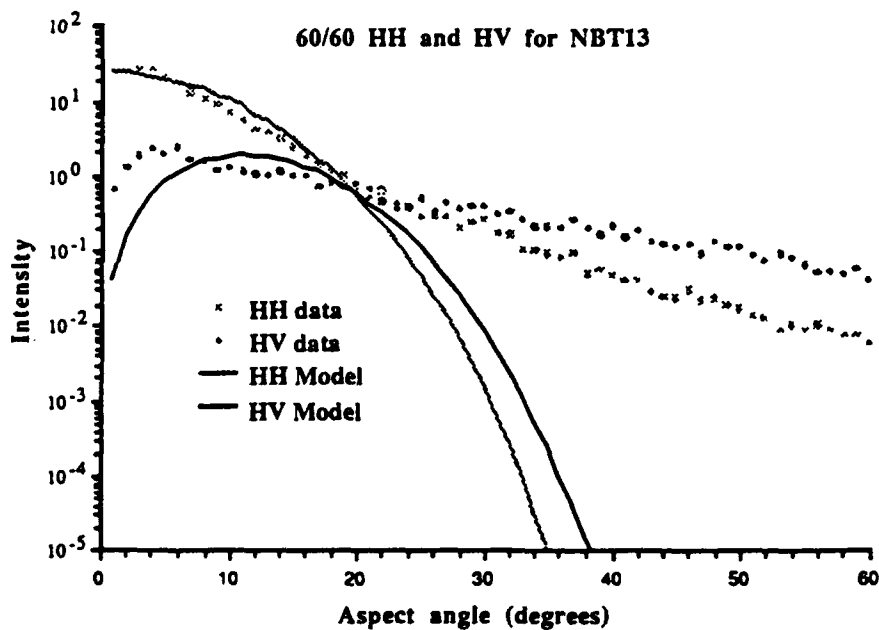


FIG. AC-148

$\sigma_0(\text{HH})$ and $\sigma_0(\text{HV})$ for laboratory depression angles $\xi_i = \xi_s = 60$

NBT 4+13

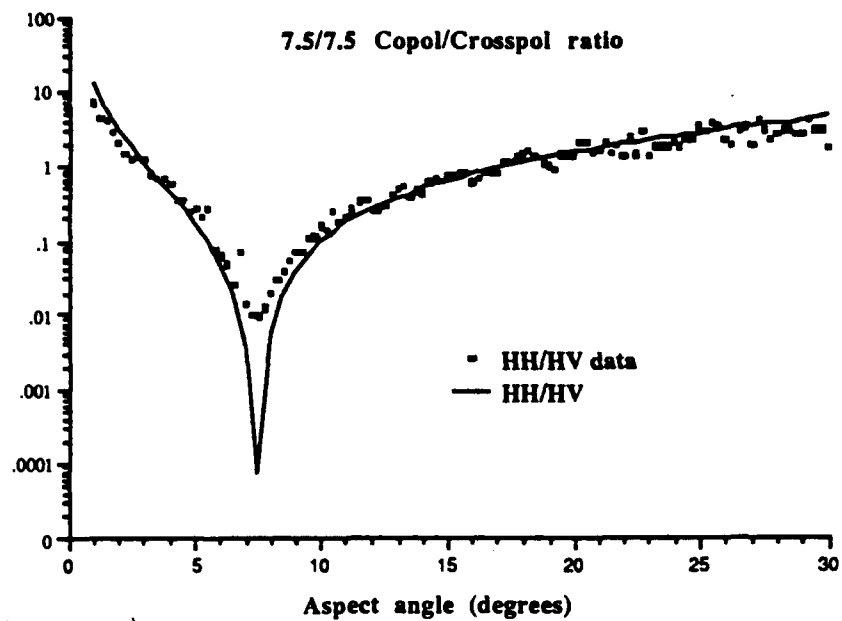


FIG. AC-149

$\sigma_o(HH)/\sigma_o(HV)$ for laboratory depression angles $\xi_i = \xi_s = 7.5$

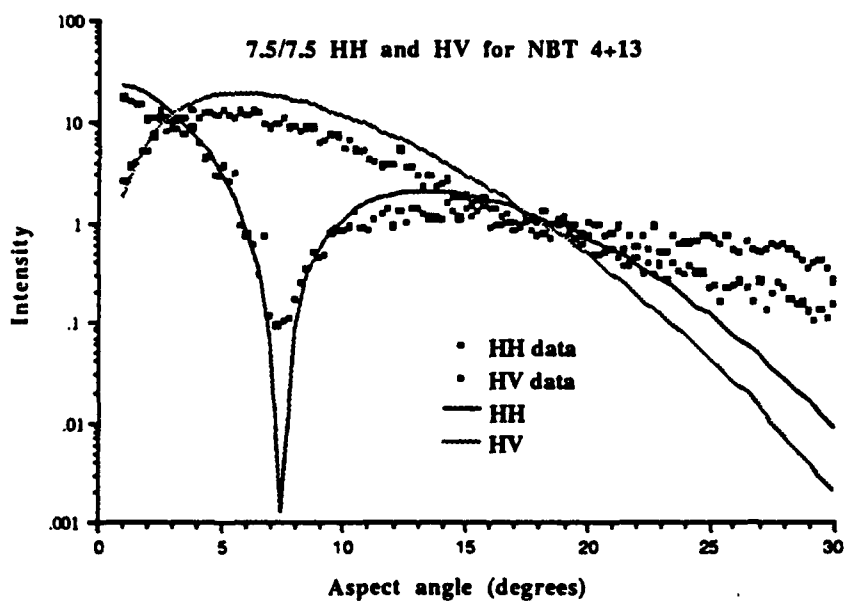


FIG. AC-150

$\sigma_o(HH)$ and $\sigma_o(HV)$ for laboratory depression angles $\xi_i = \xi_s = 7.5$

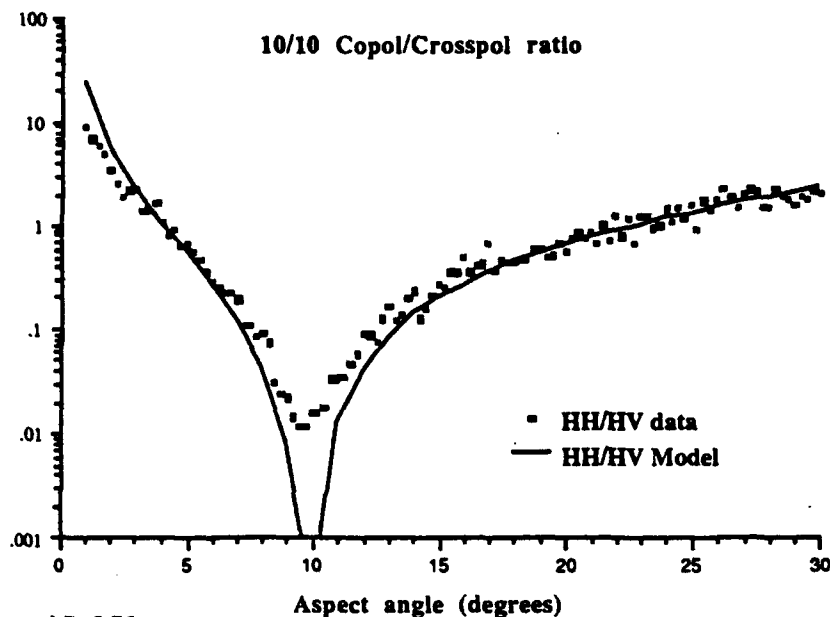


FIG. AC-151

$\sigma_o(\text{HH})/\sigma_o(\text{HV})$ for laboratory depression angles $\xi_i = \xi_s = 10$

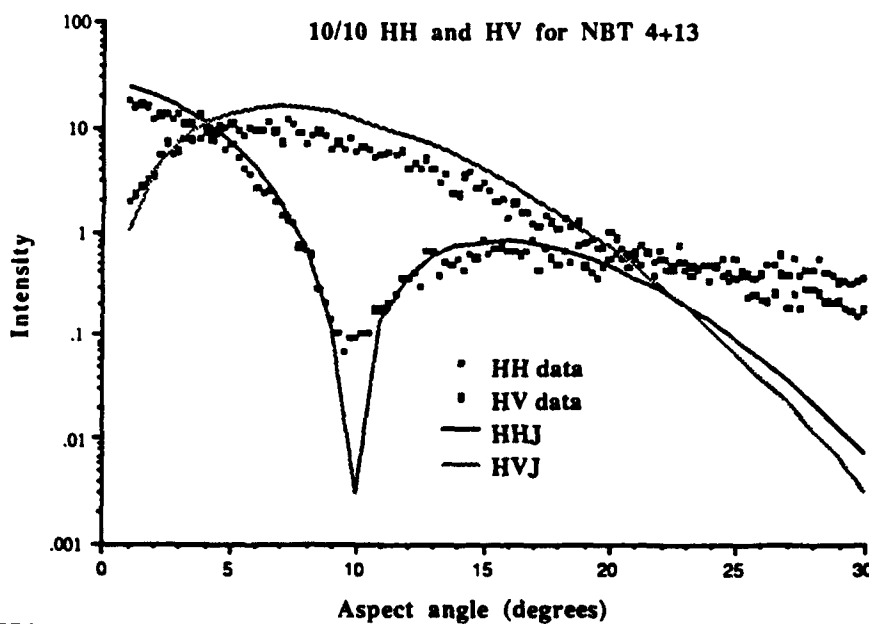


FIG. AC-152

$\sigma_o(\text{HH})$ and $\sigma_o(\text{HV})$ for laboratory depression angles $\xi_i = \xi_s = 10$

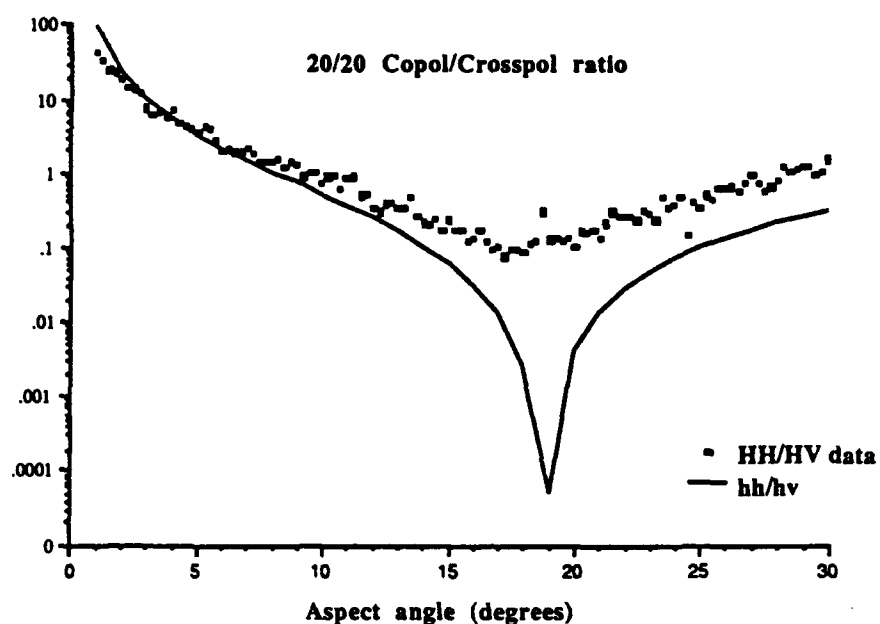


FIG. AC-153

$\sigma_o(\text{HH})/\sigma_o(\text{HV})$ for laboratory depression angles $\xi_i = \xi_s = 20$

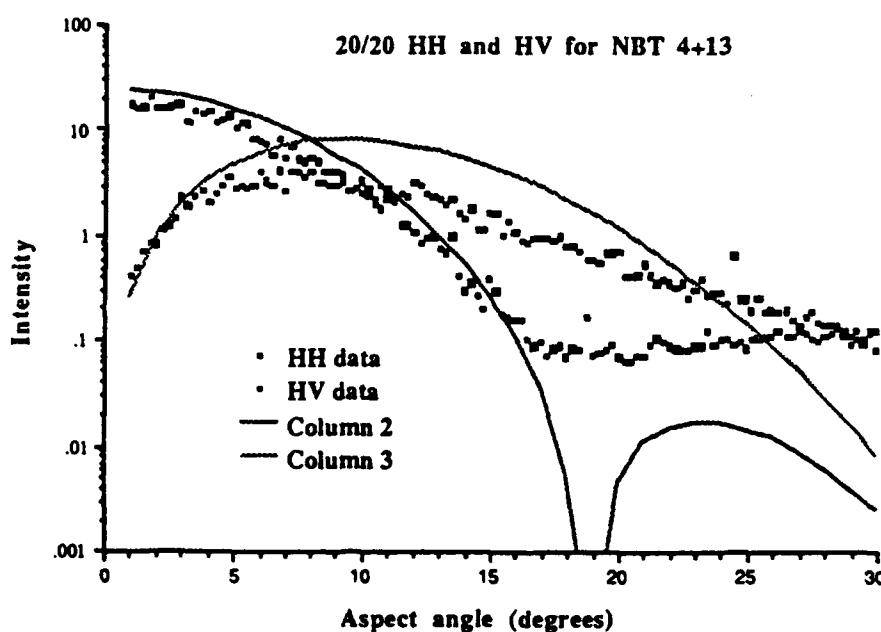


FIG. AC-154

$\sigma_o(\text{HH})$ and $\sigma_o(\text{HV})$ for laboratory depression angles $\xi_i = \xi_s = 20$

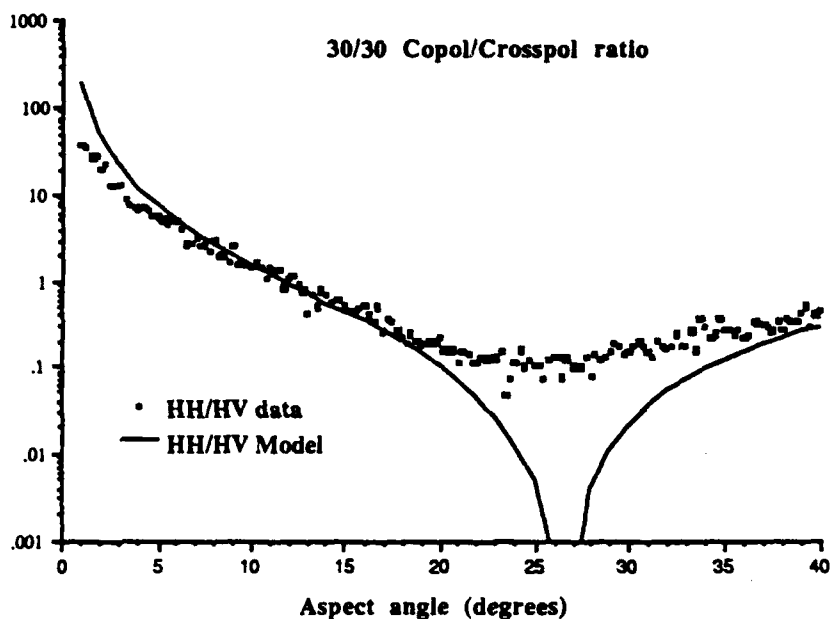


FIG. AC-155

$\sigma_o(\text{HH})/\sigma_o(\text{HV})$ for laboratory depression angles $\xi_i = \xi_s = 30$

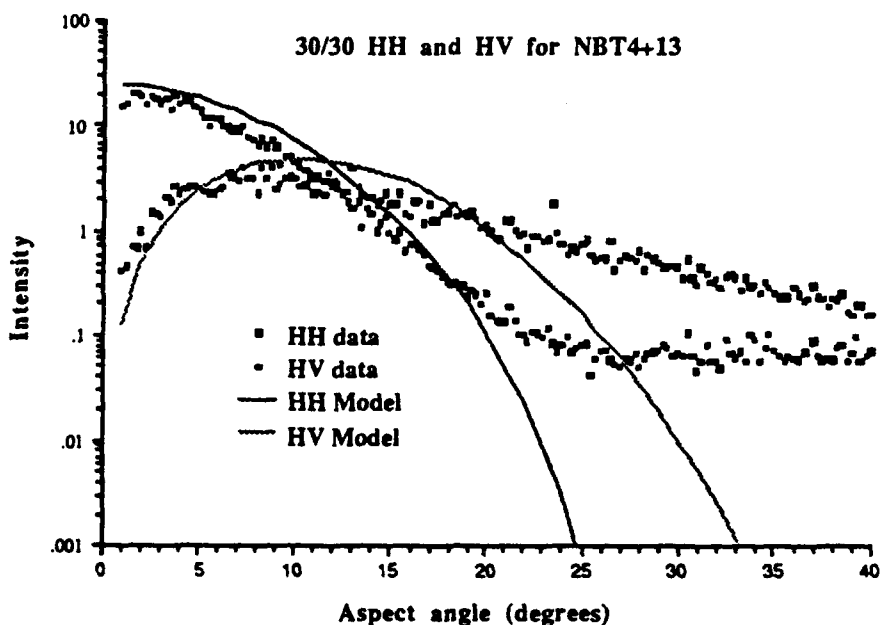


FIG. AC-156

$\sigma_o(\text{HH})$ and $\sigma_o(\text{HV})$ for laboratory depression angles $\xi_i = \xi_s = 30$

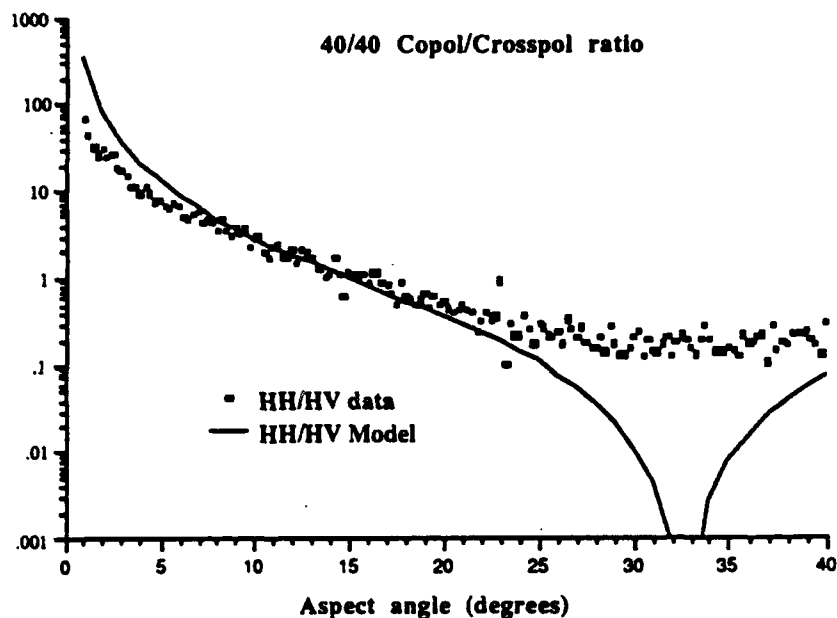


FIG. AC-157

$\sigma_o(HH)/\sigma_o(HV)$ for laboratory depression angles $\xi_i = \xi_s = 40$

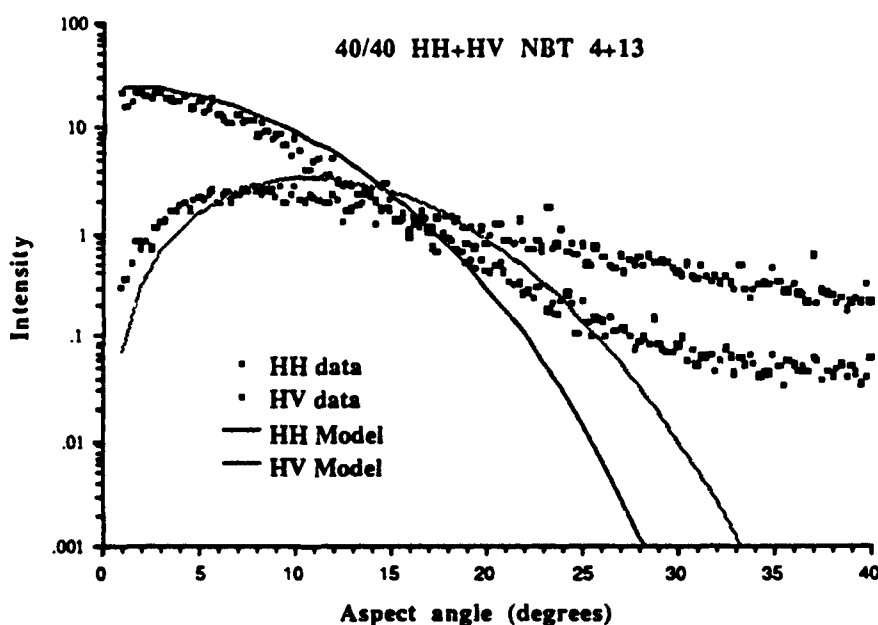


FIG. AC-158

$\sigma_o(HH)$ and $\sigma_o(HV)$ for laboratory depression angles $\xi_i = \xi_s = 40$

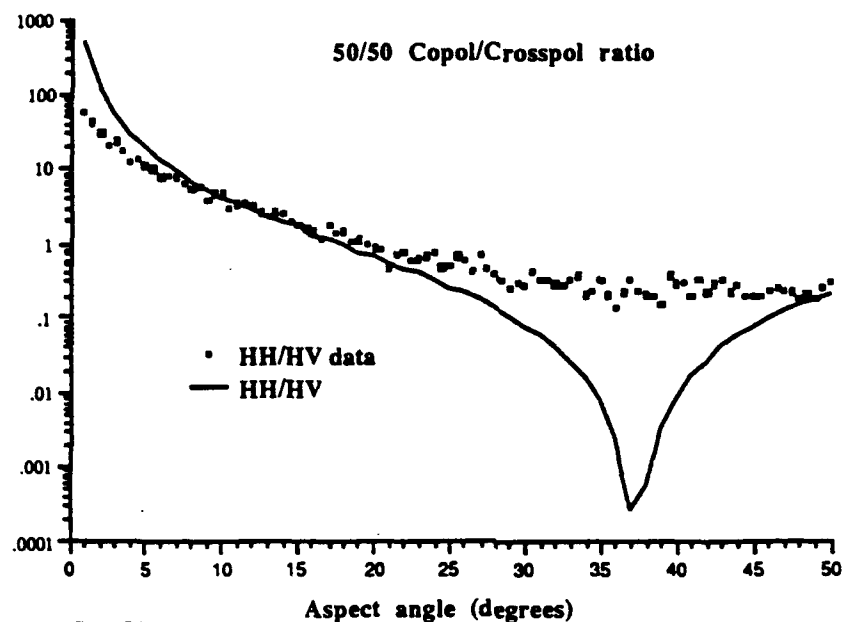


FIG. AC-159

$\sigma_o(\text{HH})/\sigma_o(\text{HV})$ for laboratory depression angles $\xi_i = \xi_s = 50$

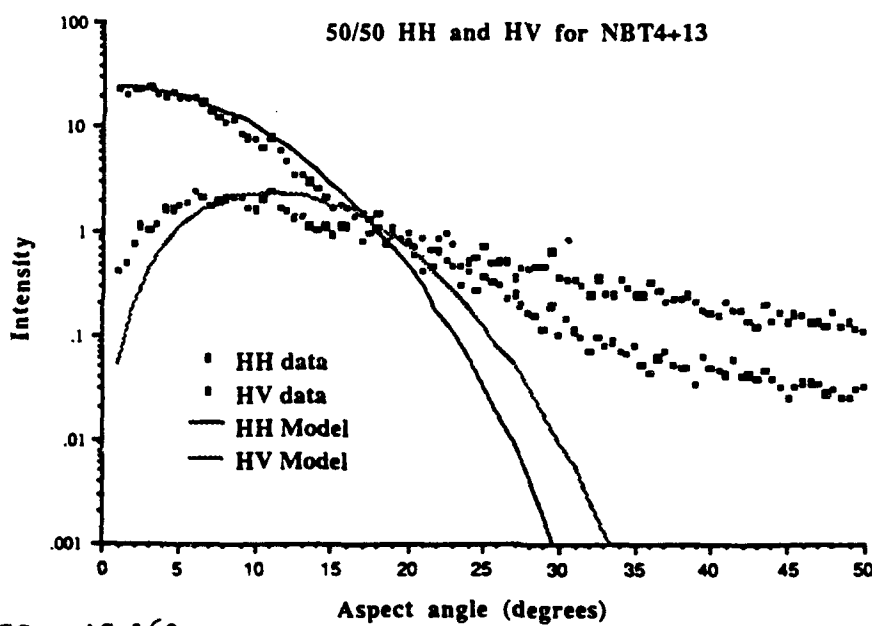


FIG. AC-160

$\sigma_o(\text{HH})$ and $\sigma_o(\text{HV})$ for laboratory depression angles $\xi_i = \xi_s = 50$

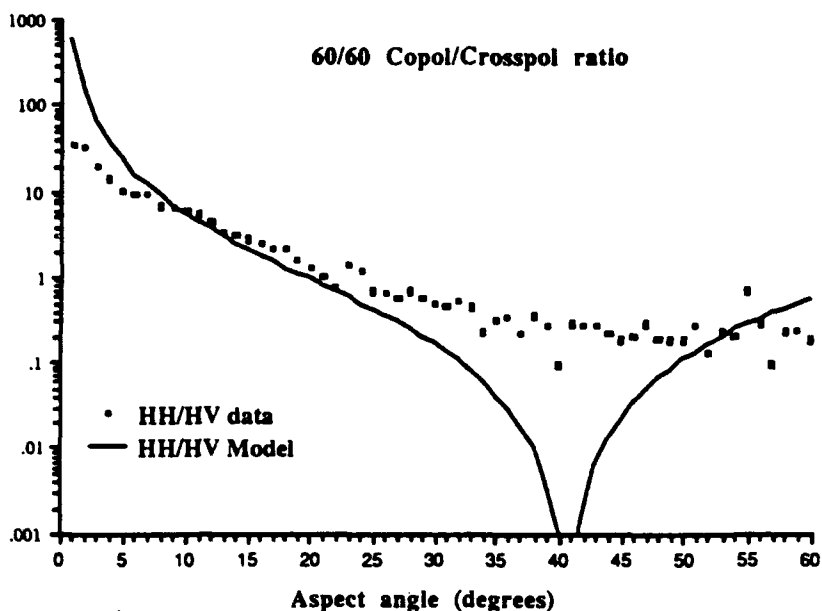


FIG. AC-161

$\sigma_0(\text{HH})/\sigma_0(\text{HV})$ for laboratory depression angles $\xi_i = \xi_s = 60$

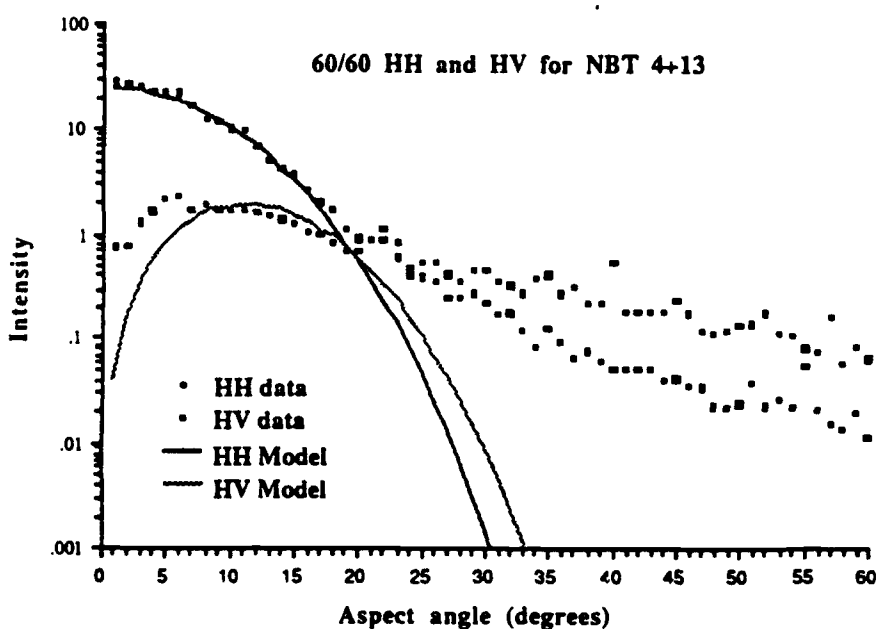


FIG. AC-162

$\sigma_0(\text{HH})$ and $\sigma_0(\text{HV})$ for laboratory depression angles $\xi_i = \xi_s = 60$

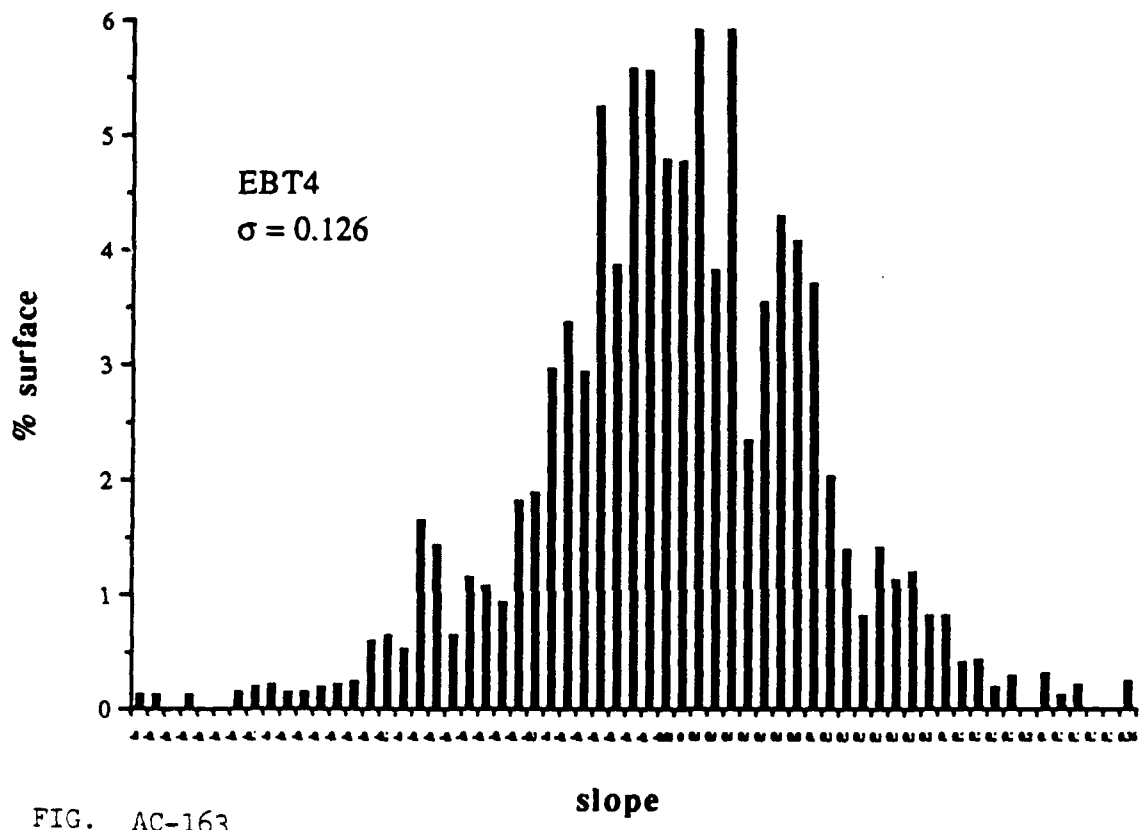
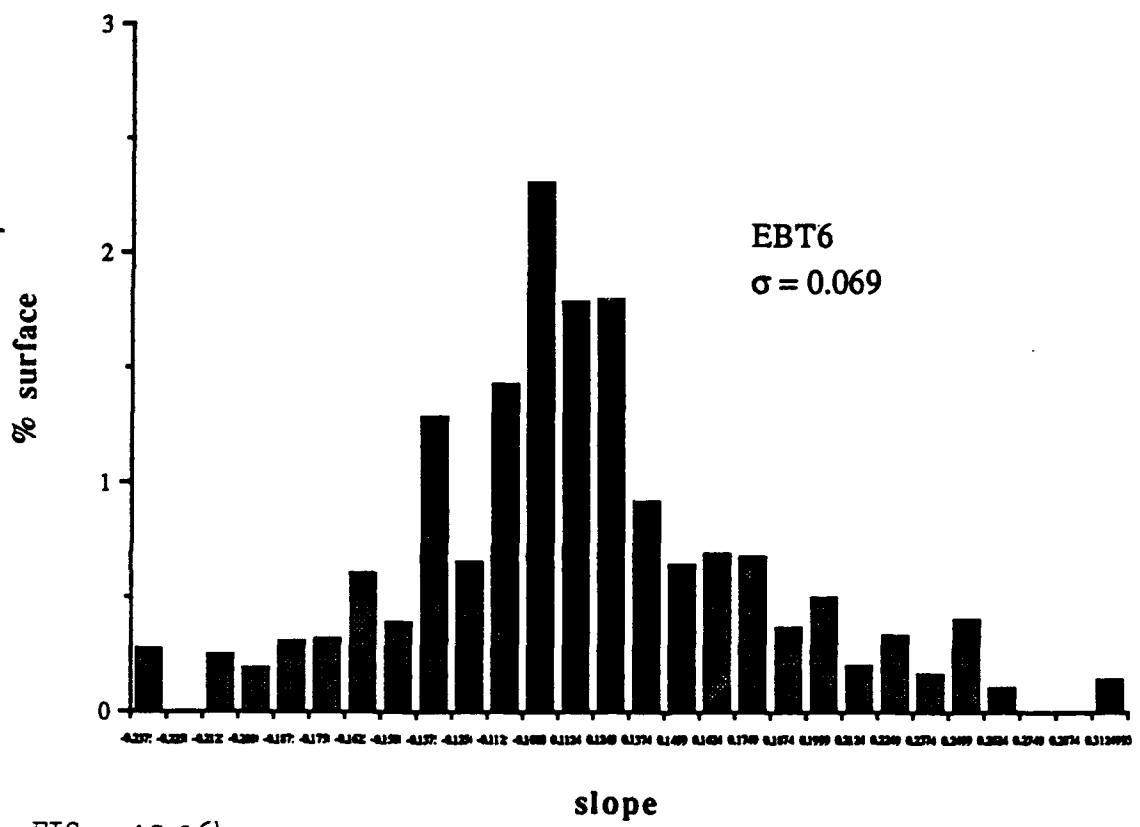


FIG. AC-163



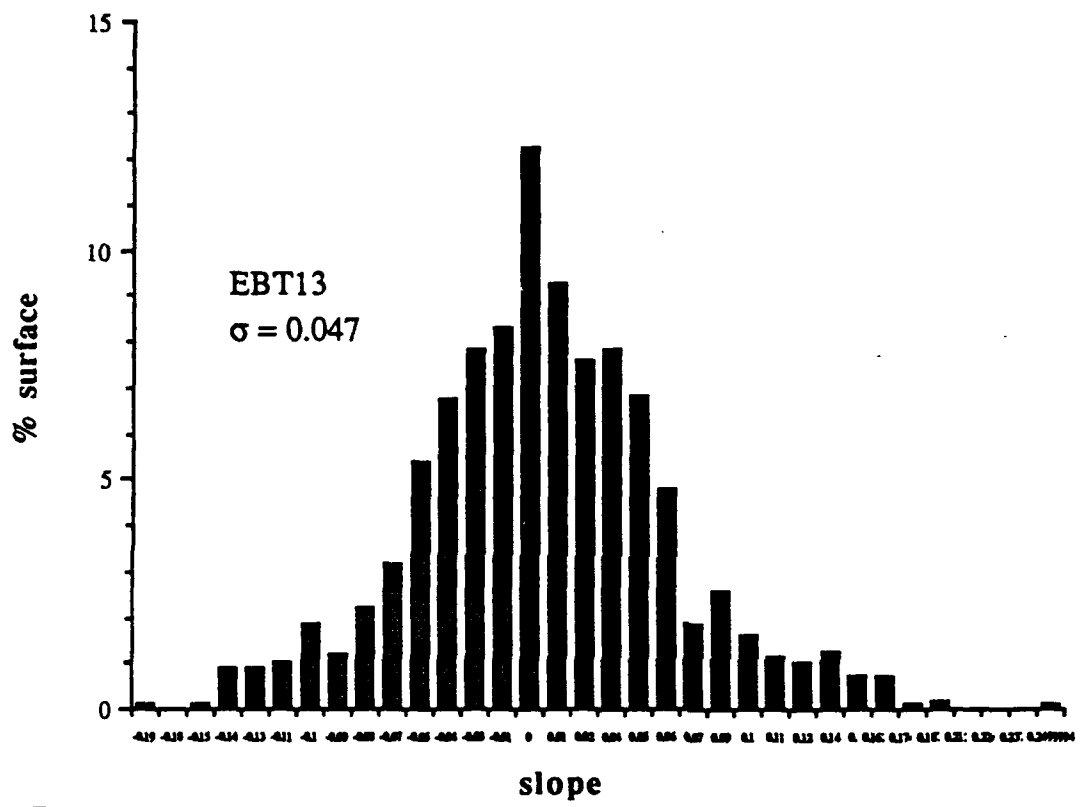


FIG. AC-165

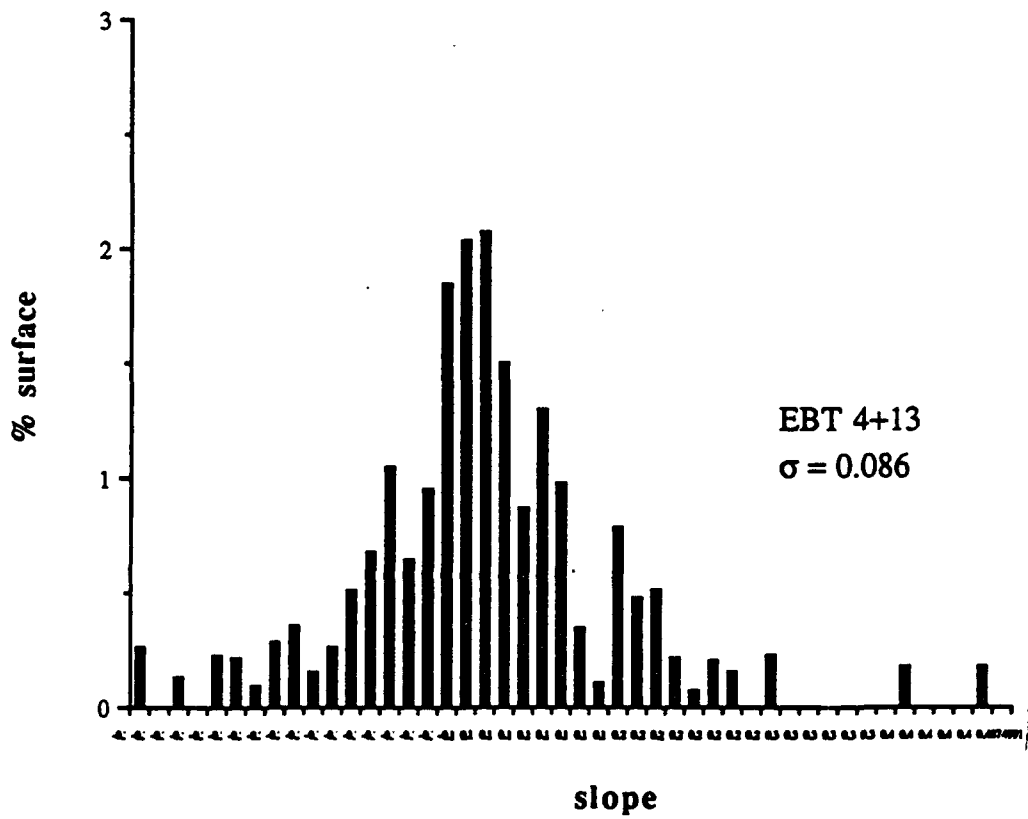


FIG. AC-166

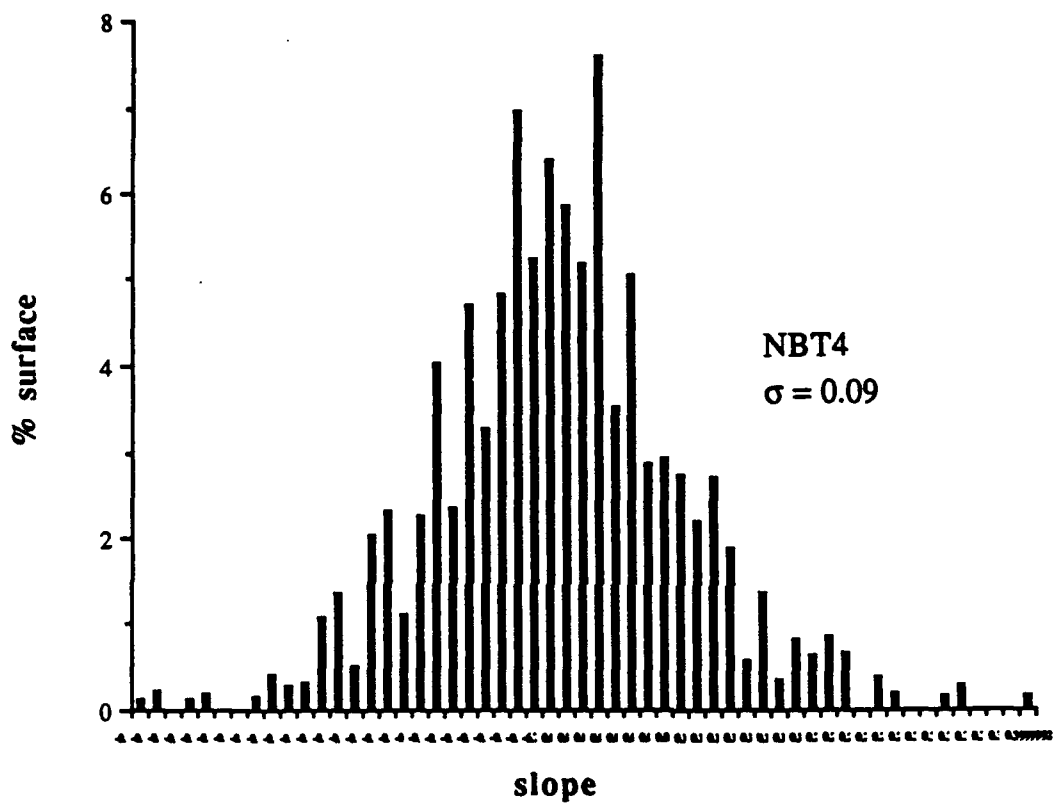


FIG. AC-167

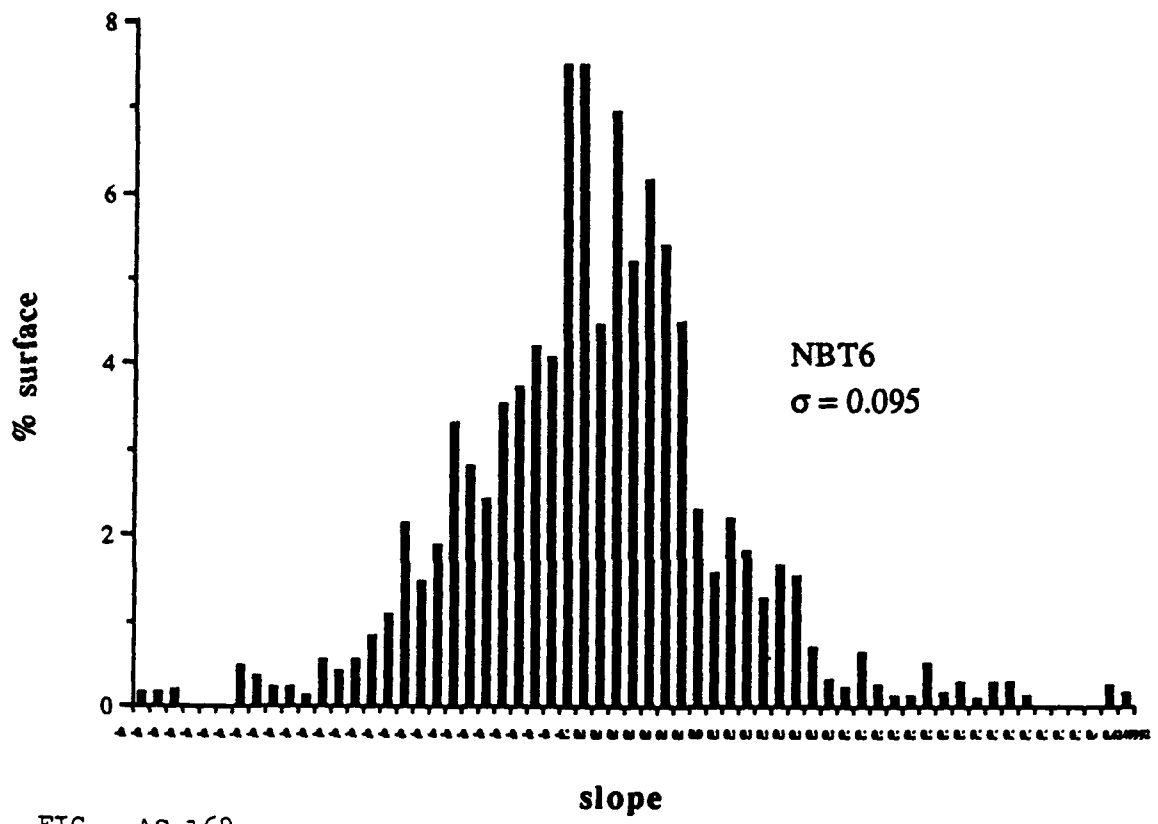


FIG. AC-168

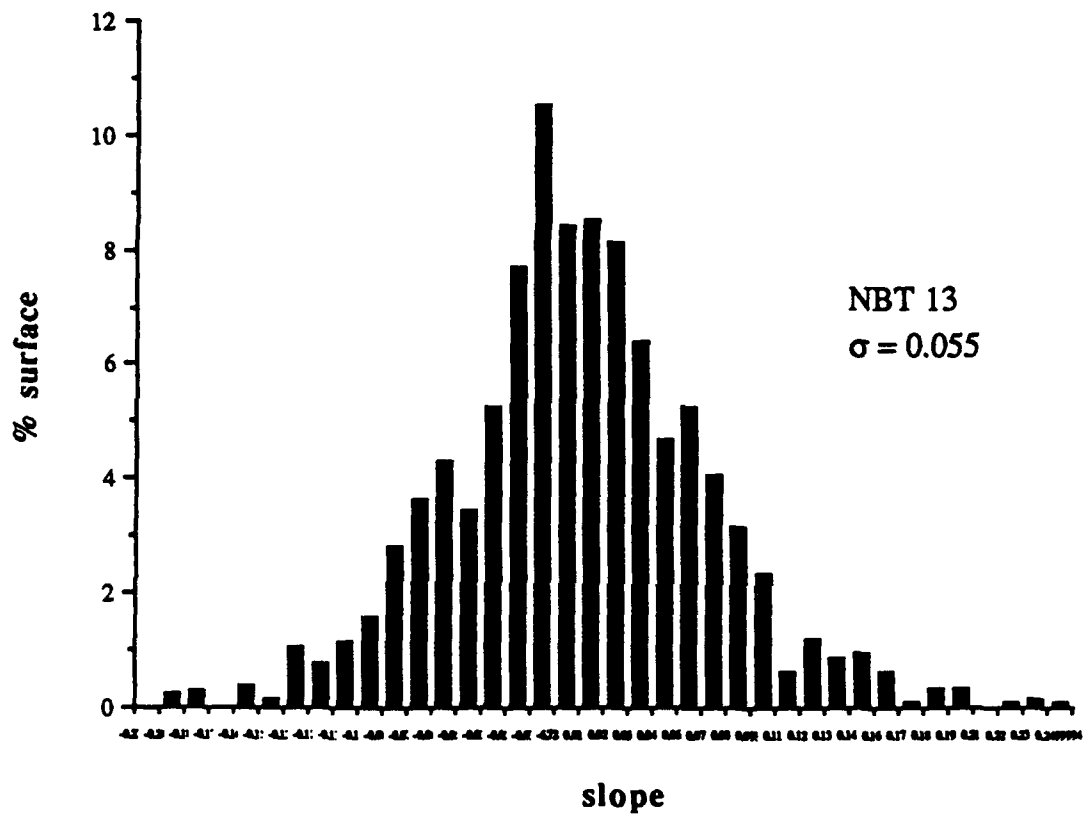


FIG. AC-169

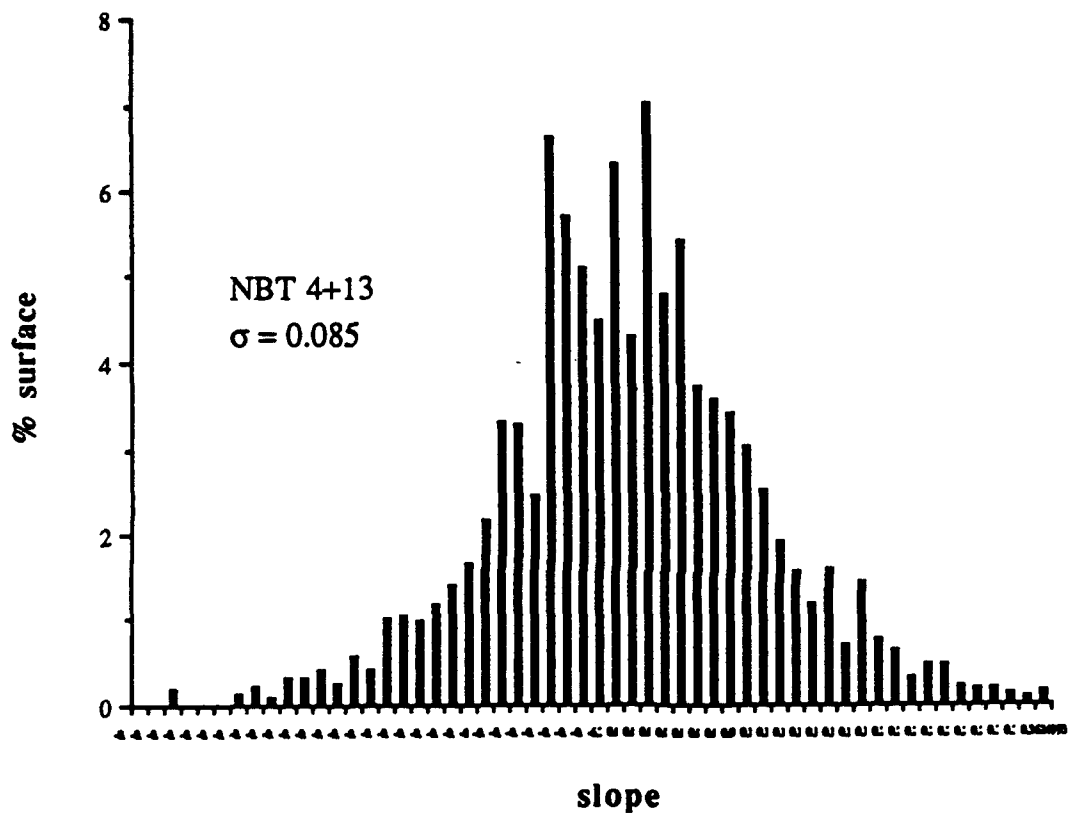


FIG. AC-170

TABLE I

TABLE OF SLOPE AND RADIUS OF CURVATURE STATISTICS FOR ROUGH SURFACES
USED IN SCATTERING CROSS SECTION MEASUREMENTS

GLASS BEAD (DIA.)	AVERAGE SLOPE	RMS SLOPE	STANDARD DEVIATION	• Radius of Curvature		% of Surface < 5 lambda	% of Surface < 6 lambda
				% of Surface < 3 lambda	% of Surface < 4 lambda		
E BT4 (500)	0.112	0.169	0.126	4.76	8.04	11.48	15.01
N BT4 (500)	0.091	0.129	0.09	4.61	6.86	10.57	13.64
E BT6 (250)	0.075	0.102	0.069	2.2	4.4	6.6	10.1
N BT6 (250)	0.094	0.134	0.095	7.1	11.8	17.4	21.9
E BT13 (50)	0.052	0.07	0.047	1.31	2.02	3.14	5.06
N BT13 (50)	0.058	0.08	0.055	1.98	4.41	7.05	9.43
E BT4+BT13 (Mix)	0.081	0.116	0.086	3.56	5.47	7.76	10.54
N BT4+BT13 (Mix)	0.092	0.125	0.085	4.88	8.62	12.64	16.11

* E = electropolished, N = not electropolished; slope and radius calculation based on 3000 points in 5 point groupings; profilometer measurements are one dimensional tracings in three directions through a point on the surface; % means percent of total number of data points; lambda = 10.6 microns.

Table II
Distribution of Slopes for Electropolished and Non-Electropolished Surfaces

GLASS BEAD (DIA.)	AVERAGE SLOPE	RMS SLOPE	STANDARD DEVIATION	Surface slope % of Surface < 0.05		Surface slope % of Surface < 0.10		Surface slope % of Surface < 0.15		Surface slope % of Surface < 0.20		Surface slope % of Surface < 0.25	
				•	•	•	•	•	•	•	•	•	•
E BT4 (500)	0.112	0.169	0.126	40.1	68.8	82.4	91.8					95.6	
N BT4 (500)	0.091	0.129	0.09	45.5	73.5	88.5	94.9					97.5	
E BT6 (250)	0.075	0.102	0.069	49.2	82.4	93.2	97.1					98.9	
N BT6 (250)	0.094	0.134	0.095	46.0	72.2	87.9	93.6					95.8	
E BT13 (50)	0.052	0.07	0.047	66.6	89.5	98.2	99.7					99.8	
N BT13 (50)	0.058	0.08	0.055	59.6	88.6	96.7	98.9					99.6	
E BT4+BT13 (MIX)	0.081	0.118	0.086	52.8	79.5	90.7	95.4					97.6	
N BT4+BT13 (MIX)	0.092	0.125	0.085	42.9	72.2	85.8	93.7					96.8	

Table III Null Depth at Three angles for Surfaces Studied

Incident/Scattered angles	EBT4	EBT6	EBT13	EBT 4+13	EBT4 (original)
7.5/7.5	0.015	0.01	0.007	0.009	0.026
10/10.	0.015	0.006	0.007	0.011	0.021
20/20	0.054	0.02	0.008	0.035	0.027
SUM OF AVG.	0.084	0.036	0.022	0.055	0.074

Table IV Surfaces Ranked from Deepest to Shallowest by Depth of Null

Rank (Depth of Null)	Surface	Facet Depth (Microns)	% Slope < .10	Radius of Curvature % of surface < 3 lambda
1	EBT13	3.12	89.5	1.31
2	EBT6	4.20	82.4	2.20
3	EBT 4+13	5.76	79.5	3.56
4	EBT4(original)	8.68	65.2	4.23
5	EBT 4	7.08	68.8	4.76

MISSION
OF
ROME LABORATORY

Rome Laboratory plans and executes an interdisciplinary program in research, development, test, and technology transition in support of Air Force Command, Control, Communications and Intelligence (C³I) activities for all Air Force platforms. It also executes selected acquisition programs in several areas of expertise. Technical and engineering support within areas of competence is provided to ESD Program Offices (POs) and other ESD elements to perform effective acquisition of C³I systems. In addition, Rome Laboratory's technology supports other AFSC Product Divisions, the Air Force user community, and other DOD and non-DOD agencies. Rome Laboratory maintains technical competence and research programs in areas including, but not limited to, communications, command and control, battle management, intelligence information processing, computational sciences and software producibility, wide area surveillance/sensors, signal processing, solid state sciences, photonics, electromagnetic technology, superconductivity, and electronic reliability/maintainability and testability.